Structural Chemistry of Hybrid Halide Perovskites for Thin Film Photovoltaics

Weber, Oliver

Award date:
2018

Awarding institution:
University of Bath

Structural Chemistry of Hybrid Halide Perovskites for Thin Film Photovoltaics

submitted by

Oliver Jacob Weber

for the degree of Doctor of Philosophy

of the

University of Bath

Centre for Sustainable Chemical Technologies

May 2018

Se vogliamo che tutto rimanga com'è bisogna che tutto cambi.

(For things to remain the same, everything must change.)

Tancredi to Don Fabrizio - THE LEOPARD

Abstract

Hybrid lead halide perovskites, AMX_3 compounds in which A = CH_3NH_3 (MA), $CH(NH_2)_2$ (FA), Cs; M = Pb,Sn; X = I, Br, Cl, display remarkable performance in solution-processed optoelectronic devices, including $>$ 22% efficient thin film photovoltaic cells. These compounds represent the first class of materials discovered to exhibit properties associated with high performance compound semiconductors, while being formed at or near room temperature using simple solution chemistry techniques. This thesis is focused on the synthesis, structural characterisation and phase behaviour of $MAPbI_3$, $FAPbI_3$, A-site solid solutions and novel organic metal halide framework materials.

The complete atomic structure and phase behaviour of methylammonium lead iodide is elucidated for the first time, including hydrogen positions, using high flux, constant wavelength neutron powder diffraction. At 100 K an orthorhombic phase, space group *Pnma*, is observed, with the methylammonium cations ordered as the C–N bond direction alternates in adjacent inorganic cages. Above 165 K a first order phase transition to tetragonal, *I4/mcm*, occurs with the unlocking of cation rotation, which is disordered primarily in the *ab* plane. Above 327 K a cubic phase, space group $Pm\bar{3}m$, is formed, with the cations isotropically disordered on the timescale of the crystallographic experiment.

The high temperature phase of formamidinium lead iodide, α-$FAPbI_3$ is shown for the first time to be cubic, ($Pm\bar{3}m$), at room temperature using time-of-flight, high resolution neutron powder diffraction. Polymorphism and the low temperature phase behaviour of $FAPbI_3$ have been further investigated using reactor and spallation neutron sources with high resolution in temperature. A tetragonal phase, *P4/mbm*, is confirmed in the temperature range 140-285 K.

The composition, structural and optical parameters of 'A' site solid solutions $(MA/FA)PbI_3$ have been investigated by single crystal X-ray diffraction, UV-vis spectroscopy and ^{1}H solution NMR. A composition-dependent transition in the crystal class from tetragonal to cubic (or pseudo-cubic) at room temperature is identified and correlated to trends in the optical absorption. Novel hybrid materials with inorganic frameworks of varying dimensionality from 0D to 2D, including imidazolium lead iodide and piperazinium lead iodide, have been synthesised using various templating organic cations and their atomic structures solved by single crystal X-ray diffraction.

Acknowledgements

First of all, I want to express my sincere gratitude to my supervisor Mark, for guiding me through all the ups and downs of research throughout my Master's degree and PhD.

Thank you to all of the members of the Weller group for all of your help and support over the course of this project. To Toni, Mako, Adam, Dom, Kayleigh, Beth and Pascaline. I hope there are many more cider festivals in future!

I also would like to thank all of the researchers who have helped, supported and worked in collaboration with me during my time in Bath. Thank you Chris Bowen, Aron Walsh, Petra Cameron and Mary Mahon. Keith and Jarvist - for showing me under the bonnet of DFT. Mariano Campoy Quiles, Alejandro Goni, Isabel Alonso, Federico Brivio, Aurelien Leguy, Thomas Hansen, Ivan da Silva, Paul Henry, Tristan Watson and Katherine Hooper. Also all support staff in Bath Chemistry, who keep the department running. To Laura Miranda-Perez and Alice Taylor for supervision at Oxford PV and to the whole team in Oxford for making me feel welcome.

DTC cohort '13, it has been a pleasure. Holey cheese, fine wine, quantum love, BEADS, terps, "what's the significance?", community service, deer tails, etc. etc.

To all my friends in Bath, I would not be finishing this PhD without your input, keeping everything in perspective.

To my family, who have helped and supported me without fail.

Declaration of Authorship

I declare that I am the author of this thesis, and the work described therein was carried out by myself personally between October 2014 and October 2017, at the University of Bath, under the supervision of Prof. Mark Weller and Prof. Chris Bowen, except where explicit reference is made to the input of others. Much of the research in Chapters 3-5 has been carried out in collaboration with scientists at European Universities and neutron beamline facilities.

Chapter 3 The experiment on D20 was carried out by Mark Weller, Antonietta di Pumpo, Thomas Hansen and Paul Henry. Initial data analysis and structural model development was carried out by Mark Weller and Paul Henry. Raman spectroscopy and ellipsometry measurements on $MAPbX_3$ crystals were carried out at ICMAB-CSIC, Barcelona, by Aurelien Leguy and Piers Barnes (Imperial College), Mariano Campoy-Quiles, Isabel Alonso and Alejandro Goni. Solar cell fabrication was carried out at SPECIFIC, Swansea, with guidance from Katherine Hooper.

Chapter 4 The data collection on HRPD was carried out with Kevin Knight, Kayleigh Marshall, Adam Dennington and Ben Hogan. *Ab initio* calculations and molecular dynamics simulations were run by Jarvist Frost and Aron Walsh.

Chapter 5 *Ab initio* calculations and molecular dynamics simulations were carried out by Dibyajoti Ghosh, Saiful Islam and Alison Walker. Sam Gaines contributed to the development of synthetic techniques.

Chapter 6 Bethan Charles assisted in the synthesis and powder X-ray diffraction. The syntheses and kinetic analysis of thin film degradation rates were also carried out by Bethan Charles.

.....

Oliver J. Weber

May 2018

Contents

List of Figures

+

List of Symbols

Physical Constants

Symbol	Name	Value	Unit
e	elementary charge	1.602×10^{-19}	C
m	electron mass	9.109×10^{-31}	kg
m_n	neutron mass	1.675×10^{-27}	kg
c	speed of light in a vacuum	2.998×10^{-8}	$m\ s^{-1}$
ε_0	vacuum permittivity	8.854×10^{-12}	$F\ m^{-1}$
h	Planck's constant	6.626×10^{-34}	$m^2\ kg\ s^{-1}$
K_B	Boltzmann's constant	1.381×10^{-23}	$m^2\ kg\ s^{-2}\ K^{-1}$

Physical Variables

Symbol	Name	Unit
ε	dielectric function	$F\ m^{-1}$
E_B	exciton binding energy	eV
μ	electron / hole mobility	$cm^2\ V^{-1}\ s^{-1}$
L_D	electron / hole diffusion length	m
τ	relaxation time	s
K_BT	thermal energy	eV
E	Young's modulus	GPa
s	conductivity	$S\ cm^{-1}$
a	absorption coefficient	-
η	solar cell efficiency	-
n	charge carrier density	-
N	density of states	-
E_g	band gap	eV
EQE	external quantum efficiency	-
J_{SC}	short circuit current density	$mA\ cm^{-2}$
V_{OC}	open circuit voltage	V
J_0	reverse saturation current	$mA\ cm^{-2}$
q	charge	C
θ	Bragg scattering angle	rad
d_{hkl}	interplanar spacing	Å
b_n	neutron scattering length	m
L	neutron path length	m
λ	wavelength	m
Q	momentum transfer vector	$Å^{-1}$
$y_i(obs)$	observed stepwise intensity	-
R_{wp}	weighted R factor	-
χ^2	goodness of fit	-
$F_{(hkl)}$	structure factor	m
U	atomic displacement parameter	$Å^2$

List of Abbreviations

ADP	Atomic displacement parameter
CIGS	Copper indium gallium sulfide selenide
CZTS	Copper zinc tin sulfide selenide
DSSC	Dye-sensitised solar cell
FAPBr	formamidinium lead bromide
FAPI	formamidinium lead iodide
FTO	Fluorinated tin oxide
GEM	General materials diffractometer
HRPD	High resolution powder diffractometer
ITO	Tin-doped indium oxide
LED	Light-emitting diode
MAI	methylammonium iodide
MAPBr	methylammonium lead bromide
MAPCl	methylammonium lead chloride
MAPI	methylammonium lead iodide
NPD	Neutron powder diffraction
OPV	Organic photovoltaic
PTAA	poly triarylamine
PV	Photovoltaic
Spiro-OMeTAD	2,2',7,7'-Tetrakis[N,N-di(4-methoxyphenyl)amino]-9,9'-spirobifluorene
TOF	time-of-flight
XRD	X-ray diffraction

Chapter 1

Introduction

The research results in this thesis address current challenges in the materials chemistry of hybrid perovskites. These materials have become increasingly significant due to their potential applications in solution processed thin film solar cells and other optoelectronic devices. Chapter 1 sets this research in the general context of sustainable technologies, addresses the motivations for developing materials to harvest sustainable energy and assesses why this an important goal. The literature on hybrid perovskites for solar energy conversion is reviewed and a general background provided for the experimental studies undertaken.

1.1 Sustainability Indicators

Rather than one of the traditional demarcations of scientific subject, the subject area of this doctorate is 'Sustainable Chemical Technologies', so what do these denote? Since the Industrial Revolution unshackled civilisation from the primary energy limits imposed by daily biological fixation of sunlight via photosynthesis (chemoautotrophy aside), expansive human development has taken place at an unparalleled rate (Figure 1-1a). This great acceleration has been propelled forward by the chemical potential difference between reduced and oxidised forms of carbon, fossil energy combustion, 'the hidden principle behind every artefact we create.' Indicators for human development are rising and on average, year on year, more people are living longer and more affluent lives.[1] The tension between this unconstrained human development success story and the mounting physical problems created in its wake carries profound implications that are practical, yet also philosophical; an urgent design problem usually referred to as sustainability.

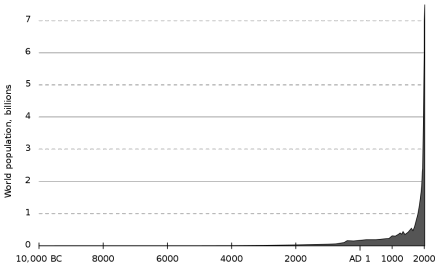

(a) Estimated human population growth since the advent of agricultural society.

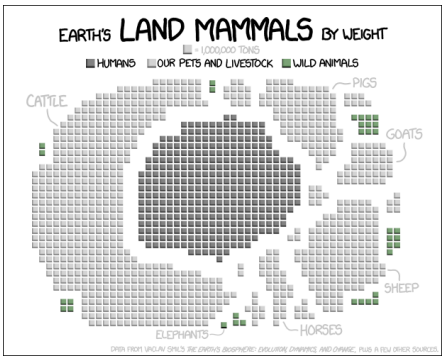

(b) Current terrestrial mammalian biomass. By XKCD, data from Smil.[8]

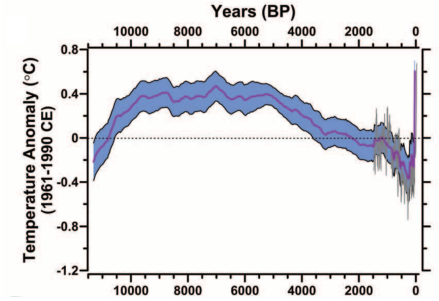

(c) Global temperature reconstruction, from Marcott et al.[9]

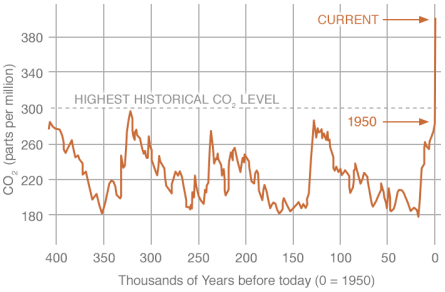

(d) Atmospheric CO_2 levels, Vostock ice cores and current measurements.[10]

Figure 1-1: Global change and sustainability indicators

The fundamental processes of modern civilisation currently support seven billion people (and two hundred thousand more every day) while degrading their surroundings and depleting renewable resources faster than they are replenished. Without consciousness of these impacts and cooperation to mitigate them, human development gains stand at risk of being undercut by these limits and excesses. This has generally been true in the past, but the accelerated pace and global reach of human activities means that these effects are increasingly a dominant driving force across multiple planetary systems.[2,3] These problems manifest mainly as resource overuse, in subsuming or crowding out the biosphere, and as pollution streams including fixed nitrogen and phosphorus,[4] particulates,[5] heavy metal and organic toxicants,[6] greenhouse gasses and physical waste including plastics.[7] With many of the previous inhibiting regulatory checks on human growth lifted, whether we preserve ecological integrity and avoid driving planetary conditions into unfavourable states for habitation will define the future. Many indicators, where data are available, display alarming trends; these are particularly clear-cut for climate change and the rate of species population decline.

Recent acceleration in species population decline is so severe that it has been called, within the peer-reviewed literature, a 'biological annihilation' or 'sixth great mass extinction.'[11–14] Terrestrial vertebrate populations have decayed, with more than 40% of the species monitored experiencing severe population declines of >80% range shrinkage (Figure 1-1b),[14] with loss in ecological function occurring well before actual extinction. On land and in the oceans, the available data tell the same story: productivity gains through technological development have partially offset the consumption patterns of a growing human population, but not enough to assuage the resultant negative impacts from accumulating in the biosphere.

Greenhouse gas emission is another indicator of humanity's impact in driving global change by failing to regulate the composition of the atmosphere (Figure 1-1d).[15,16] Atmospheric CO_2 has risen from 270 ppm to over 400 ppm since the industrial revolution, with >90% of the extra heat from greenhouse gas sourced to human emissions absorbed by the oceans, which are rising by 3.2 $\pm$ 0.4 mm per year, warming, deoxygenating and acidifying.[17,18] Earth has precedence for CO_2 above 400 ppm during the Pleiocene 3.3 - 3 Ma, when temperatures reached 2-3.5 °C above pre-industrial and sea levels were 20 $\pm$ 10 m higher than today.[19] The risks posed by rapid environmental changes are spurring huge efforts to create technologies to support a sustainable and resilient civilisation.

1.2 Renewable Energy

A 'Terawatt challenge' exists to generate energy while drastically reducing greenhouse gas emissions. Current total demand is around 17 TW of power, projected to rise to around 30 TW by 2050, with high energy consumption inextricably linked to human development and life-quality. The challenge is to supply these 30 TW while dramatically reducing greenhouse gas emissions and air pollution, which largely arise from combustion of carbonaceous fuels.[20] To become widely adopted, low carbon energy must be cost competitive and as convenient as any other alternative.

174,000 TW of sunlight are incident on the Earth, of which 30% is reflected back to space by the upper atmosphere. Harnessing the solar resource is therefore a clear route to provide worldwide sustainable energy. Renewable energy resources are diffuse ($<$ 1 kW m^{-2}) and tend to be intermittent, with both diurnal and seasonal variability, though solar thermal, hydroelectric and tidal power can be used continuously. Solar photovoltaics (PV) are optoelectronic devices that convert sunlight directly into electricity. The collection area of 15% efficient PV (the average commercial silicon module efficiency) to meet 17 TW

demand is ≈ 500,000 km^2, or 1% of the land area of the Sahara desert.

Since electricity from solar PV or wind is non-dispatchable, it must be coupled to energy storage and / or high voltage transmission lines for significant grid uptake. Additionally, more energy is currently required as fuel than electricity, so either electrification of transport and processes, or systems for conversion of sunlight to chemical fuel, are required for renewable energy to have a large impact beyond the electric grid.[21] Renewable energy is far more equitably distributed around the planet than fossil fuel resources and a future energy system integrating renewables, daily and seasonal energy storage, natural gas and nuclear power has the potential to emit far less CO_2 while providing greater resiliency towards natural or geopolitical shocks than is currently the case.

1.3 Semiconductor Materials

Since the following Sections 1.4 and 1.5 discuss different semiconductors applied in photovoltaic devices, this section briefly reviews the properties of semiconductor materials that make them integral to photovoltaic technology. In a crystalline semiconductor, electrons occupy delocalised electronic states in energy bands up to the valence band maximum (VBM). Between the VBM and the empty conduction band minimum (CBM), an energy region with zero density of states defines the band gap. Electrons may be promoted to higher energy states by thermalisation or absorption of a photon with E $>$ E$_g$. Semiconductors with an energy band gap matching the energy of photons in the visible spectrum are applied for absorbing sunlight in photovoltaic cells.

Bloch wavefunctions of the form given in Equation 1.1 describe delocalised electrons within the periodicity of a crystalline lattice.

$$\psi(\mathbf{r}, \mathbf{k}) = e^{i\mathbf{k}\cdot\mathbf{r}} u_{i\mathbf{k}}(\mathbf{r}) \tag{1.1}$$

For a wavevector **k** for each *i*th crystal band, solutions to Schrodinger's equation provide the eigenenergies E(**k**). All information about $E(\mathbf{k})$ is contained within $0 < k, \pi/a$, the first Brillouin zone, and is conventionally plotted as $E(\mathbf{k})$ versus |**k**| along lines connecting high symmetry points in the Brillouin zone, e.g. Figure 1-15 in Chapter 1.

The effective masses of electrons and electron holes in the conduction and valence bands are found from the curvature of conduction and valence bands, assuming parabolic bands (the simplest case). For many materials, $m_C^* > m_V^*$ and so electrons have greater mobility

than holes.

$$E(\mathbf{k}) = E_0 + \frac{\hbar^2 \mathbf{k}^2}{2m^*} \tag{1.2}$$

If the conduction band minimum and valence band maximum appear at the same point in momentum space, then the material possesses a direct band gap. For indirect band gap materials, CBM and VBM differ in **k**. Since crystal momentum is conserved, the change in momentum is (usually) phonon mediated and absorption for an indirect band gap material is limited by the number of available phonons with requisite **k**. Direct band gap materials consequently tend to exhibit higher absorption coefficients than indirect band gap materials.

The Fermi level is an important concept in solid state science relating the electrochemical potential of electrons to the band structure of the semiconductor. E_F is defined as the energy with exactly 50% probability of being occupied by an electron. For a perfect intrinsic semiconductor in thermodynamic equilibrium, E_F lies in the centre of E_g. At finite temperature some electrons will be thermalised to the conduction band and an equivalent number of holes will be present in the valence band. Within the Boltzmann approximation, the intrinsic carrier density is given by

$$n_i^2 = np = N_c N_v e^{\frac{-E_g}{K_B T}} \tag{1.3}$$

where $N_{c/v}$ is the density of states in the conduction / valence band. For p or n doped semiconductors, the concentration of one carrier type changes and E_F lies closer to the VB or CB, respectively. Out of equilibrium, for instance under illumination, carrier concentrations change and new quasi-Fermi levels are defined, with different chemical potentials.

1.4 Solar Cells

A photovoltaic cell is an optoelectronic device that converts the energy from light into electrical energy via the photovoltaic effect. It is comprised of semiconductor materials that absorb photons of light by excitation of electrons and transport electronic charges to an external load-bearing circuit. The electromagnetic radiant energy of the photons is converted into electrochemical potential energy by promotion of electrons within a semiconductor to higher energy excited states upon absorption. These photogenerated electrons and holes must be mobile and have to be extracted by contacting electrodes to do electrical work before they recombine, in order to harvest the energy of the cell.

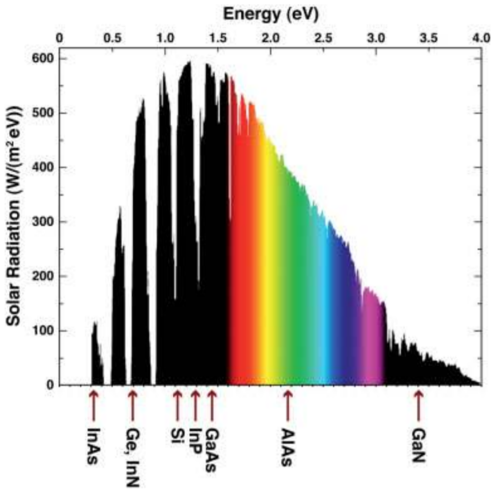

Figure 1-2: AM1.5 Spectrum compared to common semiconductor band gaps

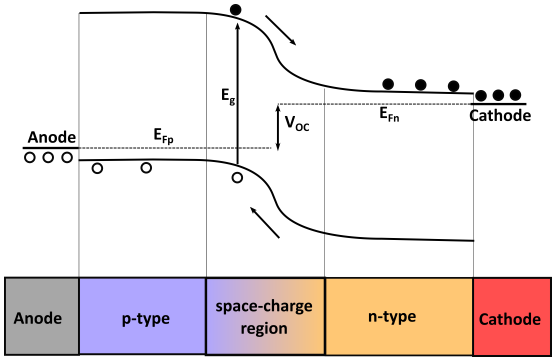

Figure 1-3: PN junction solar cell.

The sun is well approximated by a blackbody emitter at 5780 K. The solar spectrum for Earth peaks in the blue-green visible spectrum and average solar irradiance at ground level ranges from 300 W m^{-2} to 100 W m^{-2} at high latitudes. Semiconductors with band gaps well matched to the wavelengths of visible light (E_g = 1 - 1.5 eV) are well suited to harvest incident solar energy and transport photogenerated charge carriers. Figure 1-2 compares the Air Mass 1.5 (1 sun = 1000 W m^{-2}) reference spectrum to the band gaps of common semiconductors. Shockley and Quiesser found the detailed balance limit to solar cell efficiency of a single PN junction at one sun intensity to be around 33.7% for a 1.34 eV band gap material.[22]

The most ubiquitous solar cell is the silicon PN homojunction. Figure 1-3 depicts the band structure of a simple PN junction. In contact, electrons in n-region diffuse into the p-layer and vice versa for holes, leaving behind ionised donor atoms in the lattice in a depleted

space-charge region. The electric field in the depletion layer creates a diode effect and large built-in bias that drifts photogenerated electrons towards the n-side and holes towards the p-side, effectively separating charge carriers. In silicon, commonly used dopants include heterovalent ions such as phosphorus (n-doping) and boron (p-doping). By convention, negative carriers collect at the cathode, positive carriers at the anode.

PIN junctions are also employed in solar cells, in this case the built-in potential originates from the p and n regions, while the electric potential drops across the intrinsic layer. This device structure is preferred when the minority carrier diffusion length is short in the P and N layers, or the semiconductor cannot be reliably P/N doped. Asymmetric rectifying contacts further serve to collect charges and provide a potential difference across the cell.

Solar photovoltaics have advanced dramatically since their discovery (Figure 1-4). In 1883 Charles Fritts demonstrated the first solar cell of gold coated selenium at 1% efficiency.[23] Regarding this discovery, Walter von Siemens commented: *"I would say however great the scientific importance of this discovery may be, its practical value will be no less obvious when we reflect that the supply of solar energy is both without limit and without cost, and that it will continue to pour down upon us for countless ages after all the coal deposits of the earth have been exhausted and forgotten."*[24] Silicon PN junction solar cells with 6% efficiency were realised in 1954, with advances in silicon wafer processing for solid state electronics.[25] The 1970s oil crisis led to growing interest in alternative energy sources and by 1977, the price of a polysilicon solar cell was around \$77 / W. Dramatic cost reductions to $<$\$0.5 / W have been brought about by up-scaling and technological progress and electricity from PV is increasingly cost-competitive with other sources. As a result, worldwide PV generation capacity is currently rising exponentially, reaching 400 GW in 2017.

1.4.1 Silicon PV

Silicon dominates the single junction utility PV market due to high efficiency, low cost and long lifetime reliability ($>$25 years). The raw materials are cheap and abundant, a huge manufacturing ecosystem has developed to supply silicon to the microelectronics sector and Si-PV module prices continue to decline. Monocrystalline Si cells, composed of 100-300 μm thick, self-supporting Si wafers have reached 26.1% efficiency,[27] limited by remaining carrier recombination losses. The main drawbacks to Si-PV are that the embodied energy is necessarily large due to high temperature Si crystal growth, with 1-2.5 years the time for energy payback invested in manufacture and deployment of the panel, and that the panels are heavy and inflexible, since the indirect band gap of Si mandates relatively thick layers for efficient light absorption.

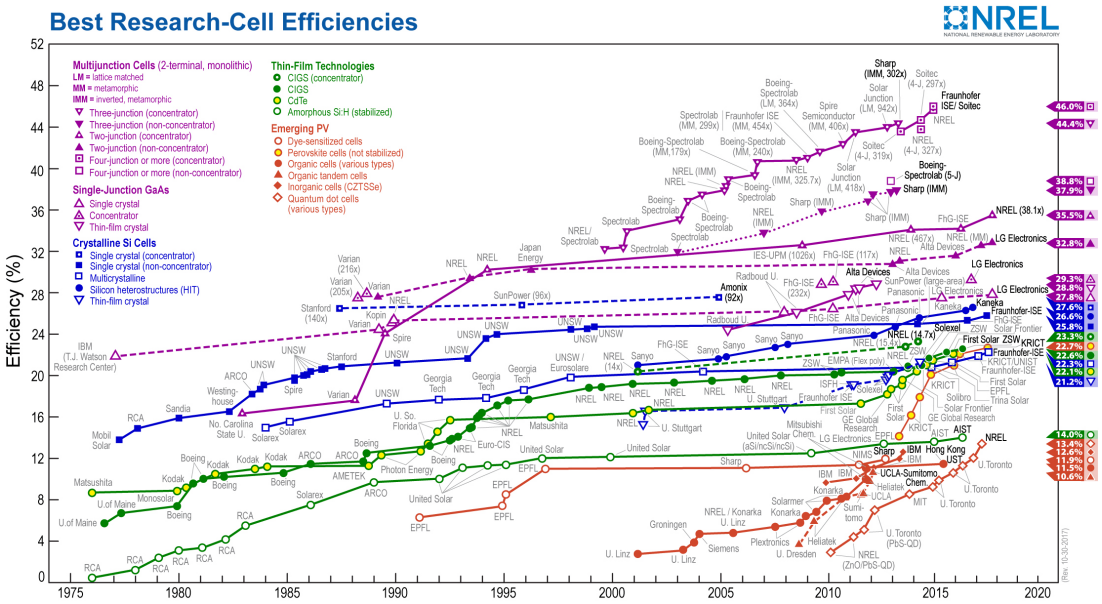

Figure 1-4: NREL efficiency chart of photovoltaic technologies, from the Solar Cell Efficiency Tables version 51.[26]

1.4.2 Thin film PV

Thin film PV technologies including GaAs, CIGS and CdTe are commercially available and use about 1% as much absorber material as Si cells, though have struggled to compete commercially due to various combinations of lower efficiencies, higher material costs and the aggressive cost-reductions of Si panels. III-V semiconductors, e.g. InP / GaInP, are used in multijunction devices (efficiency η <46%) in specialist applications including space and concentrated solar power.[28] GaAs single junction efficiency has improved dramatically in recent years thanks to high luminescence efficiency and improved photon management, reaching 28.8% with minimal recombination losses, making GaAs the highest efficiency single junction material.[29]

Compound chalcogenide CIGS cells, $Cu(In,Ga)(Se,S)_2$, have reached 21.7% efficiency.[30] Typically 2-3 μm polycrystalline CIGS films are sputtered or evaporated onto Mo on soda-lime glass, with an overall device stack of Mo/CIGS/CdS/ZnO:Al. Other multi-ternary chalcogenides are being explored for thin film photovoltaics, for instance CZTS, $Cu(Zn,Sn)(S,Se)_2$, which is derived from CIGS by isovalent substitution of In^{3+}/Ga^{3+} for Zn^{2+}/Sn^{4+} and formed only of earth abundant elements. Current record efficiencies for CZTS are around 12.6%, limited by large voltage losses which stem from its bulk defect structure and interfacial losses.[31,32]

Cadmium telluride, a II-VI compound semiconductor with zinc blende structure, has been commercially developed up to 22.1% efficiency.[26] Part of the attraction of this technology is the practicality of CdTe deposition from its elements as a congruently sublimed layer in FTO/CdS/CdTe/Al device stacks. Despite containing cadmium, toxicity of CdTe is not currently considered a major problem due to the low biological availability of Cd in compound form.[33] Scarcity of Te is a factor in determining ultimate scalability of CdTe technology.[34]

1.4.3 Emerging PV Materials

Organic photovoltaics (OPV) composed of small molecule or polymer organic semiconductors have been extensively researched. The attractiveness of these materials lies in the possibilities for high volume processing, though OPV efficiencies are lower than other PV technologies at 11.2% (single junction).[35,36] The low dielectric constants of organic materials result in high exciton binding energies, while low carrier mobilities result in short diffusion lengths, on the order of 10 nm, before photogenerated charge carriers recombine.[37] The donors and acceptors in absorber layers (e.g. P3DT/PEDOT:PSS) are therefore blended with intermixing on the nanometre scale in bulk heterojunctions to facilitate exciton dissociation and charge extraction.

Dye-sensitised solar cells (DSSCs) consist of organic or inorganic dyes affixed to nanostructured wide-band gap semiconductor supports, most often TiO_2, on top of a transparent conducting contact.[38] These dyes absorb sunlight extremely efficiently for the photogeneration of excitons, however do not exhibit long-range charge transport. Dissociation of photogenerated charge carriers by injection of electrons into the TiO_2 scaffold must therefore occur before the charge carriers recombine within the dye molecule. Regeneration of the oxidised dye takes place via a redox couple, often solutions of I^-/I_3^-, which is itself reduced at a counter electrode (e.g. Pt). Despite their status as a moderately mature technology, with several commercial ventures, DSSCs have so far struggled to reach mature commercial status due to relatively limited efficiencies (record $\eta = 14.1\%$) and problems with liquid electrolyte lifetime stability.

Ideal solar cells should be: a) composed of abundant elements, b) non-toxic, c) low cost, d) low in embodied energy, e) highly stable and f) highly efficient.[39] Emerging materials for PV including SnS, Sb_2S_3, Cu_3N and Zn_3P_2, which have been predicted to display suitable material properties as PV absorbers, but have yet to be demonstrated in reasonable ($>$10%) efficient solar cells.[40,41] Figure 1-5 summarises the status of different PV technologies in terms of their efficiency and from where device losses arise.

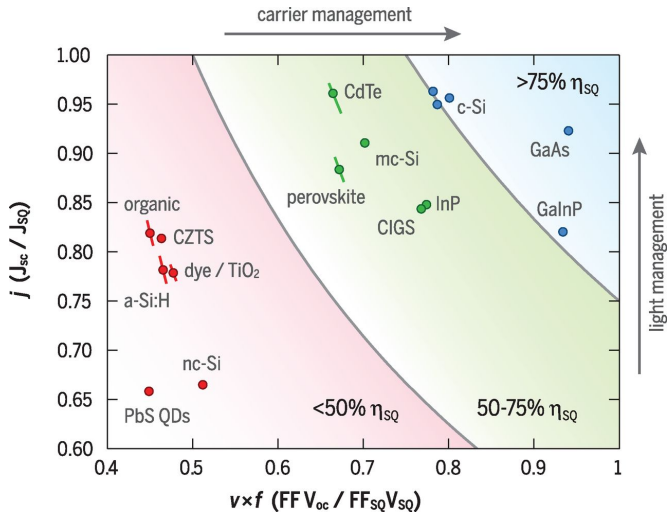

Figure 1-5: Comparing the efficiency, charge carrier and photon losses in different PV technologies. From Polman et al., reprinted with permission from the AAAS.[42]

1.5 Hybrid Organic-Inorganic Perovskite PV

Organic-inorganic hybrid perovskites have sparked intense research since it was widely recognised in 2012 that they could be applied as the light absorbing layer in solution processed, high efficiency solar cells.[43–48] These materials, based on late group IV M(II) halide salts and organic molecular cations, display many properties suitable for PV absorbers. The following sections review the literature on metal-halide perovskite materials and technology, focusing on the current state of understanding of the chemistry, atomic structure, optoelectronic properties and application in photovoltaic devices. Figure 1-6 displays the atomic structure of methylammonium lead iodide, while the perovskite crystal structure is explored in detail in Section 1.6.

The synthesis of hybrid perovskite materials is reviewed in Section 1.7, while the electronic band structure that makes these materials so applicable for optoelectronic applications is outlined in Section 1.8. Other relevant physical properties, including atomic defect structure and ionic conductivity in hybrid perovskites, are explored in Section 1.9.

1.5.1 Initial Development

Hybrid lead and tin halide perovskites were investigated by David Mitzi's group at IBM throughout the 1990s for solution processable optoelectronics, though with the focus on layered hybrid perovskites for transistors and LEDs, rather than solar cells.[49–52] The first

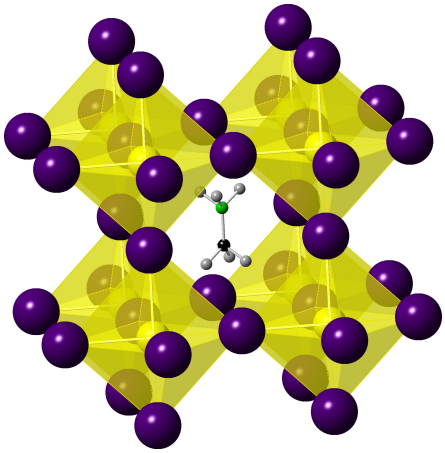

Figure 1-6: Methylammonium lead iodide atomic structure with vertex connected $[PbI_6]^-$ octahedra and a methylammonium cation (MA^+) occupying the central cubeoctahedral void space. MA^+ depicted in one orientation for clarity. Atom colours: Pb - yellow, I - purple, C - black, N - green, H - grey.

solar cells based on hybrid perovskites were created in 2009 and employed these as a drop-in replacements for the dye in liquid dye-sensitised solar cells, with an efficiency of 6.5% and very poor stability.[47] In 2011, a 6.5% efficient perovskite quantum dot sensitised solar cell was also reported.[53]

The first reports of solid state hybrid perovskite solar cells in 2012 employed mesoporous TiO_2 infiltrated with methylammonium lead iodide ($MAPbI_3$), with efficiencies of 9.7%,[54] and 10.9% respectively.[55] These meso-superstructured solar cells utilised mesoporous TiO_2 both to template crystallisation and as a selective electron extraction layer. One significant development of Lee et al.[55] was to replace the mesoporous TiO_2 (a legacy of DSSCs) with Al_2O_3, which as an insulating scaffold demonstrated that long range charge transport occurred within the perovskite layer. Planar devices were then demonstrated, indicating categorically that ambipolar charge transport occurred within $MAPbI_3$, with both electrons and electron holes exhibiting significant mobility.[56,57] Another early demonstration of all-inorganic perovskite solar cells employed $CsSnI_3$ / N719 dye in a perovskite / solid state dye cell hybrid.[58]

Figure 1-7 depicts typical device architectures of perovskite PV cells. The cells are formed on top of a transparent conductive contact and substrate, in research devices usually FTO or ITO glass. A rectifying contact of a low workfunction, electron transport / hole blocking layer is deposited onto the transparent contact, followed by sub-micron film of perovskite absorber. A high workfunction hole transport / electron blocking layer and a back contact, typically vacuum deposited Au or Ag, complete the asymmetric device.

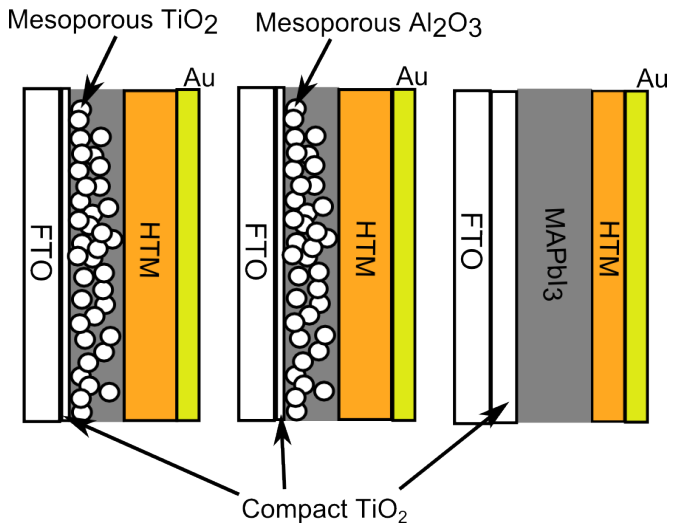

Figure 1-7: Device layers in perovskite solar cells for mesoporous TiO_2, Al_2O_3 and planar devices.

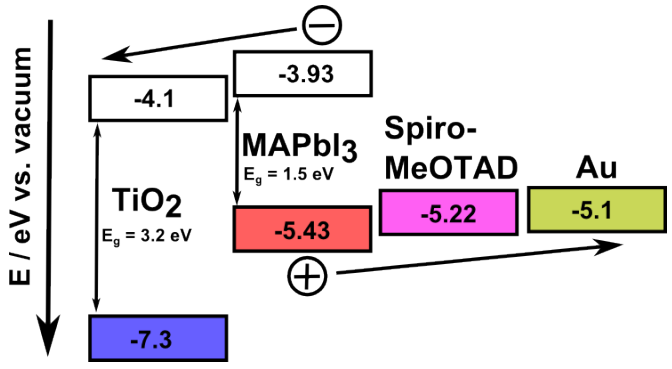

Figure 1-8: Energy levels and charge transfer within perovskite solar cells.

Since the first demonstration of solid state perovskite photovoltaic devices in 2012, development has been explosively fast. After decades of progress on successive generations of photovoltaic materials, a large research community was well prepared to interrogate and push forward a promising new candidate material. Deposition of the active device layers can be accomplished by simple techniques, using readily available laboratory equipment rather than high-specification semiconductor processing equipment, so the barrier to entry into the field has been substantially lower than for other solar cell technologies and many diverse strategies could be quickly explored, leading to rapid evolution and technological maturation.

Despite large scale physical and computational efforts towards screening new candidate compounds for potential solar cell absorbers, hybrid organic-inorganic perovskites arrived completely unexpectedly in high-performance solar cell technology. Hybrid perovskites represent the only known class of high performance ionic halide semiconductors and the only known solution processable, high efficiency ($>$15%) solar cells. Within a rapidly evolving evidence base concerning their fundamental properties, what has become abundantly clear is that the electronic defect structure within these highly defective materials does not seriously inhibit their function within optoelectronic devices, as it does for many conventional inorganic semiconductors. It is likely that several aspects of the dynamic physical properties hybrid perovskites display work synergistically for this to be the case.

To develop a new solar cell material, it has generally been necessary to understand in atomic level detail the structure and defect chemistry in order to engineer-out the causes of non-radiative recombination and voltage losses, by designing processing conditions to passify all efficiency-killing defects. Surfaces and interfaces to other materials in the device architecture also play crucial roles in defining current and voltage deficits. For this reason, Si photovoltaics are dependent on industrial production of high quality crystalline silicon as a feedstock. In contrast to Si, perovskites are at deposited at low temperature from solution, are necessarily highly defective, yet have efficiencies approaching those of single crystal Si. While solar grade Si is generally 6N pure (99.9999%), to minimise inclusion of defects arising from extrinsic impurities, perovskites have been shown to support inclusion of most transition metal ions up to a few parts-per-hundred without appreciable loss in device efficiency.[59] For this to be the case, their electronic defect structure must be intrinsically benign, or physical processes exist, to protect charge carriers from non-radiative recombination pathways.

Hybrid perovskites also present a series of unique challenges for experimental characterisation compared to inorganic semiconductors. These include dynamic properties over multiple time and length scales involving ionic conduction, electronic charge transport, local struc-

tural ordering and molecular dynamics. Hybrid perovskites display a lack of stability on exposure to many environmental factors, or thermodynamic metastability for certain compositions, which creates challenges for the accurate determination of material properties. A practical solar module must withstand the combined effects of light, heat and thermal cycling, humidity and chemical interaction with other device layers for a lifespan of years to decades. While stability is currently the limiting factor in perovskite technology, advances have seen modules start to pass standard industry damp-heat tests (1000 h, 85% RH, 85 °C).[60]

1.5.2 Advances in Photovoltaic Devices

Hybrid perovskites research has diverged into several strands, including tandem cells,[46,61] printed flexible perovskite cells with carbon electrodes,[62] inorganic perovskite nanocrystal PV and other optoelectronic devices including quantum dot LEDs, photodiodes, X-Ray / γ-Ray detectors and memristors.[63–65] A wide range of chemical substitutions are possible, leading to greatly varied properties. Improvements have stemmed from compositional variation within the perovskite layer to tune bulk properties, including band gap and stability, judicious choice of adjacent cell layers, overall cell architectures, processing procedures and techniques to optimise the growth of polycrystalline thin films.

The current record efficiency for single junction perovskite PV is 22.7% for small area cells and 20.9% for 1 cm^2 cells.[66] These cells employ FTO / TiO_2 / meso-TiO_2 / FAPI/MAPBr / PTAA / Au and are included in solar cell efficiency tables, though are listed as 'not stabilised' to environmental conditions.[26] FAPI refers to formamidinium lead iodide and MAPBr to methylammonium lead bromide. Current trends in perovskite solar cell research are focused on long term device stability,[64,67,68] 3D/2D perovskites,[69] all-inorganic halide perovskite cells,[70] quantum dots and nanocrystals for PV and LEDs.[71] Triple A-site cation cells combining Cs/MA/FA are extensively researched for increased stability,[72] along with scale-up of process engineering from cell to module, involving roll-to-roll solution processing or vacuum deposition, and the economic viability of these modules.[73] A search for lead-free ns^2 defect tolerant absorbers is also ongoing.[74]

Many of the already described processing and device layer advances have yet to be combined together. Fill factor and short circuit current can be improved through optimisation of perovskite films, identifying recombination pathways and developing more optimal interfacing and electrode materials. To take examples of the likelihood of further advances through simple chemical treatments: photoluminescent quantum efficiency in tri-n-octylphosphine oxide-treated perovskite films increased to 35$\pm$1% and charge carrier lifetimes, τ, as long

as 8.82±0.03 μs.[75] A room temperature pyridine mediated recrystallisation process turned 9.5 % efficient cells into 18 % cells in one step.[76] The Lewis basic pyridine vapour reacts with perovskite to form an amorphous adduct of py_2PbI_2, followed by spontaneous recrystallisation to large grain, pinhole free perovskite phase, as the chemical potential of pyridine determined by partial pressure above the film leads to the formation / dissociation of this adduct.

Tandem Cells

The ability to tune perovskite band gaps over the whole visible spectrum is particularly advantageous for tandem cell applications, creating the prospect of optimised 1.7-1.8 eV band gap, semi-transparent perovskite cells on top of a range of current single junction technologies, including Si and CIGS. Quadruple A-site cation compositions using Cs/Rb/MA/FA have been used in 26.4% efficient mechanically stacked tandem of perovskite on silicon,[77] though the available evidence indicates Rb is not included in the bulk perovskite structure.[78] Notably, 23.6% monolithic silicon-perovskite tandem PVs employing an atomic layer deposited SnO_2 buffer layer, have been demonstrated to pass industry standard damp heat tests of 85 °C / 85% relative humidity for 1000 hours.[46] Perovskite-perovskite tandem devices have also been demonstrated employing a narrow band gap Sn/Pb bottom cell.[61] A four terminal mechanically stacked tandem cell with a 1.25 eV band gap perovskite, $(FASnI_3)_{0.6}(MAPbI_3)_{0.4}$, and a 1.75 eV band gap, $FA_{0.8}Cs_{0.2}Pb(I_{0.7}Br_{0.3})_3$, has been reported with 23.1% efficiency.[79]

Surfaces and Interfaces

Passivation of surfaces and interfaces is particularly important to remove electronic defects associated with dangling bonds, leading to fewer non-radiative losses and improved cell stability. Non-radiative surface recombination dominates over recombination at grain boundaries / in the bulk of $MAPbI_3$.[80] Excess PbI_2 has been shown to passify grain boundaries in perovskite films.[81] Effective surface passivation has also been achieved using chlorine-capped TiO_2 colloidal nanocrystals film at the TiO_2 / perovskite interface, resulting in Cs/FA/MA cells with $\eta = 21.4\%$ (certified, unencapsulated) for 0.049 cm^2 and 19.5% for 1.1 cm^2 cells.[82]

Flexible, Ultra-thin Cells

Ultra-thin, flexible perovskite PV cells display a power to weight ratio of 23 W g^{-1}, rivalling GaAs and indicating a particular advantage for mobile applications.[83] Cells employing extremely thin hole and electron transport layers, <20 nm PTAA and C60, have been shown to maximise the fill factor up to 84%, close to the theoretical maximum, with the relatively low conductivity within the hole transport material shown to limit fill factor. 95% of this device volume is the perovskite itself, indicating further advances in ultra-thin PV devices are possible.[84]

Carbon-Perovskite Cells

Perovskite cells in which the perovskite layer is formed by percolating a precursor solution through a 6-10 μm thick mesoporous carbon electrode layer display lower ($< 15\%$) efficiency, but promising stability and up-scaling potential.[69,85] The chemically inert and hydrophobic carbon electrode avoids the degradation issues of perovskite - metal electrodes and consequently printed commercial modules are under active development.[86]

Open Circuit Voltage Deficit

One early indication of the promise of perovskite solar cells was the low loss in open circuit potential (V_{OC}, Figure 1-9). The thermodynamic minimum loss is around 250-300 meV,[22] while perovskite cells with a band gap of 1.55 eV displayed V_{OC} of 1.1 eV, a loss of only 450 meV, comparable to Si and CIGS and better than commercial CdTe. Emerging absorbers such as CZTS have seen efficiencies hamstrung by low V_{OC} stemming from electronic defect structure. That high voltages are achieved from spin coated perovskite films is remarkable. While V_{OC} loss for narrow band gap perovskite cells rivals GaAs, wider band gap perovskites suitable for tandems with Si / CIGS currently suffer from a larger voltage deficit due to phase segregation within the active layer and also non-ideal selective contact materials. A 1.7 eV band gap perovskite top cell employing an isomerically pure fullerene derivative, indene-C60 bisadduct (ICBA-tran3), as the electron transport layer has reduced the V_{OC} deficit to 0.5 V.[87]

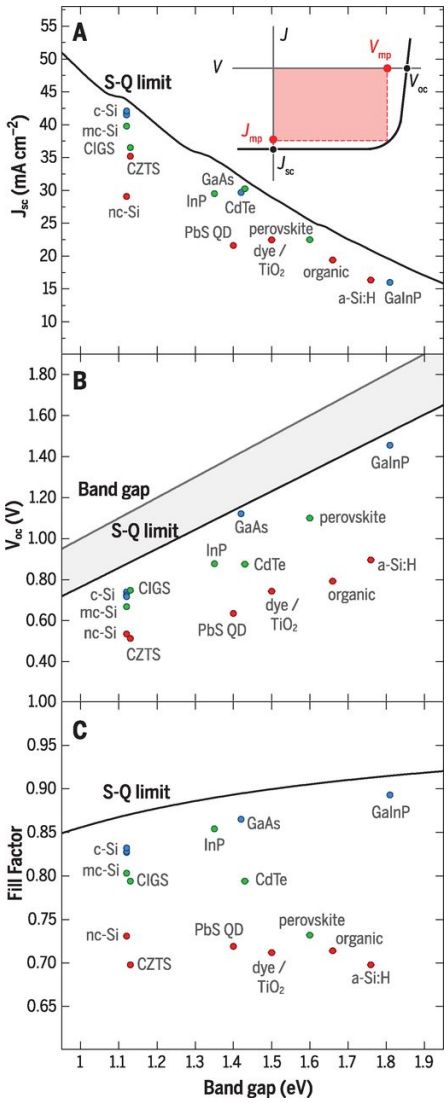

Figure 1-9: Current, voltage and fill factor losses in PV technologies, from Polman et al.,[42] Reprinted with permission from the AAAS.

Current-Voltage Hysteresis

Anomalous hysteresis in the forward and reverse I-V curves of perovskite solar cells were reported early on in their development.[88] This dynamic response under illumination and electrical bias has been the subject of debate in the literature. Ionic conductivity results in a chemical capacitance that responds on the millisecond to second timescale to external stimuli, for example when potentials are applied across the material, as well as in response to the built-in asymmetric potential of the device.[89] Ionic motion combined with interfacial recombination has been shown to result in hysteretic devices,[90] which is suppressed by effective passivation of interfaces and improved crystallinity.[91] Imbalanced charge transport across electron and hole transport layers' interfaces has also been shown to cause I-V hysteresis.[92]

Charge Transport

Perovskite materials are notable for exceptionally high charge carrier diffusion lengths, L_D, on the order of $>$1 μm in thin films and $>$175 μm in single crystals.[93–96] Numerical modelling of electrical measurements suggest that the perovskite cell operates as a model *p-i-n* diode.[97,98] By contrast, charge-carrier mobilities, effective masses, doping densities and absorption coefficients in perovskites are comparable or even modest compared to other thin films such as CdTe, CIGS, CZTS. The product of the minority carrier lifetime τ and mobility μ is an important indicator for a material's prospects of achieving high efficiency in PV devices.[99] In MAPI, a measured Hall mobility of $\mu = 60$ cm^2 V^{-1} s^{-1} is far lower than for other inorganic semiconductors, yet carrier lifetimes ($\tau < 3$ ms) from Hall effect measurements and diffusion lengths ($L_D < 650$ μm) from photoconductivity measurements of single crystals are significantly longer than even highly crystalline inorganic semiconductor materials.[100]

1.6 Atomic Structure

1.6.1 Perovskite Structure

Perovskites are compounds with the stoichiometry ABX_3, in which A and B are two dissimilar cations and X is the counter-anion. The perovskite structure is based on a primitive cubic unit cell and formed of vertex linked $[BX_6]^{4-}$ octahedra (6 co-ordinate 'B' cations), with the 'A' cation occupying the central cuboctahedral cavity (12 co-ordinate site). The

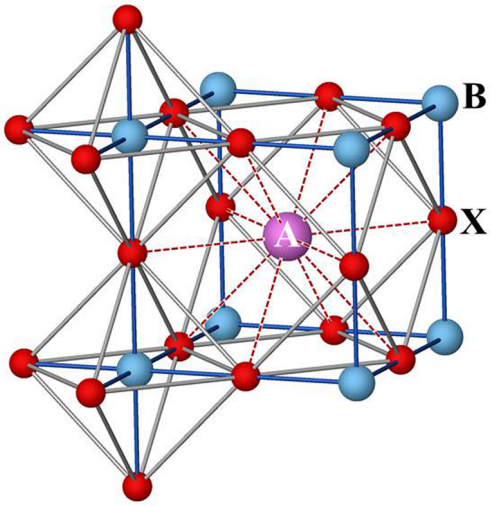

Figure 1-10: Ion coordination in the perovskite structure ABX_3. Reproduced from R. H. Mitchell et al.[103] with permission from Cambridge University Press.

'X' anions are coordinated to two B-site and four A-site cations (Figure 1-10). Perovskites are named after the archetypal mineral perovskite $CaTiO_3$ which, due to the number of possible chemistries adopting this structure, represents one of the most diverse and widely applied crystal families in materials science and engineering. Oxide perovskites are far more prevalent than any other anion type, with applications spanning supercapacitors, solid oxide fuel cell electrolytes and electrodes and multiferroic materials.[101,102]

The Goldschmidt tolerance factor (t) defines a geometrical relationship for whether a set of ions may adopt the perovskite structure, Equation 1.4, which assumes ionic bonding and well-defined ion sizes. This is a reasonable assumption for oxide and fluoride perovskites with high ionicity, though less so for the later halides and organic 'A' site molecular cations. An ideal perovskite, typified by $SrTiO_3$ or $KMgF_3$, has A, B and X ion sizes such that $t = 1$. Lower values of t will tend to lower the symmetry of the observed structure down to $t = 0.8$, below which the perovskite structure is not adopted. For $t > 1$ hexagonal perovskites with face-sharing chains of octahedra are observed. The archetypal cubic perovskite adopts the space group $Pm\bar{3}m$ ($P4/m\bar{3}2/m$, #221).

$$t = \frac{r_A + r_X}{\sqrt{2}(r_B + r_X)} \tag{1.4}$$

Phase transitions away from the ideal cubic structure may occur due to distortions within BX_6 octahedra, or more commonly from tilting of the octahedra as single units relative to each other. Many perovskites display ideal cubic symmetry at high temperature, while

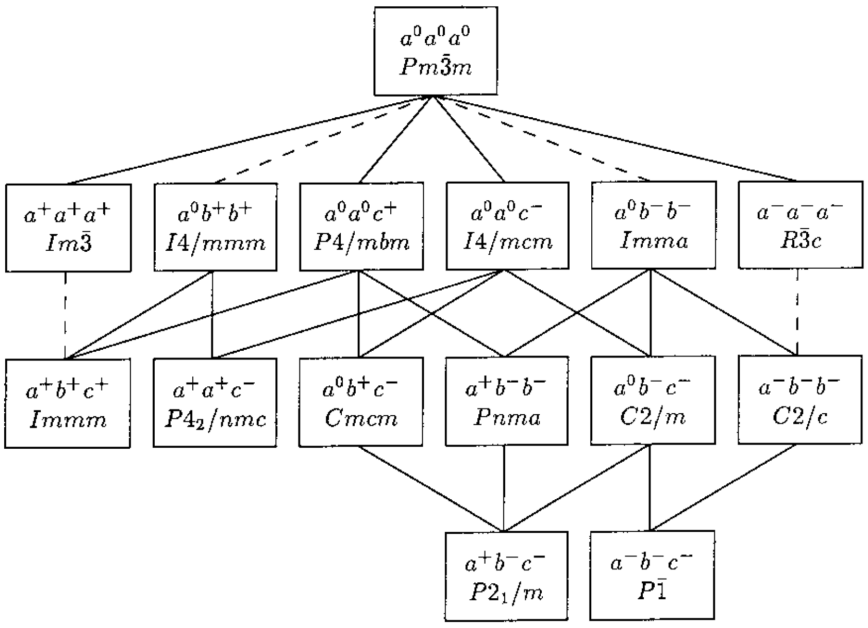

Figure 1-11: Perovskite group / subgroup relationships by Howard and Stokes.[105,106]

descending through symmetry-lowering phase transitions as the temperature decreases and the lattice contracts. The symmetry of octahedral tilting patterns that may occur while preserving the integrity of the 3D vertex-connected $[BX_3]^-$ lattice has been investigated by Glazer, Woodward, Howard and Stokes.[104–107] A summary of the group / subgroup relations for pure tilt systems from Howard & Stokes, 1998, is reproduced in Figure 1-11.[105]

Many structural derivatives of ABX_3 perovskites exist, include ordering of A/A' or B/B' cations, and A-, B- or X-site vacancy structures. These include formation of related layered perovskites including Ruddlesden-Popper phases ($A_{n-1}B_nX_{3n+1}$), Aurivillius and Dion-Jacobson phases; double perovskites (elpasolites) e.g. Sr_2FeMoO_6 and related anion-deficient structures such as brownmillerites. A hierarchy of structural types among perovskite related compounds is given in Figure 1-12.

1.6.2 Hybrid Halide Perovskite Atomic Structure

Inorganic lead halide perovskites were first reported on in 1893 by Wells, who described these compounds as 'peculiar'.[108] The crystal structure of $CsPbX_3$ (X = Br, Cl) was determined to be cubic perovskite in the high temperature phase in 1958 by Möller, who noted their

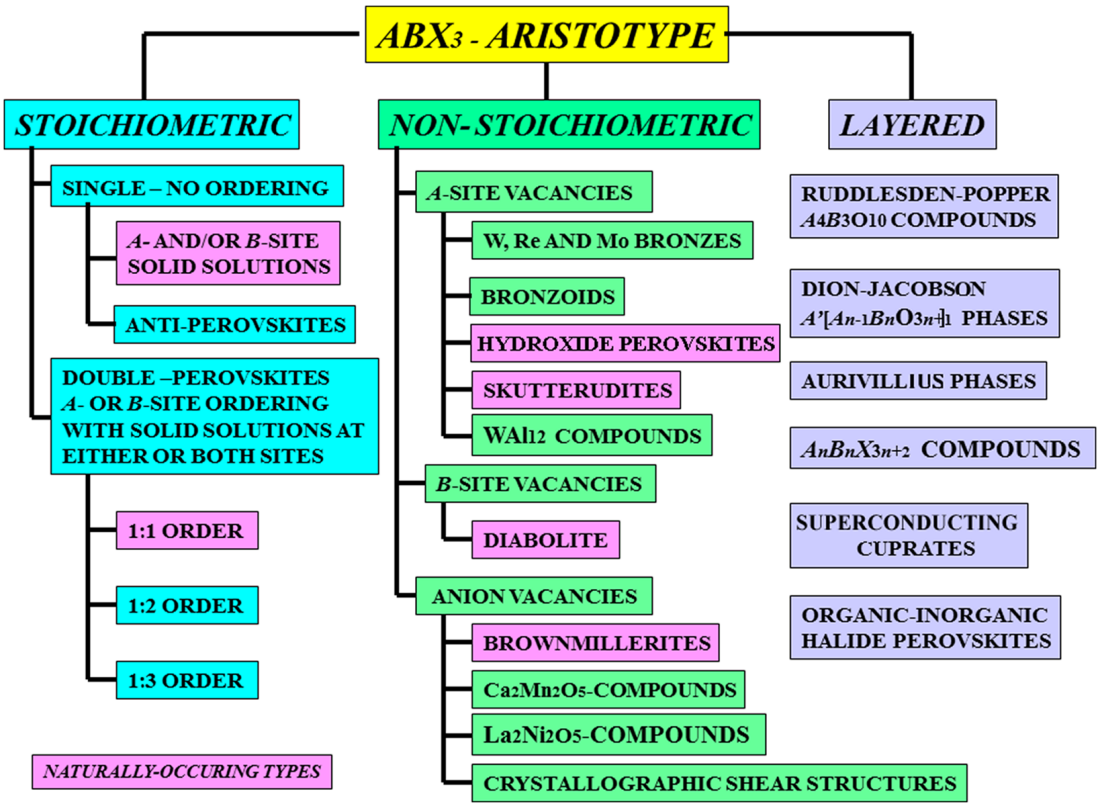

Figure 1-12: Structural derivatives of the ABX_3 perovskite aristotype. Reproduced from Mitchell et al.,[103] by permission of Cambridge University Press.

photoconductivity.[109] Hybrid perovskites bridge the divide between conventional inorganic and organic materials. Hybrid organic-inorganic perovskites have a much briefer history than the inorganic compounds, with the first example, methylammonium lead iodide, synthesised by Dieter Weber in 1978.[110] The phase behaviour of hybrid perovskites has only recently begun to be extensively explored, and many of the studies cited in the following sections post-date the results presented in Chapter 3, which provided the first description of the complete crystallographic phase behaviour of methylammonium lead iodide.

As with conventional oxide perovskites, halide perovskites undergo successive phase transitions, with increasing crystal symmetry as the temperature is raised. Thermal expansion of the lattice and thermal motion of the ions with increasing temperature enables accommodation of those ions with successively fewer distortions. Unlike oxide perovskites, in which phase transitions of interest may occur at hundreds of degrees above room temperature, halide perovskite display these successive phase transitions at or around room temperature and are unstable at high temperature ($> 400^{\circ}$C). This observation is intimately tied to their electrostatic stabilisation and lattice energies, which are lower than for oxide perovskites, with $E_{latt} = 29.71$ eV per ABX_3, less than half of the value for II-IV-VI_3 compounds.[111] The temperature range at which halide perovskites are stable, display large thermal displacements and phase transitions is consequently shifted lower. The bonding within the $[BX_3]^-$ framework is mixed ionic / covalent and large deviations are observed in the ionic radii of metal iodide / bromide compounds from those expected from Shannon's tables, which are derived from hard anion O and F compounds.[112]

For hybrid perovskites, further symmetry and bonding considerations are necessary compared to completely inorganic compounds. To take the example of methylammonium lead iodide, in the cubic phase, a non-spherical organic cation with a permanent dipole moment resides at a crystallographic site of octahedral symmetry ($m\bar{3}m$ / O_h) to which its point group symmetry (C_{3v}) does not conform. This molecular cation exists in a dynamically disordered state, distributed in equivalent positions around the centre of the unit cell, thus averaging to cubic symmetry. The inorganic lattice is highly polarisable, and while electrostatic attraction between the anionic framework and cation is the primary bonding interaction, directional hydrogen bonding between the organic molecular ion and the inorganic lattice is also an important factor in the observed phase behaviour. This becomes increasingly significant at lower temperatures as the thermal energy inducing disorder is reduced below the strength of hydrogen bonding. Interaction between adjacent organic ions is also expected and the dipole-dipole interaction energy for MA ions in adjacent unit cells has been estimated to be 25 meV, comparable to thermal energy at room temperature.[113]

1.6.3 Local Instantaneous Structure

One result of the dynamic behaviour of hybrid perovskite materials is that the local, instantaneous picture of the material, probed by techniques sensitive to local structure, deviates substantially from the average long-range structure described by crystallographic techniques, which sample a large number of unit cells with low temporal resolution. To take $MAPbI_3$ as an example, above room temperature the organic cation is disordered symmetrically about the C-N axis across a high symmetry lattice point and rotates freely on time-scales relevant to crystallographic experiments. Therefore the overall symmetry averages to the high symmetry cubic phase.[114] The characteristic rotation time for methylammonium around the C–N is on the order of picoseconds.[115–117]

Local structure analysis from total scattering experiments on $MAPbI_3$ indicate that a cubic structure describes the pair-distribution function (PDF) well for long-range interactions, however for very short lengths of 1-10 Å, the fit is poor and a lower symmetry tetragonal structure describes the PDF better.[118,119] Raman scattering measurements on $CsPbBr_3$ and $MAPbBr_3$ suggest that local polar anharmonic motion is equivalent between the two compounds, indicating that local polar fluctuations are non-specific to structures containing a polar non-spherical cation.[120] Both inelastic neutron scattering and dielectric spectroscopy indicate that the MA cation is not fully frozen even down to 10 K,[121,122] while inelastic X-ray scattering indicate nano-regions of non-cubic structure above the tetragonal / cubic phase transition temperature.[123]

Theoretical calculations and high resolution X-ray inelastic scattering indicate that cubic $MAPbI_3$, rather than representing an energy minimised structure, is at a saddle-point in potential energy with respect to equivalent tetragonal distortions (Figure 1-13).[118] This local dynamic symmetry breaking is not observed by Bragg diffraction, so long as the average long range ordering is maintained, and short range dynamic effects are often indistinguishable from thermal fluctuations.

Light-induced, fully reversible structural effects have regularly been observed in hybrid perovskites,[124–126] including a photostriction effect that cannot be accounted for by a thermally-induced mechanism and fully reversible, light-induced phase segregation.[127,128] Ultrafast electron diffraction results indicate that in $MAPbI_3$, light-induced rotational disordering of PbI_6 octahedra is observed, as the I-I correlation function increases while preserving Pb-I bond lengths, with the structural deformation of inorganic lattice not merely due to non-equilibrium thermal excitation.[129] Recently it has been definitively shown that constant illumination with a visible light source significantly increases ionic conductivity in $MAPbI_3$, mediated by iodide vacancies (see Section 1.9), and that this technique can be

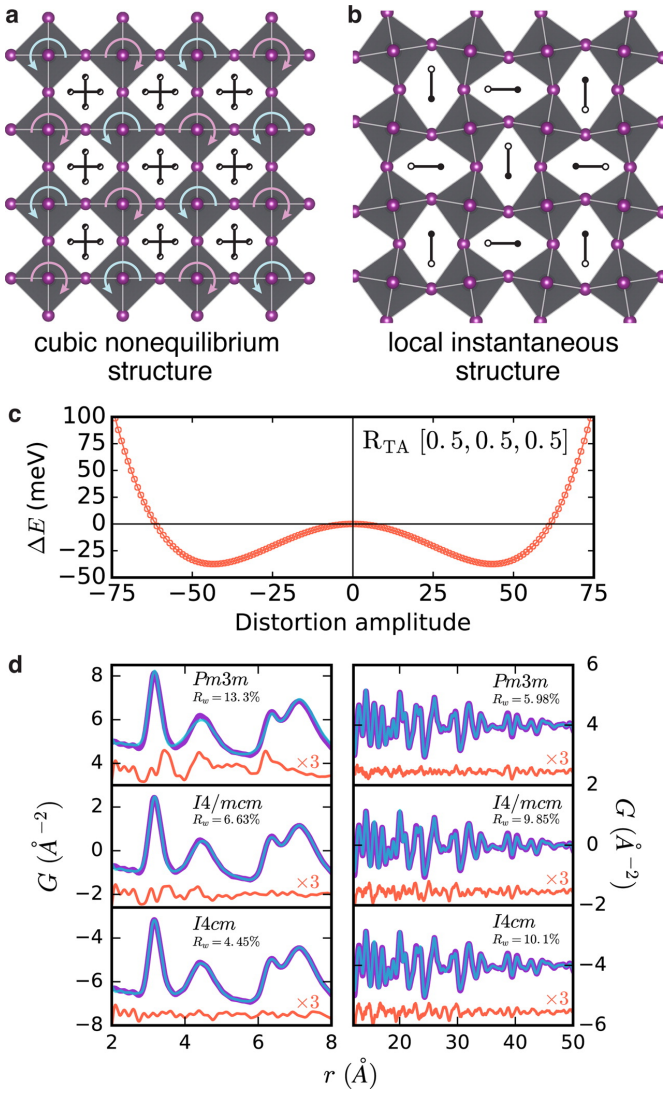

Figure 1-13: Reproduced from Beecher at al.[118] with permission from the publisher. Exploring the local structure of $MAPbI_3$, comparing the cubic cell (saddle-point) to local potential minimum for instantaneous distorted structures. Shallow potential energy wells indicate the structure will fluctuate between energy minima. The pair-distribution function fits a distorted structure at short range ($<$ 5 nm).

leveraged to 'light-heal' perovskite solar cells.[130,131]

1.6.4 Glass Formation and Plastic Crystals

Hybrid perovskites share dynamic structural attributes with plastic crystals such as KCN.[132] In plastic crystals, molecular centres of mass are located in crystallographically well-defined positions, while molecular rotations display liquid-like behaviour.[133] Upon cooling, phase transitions may occur as molecular rotational motion freezes in an ordered crystalline phase. Another possibility is for disordered (stochastic) freezing into orientational glasses. A further possibility is that no phase transition is observed and residual entropy is retained at 0 K, when the crystal may reach a glassy state, i.e. ordering is a thermally activated process.[134]

The low temperature dielectric loss behaviour, solid state NMR and calorimetry of $FAPbI_3$ display slowing of relaxation dynamics consistent with glassy freezing of the molecular ions and quenched disorder.[122,135] Crystallographic and inelastic neutron scattering data of $MA_{1-x}Cs_xPbBr_3$ indicates that plastic crystal behaviour is observed in the room temperature cubic phase, with the organic molecular ions exhibiting slowing of reorientation and formation of an orientational glass at lower temperatures, while the inorganic framework continues to undergo crystallographic phase transitions.[136] The apparent frustration of preferred molecular orientations and cage tilt patterns in these A-site solid solutions underlines the difference in low temperature phase behaviour to $MAPbI_3$, in which an octahedral titling pattern consistent with an ordered arrangement of molecular cations.[137]

1.6.5 Layered Hybrid Perovskites

Organic cations that are too large to fit the cuboctahedral cavity of the lead halide perovskite structure have been employed to synthesise 2D layered perovskites, in which monolayers of lead iodide octahedra are separated by bilayers of the organic cation. Many aliphatic and aromatic primary ammonium cations have been applied to form 2D hybrid perovskites.[48,138] Huge structural versatility for 3D / 2D hybrid perovskites is also available, in which a finite number of 3D perovskite layers are interspersed with 2D layers of larger organic cations with the general formula $(RNH_3)2A_{n-1}B_nX_{3n+1}$. Among other properties, the band gap and stability of these materials can be greatly modified relative to 3D hybrid perovskites.

$(RNH_3)_2BX_4$ compounds display quantum confinement effects and higher exciton binding energies due to their 2D quantum well electronic structure.[139] Figure 1-14 displays families

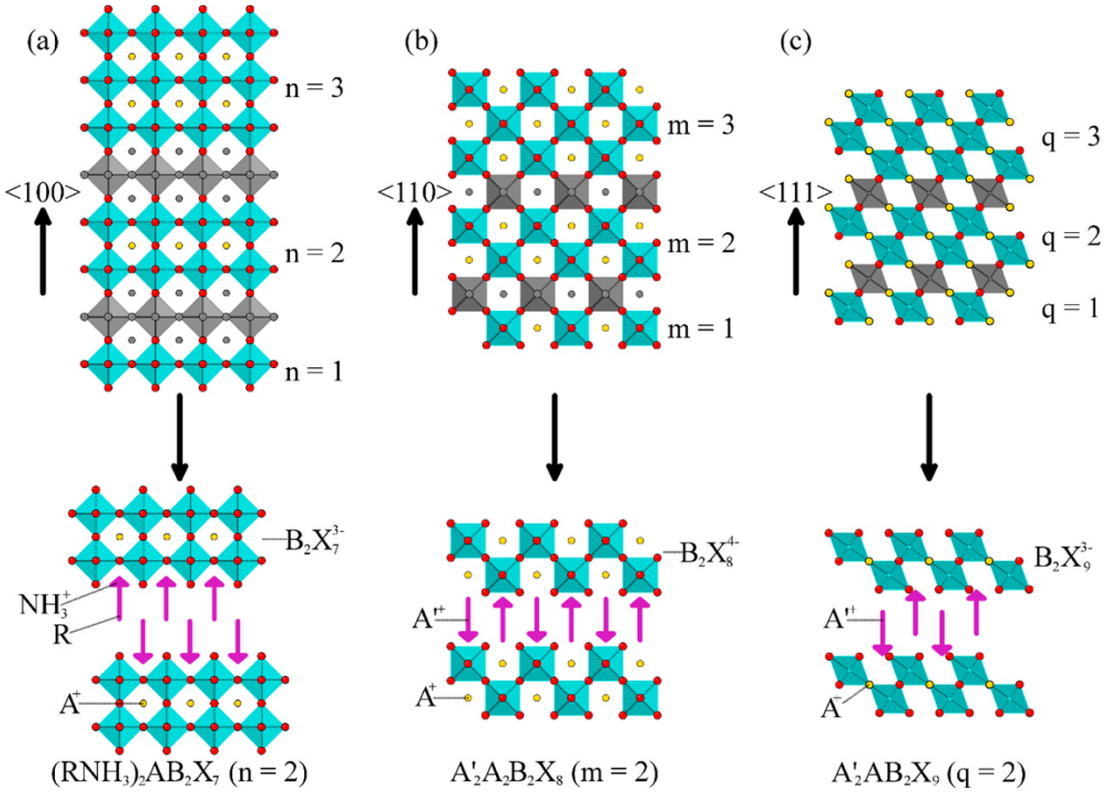

Figure 1-14: Reproduced from Saparov et al.[139] with permission from the publisher. Families of layered 2D and 2D / 3D hybrid perovskite compounds templated by specific organic cations.

of 2D hybrid perovskites obtained from cuts through different planes of the 3D perovskite lattice. Organic cations that are sterically unsuitable to form 2D perovskites template a wide variety of hybrid organic-inorganic framework compounds.[140,141]

1.7 Synthesis and Chemistry

A wide range of synthetic methods are applicable to form hybrid perovskites and the adage "same compound, different material" holds true. For solar cell device layers, the perovskite is generally deposited from precursor solutions using dipolar aprotic solvents such as DMF, DMSO and γ-butyrolactone, followed by heating to drive off the solvent and induce crystallisation of the perovskite phase.[142] Sequential deposition is another commonly applied route to form perovskite thin films, in which a PbI_2 film is exposed to halide salts of the A-site cation dissolved in solvents such as isopropanol, in which PbI_2 and the perovskite product have low solubility.[143] Mechanochemical synthesis is also possible and if

methylammonium iodide and PbI_2 are combined at room temperature using a mortar and pestle, the perovskite phase will form within seconds.[144] Single crystals have been grown by anti-solvent vapour diffusion,[94], seeded solution growth,[145] temperature gradient growth in hydrohalic acids,[146] and inverse solubility gradients in γ-butyrolactone for specific perovskite compositions.[147] Vapour phase co-deposition has also been demonstrated for thin films.[56]

Inorganic halide perovskites such as $CsPbX_3$ are also obtainable from high temperature melts: conditions unsuitable for hybrid perovskites containing organic components.[148] Reactive polyiodide melts have also been exploited to form perovskite materials,[149] in which simple mixing of methylammonium iodide with crystalline iodine resulted in immediate formation of a highly viscous melt of MAI_{3+x}. In contact with metallic lead, the hybrid perovskite phase is formed, with the polyiodide melt acting as both solvent and oxidant.

Solid solutions have been obtained for A, B and X sites of ABX_3, with A = MA / FA / Cs; B = Pb / Sn / Ge and X = I / Br / Cl. Not all of the combinations of these ions display solid solution growth across the whole composition range. Chloride is often included in precursor solutions for methylammonium lead iodide thin films, though the evidence suggests it is not necessarily included in the bulk perovskite composition.[150] The range of compositions that are likely to adopt the perovskite structure has been rationalised by Travis et al.[112] using experimentally derived metal halide ionic radii. Stabilisation of the cubic perovskite structure by alloying the A-site cation to obtain a tolerance factor close to unity has been exploited to form stable and high efficiency solar cells, possibly due to a decrease in local lattice strain with well-matched ion sizes.[91] Formamidinium and caesium solid solutions are regularly applied for this purpose, on account of superior thermal stability compared to methylammonium-containing perovskites.[151] Links have been drawn between crystallinity, phase stability and superior optoelectronic quality in mixed cation systems. $Cs_xFA_{1-x}PbI_yBr_{3-y}$, $0.10 < x < 0.30$, displayed the lowest broadening of XRD peaks and halide phase segregation was suppressed, leading to more photostable compounds that also coincide with a phase region of longer charge carrier lifetimes and higher mobilities.[91]

The oxidative stability of 2+ ions in group IV trends as Pb $>$ Sn $>$ Ge. Pb(II) is stabilised relative to Pb(IV) by the relativistic inert pair effect. For hybrid perovskites, the observed stability is for Pb(II) compounds to be the most stable under atmospheric conditions (though still susceptible to attack by oxygen and water), while Sn and Ge are not air stable.[152] The thermodynamic stability of X site-substituted perovskites trends as Cl $>$ Br $>$ I.[153] The band gap also increases significantly from I $<$ Br $<$ Cl, with chloride perovskites unsuitable for photovoltaic applications due to a $>$ 3 eV band gap.

1.7.1 Compositional Engineering and Doping

Site-substitution and doping in hybrid perovskites are further methods to control and exploit material properties. Doping densities in perovskite crystallites in PV cells are currently more a function of adventitious conditions than controlled parameters. High defect densities in perovskites do not translate into high doping densities, with carrier densities for single crystals as low as 10^9 - 10^{10} cm^{-3} reported.[94] The introduction of heterovalent dopants to modify the optoelectronic properties of a semiconductor has been integral to the development of Si, yet is currently largely unmapped in the field of perovskites. Abdelhady et al.[154] grew single crystals of $MAPbBr_3$ and $MAPbI_3$ by the inverse solubility method that incorporated Bi^{3+}, Au^{3+} or In^{3+}. In the case of bismuth this resulted in a significant reduction in the optical band gap, increase in free carrier concentration and consequent increase in conductivity, as evidenced by four-point probe and Hall effect measurements. Introduction of Bi^{3+} into $MAPbBr_3$ was shown to introduce mid-band gap states that accounted for the increase in sub-band gap absorption.[155]

Homovalent ions may also be substituted into the perovskite lattice to modify chemical properties. Navas et al.[156] studied the inclusion of Sn^{2+}, Sr^{2+}, Cd^{2+} and Ca^{2+} into $MAPbI_3$. Elemental analysis by CHNS and XRF showed the stoichiometry of deposited compounds to match that of the precursor solution within experimental error, though uptake of these ions at the B-site of the perovskite structure, save for Sn, has not been definitively demonstrated. Unfortunately two of the most likely candidates for homovalent B-site substitution, Hg, Cd, are of no assistance for decreasing the toxicity of lead halide perovskites.[157]

1.7.2 Stability

Hybrid perovskites are unstable with respect to multiple environmental and intrinsic factors via several chemical degradation pathways.[158] The solubility of lead salts in water and the hygroscopic nature of the organic cation are root causes of the degradation of these compounds by humid atmospheres and concerns over lead release to the environment. The energy of formation of hybrid lead iodide perovskites at room temperature is low, or positive for certain metastable / entropically stabilised compositions, so there is little thermodynamic driving force to halt the degradation to lead salts and organic species.[153] Calculations have suggested that the disproportionation reaction of tetragonal $MAPbI_3$ to MAI and PbI_2 is slightly exothermic.[159]

Grain boundaries within the polycrystalline thin film of $MAPbI_3$ solar cells have been impli-

cated in recombination of charge carriers, ionic conductivity enhancements and hydrolytic decomposition.[160] The stability of hybrid perovskites has been shown to be dramatically improved by chemical intervention at the grain boundaries, which can impede or energetically disfavour the ingress of water into the perovskite layer. Chemical tuning within the bulk material by cation mixing also improves moisture tolerance of the compound due to the increase of cohesive energy of the phase, or decreasing hydrophilicity, which is undoubtedly the case for 3D/2D perovskites employing ammonium cations with hydrophobic alkyl chains.[161]

1.7.3 Toxicology

The other main shortcoming of hybrid perovskite materials is toxicity. Unlike thermally and chemically stable CdTe ($K_{sp} = 10^{-27}$), Pb in hybrid perovskites is present in a soluble and bioavailable form, with PbI_2 $K_{sp} = 10^{-9}$. Strict regulatory environments limit the use of lead, as its ecotoxicity and harmful effects on human health is well established, including cardiovascular, neurological and reproductive damage.[162–165]

The quantity of Pb per solar cell is low, on the order of 100 mg m^{-2}, however modules must be demonstrated to be intrinsically safe in the event of catastrophic failure in order to succeed as a commercial technology. End of life recycling may be crucial for perovskite technology, as is currently practised for lead-acid batteries. Since there are not yet examples of commercial perovskite solar panels, it is currently unclear how regulatory regimes will react to perovskite technologies. Decreasing or eliminating Pb from perovskite solar cells is a pressing research aim, however a challenging one given the integral role of lead in the electronic structure of these compounds (Section 1.8).

1.8 Electronic Structure

The characteristic electronic band structure of halide perovskites is depicted in Figure 1-15.[166] For $MAPbI_3$, I $5p^6$ orbitals form the upper valence band, admixed with Pb $6s^2$ orbitals. In perovskite strong coupling between Pb 's' and anion 'p' orbitals in the valence band close to the valence band maximum results in a more dispersive valence band structure than typical for other localised 'p' orbital derived valence band structures, e.g. GaAs.[167] The unoccupied $6s^26p^0$ Pb p orbitals form the conduction band.[111] The valence band maximum and conduction band minimum in cubic $MAPbI_3$ occur at the R point of the Brillouin zone boundary, thus cubic MAPI is calculated to be a direct-gap semiconductor,

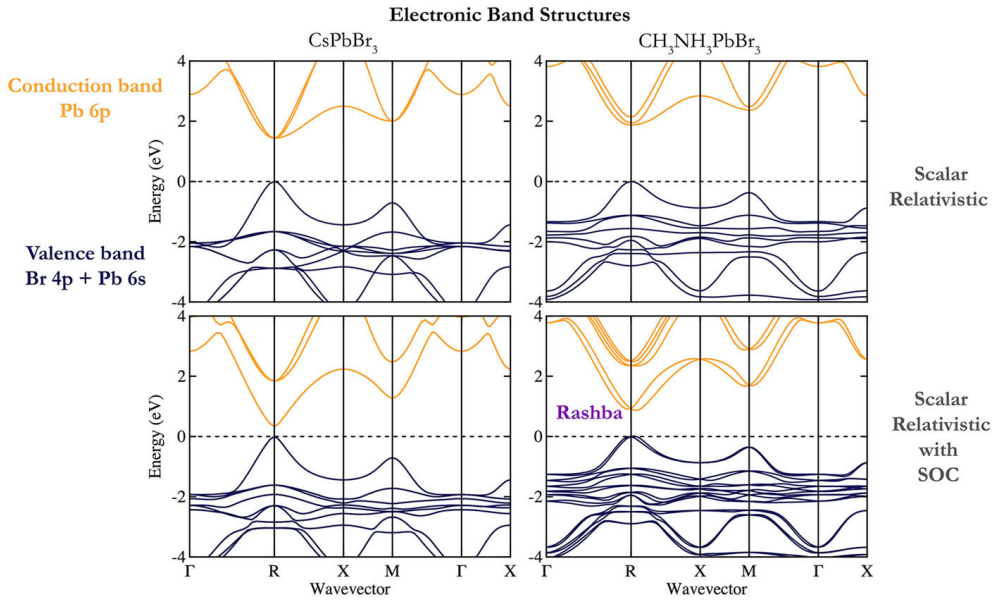

Figure 1-15: Electronic band structure calculations for $MAPbBr_3$ and $CsPbBr_3$ with and without correction for spin-orbit couplings. From Whalley et al.[166] Reproduced with permission from the AIP.

in agreement with the high observed optical absorption coefficient.[168] The A-site cation does not contribute directly to the frontier density of states, but nonetheless influences the electronic properties of the material through its structural interactions with the inorganic lattice and, in the case of organic cations, through the dynamic reorientation of permanent dipoles.[169]

The lead halide perovskites are semiconductors with optical band gaps ranging from around 1.5 eV for iodides to over 3 eV for chlorides, while tin halide perovskites display narrower band gaps ($>$ 1.1 eV).[61] The fundamental band gap differs from the experimentally observed optical band gap by the exciton binding energy: the electrostatic attraction between electrons and electron-holes. The exciton binding energy, E_B, necessary to separate charge carriers in $MAPbI_3$ has been estimated to be between 5-55 meV.[169,170] Uncertainty in E_B for hybrid perovskites stems from the experimental difficulty of determining the dielectric response at low frequency, where slow diffusive processes dominate. Hybrid perovskites display sharp absorption onsets, high absorption coefficients (10^5 cm^{-1}) and small Urbach tails (15 meV), reflecting a low density of sub-band gap states near the band edge.[171] All of these factors are indicative of a low degree of electronic disorder and suitable properties for use in optoelectronic devices.

The effective masses for electrons and electron holes are inversely proportional to the curva-

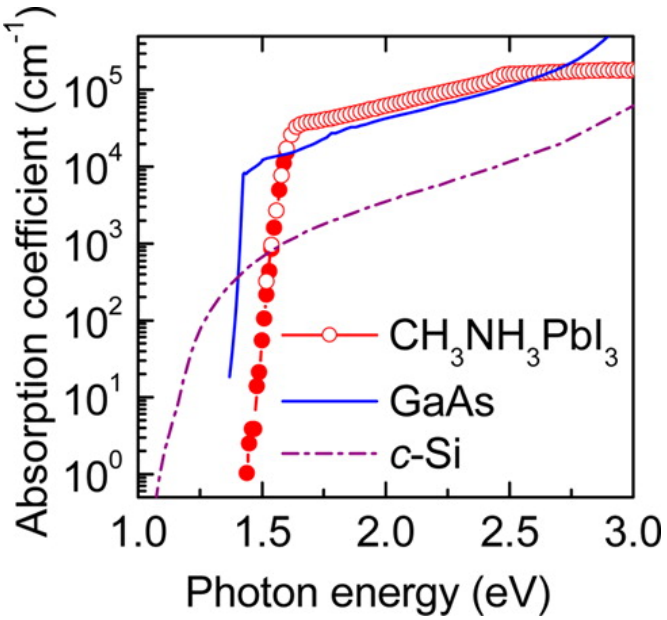

Figure 1-16: Absorption coefficient of $MAPbI_3$, GaAs and Si. Reproduced with permission from the publisher.

ture of the CBM / VBM. For $MAPbI_3$ these are calculated to be in the range of 0.1-0.15 m_0, where m_0 is the free electron mass.[168] These values imply high-mobility transport of charge carriers that is balanced for both signs of charge, in theory up to ≈1000 $cm^2\ V^{-1}\ s^{-1}$, close to values of GaAs. However the observed mobilities of 1-30 $cm^2\ V^{-1}\ s^{-1}$ for thin films and 100 $cm^2\ V^{-1}\ s^{-1}$ for single crystals are far more modest that might be expected.[95,172]

Relativistic effects become significant for large nuclear charges on heavy elements such as Pb and I. One consequence of this is the Rashba-Dresselhaus effect: spin-dependent splitting of energy bands in momentum space.[173] Spin-orbit coupling causes Rashba effect splitting of the conduction band of $MAPbI_3$. ARPES measurements on $MAPbBr_3$ display evidence of strong spin-orbit coupling.[174] This band splitting is shown in Figure 1-15 and it has been suggested that the direct band gap originally calculated for MAPI is in fact a spin-split indirect band gap.[175] Low excitation density photoluminescence and photothermal deflection spectroscopy suggest an indirect band gap 60 meV below the direct gap.[175] Since the direct and indirect band edges are close in energy absorption is not significantly reduced, but charge carriers thermalised to the conduction band edge could potentially be protected from recombination by band cross-over.[175] Charge carrier recombination was shown to be 5 times faster at high pressure following an indirect to direct band gap transition under hydrostatic pressure above 325 MPa, in agreement with computational calculations.[175,176] Transient photoconductance experiments also suggest slow phonon-assisted recombination

from an indirect band gap.[177]

1.9 Defects, Mobile Ions and Permittivity

Hybrid perovskite compounds are formed near room temperature and show poor stability at higher temperatures. From a statistical thermodynamics point of view, given their low formation energies these are expected to be highly defective materials, with low ionisation potentials (work functions) and small energies for vacancy defect formation expected.[178] The equilibrium charged vacancy concentration for $MAPbI_3$ is predicted to be above 0.4% at room temperature, with a Schottky formation energy of 0.14 eV: far lower than for conventional semiconductors (Equation 1.5).[179] This energy is calculated to be even lower (0.08 eV) for partial Schottky formation through loss of MAI, suggesting that, in an open system, as much as 4% of the CH_3NH_3 sublattice would be vacant at equilibrium, resulting in a partially hollow perovskite structure. The formation of a charge-neutral full Schottky defect is shown in Equation 1.5 in Kröger-Vink notation.

$$nil \rightarrow V'_{MA} + V''_{Pb} + 3V^{\bullet}_{I} + MAPbI_3 \tag{1.5}$$

Point defects in other semiconductors such as CZTS lead to charge carrier densities for holes up to 10^{18} cm^{-3}.[180] For MAPI, a high concentration of Schottky defects minimises the free energy without formation of other point defects that would introduce additional charge carriers, hence MAPI can be at once highly defective while displaying a low charge carrier concentrations ($> 10^9$ cm^{-3}), similar to pristine Si or Ge.[179]

$CsPbI_3$, $MAPbI_3$ and $FAPbI_3$ have been shown to be ionic conductors, with reports of both anions and cations mobile under applied potential.[181,182] In 1983 Misukai et al.[183] studied ionic conductivity in caesium halide perovskites $CsPbCl_3$, $CsPbBr_3$, concluding that the mobile ion was likely the halide anion. $PbCl_2$ and $PbBr_2$ are known halide ion conductors.[184] Vacancy-mediated ion conduction is likely given the calculated high density of Schottky defects.[185] Many of the slow dynamic responses observed in perovskite optoelectronic devices are rooted in the mixed ionic-electronic conduction these materials display, with dynamic responses to external stimuli including applied potential and illumination.

Activation energies for ion migration have been calculated to be 0.58 eV for I^- and 0.84 eV for MA^+, suggesting that I^- is the majority ionic carrier. The diffusion coefficient is calculated to be 10^{-12} cm^2 s^{-1}.[181,186] Experimental observation of B-site metal exchange in thin films indicates that metal ions too are implicated in ionic conduction processes.[187] Fast

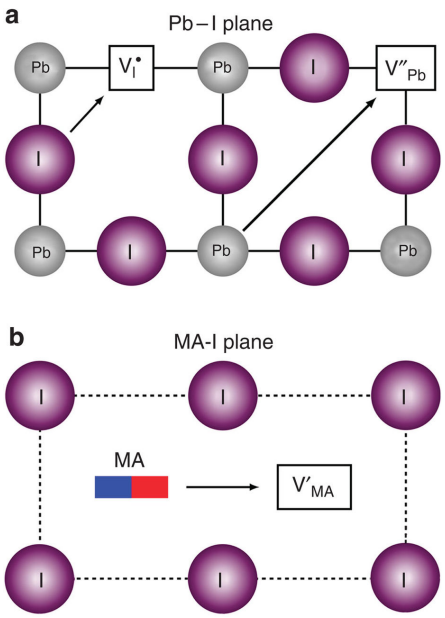

Figure 1-17: Vacancy assisted ionic conduction in MAPI. From Eames et al.,[181] reproduced with permission from the publisher.

anion exchange has been observed for perovskite nanocrystals.[188] The thermal activation of ion transport via lattice expansion has also been studied,[189] and ion migration has been shown to take place in solar cells even with minimal hysteresis.[90,190]

The dielectric permittivity of hybrid perovskite materials is highly relevant to many of the reported characteristics of perovskite solar cells.[191] These materials display a particularly high static dielectric constant $\epsilon_0 > 20$, compared to more conventional semiconductors $\epsilon_0 < 20$, which may benefit charge carrier dissociation and slow recombination due to better screening of mobile charge carriers.[111] The permittivity response of hybrid perovskites, given by Equation 1-18, where $\epsilon_0 \approx 34$ is the static dielectric constant, $\epsilon_\infty \approx 5$ the optical dielectric constant and $\epsilon_{ionic} \approx 20$ the lattice polarisation. Equation 1-18 also contains an additional term, $\epsilon_{rot} \approx 9$ due to the dynamic response of the molecular A-site ion. In $MAPbI_3$, polar liquid-like dielectric behaviour is observed above the orthorhombic - tetragonal phase transition (Figure 1-18), when dipole reorientation of the MA cation is unlocked.[134]

$$\epsilon_0 = \epsilon_\infty + \epsilon_{ionic} + \epsilon_{rot} \tag{1.6}$$

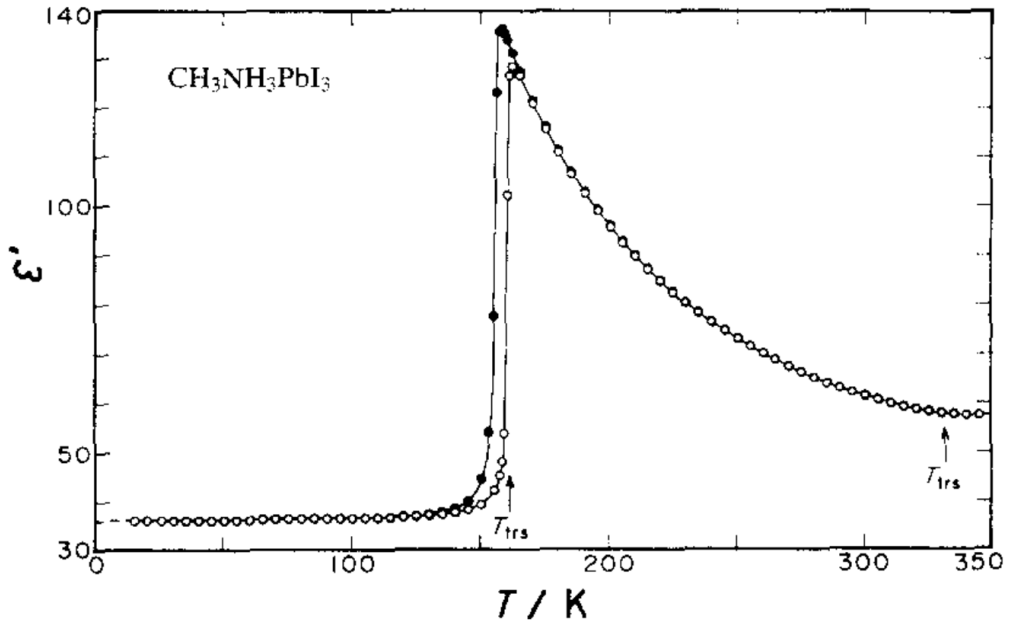

Figure 1-18: Real part of the dielectric permittivity of MAPI. Reproduced from Onoda-Yamamuro et al. by permission of Elsevier.[192]

1.10 Beyond Perovskites

Research efforts are increasingly devoted to finding alternative materials that, while sharing the characteristics of hybrid perovskites that underpin their solar cell performance, are less toxic and more stable. This search of compositional space has spanned other ns^2 compounds containing Sn^{2+}, Ge^{2+}, Sb^{3+} or Bi^{3+}.[74] These late p-block elements tend to lose only p-electrons when ionised, retaining a lone-pair s orbital and have been suggested for forming the basis of "defect-tolerant" photovoltaic materials.[99]

Double perovskites such as $Cs_2AgBiCl_6$ and $Cs_2AgBiBr_3$ are derived by isovalent substitution of M(I)/M(III) for Pb(II). However, these materials have not been reported to display optoelectronic properties suitable for application in solar cells.[193] $Cs_2Au(I)Au(III)Cl_6$, a distorted perovskite structure, is jet-black in colour due to mixed valency Au. $(MA)_2Au_2I_6$ formation, from reactive polyiodide melts of MAI and I_2, has been implicated in the degradation of perovskite solar cells containing Au electrodes.[194]

Compounds with the K_2PtCl_6 structure, e.g. Cs_2SnI_6, contain a B cation with formal oxidation state +4 and $\frac{1}{2}$ the ABX_3 sites vacant. Cs_2SnI_6, $E_g = 1.3$ eV, has been applied as an absorber material in solar cells. Band structure calculations of Cs_2SnI_6 indicates

significant energy dispersion around the conduction band edge, but a flat valence band. Recently Cs_2TiBr_6 has been employed in 3.3 % efficient photovoltaic cells.[195] Skutterudites, A-site vacant quadruple perovskites, e.g. $IrSb_3$, are predicted by DFT to display lower effective hole / electron masses than hybrid perovskites, with an E_g = 1.1-1.4 eV.[167]

Compounds based on Bi and Sb, from M(II) to M(III), e.g. $Cs_3Sb_2I_9$, E_g = 2.05 eV, form defect perovskite structures in which $\frac{1}{3}$ of B-site of the ABX_3 structure are vacant.[196] Silver iodobismuthates, including $AgBiI_4$ and $AgBi_2I_7$ have also been suggested as potential photovoltaic materials.[197] Ag_3BiI_6 cells have been demonstrated, with a conversion efficiency of 4.3%.[198] An ordered layered perovskite $Cs_4CuSb_2Cl_{12}$ with a 1.0 eV band gap has been reported, though the orbitals involved in this optical absorption most likely stems from localised *d-d* Cu(II) transitions, which may negate its use in solar cells.[199] BiI_3 and chalcohalides, e.g. BiSI, are also of interest for photovoltaics.[200]

Chapter 2

Background Technical Theory

This chapter provides the technical principles for diffraction and crystallography, semiconducting properties of materials and solar cell physics that underpin the results obtained. The applications of neutron diffraction as an experimental probe of hybrid materials and neutron facilities are outlined.

2.1 Photovoltaics

A solar cell behaves as a diode in the dark, admitting a far larger current under forward bias ($V > 0$) than reverse ($V < 0$) and, under illumination, delivers 0.5 to 1 volt photovoltage and tens of milliamps direct photocurrent per cm^2.[201] This photocurrent depends on incident light. The relationship between incident light and short circuit photocurrent density, J_{SC} gives the quantum efficiency $QE(E)$ of the cell:

$$J_{SC} = q \int b_s(E) QE(E) dE \tag{2.1}$$

where $b_s(E)$ is the incident spectral photon flux density. The reverse current flows in the opposite direction to photocurrent and approximately equal to the dark current, J_{dark}. Conventionally photocurrent is given as positive.

$$J(V) = J_{SC} - J_{dark}(V) \tag{2.2}$$

where

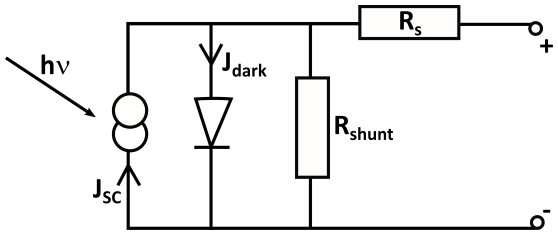

Figure 2-1: Equivalent circuit diagram of a solar cell

$$J_{dark}(V) = J_0\Big(\exp\frac{qV}{mk_BT} - 1\Big) \tag{2.3}$$

J_0 is the reverse saturation current and m is an ideality factor accounting for non-ideal diode behaviour.

Figure 2-1 provides the equivalent circuit diagram of a working solar cell. While parasitic resistances may have multiple underlying physical causes, they can be modelled as two equivalent circuit components representing contact resistance and leakage current. Series resistance, R_S, stems from ohmic resistances across cell materials and interfaces, while the parallel shunt resistance R_{shunt} reflects local imperfections in the cell providing alternative current pathways and should be maximised in an ideal cell.

Under open circuit conditions, contacts are isolated, the maximum potential difference in the cell is realised and the value of open circuit voltage V_{OC} obtained.

$$V_{OC} = \frac{kT}{q}ln\Big(\frac{J_{SC}}{J_0} + 1\Big) \tag{2.4}$$

High V_{OC} depends on low reverse current, J_0, which is minimised when the PV device exhibits well-rectifying diode behaviour.

2.1.1 Power and Efficiency

Figure 2-2 depicts the photocurrent / voltage curve of a representative solar cell. At V_{OC} no current flows, while at J_{SC} no photovoltage is generated. The power density of a solar cell is given by

$$P_{out} = JV \tag{2.5}$$

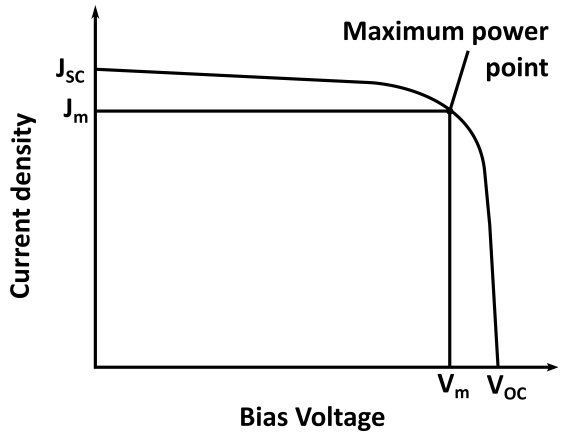

Figure 2-2: Current voltage characteristics of a solar cell.

Power output is maximised at the maximum power point (mpp), which is obtained at some value of photovoltage (V_m) and photocurrent (J_m). The fill factor, FF, is defined by the ratio of the mpp voltage and current to those obtained at open or short circuit conditions. The fill factor is therefore a good indicator of the quality of the PV device, with values ranging from 0.5-0.8 for different technologies.

$$FF = \frac{J_m V_m}{J_{SC} V_{OC}} \tag{2.6}$$

The efficiency of the cell is related to V_{OC} , J_{SC} and FF by

$$\eta = \frac{J_{SC} V_{OC} FF}{P_{in}} \tag{2.7}$$

where P_{in} is the incident light power density.

2.1.2 Generation and Recombination

Optical losses in solar cells arise due to reflection, transmission and re-emission of light. The wavelength-dependent absorption coefficient, α, of a material defines the thickness required for efficient absorption of photons

$$\frac{dI}{dx} = -\alpha I \tag{2.8}$$

as light with intensity I is attenuated over distance x.

Once charge carriers are photogenerated in an illuminated solar cell, it is possible they will recombine by radiative or non-radiative pathways. The change in carrier concentration with time is given by

$$\frac{dn}{dt} = G - k_1 n - k_2 n^2 - k_3 n^3 \tag{2.9}$$

where G is the charge generation rate, k_1 is the monomolecular charge recombination rate constant, k_2 the bimolecular rate constant and k_3 the Auger charge recombination rate (generally weak under one sun conditions). The monomolecular rate may be direct band to band or trap assisted. Shockley-Read-Hall trap assisted recombination is often the most important process for indirect band gap semiconductors. In Auger recombination, a third carrier is excited in energy within the same band. This process is an important source of recombination in silicon solar cells. Imperfections at grain boundaries, surfaces and interfaces will strongly influence recombination rates in real materials and devices.

In a direct semiconductor, the bimolecular recombination between electrons and holes can be viewed as the process of radiative emission. Photons are spontaneously emitted in the reverse process to absorption. The potential energy is released as an excited electron relaxes to ground state by emission of a photon. The wavelength dependent external quantum efficiency of a solar cell is defined as

$$EQE = \eta_{ext} = \frac{i}{\phi} \tag{2.10}$$

Where i is the number of charge carriers collected and ϕ is the photon flux. Over all wavelengths of light this relationship gives the EQE / IPCE spectrum. The external efficiency is related to the open circuit voltage by

$$V_{OC} = V_{OC}(ideal) + \frac{kT}{q} ln(\eta_{ext}) \tag{2.11}$$

Since the ideal V_{OC} is only reached when the external quantum efficiency is 100%, a good solar cell must be highly emissive, i.e. a good LED. In other words, once no non-radiative recombination pathways remain, at V_{OC} when no current is collected, the only pathway left for charge carriers to recombine is radiatively.[202]

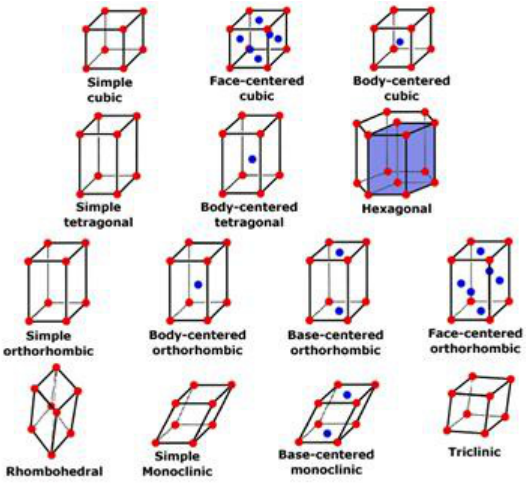

Figure 2-3: Unit cells of the fourteen crystal systems

2.2 Diffraction and Crystallography

Crystalline materials are characterised by a periodic arrangement of atoms in the solid state with translational symmetry, such that any particular section of the crystal, defined by unit cell axes in three dimensions, appears identical to any other. The lattice translation vector, $\mathbf{r}_n$, is given by Equation 2.12 where n_i are integers.

$$\mathbf{r_n} = n_1\mathbf{a} + n_2\mathbf{b} + n_1\mathbf{c} \tag{2.12}$$

The symmetry of a crystal is constrained by the requirement that unit cells stack perfectly with no gaps between cells. The relationship between the lengths (a, b and c) and angles (α, β and γ) of the parallelpiped of the unit cell, the unit cell parameters, define which of the seven crystal classes is adopted. Four types of lattice: primitive (P), body-centred (I), face centred (F or C), combined with seven crystal systems give fourteen unique Bravais lattices, as shown in Figure 2-3. The Bravais lattice, combined with the 32 unique point groups and the symmetry elements of inversions, rotations, roto-inversions, reflections, and glide and screw translations give rise to 230 unique space group symmetries that crystalline matter can adopt.

These symmetry relationships provide the most powerful means for experimentally discovering the atomic structure of crystalline materials by diffraction methods. In order to do this, probes are required on the same length scale as interatomic distances. Electromagnetic radiation in the X-ray region of the spectrum, beams of electrons accelerated to appro-

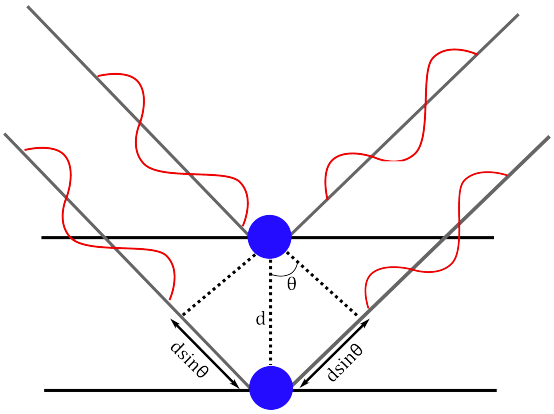

Figure 2-4: Bragg scattering by parallel planes of atoms.

priate velocities or thermal neutrons, with wavelengths defined by the de Broglie relation $\lambda = h/m\nu$, are all utilised.

Bragg diffraction occurs due to the constructive interference of the coherent elastic scattering of waves from a regular lattice (Figure 2-4), where d is the distance between adjacent parallel planes of atoms. Interference patterns of the scattered waves display intensity peaks when the angle of incidence fulfils the Bragg condition, given by Equation 2.13. The interplanar d-spacings are denoted d_{hkl}, where h, k, l are the integer Miller indices of each lattice plane. It is often also convenient to display diffraction data in terms of a momentum transfer vector, Equation 2.14, which has the advantage of being independent of the source wavelength.

$$n\lambda = 2d\sin(\theta) \tag{2.13}$$

$$Q = \frac{4\pi}{\lambda}\sin\left(\frac{2\theta}{2}\right) \tag{2.14}$$

Lattice parameters and d-spacings are related by equations dependent on the crystal system, for example for cubic crystals, Equation 2.15 holds.

$$\frac{1}{d_{hkl}^2} = \frac{(h^2+k^2+l^2)}{a^2} \tag{2.15}$$

2.3 Powder Diffraction

Powder diffraction measures the diffraction pattern from polycrystalline powders or crystalline thin films. A monochromatic X-ray beam incident on a powder sample will sample a large number of crystallites in various orientations and be diffracted in all directions governed by the Bragg equation. The result is concentric cones of diffracted intensity for lattice d-spacings. The concentric circles of the diffraction cones can be measured as a series of peaks as a detector is scanned through the angle, θ, of Bragg scattering.

While the basic use of powder diffraction is for phase identification, high quality data can be used in structure determination and refinement. The first step in data analysis is identification of powder diffraction pattern peak positions and indexing of those peaks, either to that of a known phase in a database, or to identify the cell symmetry and unit cell parameters through peak positions and systematic absences.

Powder diffraction condenses 3D structural information down to one dimension. Reflections all occur along single 2θ axis, leading to frequent reflection overlap, especially at high 2θ values, leading to difficulty in intensity extraction for individual reflections necessary for structure determination. It is necessary to find the contribution of individual reflections to the observed intensity peaks, for which various computational strategies have been developed.

Structureless fitting can be used to obtain unit cell parameters, peak functions and zero point errors without taking into account the structure factors, F_{obs}, of a structural model. Le Bail extraction or similar methods can be used to extract a set of intensities (I_{hkl}) without having to fit the data to a full structural model. Unit cell and peak shape parameters are obtained and Le Bail fitting also represents the best fit that can be obtained in a subsequent Rietveld refinement.

$$y_{ik}(obs) = \frac{y_i(obs)y_{ik}(calc)}{y_i(calc)} \tag{2.16}$$

Equation 2.16 is given for Le Bail intensity extraction, where the intensity $y(obs)$ is found at every ith step for each reflection k with arbitrary starting values for $y_i(calc)$.

2.3.1 Rietveld Refinement

Many of the challenges with solving and refining structures from powder data stem from overlapping reflections and not knowing *a priori* to what extent individual reflections contribute to an observed intensity peak. Rietveld (1967) introduced a method to compare step-by-step intensities calculated from a model $y_i(calc)$ to observed data $y_i(obs)$. Calculated intensities for a unit cell and trial structure are compared to the experimental pattern. Structural parameters are adjusted to obtain the best fit between calculated pattern and experimental data, within physically and chemically meaningful limits. $\overline{S}$ in Equation 2.17 is the sum difference of squares, the value to be minimised by least squares method against parameters for unit cell, peak profiles, atom positions and temperature and displacement effects

$$\overline{S} = \sum_i w_i(y_i(obs) - y_i(calc))^2 \tag{2.17}$$

where w_i is a weighting on the variance (σ) of $y_i(obs)$.

$$w_i = \frac{1}{\sigma^2(y_i)} \tag{2.18}$$

Different measures of the quality of the refinement fit exist, providing slightly different information. The weighted R factor, R_{wp}, is given in Equation 2.19, where the numerator is the quantity minimised in Rietveld refinement.

$$R_{wp} = \Big(\sum_i w_i[y_i(obs) - y_i(calc)]^2 \; / \sum_i w_i[y_i(obs)]^2 \Big)^{1/2} \tag{2.19}$$

$$R_{exp} = \Big((N - P) / \sum_i^N w_i[y_i(obs)]^2 \Big)^{1/2} \tag{2.20}$$

The final R_{wp} should approach the statistically expected R value, R_{exp}. Where there are N observations for P parameters and the ratio of R_{wp} and R_{exp} is the goodness-of-fit, χ^2, which should approach unity for an ideal refinement.

$$\chi^2 = R_{wp}/R_{exp} \tag{2.21}$$

An R factor based on observed and calculated structure factors, R_F, is more often used in single crystal refinement and given in the single crystal refinement section, Equation 2.27.

2.4 Single Crystal Diffraction

Single crystal diffraction is usually the method of choice for solving unknown structures.[203] Diffraction patterns are recorded as a pattern of spots by rotating a crystal in an X-Ray beam and detecting the diffracted pattern. The geometry, symmetry and intensities of diffraction spots contain information on the atomic positions in the crystal unit cell. Typically a suitable crystal is mounted on a kappa goniometer and rotated in an X-ray beam generated from a Mo or Cu source. CCD area detectors are commonly used to measure the diffracted beam.

Diffraction patterns are the Fourier transforms of the real-space arrangement of atoms. Each diffraction spot carries information from all points in the object. The structure factor (Equation 2.22) is a key parameter in crystallography. The structure factor describes the amplitude and phase of a diffracted wave from each lattice plane. F_{hkl}^{calc} may be calculated for every hkl, given the atomic coordinates in the unit cell. The scattering factor for X-rays is proportional to the atomic number Z and decreases with increasing θ.

$$\overline{F} = \sum f_i \exp[2\pi i(hx_j + ky_j + lz_j)] \tag{2.22}$$

Where $\sum f_i$ is the sum over atomic form factors in the unit cell. The intensity for each diffraction spot (hkl direction) is the sum of X-rays scattered by individual atoms. The square modulus of the structure factor is proportional to the intensity I of the hkl reflection.

$$I_{hkl} \propto | F_{hkl} |^2 \tag{2.23}$$

The variation of scattering factor of X-rays with angle, $f(\theta)$, is shown in Figure 2-6, which at $\theta = 0$ is equal to the atomic number. The exponential term in equation 2.24 contains an atomic displacement parameter, which affects how scattering intensity varies with temperature.

$$f_i(\theta) = f(\theta) \cdot exp\Big(- \frac{8\pi^2 \sin^2\theta \cdot U}{\lambda^2} \Big) \tag{2.24}$$

Putting together Equations 2.22 and 2.24, equation 2.25 is obtained.

$$F(hkl) = \sum_i f_i(\theta) \cdot exp\Big(- \frac{8\pi^2 U_i \sin^2(\theta)}{\lambda^2} \Big) \cdot exp[2\pi i(hx_i + ky_i + lz_i)] \tag{2.25}$$

The diffracted wave $F(hkl)$ is the sum of X-rays scattered by individual atoms at positions (xyz) as the atoms contribute to each diffracted wave. The reverse Fourier transform of the diffraction pattern gives the electron density, ρ, where the sum of the structure factor $\Sigma F(hkl)$ is now the sum over all reflections in the dataset.

$$\rho(xyz) = \frac{1}{V} \Sigma \overline{F}(hkl) \cdot exp[-2\pi i(hx + ky + lz)] \tag{2.26}$$

Solution of an unknown crystal structure typically requires the following steps:

1. Find a suitable single crystal
2. Pre-experiment to obtain unit cell and plan collection strategy
3. Measure intensity data
4. Data reduction
5. Structure solution by Patterson or Direct methods
7. Structure refinement

Once the observed structure factors, F_{obs} are obtained, these are compared to the F_{calc} of the structural model to find the differences with a residual factor e.g.

$$R = \frac{\Sigma \| F^{obs}| - |F^{calc} \|}{\Sigma |F^{obs}|} \tag{2.27}$$

An R value of $<$0.05 is typical for a solved structure.

2.4.1 X-Ray Generation

Copper ($K_{\alpha 1}$ λ= 1.5406 Å) and molybdenum (K_α λ= 0.71073 Å) are the most common laboratory X-ray sources for single crystal diffraction. Beam of electrons accelerated to around 40 kV strike a metal plate. The electrons are sufficiently energetic to ionise some of the 1s (K shell) electrons. An outer shell electron drops down to the now vacant level, e.g. 2p$\rightarrow$ 1s, and the difference in energy is released as radiation in the X-ray part of the spectrum, wavelength 0.5 to 3.0 Å. Background bremsstrahlung radiation and the $K_{\alpha 2}$ line

are removed using a filter such as Ni, or a crystal monochromator using a particular θ angle to select one wavelength.

2.5 Neutron Diffraction

Neutrons are uncharged subatomic particles with a mass of 1.68×10^{-27} kg, spin $\frac{1}{2}$, and a magnetic moment of -1.913 μ_N. Diffraction using neutrons was demonstrated in 1936, just four years after the neutron was discovered. Nuclear reactors provided the first intense neutron sources. Fission of ^{235}U releases MeV neutrons, which are slowed to thermal energies by a moderator, e.g. D_2O. Neutron flux from a reactor source has a Maxwellian distribution, with the peak wavelength given by Equation 2.28. Thermal neutrons (T $\approx$ $300\ K$) have a de Broglie wavelength of around 10^{-10} m.

$$\lambda = \frac{h}{\sqrt{5mk_BT}} \tag{2.28}$$

Several differences between the properties of neutrons and X-rays means that these techniques can be used to yield different and often complimentary structural information. Unlike X-rays, the scattering length for neutrons is not dependent on the atomic number Z, since scattering occurs from the nucleus and not the electron cloud (Figure 2-5). As a result, nearly isoelectronic elements are distinguishable, as are isotopes of the same element. X-ray methods are far less sensitive to light atom positions, particularly hydrogen. Neutrons are ideal as non-destructive probes, however with the low flux relative to X-ray synchrotron sources and weak scattering power (neutrons are highly penetrating), large sample sizes are required (grams of powder, large single crystals). By contrast, synchrotron X-rays may damage samples through ablation in the X-ray beam. There is no neutron form factor variation with θ angle as for X-rays, meaning no fall off in intensity at high angle (Figure 2-6). Magnetic studies are also possible via interaction of the neutron magnetic moment with the magnetic moment of the atoms.

Neutrons are increasingly produced at pulsed spallation sources, including ISIS in the UK. A proton beam accelerated to 800 MeV is aimed at a heavy metal target, e.g. tungsten, at around 50 Hz repetition rate. Neutrons are spalled from the target at a wide range of energies and the differing velocities of these neutrons are used for time-of-flight (TOF) diffraction experiments, covering the wavelength range 0.5 to 20 Å.

The relationship between time-of-flight, path length and d-spacing is given by equation

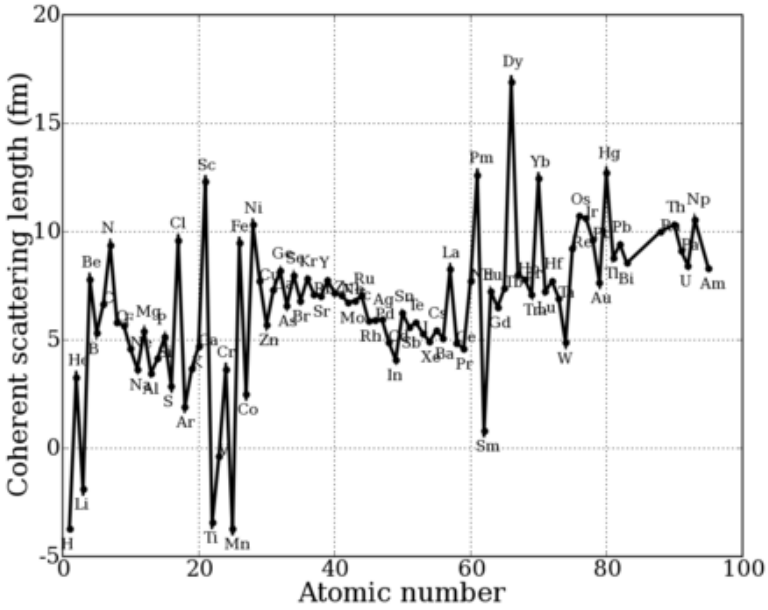

Figure 2-5: Neutron scattering factors of the elements

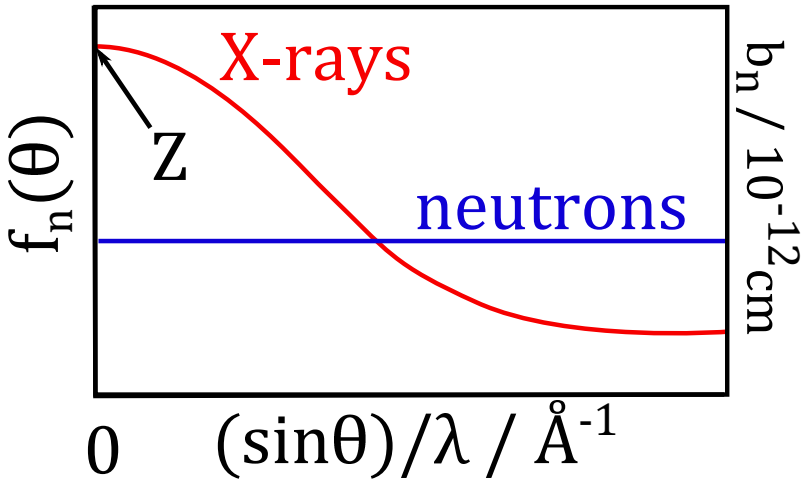

Figure 2-6: X-ray and neutron scattering factors variation with diffraction angle. $f_n(\theta)$ is the X-ray form factor and b_n the neutron form factor. Z is the atomic number of an element.

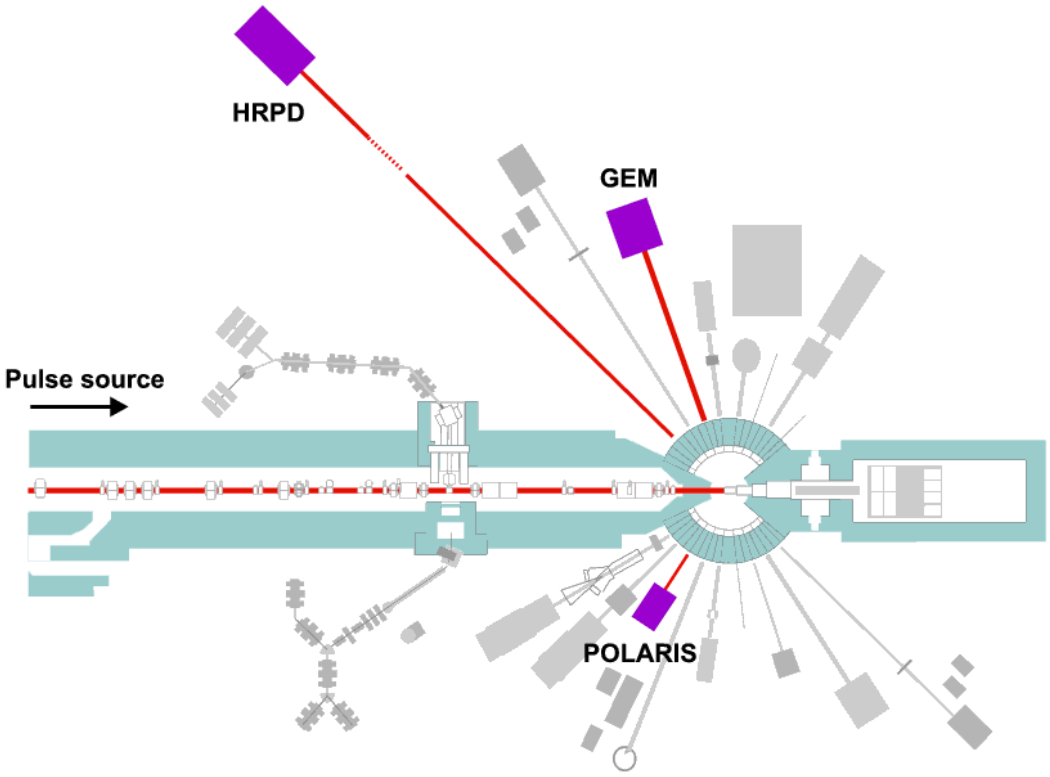

Figure 2-7: Layout of diffraction instruments at ISIS Target Station 2

2.29, by combining Bragg's Law with the de Broglie relationship and using the neutron mass of 1.67×10^{-27} kg.

$$\begin{aligned} t &= 505.56\ L \sin(\theta)\ d \\ d &= 1.977 \times 10^{-3}\ t\ L \sin(\theta)^{-1} \end{aligned} \tag{2.29}$$

where TOF is measured in μs, flight path L in metres and *d*-spacing in Ångstroms. The resolution of TOF diffractometers is given by equation 2.30, such that the highest resolution is achieved with long TOF (path length) and at high angle scattering.

$$\frac{\Delta d}{d} = \left(\left(\frac{\Delta t}{t} \right)^2 + \left(\frac{\Delta L}{L} \right)^2 + (\Delta\theta \cot\theta)^2 \right)^{\frac{1}{2}} \tag{2.30}$$

Figure 2-7 shows the layout of instruments surrounding ISIS target station 2, highlighting the stations related to neutron powder diffraction.

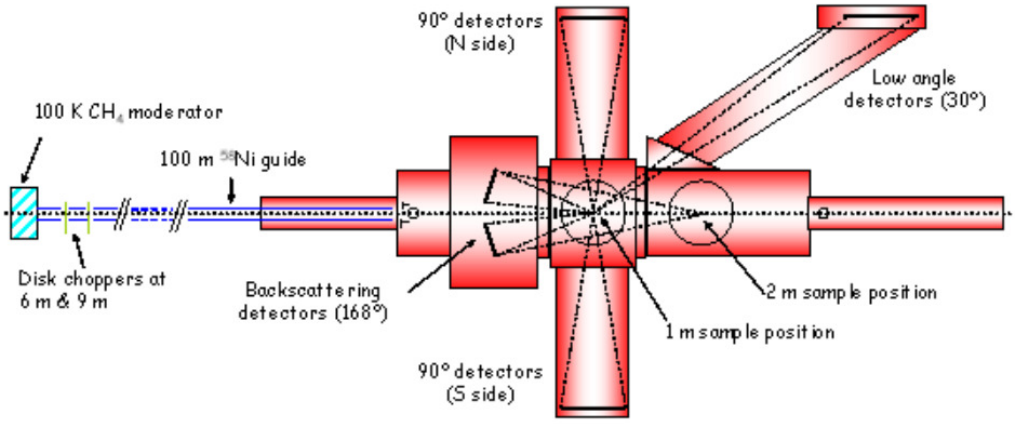

Figure 2-8: High resolution powder diffractometer instrument at ISIS Target Station 2

2.5.1 HRPD

The high resolution powder diffractometer at ISIS, Figure 2-8, has a primary path length of 100 m, providing unparalleled resolution, at the expense of neutron flux, in the backscattering detector banks.[204,205] The problem of frame overlap between successive pulses of neutrons at the 50 Hz source with such a long path length is overcome with mechanical choppers, reducing the incident beam to 5 Hz or 10 Hz. The maximum resolution in the ZnS scintillator backscatter detector is $\Delta d/d = 4 \times 10^{-4}$. Overall, the instrument covers the d-spacing range 0.6 - 16.5 Å.

2.5.2 GEM

The general materials diffractometer (GEM) at ISIS enables neutron powder diffraction of ordered and partially ordered materials over a very wide d-spacing range, equivalent to scattering angles of 1.1° to 169.3° and resolution of $\Delta d/d = 5 \times 10^{-3}$. Primary flight path of 17 m.

2.5.3 D20

The Institut Laue-Langevin in Grenoble is a reactor neutron source providing the most intense constant neutron flux in the world with 1.5×10^{15} cm^{-2} s^{-1} at the moderator. The D20 instrument is a two-axis medium resolution, high flux diffractometer at the ILL. D20

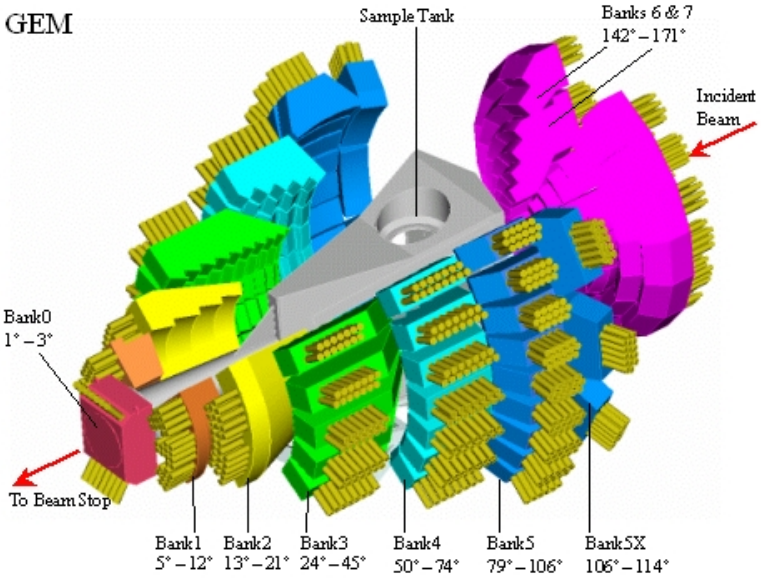

Figure 2-9: GEM diffractometer, ISIS Target station 2, detector bank layout

is the instrument of choice for thermodiffractometry experiments, in which fast collection times enable parametric evolution of structural changes with temperature or kinetics. It employs a position sensitive microstrip detector covering an angular range of 153.6°. In high resolution mode, using Ge115 as a monochromator, a resolution of $\Delta d/d = 3 \times 10^{-3}$ is achieved. These characteristics mean that reasonable counting statistics at reasonable resolution are collected on a short timescale, enabling changes to the sample to be effectively tracked by diffraction methods.

2.5.4 UV-vis Spectroscopy

Ultraviolet-visible spectrophotometry (UV-vis) measures the intensity of light relative to its interaction with a sample. It is the standard laboratory method of determining the absorptance, reflectance or transmittance spectrum of a material, which provides insight into its electronic transitions. In the case of semiconductor materials for photovoltaics, the transmittance of thin films is often measured, while for bulk materials with thicknesses greater than the optical absorption length the reflectance is measured. The band gap of the semiconductor corresponds to a sharp decrease in the reflectance of a sample as photons with energy above the band gap are absorbed. The reflectance spectra were collected on a Perkin Elmer Lambda 750S UV/vis/NIR dual beam spectrophotometer employing tungsten-halogen and Deuterium lamps, equipped with an integrating sphere.

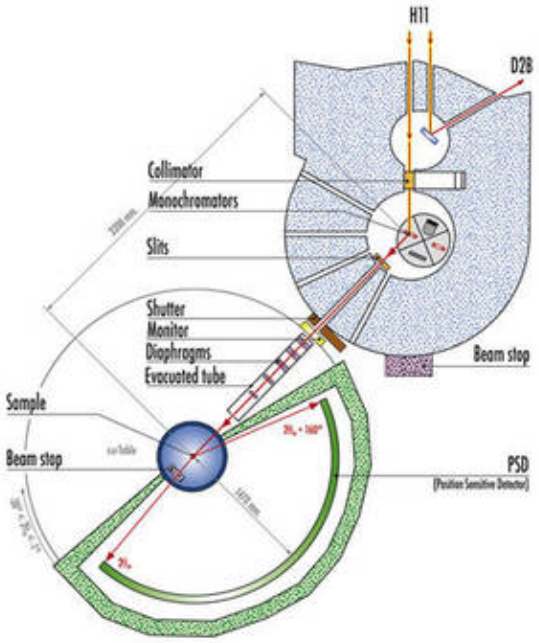

Figure 2-10: D20 diffractometer at the Institut Laue-Langevin

2.5.5 Scanning Electron Microscopy

Electron microscopy utilises a beam of thermionically emitted electrons to image samples down to the micormetre / nanometre scale. Typically the electrical signal from secondary electrons ejected from the sample is detected. Electron microscopy was carried out using a JEOL SEM6480LV microscope.

2.5.6 Raman Spectroscopy

Raman spectroscopy probes materials' roto-vibrational characteristics from the inelastic (Raman) scattering of monochromatic light by the polarisable electron density of a sample. In extended crystalline materials these vibrational properties correspond to the characteristic lattice vibrations (phonon modes). Infra-red (IR) inactive modes are often Raman active due to different selection rules. Raman measurements reported in Chapter 3 were carried out by Aurelien Leguy and Alejandro Goni at the Institut de Cincia de Materials de Barcelona (ICMAB-CSIC, Spain). A LabRam HR800 spectrometer was employed, using the 785 nm IR line of a diode-pumped solid-state laser, the 488 nm (blue) and 514.5 nm (green) lines from an Ar^{+} ion gas laser, and the 632.5 nm (red) line from a HeNe gas laser.

2.5.7 Nuclear Magnetic Resonance Spectroscopy

Nuclear magnetic resonance (NMR) spectroscopy relies on the excitation of nuclei with radio frequency pulses of electromagnetic radiation. NMR spectroscopy is sensitive to the local magnetic fields around atomic nuclei with non-zero spin, with NMR active nuclei absorbing electromagnetic radiation at a characteristic frequency. The chemical shift, coupling constants and integration of the NMR peaks provide a fingerprint of the chemical species. ^{1}H solution NMR is shown in Chapter 6 to be an effective method for the quantitative determination of the composition of solid solutions of hybrid perovskites containing dissimilar organic cations. All NMR experiments were carried out on a 300 MHz Bruker Avance spectrometer, using crystalline samples of hybrid perovskites dissolved in deuterated solvents.

2.5.8 Thermogravimetric analysis

Thermogravimetric analysis (TGA) measures the accurate mass change of a sample with changing temperature. As well as the thermal stability of the sample, TGA provides potential information on phase transitions and any adsorbed or absorbed gas species. Coupled to inline mass spectrometry, the chemical nature of the degradation products may also be elucidated. Thermogravimetric analysis and coupled mass spectrometer was carried out on a Setaram Setsys Evolution 16 TGA-DTA-DSC equipped with Pfeiffer GSD 320 mass spectrometer under flowing argon.

Chapter 3

Phase Behaviour of Methylammonium Lead Iodide

This chapter reports results on the synthesis, characterisation and phase behaviour of methylammonium lead iodide. The following published peer-reviewed work is reproduced in full by permission of the Royal Society of Chemistry, alongside further laboratory data:

Complete structure and cation orientation in the perovskite photovoltaic methylammonium lead iodide between 100 and 352 K. M. T. Weller, O. J. Weber, P. F. Henry, A. M. Di Pumpo, and T. C. Hansen, *Chem. Commun.*, 2015, **51**, 41804183

Link to online version:
http://pubs.rsc.org/en/content/articlelanding/2015/cc/c4cc09944c

3.1 Commentary

Methylammonium lead iodide, $MAPbI_3$, was the first compound to be used in perovskite photovoltaic cells, first as a sensitiser in solid liquid junction cells in 2008 and then in solid state perovskite solar cells in 2012.[47,55] $MAPbI_3$ has subsequently become a platform compound for the field of hybrid perovskite materials research. Despite the rapidly expanding knowledge base surrounding the optoelectronic applications of this material, structural characterisation remained incomplete and under-explored at the time of this study. No experimental evidence was available of the atomic positions of the methylammonium ion across each phase, particularly for the room temperature stable tetragonal phase relevant for photovoltaic devices. Neutron diffraction studies of bulk polycrystalline powders of

$MAPbI_3$ were therefore undertaken to understand the atomic structure and variable temperature phase behaviour of this increasingly important material.

Neutron powder diffraction experiments on D20 powder diffractometer at the Institut Laue-Langevin yielded information on the complete phase behaviour and light atom (C, N, H) positions of $MAPbI_3$ in each phase, as well as providing the temperature evolution of key structural parameters. In particular, the advantages of neutrons as an experimental probe for hybrid materials were underlined by the information gleaned on hydrogen atom positions and hydrogen bonding between the methylammonium cation and the inorganic lattice: information inaccessible from X-ray diffraction data.[137] The atomic structure of optoelectronic materials is integral to their function. The ability to extract key structural parameters at multiple temperature points across all three phases of the material, including the extent of disorder of the organic molecular ion and its interaction with the inorganic lattice, is a particular advantage of high flux, constant wavelength neutron powder diffraction. These structural results have underpinned further theoretical studies into the electronic structure of $MAPbI_3$ and the dynamics of the material.[168,206]

Methylammonium lead iodide was first synthesised by Weber in 1978 and the structure was reported as a cubic perovskite (a = 6.27 Å).[110] Seven years elapsed before further investigation into the material, when solid state ^{1}H and ^{14}N NMR revealed the existence of two phase transitions, with MA^{+} reorientation about the C-N axis present in the two higher temperature phases and restriction of C-N axis rotation in the low temperature phase.[207] The low temperature phase was assigned as orthorhombic *Pna2*$_1$ below 150 K, which was later revised to *Pnma* on the strength of neutron powder diffraction of N-deuterated methylammonium lead bromide at 11 K.[208]

The intermediate temperature phase was described as tetragonal, *I4/mcm*, below 327 K and the highest temperature phase cubic, *Pm-3m*, above 327 K by single crystal XRD.[209] Relaxation times extracted from millimetre wave and NMR of a few picoseconds, approaching that of a freely rotating methylammonium cation,[207,209] are in excellent agreement with more recent measurements.[116,210,211] Knowledge regarding the phase behaviour of $MAPbI_3$ was further expanded by Onoda-Yamamuro, by measurement of heat capacities, infra-red spectra and dielectric permittivities.[114,192] The methylammonium ion is dipolar, with the molecular polarisation tensor = 2.3 D.[178] The dielectric response above the orthorhombic/tetragonal transition temperature is described by the Kirkwood-Frölich behaviour for a polar liquid.[192] From the collated evidence, $MAPbI_3$ was understood to undergo two phase transitions of the order-disorder type. In the orthorhombic phase The C-N bond normal to the b axis, with the orientation alternating in adjacent unit cells along this axis in an antiferroelectric arrangement. Previous single crystal XRD and powder XRD of MAPI had

refined heavy atom structures, identifying an orthorhombic (*Pnma*) phase at low temperature, transitioning to an intermediate temperature tetragonal phase above 165 K and finally a cubic phase above room temperature.[146,152]

Pnma is the most common space group for pure tilting phase transitions of the perovskite system (cf. $GdFeO_3$). However, there is no group-subgroup relation between *I4/mcm* and $Pm\bar{3}m$ (Chapter 1, Figure 1-11), so formally it should not be possible to descend continuously through this phase transition sequence, (Figure 1-11), however no experimental evidence of an intermediate phase has been observed. A further complication in the structural analysis of hybrid perovskites stems from dynamic disorder. In $MAPbI_3$ For example, the C_{3v} point group of the MA^+ cation does not conform to the $m\bar{3}m$ symmetry of the Wyckoff position *1b* at which it resides in the high temperature cubic phase of $MAPbI_3$, space group $Pm\bar{3}m$.[212] This seeming discrepancy can be explained by orientational disorder, defined as the situation in which a polyatomic molecule or moiety has more than one distinguishable orientation in the crystalline lattice, preserving higher symmetry on average by its dynamic motion.

The neutron powder diffraction patterns for methylammonium lead iodide were measured on the D20 instrument at the ILL over the temperature range 100 - 352 K.[137] Neutron diffraction provides an ideal probe of the atomic structure of hybrid halide perovskites, comprised of light atoms (C, N, H) within a heavy atom frameworks (Pb, I). Since the scattering factors for neutrons do not scale with atomic number as for X-rays, full structural refinement of atom positions including hydrogen positions and almost isoelectronic C and N can be achieved. While use of hydrogen containing materials in neutron experiments results in a high background due to incoherent scattering from hydrogen, the high flux (up to 10^8 s^{-1} cm^{-2}), constant wavelength neutron beam at D20 results in sufficient signal to noise ratio within a reasonable counting time for structural analysis. D20 provides the ideal instrument for this manner of thermodiffractometry experiment, enabling short data collection segments to track phase behaviour over narrow temperature steps with reasonable resolution ($\Delta d/d \approx 2 \times 10^{-3}$).

Immediately apparent from the variable temperature data is the abrupt first order phase transition at 165 K from the low temperature orthorhombic to the tetragonal phase stable at intermediate temperature. The peak intensities of the tetragonal phase then gradually coalesce over the temperature range 165 - 327 K. Above this temperature the cubic phase is observed. Structural models for each phase were developed from longer data collections at 100 K, 180 K and 352 K, which are described in the following sections. Further structural studies of $MAPbI_3$ have subsequently been published. Neutron single crystal diffraction has confirmed the best description of tetragonal phase in space group *I4/mcm*.[213] A slight

off-centring of MA cation was detected in the cubic phase at 350 K, indicative of some hydrogen bonding interaction. Four orientations of NH_3 group, eight orientations of CH_3 in tetragonal phase reflecting differing interaction with the lattice, C–N axis mainly along [001]. A joint neutron and synchrotron X-Ray diffraction study of $MAPbI_3$ indicated the cubic / tetragonal transition to be first-order, close to tricritical.[214]

The orthorhombic phase of $MAPbI_3$ was studied by inelastic neutron scattering, which suggested that the local symmetry inside the inorganic cage led to improved description of the atomistic model of the organic molecular ion.[121] Compared to the long-range order probed by diffraction methods, neutron spectroscopy is sensitive to the local environment of the organic cations, which may differ considerably from the time and space averaged crystallographic symmetry. This report is in agreement with further spectroscopic data on perovskites, which indicate that while crystallographic techniques provide excellent description of the long range ordering, local structure and local structure dependant properties (tens of nanometres, picoseconds) vary significantly from the time and space averaged descriptions.[118]

In the case of single crystal diffraction, a well established problem in the analysis of hybrid halide perovskites, that powder diffraction avoids, is pseudomerohedral twinning of crystals. Szafranski and Katrusiak showed that almost every crystal in a sample of $MAPbI_3$ was twinned as grown.[215] Rothmann et al. directly observed intrinsic 100-300 nm twin domains in single crystal tetragonal $MAPbI_3$ using low-dose SAED to avoid damaging the sample.[216] This domain formation was seen to be reversible when samples are heated across the cubic transition ($57\ ^\circ$C) and then cooled, with the scale and orientation of the previous domains is retained. Similar effects have been observed by KPFM and ascribed to ferroelectric domain structure.[217]

3.2 Complete Structure and Cation Orientation in Methylammonium Lead Iodide Between 100 and 352 K

The following paper is reproduced in full from the original publication and spans thesis pages 67-82.

Statement of Authorship

This declaration concerns the article entitled:									
Complete structure and cation orientation in the perovskite photovoltaic methylammonium lead iodide between 100 and 352 K									
Publication status (tick one)									
draft manuscript		**Submitted**		**In review**		**Accepted**		**Published**	✓
Publication details (reference)	M. T. Weller, O. J. Weber, P. F. Henry, A. M. Di Pumpo and T. C. Hansen, *Chem. Commun.*, 2015, **51**, 4180–4183.								
Candidate's contribution to the paper (detailed, and also given as a percentage).	The candidate contributed to/ considerably contributed to/predominantly executed the… Formulation of ideas: OJW suggested initiating the project, MTW suggested use of neutrons as a structural probe. Design of methodology: MTW planned the D20 experiments and applied for beamtime. Experimental work: OJW synthesised the samples. MTW, PFH, AMP and TCH undertook the experiment on D20. Presentation of data in journal format: MTW and PFH developed the initial structural models and variable temperature data analysis. OJW undertook subsequent structural analysis using the developed models and contributed to writing the paper in journal format.								
Statement from Candidate	This paper reports on original research I conducted during the period of my Higher Degree by Research candidature.								
Signed						**Date**			

ChemComm

COMMUNICATION

View Article Online
View Journal | View Issue

Cite this: *Chem. Commun.*, 2015, 51, 4180

Received 12th December 2014,
Accepted 22nd January 2015

DOI: 10.1039/c4cc09944c

www.rsc.org/chemcomm

Complete structure and cation orientation in the perovskite photovoltaic methylammonium lead iodide between 100 and 352 K†

Mark T. Weller,*[a] Oliver J. Weber,[a] Paul F. Henry,[b] Antonietta M. Di Pumpo[ac] and Thomas C. Hansen[c]

The methylammonium cation in $[CH_3NH_3]PbI_3$ demonstrates increasing positional disorder on heating from 100 K to 352 K. In the tetragonal phase, stable between 165 K and 327 K, the cation is disordered over four sites directed toward the faces of the distorted cubic $[PbI_3]^-$ framework and migrates towards the cavity centre with increasing temperature.

The hybrid perovskite phase methylammonium lead iodide ($MAPbI_3$) has attracted increasing amounts of scientific attention since its identification as a highly efficient and low cost photovoltaic material.[1] Device efficiencies have rapidly risen to 17.9%,[2] while significant questions still remain regarding the device physics, especially the dynamic response under working conditions,[3] and also the fundamental structural properties of the material as a bulk solid and dynamically *in operando*. Full structural definition of the phases of $MAPbI_3$ has been hindered by the inherent complexity of the hybrid perovskite, with disorder in both organic and inorganic components observed in the higher temperature phases,[4] and the inherent limitations of X-ray diffraction techniques; these include an inability to distinguish the near isoelectronic atoms carbon and nitrogen, and difficulty in locating the light atom positions in the presence of the heavy atoms, Pb and I.

In previous studies the highest temperature phase, $T > 327$ K, has been part-refined (heavy atoms) in the cubic $Pm\bar{3}m$ space group from powder X-ray diffraction (PXD) data[5] and in the tetragonal $P4mm$ space group from single crystal X-ray diffraction data (SXD) at 400 K.[6] The tetragonal phase, adopted between 165 and 327 K, has been refined in the space group $I4cm$ at 293 K from SXD[6] and $I4/mcm$ symmetry from PXD data.[5] Neither of these models identified hydrogen atom position and the orientation of the methylammonium cation remained unclear. Note that Swainson *et al.*[7] could not definitively extract the $[CH_3ND_3]^+$ cation position in the tetragonal phase of $CH_3ND_3PbBr_3$ but the data suggested C–N orientation towards or along ⟨001⟩ or ⟨110⟩. The orthorhombic phase, found below 165 K, had been originally modelled in the space group $Pna2_1$; however this was reclassified into $Pnma$ as a result of the powder neutron diffraction (PND) data obtained from $CH_3ND_3PbBr_3$ at 11 K.[7] The C–N bond was found to lie normal to the b-axis, with the C → N vector alternating in neighbouring unit cells along this axis direction. The tetragonal to cubic phase transition has been investigated using both PXD[5] and SXD.[4] ^{14}N and ^2H NMR data[8] have shown that the rate of reorientation of the MA cation in the cubic phase approaches that of a freely rotating MA ion on the picosecond timescale, while for the tetragonal phase this rotation is increasingly arrested, with MA cations distributed over eight disordered states. In the orthorhombic (*Pnma*) phase, the cations are fixed with rotation of the C–N axis restricted. Quarti *et al.*[9] investigated polar and apolar structural models for MA cation orientation, finding a range of stable structures accessible within 0.1 eV per unit cell. The possibility of domains with different orientations existing within the same crystal was also described.

In this work we have investigated the full structure of $[CH_3NH_3]PbI_3$ using neutron powder diffraction (NPD) on a fully hydrogenous sample. This has provided key information on light atom positions in this heavy metal compound and distinguished carbon and nitrogen, due to their contrasting scattering lengths. Investigation of hydrogenous samples also has the advantage of avoiding isotope effects, which can markedly change phase behaviour in ammonium and alkylammonium compounds[10] while also providing a strong contrast between carbon, nitrogen, and hydrogen due to the latter's negative scattering length. The ability to extract good structural information from hydrogenous materials using high flux, medium resolution neutron diffraction instruments with large area detectors has previously been reported.[11]

A sample of $MAPbI_3$ was synthesised and its structure investigated as summarised in the Experimental Section.‡

[a] *Department of Chemistry and Centre for Sustainable Technologies, University of Bath, Claverton Down, Bath, BA2 7AY, UK. E-mail: m.t.weller@bath.ac.uk*
[b] *European Spallation Source ESS AB, P.O Box 176, SE-221 00 Lund, Sweden*
[c] *Institut Laue Langevin, 71 Avenue des Martyrs, 38000 Grenoble, France*

† Electronic supplementary information (ESI) available: Full details of the structure refinements, crystallographic coordinates, profile fits and bond length and distances. See DOI: 10.1039/c4cc09944c

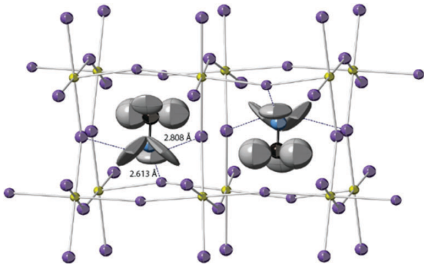

Fig. 1 The unit cell of $MAPbI_3$ at 100 K viewed close to *a*-axis the showing ADPs as 90% probability ellipsoids; lead yellow, iodine purple, carbon black, nitrogen blue and hydrogen grey.

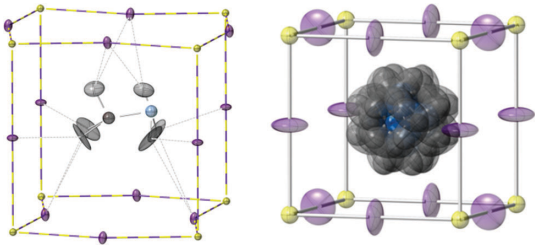

Fig. 2 Left: one orientation of the MA^+ cation in the tetragonal phase of $MAPbI_3$ at 180 K; the cation is four-fold orientationally disordered around the *c*-axis which is vertical in this diagram. Right: orientational disorder modelled in the cubic phase at 352 K. Atom key as in Fig. 1 and ADP ellipsoids at 50% probability.

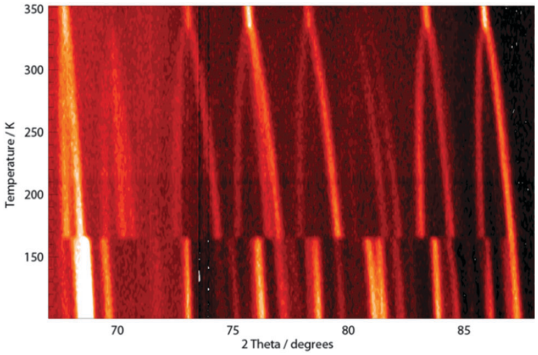

Fig. 3 Stacked plot, viewed vertically, of part of the NPD data (67–88°) collected from $MAPbI_3$ over the temperature range 100–352 K. Peaks are shown as white and pale orange on a black background. The phase changes at 165 and 327 K are clearly observed as is the overall unit cell expansion.

Orthorhombic structure, 100 K. The structure at 100 K was solved in *Pnma* previously described for $CH_3ND_3PbBr_3$ at 11 K[7] – see ESI† Section S1.1 for details of the structure refinement process, crystallographic model and derived bond lengths and angles. In this phase the MA^+ cations are fully ordered, Fig. 1, with the $-NH_3$ groups aligned and directed into the distorted square face of the parent perovskite unit cell. The PbI_6 octahedra are slightly distorted even though this is not necessary for the descent from cubic perovskite structure to *Pnma*, which is achievable through simple titling of the octahedra; the Pb–I–Pb angles are Pb–I1–Pb = 161.94(16)° (along *b*-axis) and Pb–I2–Pb = 150.75(12)° (along *a* and *c* axis); the average Pb–I–Pb bond angle is 154.5°. These tilts allow the three of the four iodide ions in one square face to move towards the $-NH_3$ end of the methylammonium cation and away from the $-CH_3$ end in the next unit cell, thereby satisfying the coordination preferences of both polar and non-polar ends of the molecules, Fig. 1. The centroid of the methylammonium cation lies near the centre of the cage giving reasonable strong hydrogen bonded NH···I distances at 2.613(7) and 2.808(9) (×2) Å (*cf.* 2.598 Å in NH_4I).[12] The refined anisotropic ADPs of the hydrogen atoms indicate that both ends of the methylammonium cation are undergoing large librations at 100 K in agreement with NMR data.[8]

Tetragonal structure, 180 K. The structure at 180 K was investigated using various models as summarized in ESI† Section S1.2. A model in *I*4/*mcm* was employed in the final structure description in which the MA cation adopts four possible orientations, along ⟨100⟩ and equivalent directions, in the unit cell pointing closely towards the centre of the distorted perovskite cube face (Fig. 2). The $[PbI_3]^-$ framework is considerably less distorted than in the orthorhombic phase with Pb–I2–Pb × 2 = 157.92(15)° and Pb–I3–Pb = 180° (average Pb–I–Pb bond angle 165.3°) and interactions between the $-NH_3$ group and the framework iodide are much weaker at 3.18(1) Å and 3.15(2) Å.

Cubic structure 352 K. See ESI† Section S1.3 for full details of the structure model development. Above 327 K in the cubic phase all Pb–I–Pb angles become, necessarily, 180° and the methylammonium cation becomes orientationally disordered at the unit cell centre primarily along the three unit cell directions with weak NH···I interactions at 3.12(2) Å and 3.52(2) Å (Fig. 2).

Variable temperature data, 100–352 K. Fig. 3 shows part of the mid-angle diffraction data collected while heating over the temperature range 100–352 K. These data clearly show the phase changes occurring at 165 and 327 K and the expansion of the respective unit cells in each of the temperature ranges for which the orthorhombic, tetragonal and cubic phase is stable. Data collected in each temperature range were binned into 2.5 K blocks for structure analysis using SEQGSAS,[13] to obtain a structural model for $MAPbI_3$ at each 2.5 K temperature point. Extracted information included lattice parameter information as well as the full coordinate and isotropic ADP information equivalent to that obtained for each phase at 100, 180 and 352 K – though esds on these values are higher due to much shorter counting times at each temperature point. However, these data clearly demonstrate the behaviour of the MA^+ cation with increasing temperature, as well as the overall response of the lead iodide framework and cell parameters. Our analysis here is restricted to a brief discussion of the key tetragonal phase that is stable at room temperature – further detailed analysis will be reported in due course.

Fig. 4 shows the variation of the reduced unit cell parameter ratio of the tetragonal phase between its formation at 165 K and its transformation to the cubic phase at 327 K. Fig. 5 shows the

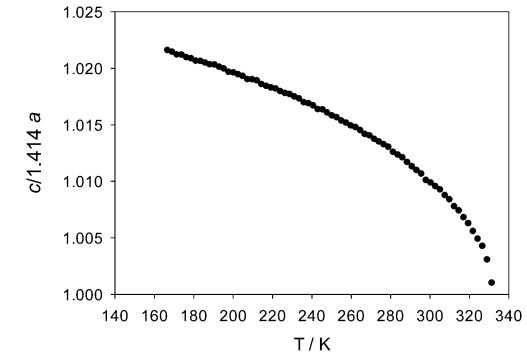

Fig. 4 Variation of the reduced lattice parameter ratio, $c/\sqrt{2}a$, over the range of stability of the tetragonal phase showing its approach to unity and formation of the cubic phase at 327 K.

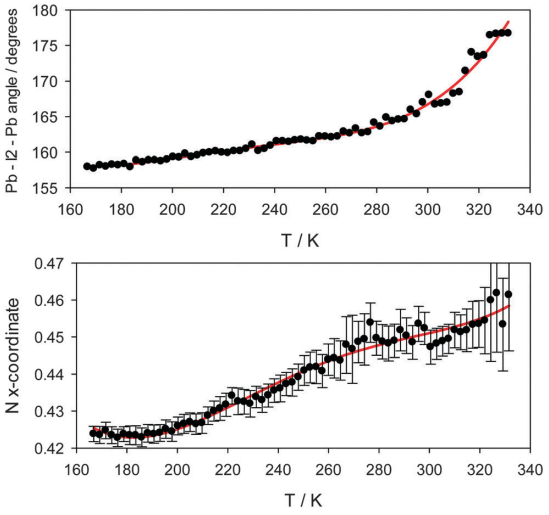

Fig. 5 Top – variation in the Pb–I2–Pb angle as a function of temperature in the tetragonal phase. Bottom – methylammonium nitrogen atom x-coordinate over the same temperature range.

evolution derived Pb–I2–Pb bond angle and the x-coordinate of the nitrogen atom of the MA^+ cation over the same temperature range. Fig. S4.3 (ESI†) shows the variation in the nitrogen atom U_{iso}. These plots demonstrate that with increasing temperature the $[PbI_3]^-$ framework becomes less distorted and the MA^+ group undergoes larger atomic displacements and migrates slowly towards the centre of the perovskite cube with the carbon and nitrogen atoms gradually adopting positions equidistant, at $x \sim 0.46$ and 0.54 respectively, from the cavity centre with $x = 0.5$. These behaviours all herald the formation of the cubic structure at 327 K.

At all temperatures the methylammonium cation in $MAPbI_3$ is oriented towards an open face of the (distorted) cube formed by the linked PbI_6 octahedra. At low temperatures the orientation of the MA cationic is fixed as a result of hydrogen bonding between the NH_3 groups and the framework iodide atoms. This acts as the driving force for the observed deformation of the $[PbI_3]^-$ framework producing three iodide sites closer to the $-NH_3$ end of the cation and three further away from the methyl groups with the MA cation adopting a staggered formation. As the temperature is increased the thermal motion of the cation increases and the NH···I interactions weaken. At the transition to tetragonal phase, at 165 K, the MA cations become rotational disordered in the *ab* plane and disordered over four similar orientations as found for the orthorhombic phase and directed towards the distorted cube faces, ⟨100⟩, ⟨010⟩, ⟨−100⟩ and ⟨0−10⟩. The MA cation is displaced slightly off centre of the unit cell with very weak hydrogen bonding interactions between N–H and I. The $-NH_3$ and CH_3 groups undergo free, or very unhindered, rotation around the C–N bond. Further heating towards room temperature results in increasingly free motion of the MA cation and a slow migration towards a central position in the perovskite A-site cavity. This is accompanied by a decrease in the reduced c/a ratio towards unity and straightening of the Pb–I–Pb bonds before the transition to the cubic phase at 327 K. In the cubic phase the MA^+ cation seems to remain directed toward the cube faces orientationally disordered over six positions – though a high level of positional and thermal disorder exists in this phase.

The observed high level of orientational motion of the MA^+ cation at room temperature seems to be related to the excellent photovoltaic performance of this material but also the anomalous hysteresis effect that have been reported from experiment.[15] Walsh *et al.*[16] have proposed that the internal electrical fields associated with microscopic polarisation domains contribute to hysteretic anomalies due to variations in electron–hole recombination process. The formation of these domains is likely to be related, in turn, to the local orientation patterns of the MA cations and further modelling work is ongoing using the full structural models discovered and reported in this work.

The ILL is thanked for the provision of ILL Director's Discretionary time. We would like to acknowledge the ILL for a PhD support for A.M. Di P. O.J.W. would like to thank EPSRC (EP/G03768X/1) for PhD studentship funding *via* the EPSRC Doctoral Training Centre in Sustainable Chemical Technologies.

Notes and references

‡ *Experimental Section.* Synthesis: methylammonium lead iodide was prepared according to the method of Poglitsch and Weber.[14] 2.5 g of lead acetate (Sigma) was dissolved in 10 mL hydroiodic acid (aq., 57 wt%, Sigma) in a 50 mL round bottom flask and heated to 100 °C in an oil bath. Separately, 0.597 g of CH_3NH_2 (aq., 40%, Sigma) was added drop-wise to a further 2 mL of hydroiodic acid kept at 0 °C in an ice bath under stirring. The methylammonium iodide solution was then added to the lead acetate solution and cooled over two hours to 46 °C, affording a black precipitate that was filtered and dried for 12 h at 100 °C. Average yield 3.1 g, 75.2%. The synthesis was repeated until 8 g of product had been obtained. Neutron powder diffraction. Data were collected using the D20 instrument at the ILL Grenoble operating in high take-off angle, higher resolution mode. 8 g of finely ground $MAPbI_3$ was placed in a 7 mm diameter vanadium can and cooled in a cryofurnace to 180 K. Data were collected for 90 minutes before further cooling the sample to 100 K. A second 90 min data collection was performed at this temperature before the sample was heated at 0.5 K min^{-1} to 350 K over 8.5 h. During this temperature ramp diffraction data were collected continuously and

binned into five minute blocks corresponding to 2.5 K data resolution. A final data collection over 90 min was performed at 350 K. Raw diffraction data were corrected against detector efficiency and analysed using the GSAS/EXPGUI program suite;[13] structure refinements for the long data collections at 100, 180 and 350 K were undertaken as described in the ESI;† SEQGSAS was used to analyse data collected during the heating ramp in sections corresponding to the three regions of phase stability, orthorhombic, 100–165 K; tetragonal 165–327 K and cubic above 327 K. Further details of the crystal structure investigation(s) for the 100 K, 180 K and 350 K data sets may be obtained from the Fachinformationszentrum Karlsruhe, 76344 Eggenstein-Leopoldshafen (Germany), on quoting the depository number CSD 428898 (100 K), 428899 (180 K) and 428900 (352 K) respectively.

1 M. M. Lee, J. Teuscher, T. Miyasaka, T. N. Murakami and H. J. Snaith, *Science*, 2012, **338**, 643–647; H.-S. Kim, C.-R. Lee, J.-H. Im, K.-B. Lee, T. Moehl, A. Marchioro, S.-J. Moon, R. Humphry-Baker, J.-H. Yum, J. E. Moser, M. Grätzel and N.-G. Park, *Sci. Rep.*, 2012, **2**, 591.
2 M. A. Green, K. Emery, Y. Hishikawa, W. Warta and E. D. Dunlop, *Prog. Photovoltaics*, 2014, **22**, 701–710.
3 R. Gottesman, E. Haltzi, L. Gouda, S. Tirosh, Y. Bouhadana, A. Zaban, E. Mosconi and F. De Angelis, *J. Phys. Chem. Lett.*, 2014, **5**, 2662–2669.
4 Y. Kawamura, H. Mashiyama and K. Hasebe, *J. Phys. Soc. Jpn.*, 2002, **71**, 1694–1697.
5 T. Baikie, Y. Fang, J. M. Kadro, M. Schreyer, F. Wei, S. G. Mhaisalkar, M. Graetzel and T. J. White, *J. Mater. Chem. A*, 2013, **1**, 5628–5641.
6 C. C. Stoumpos, C. D. Malliakas and M. G. Kanatzidis, *Inorg. Chem.*, 2013, **52**, 9019–9038; Y. Dang, *et al.*, *CrystEngComm*, 2015, **17**, 665–670.
7 I. P. Swainson, R. P. Hammond, C. Soullière, O. Knop and W. Massa, *J. Solid State Chem.*, 2003, **176**, 97–104.
8 R. E. Wasylishen, O. Knop and J. B. Macdonald, *Solid State Commun.*, 1985, **56**, 581–582.
9 C. Quarti, F. Mosconi and F. De Angelis, *Chem. Mater.*, 2014, **26**, 6557–6569.
10 Y. Kume, Y. Miyazaki, T. Matsuo, H. Suga, W. I. F. David and R. M. Ibberson, *Europhys. Lett.*, 1991, **16**, 265–270.
11 M. T. Weller, P. F. Henry, V. P. Ting and C. C. Wilson, *Chem. Commun.*, 2009, 2973–2989; C. C. Wilson, P. F. Henry, M. Schmidtmann, V. P. Ting, E. R. Williams and M. T. Weller, *Crystallogr. Rev.*, 2014, **20**, 162–206; P. F. Henry, M. T. Weller and C. C. Wilson, *J. Appl. Crystallogr.*, 2009, **42**(6), 1176–1188.
12 R. S. Seymour and A. W. Pryor, *Acta Crystallogr., Sect. B: Struct. Crystallogr. Cryst. Chem.*, 1970, **26**, 1487–1491.
13 A. C. Larson and R. B. Von Dreele, ''General Structure Analysis System (GSAS)'', Los Alamos National Laboratory Report LAUR, 2000, 86-748; B. H. Toby, EXPGUI, a graphical user interface for GSAS, *J. Appl. Crystallogr.*, 2001, **34**, 210–213.
14 A. Poglitsch and D. Weber, *J. Chem. Phys.*, 1987, **87**, 6373–6378.
15 H. J. Snaith, A. Abate, J. M. Ball, G. E. Eperon, T. Leijtens, N. K. Noel, S. D. Stranks, J. T.-W. Wang, K. Wojciechowski and W. Zhang, *J. Phys. Chem. Lett.*, 2014, **5**, 1511.
16 J. M. Frost, K. T. Butler and A. Walsh, *APL Mater.*, 2014, **2**, 081506.

Electronic Supplementary Material (ESI) for ChemComm.

Electronic Supporting Information

Structure and cation orientation in the perovskite photovoltaic methylammonium lead iodide between 100 and 352 K.

Mark T. Weller, Oliver J. Weber, Paul F. Henry, Antonietta M. Di Pumpo, Thomas C. Hansen

S1-4. Structure Refinements and Results

Reference numbers refer to main text

S1 Orthorhombic Phase at 100 K.

Structure refinement.

The previous descriptions for the structures for methylammonium Group IV halides were investigated as possible models for that of $MAPbI_3$. Le Bail extractions on the raw diffraction data yielded similarly good fits in both Pnma and $Pna2_1$ space groups. Therefore, the Pnma model by Swainson[7] for $CH_3ND_3PbBr_3$ was used as the basis for the full structural model refinement. Atomic positions were taken from this work and soft constraints added for just the C-N (1.460(1) Å) and C-H and N-H bond lengths (1.10(5) and 1.00(5) respectively) – rather than the rigid body model employed by Swainson.[7] Initial cycles of refinement included the full profile parameters and atomic position and atomic displacement parameters (ADPs) for lead and iodine. Latter cycles of refinement included all atomic coordinates and ADPs including anisotropic ADPs for iodine and hydrogen atoms in order to model the expected significant anisotropy for these species. A model was also constructed and refined in the $Pna2_1$ space group but did not lead to significant improvement of the fits. Final cycles of the Pnma refinement converged smoothly to give the data summarized in Table S1.1 and the final fit to profile is shown in Figure S1.1.

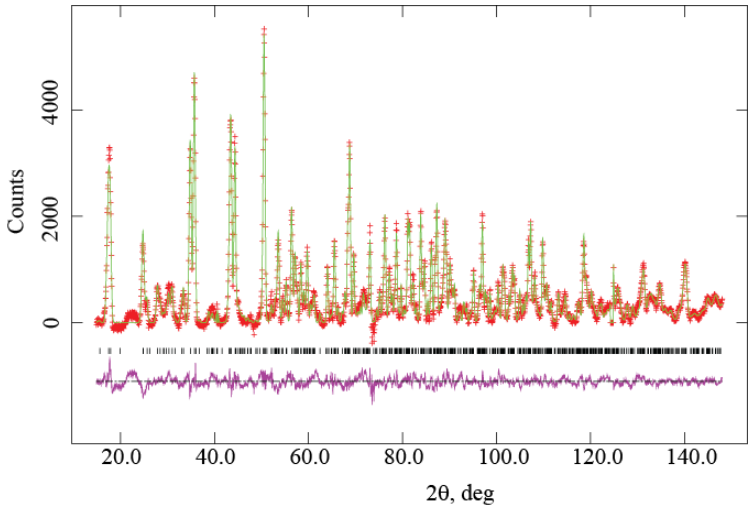

Figure S1.1 Profile fit achieved to the NPD data (background subtracted) from $MAPbI_3$ at 100K. Red crosses mark observed intensities, upper green line the calculated profile and lower purple line the difference. Tick marks show reflection positions.

Table S1.1 Refined structural model for $MAPbI_3$ in the orthorhombic phase, space group Pnma, at 100 K. a = 8.86574(30) Å, b = 12.6293(4) Å, c = 8.57689(31) Å.

Atom	x	y	z	U_i/U_e*100 [Å^2] [(a)]	Site	Mult
Pb1	0.500000	0.000000	0.000000	0.77(9)	-1	4
I1	0.4842(7)	0.250000	-0.0562(5)	0.91(14)	M(010)	4
I2	0.1886(4)	0.0147(4)	0.1844(4)	1.41(12)	1	8
N	0.9421(4)	0.750000	0.0297(4)	2.36(12)	M(010)	4
C	0.9372(17)	0.250000	0.0575(5)	2.52(16)	M(010)	4
CH1	0.9372(17)	0.250000	0.1874(6)	5.14*	M(010)	4
CH2	0.8661(11)	0.1701(5)	0.0290(14)	7.50*	1	8
NH1	0.1275(11)	0.1891(6)	-0.0085(15)	8.61*	1	8
NH2	0.9543(20)	0.750000	0.1459(5)	6.36*	M(010)	4

* U_e values calculated from anisotropic values modelled for hydrogen atoms

Final profile fit parameters R_P=0.86%, R_{wP} = 0.69 %, χ^2 = 12.6 R_F2 = 7.49. (Note that R values for hydrogen containing samples are artificially low due to the low residuals in fitting high intensity background points)

Table S1.2 Derived bond lengths and angles of interest for $MAPbI_3$ in the orthorhombic phase, space group Pnma, at 100 K.

Bond / Å	Bond length (esd)	Bond Angle	Bond Angle / degrees (esd)
Pb-I1 x2	3.1970(7)	Pb-I1-Pb	161.94(16)
Pb-I2 x2	3.1874(33)	Pb-I2-Pb	150.75(12)
Pb-I2 x2	3.1868(32)		
C-N	1.460(3)*		
C-CH1	1.129(4) *		
C-CH2	1.131(3) *		
N-NH2	1.002(3) *		
N-NH2	1.002(3) *		
NH….I1	2.613(7)		
NH….I2	2.808(9)		

*** constrained – see text**

S2. Tetragonal phase at 180 K.

Structure refinement.

No full structural model, including hydrogen atom positions or detailed orientation information for the C-N axis, for a tetragonal phase of methylammonium Group IV halides has been published. Swainson[7] was unable to determine the position of the partially deuterated $[CH_3ND_3]^+$ cation in $CH_3ND_3PbBr_3$ from high quality neutron powder diffraction data – though this work reports a preference for the a structure description in I4/mcm and disordering of the MA in the <001> or <110> planes. (Such a disordered cation would be hard to model due to the close superposition of hydrogenous CH_3 and deuterated ND_3 with the opposing scattering lengths of H and D). Initially, both the I4/mcm and I4cm descriptions of Swainson[7] and Stoumpos[6] were investigated with just the reported / inferred carbon and nitrogen positions. Both models gave very poor fits to the experiment data with just Pb, I, C and N positions (see Figure S2.1), confirming the high sensitivity of the powder neutron diffraction data to the hydrogen positions. Difference Fourier maps were calculated for both space groups and hydrogen positions (negative peaks around 1 Å from C/N) were rapidly identified for I4/mcm but not for I4cm and only the former structure model was developed further. The C and N positions were assigned to (x,½-x, z) sites with x~0.45 and z~0.25 either side of, but close to, the centre of the distorted perovskite cube and the soft constraint C-N = 1.460(1) Å introduced. This model, with a ¼ site occupation, allows the C-N unit to adopt four positions directed near to the four cube faces in the *xy* plane. A new difference Fourier map was calculated with this model and hydrogen was assigned (with appropriate site fractional occupancies) to two negative peaks identified ~1 Å from C or N and soft constraints introduced with C/N-H at 1.05(1)Å. This model is a relatively simple representation of the $[CH_3NH_3]^+$ cation using just two hydrogen positions, note that it averages the CH_3 and NH_3 ends of the cation and thereby the C/N-H distances (hence the use of the C/N at 1.05 Å constraint) and formally produces an eclipsed conformation for the molecular cation. However, the simplicity of this model also allowed introduction of anisotropic ADPs for the hydrogen atoms which models the likely (near) free rotation of the ends of the molecular cation around the C-N bond. Full refinement of atom positions and ADPs for all atoms (anisotropic for iodine and hydrogen) rapidly converged to give a very good fit to the experimental diffraction profile (Figure S2.2). The final structural model developed is summarised in Table S2.1 and derived bond lengths and angles given in Table S2.2. Figure S2.3 represents possible orientations of the methylammonium cation in adjacent sites.

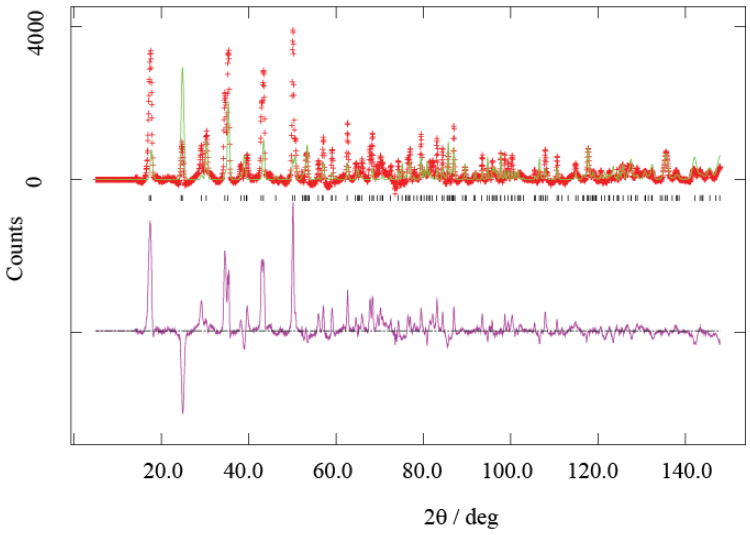

Figure S2.1. Profile fit achieved to the NPD data (background subtracted) from $MAPbI_3$ at 180K in the space group I4/mcm with just Pb, I, C and N positions. Red crosses mark observed intensities, upper green line the calculated profile and lower purple line the difference. Tick marks show reflection positions.

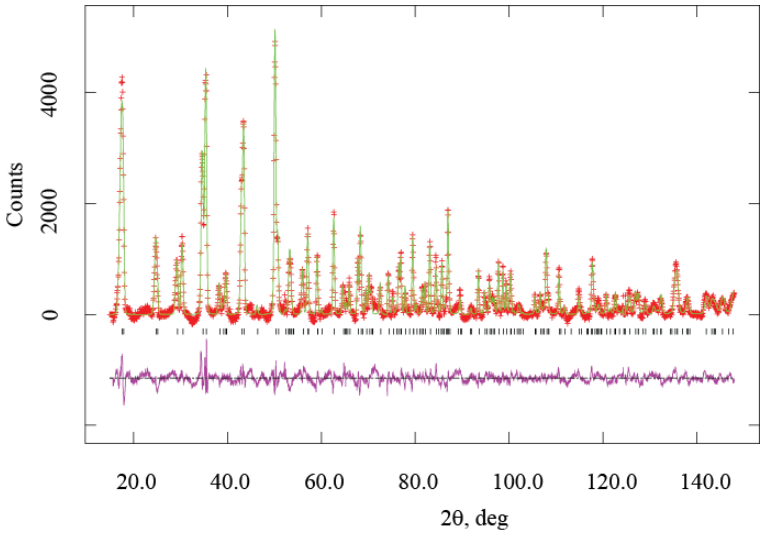

Figure S2.2. Final profile fit achieved to the NPD data (background subtracted) from $MAPbI_3$ at 180K. Red crosses mark observed intensities, upper green line the calculated profile and lower purple line the difference. Tick marks show reflection positions.

Final Crystallographic Model

Table S2.1. Refined structure model for $MAPbI_3$ in the tetragonal phase, space group I4/mcm, at 180K. a = 8.80625(28) Å, c = 12.7127(5) Å

Atom	x	y	z	Ui/Ue*100 [Å^2][(a)]	Site	Mult	Fractn
PB1	0.500000	0.500000	0.500000	2.16(13)	4/M(001)	4	1.0
I2	0.20122(34)	0.29878(34)	0.500000	4.68*	MM2(+-0)	8	1.0
I3	0.500000	0.500000	0.750000	4.03*	422(001)	4	1.0
N4	0.4128(8)	0.0872(8)	0.2833(10)	5.3(4)	M(110)	16	0.25
H5	-0.0381(41)	0.3531(14)	0.2203(18)	25.79*	1	32	0.50
C6	0.5273(7)	-0.0273(7)	0.2588(13)	7.2(4)	M(110)	16	0.25
H7	0.4297(14)	0.0703(14)	0.3336(16)	15.54*	M(110)	16	0.50

*U_e values calculated from anisotropic values modelled for hydrogen and iodine atoms
Final profile fit parameters R_P=0.90%, R_{wP} = 0.69 %, χ^2 = 13.5 R_F2 = 9.83

Table S2.2 Derived bond lengths and angles of interest for $MAPbI_3$ in the tetragonal phase, space group I4/mcm at 180 K.

Bond	**Bond length (esd) / Å**	**Bond Angle**	**Bond Angle / degrees**
Pb-I2 x4	3.1722(8)	Pb-I2-Pb x 2	157.92(15)
Pb-I3 x2	3.174(33)	Pb-I3-Pb	180
Pb-I2 x2	3.17818(13)		
C6-N4	1.459(3)*		
N4-H5	1.05(4) *		
N4-H7	0.67(3) *		
C6-H5	1.16(2) *		
C6-H7	1.09(3) *		
(C/N)H5….I2	3.184(12)		
(C/N)H7….I2	3.394(16)		

* Constrained – see text

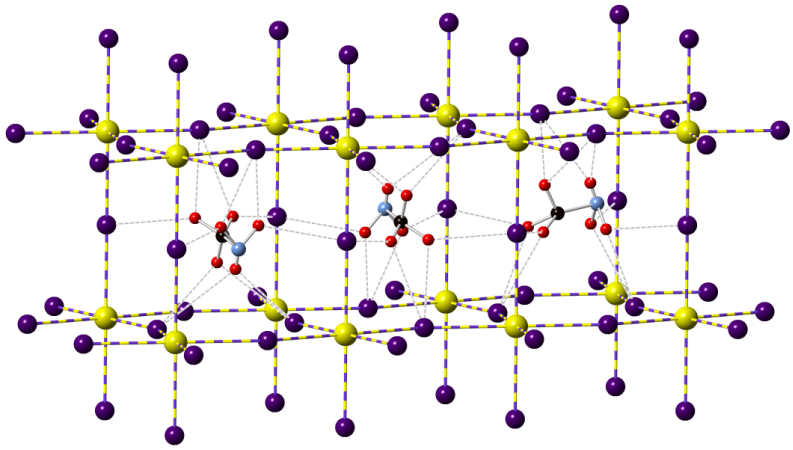

Figure S2.3. Representation of the structures of $MAPbI_3$ in the tetragonal phase showing three adjacent cells. Pb-yellow, I-purple, N-blue, C-black and H-red. The orientation of the methylammonium cation in neighbouring unit cells is shown in three of the four possible orientations. *c*-Axis vertical and *a* or *b* horizontal.

S3 Cubic Phase at 352 K.

Structure refinement

The structure refinement was undertaken in Pm-3m with Pb on (0 0 0) and I on (0.5 0 0). Based on the orientation of the methylammonium cation in both the orthorhombic and tetragonal phases, a model was developed with the C-N bond directed at the square window of the perovskite cube with an atom representing fully disordered C and N situated at (x, 0.5, 0.5), site multiplicity 6, site occupancy 1/3, with x~0.4 producing a C-N distance of ~1.4Å. Refinement of this structural model, employing an anisotropic ADP for iodine, yielded a χ^2 of ~130. Difference Fourier maps were calculated using this model and a hydrogen atom position identified ~1 Å from C/N near (0.3, 0.45, 0.38), site multiplicity 48. Hydrogen was assigned to this site with an occupancy of 1/8 (yielding 6 hydrogen atoms in the unit cell). A full structure refinement using this model and including all coordinates and ADPs (anisotropic for I and H) but no bond length constraints converged to the structure description and refinement parameters given in Table S3.1. Note that because of the high thermal motion in this phase an alternative structural model in which the C-N direction was orientated along <111> was also investigated – refinement of this model using similar hydrogen positions gave a slightly worse χ^2 value (10% higher) and shorter C/N-N/C bond length at 1.31Å – such a structural model, which would also reflect a very freely re-orientating MA cation, cannot be fully ruled out - but seems a poorer description of the structure.

The final profile fit achieved is shown in Figure S3.1. Figure 2 (main text) shows a summary of all possible orientations of the methylammonium cation indicating effectively free rotation of the cation around the cube centre and Figure S3.2 shows one possible orientation of the molecular cation.

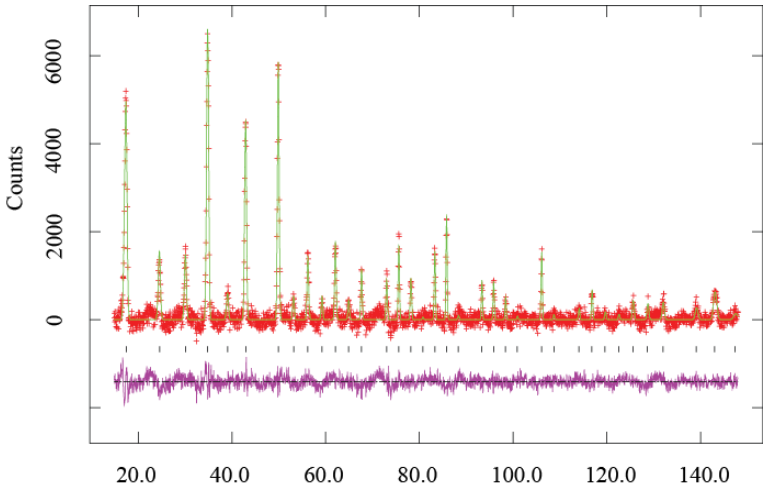

Figure S3.1. Final profile fit achieved to the NPD data (background subtracted) from $MAPbI_3$ at 352K. Red crosses mark observed intensities, upper green line the calculated profile and lower purple line the difference. Tick marks show reflection positions.

Final Crystallographic Model

Table S3.1 (Refined structure of $MAPbI_3$ in the cubic phase, space group Pm-3m, at 352 K, a = 6.31728(27) Å)

Atom	x	y	z	Ui/Ue*100 [Å^2]	Site	Mult	Fractn
PB1	0.000000	0.000000	0.000000	4.20	M3M	1	1.0000
I2	0.500000	0.000000	0.000000	12.30*	4/MMM100	3	1.0000
C3	0.393308	0.500000	0.500000	17.75	4MM(100)	6	0.3333
H4	0.305848	0.448981	0.379518	14.74*	1	48	0.1250

*U_e values calculated for anisotropic values modelled for hydrogen and iodine atoms

Final profile fit parameters R_P=1.34%, R_{wP} = 1.06 %, χ^2 = 1.61 R_F2 =13.6%

Table S3.2. Derived bond lengths and angles of interest for $MAPbI_3$ in the cubic phase, space group Pm-3m at 352 K.

Bond	**Bond length (esd) / Å**	**Bond Angle**	**Bond Angle / degrees**
Pb1-I2 x6	3.1586(2)		
		Pb-I2-Pb	180
C/N – C/N	1.348(1)		
(C/N) – H4	0.994(1)		

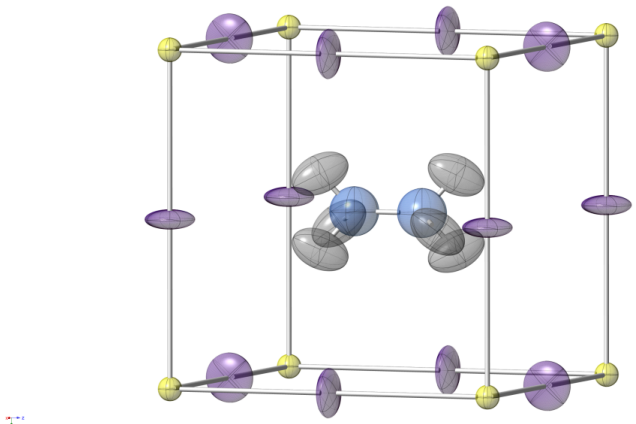

Figure S3.2. Representation of the structures of $MAPbI_3$ in the cubic phase showing one of the possible methylammonium cation orientations. Pb-yellow, I-purple, N-blue, C-black and H-red.

S4 Variable temperature data analysis

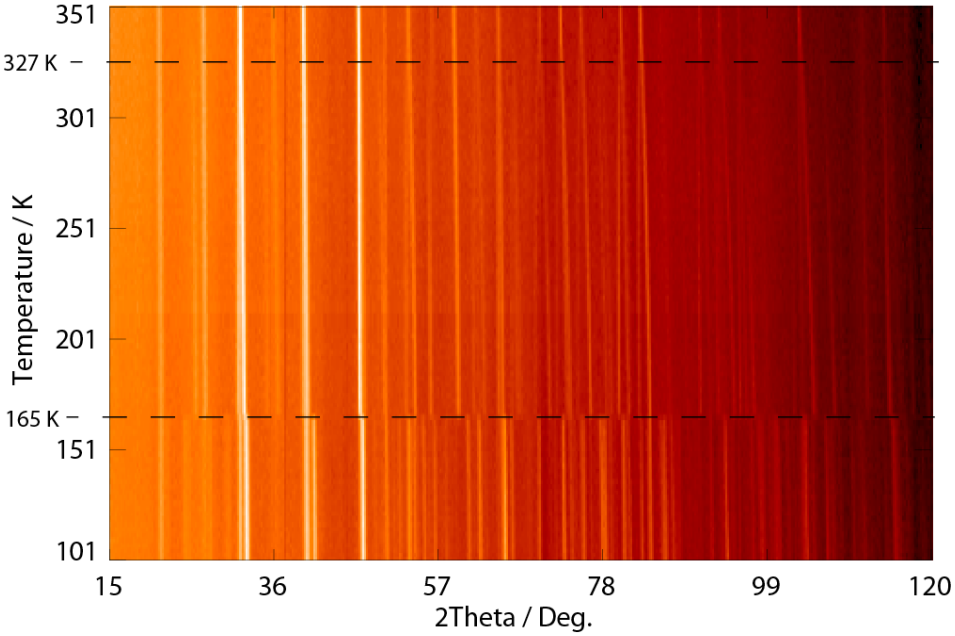

Figure S4.1. Stacked plot of the NPD patterns viewed vertically for the full temperature and diffraction angle range. The transition temperatures at 165 and 327 K are marked. Intensities on the out of page axis are shown on a scale from white (high intensity) to dark red.

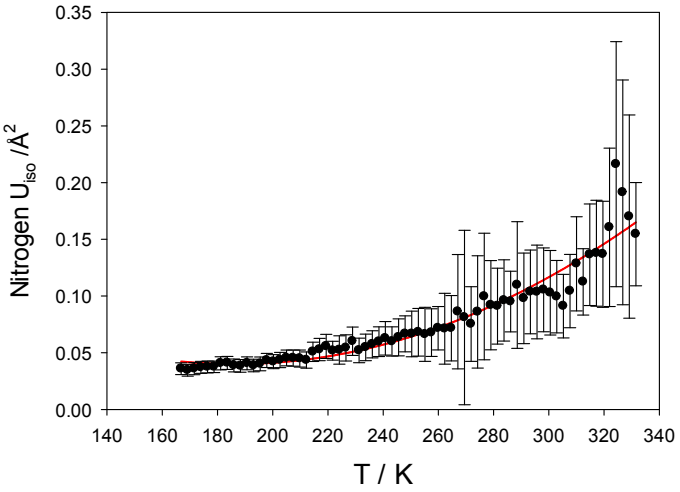

Figure S4.3. Variation of the nitrogen atom U_{iso} over the range of stability of the tetragonal phase showing an increase due to greater thermal motion of the methylammonium cation.

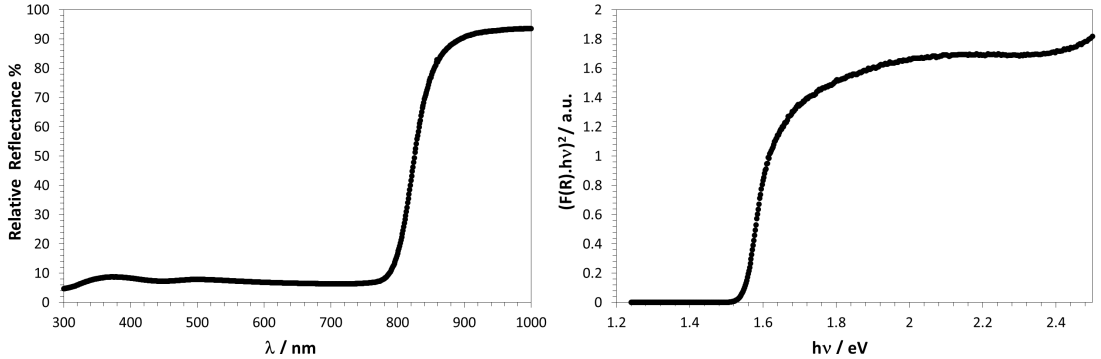

Figure 3-1: Reflectance spectrum of $MAPbI_3$ versus wavelength in nanometres (left). Tauc plot of Kubelka-Munk transformed $MAPbI_3$ diffuse reflectance spectrum versus energy in electronvolts for band gap determination (right)

3.3 Further Results on MAPI

3.3.1 UV-vis Spectroscopy

The UV-vis reflectance spectrum of the sample of $MAPbI_3$ used in the D20 experiments is shown in figure 3-1. The powder crystalline sample was loaded into a custom-built sample holder with an optical glass window. The reflectance of the sample was measured on a Lambda 750S spectrometer equipped with an integrating sphere, relative to a $BaSO_4$ reflectance standard. The sharp drop in reflectance above the band gap underlines the suitability of hybrid perovskites for light harvesting applications. The right-hand plot shows a Kubelka-Munk transform of the reflectance spectrum and the band gap of $MAPbI_3$ was taken from the intercept of the rise in $F(R)$ to the background baseline. A band gap of 1.55 eV was extracted, in excellent agreement with other reports throughout the literature.

3.3.2 Thermal Analysis

The thermal degradation of MAPI was investigated by thermogravimetric analysis (TGA), Figure 3-2a. The sample displayed 24.3% mass loss by 400 ^{o}C. The gas outflow of the TGA was coupled to a mass spectrometer (TGA/MS) for analysis of the chemical degradation products, Figure 3-2b. Degradation products are observed by MS after 100 mins, corresponding to 300 ^{o}C, the temperature at which MAPI thermal degradation is observed.

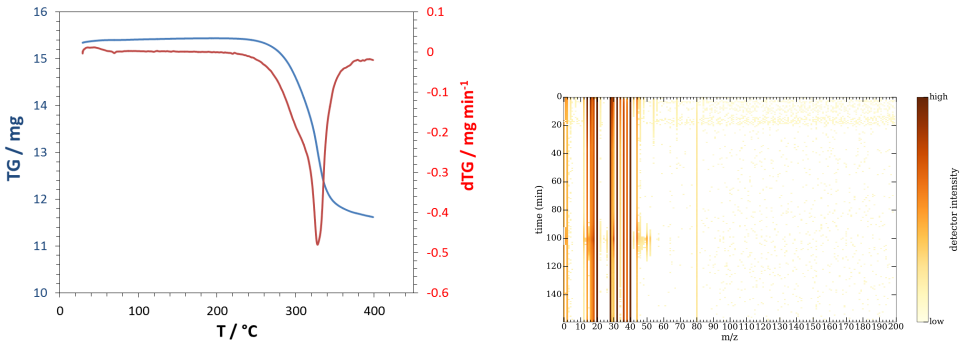

(a) (b)

Figure 3-2: a) Thermogravimetric analysis of $MAPbI_3$ heated from 20 °C to 400 °C, plotting weight loss curve (blue line) and its first derivative (red line). b) Coupled mass spectrometry of degradation products of MAPI produced from TGA.

3.3.3 Photovoltaic cells

Thin film solar cells utilising $MAPbI_3$ as the absorber layer within mesoporous titania were fabricated by the sequential deposition route. Figure 3-3 summarises the deposition of active layers of the device.

TEC7 FTO glass was scored using a diamond scribe and cut into 25x25 mm square peds, masked with masking tape and selectively etched using Zn/ HCl(4M). The FTO glass was sequentially cleaned with washing up liquid, Hellmanex solution at 70 ^{o}C, DI water, acetone, iso-propanol and dried with an air gun between each step. The FTO was then plasma cleaned for 10 mins prior to use. A TiO_2 compact blocking layer was deposited onto the FTO from 1.5 mL titanium isopropoxide (Sigma) in 13.5 mL anhydrous isopropanol via spray pyrolysis. A hand-held spray gun attached to a compressor at 25 psi was used for the application of the titania precursor solution, with 25 passes of the spray gun over the FTO surface held at 300 ^{o}C on a hotplate.

A mesoporous TiO_2 layer was then deposited on top of the compact blocking layer using titania paste (Dyesol, NR-T paste) 2:7 wt/wt% in anhydrous ethanol, which had been mixed on rollers for 12 hours. This was applied by spin coating 150 μL per ped at 5000 rpm for 30 s and subsequently dried on a hotplate at 150 ^{o}C. After cooling to room temperature, the blocking layer and compact layer were sintered in a carbolite furnace at 550 ^{o}C for 30 minutes.

Lead iodide (462 mg, 99%, Sigma Aldrich) was dissolved in 1 mL anhydrous DMF under an N_2 atmosphere. PbI_2 was spin coated onto the mesoporous layer 6000 rpm for 1 minute

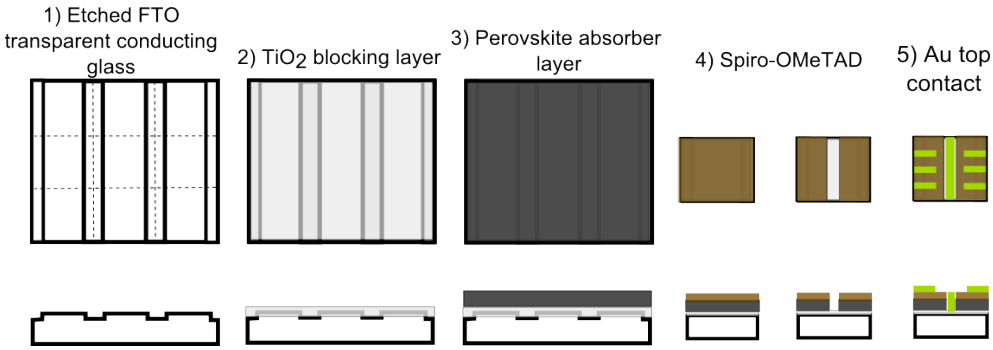

Figure 3-3: Architecture of perovskite solar cells

inside a glovebox. This allows the PbI_2 solution to percolate and crystallise within the mesoporous layer as well as capping the mesoporous layer with a planar perovskite layer. The PbI_2 layer was dried at 70 ^oC for 10 mins on a hotplate. Methylammonium iodide (Dyesol) was dissolved in anhydrous isopropanol at a concentration of 10 mg / mL. Each ped was then submerged in the MAI/IPA solution for 5 mins, with the perovskite phase observed to form while submerged, as the cell turned from yellow to black. The ped was then extracted and washed with isopropanol, which was removed by spinning the ped on the spin coater again at 6000 rpm for 1 minute to remove the solvent. The cells were then heated on hotplate at 70 ^oC for 30 mins to complete the crystallisation of the perovskite phase.

The hole transport layer, doped Spiro-OMeTAD, was then deposited onto the perovskite layer by spin coating at 2500 rpm for 45 s. The Spiro solution was prepared by dissolving 75 mg Spiro-OMeTAD in 1 mL chlorobenzene, along with 30 μg 4-tert-butylpryidine (tBP, Sigma 96%) and 20 μg lithium bis(trifluoromethane) sulfonimide (LiTFSI, Sigma). The solution was filtered through a 22 μm PTFE syringe filter prior to use. Chlorobenzene, being an antisolvent for the perovskite layer, can be used to deposit the hole transport layer while keeping the underlying perovskite layer intact. Following the deposition of the hole transport layer, the cells were stored for 12 hours in a dry ambient atmosphere, which enables further doping of the Spiro layer from atmospheric oxygen. Following this, part of the perovskite layer was selectively removed using a razor blade to enable contacting of the device. The Au top contact layer was then deposited via thermal evaporation, with each ped selectively masked to expose 1 cm^2 areas for each cell.

The efficiencies of the MAPI solar cells were determined using an Oriel Sol3A solar simulator (94023A) illuminated at sun (100 mW cm^{-2}, AM 1.5) calibrated using a certified silicon reference cell (91150V Oriel). A typical current / voltage response of these MAPI perovskite cells is given in Figure 3-5, which displays clear hysteresis depending on the scan direction.

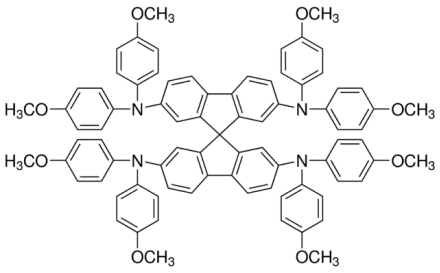

Figure 3-4: Structure of N2,N2,N2,N2,N7,N7,N7,N7-octakis(4-methoxyphenyl)-9,9-spirobi[9H-fluorene]-2,2,7,7-tetramine (Spiro-OMeTAD) hole transport material.

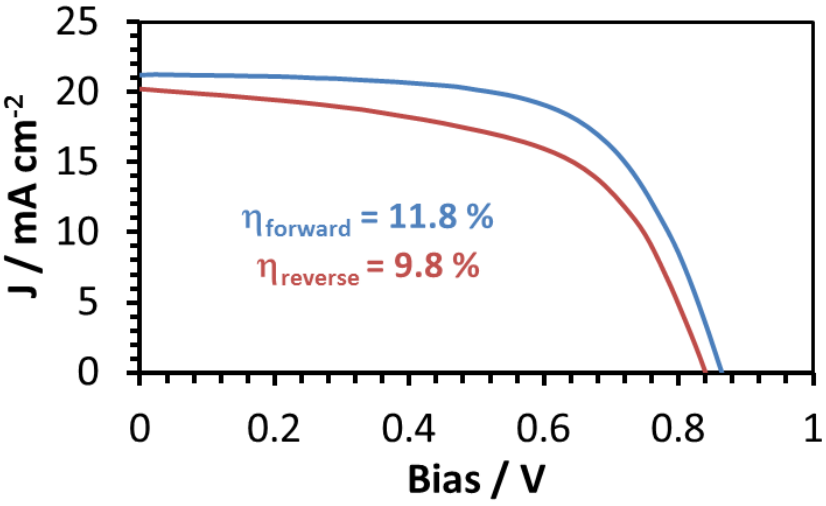

Figure 3-5: Current-voltage curve of representative $MAPbI_3$ solar cell performance.

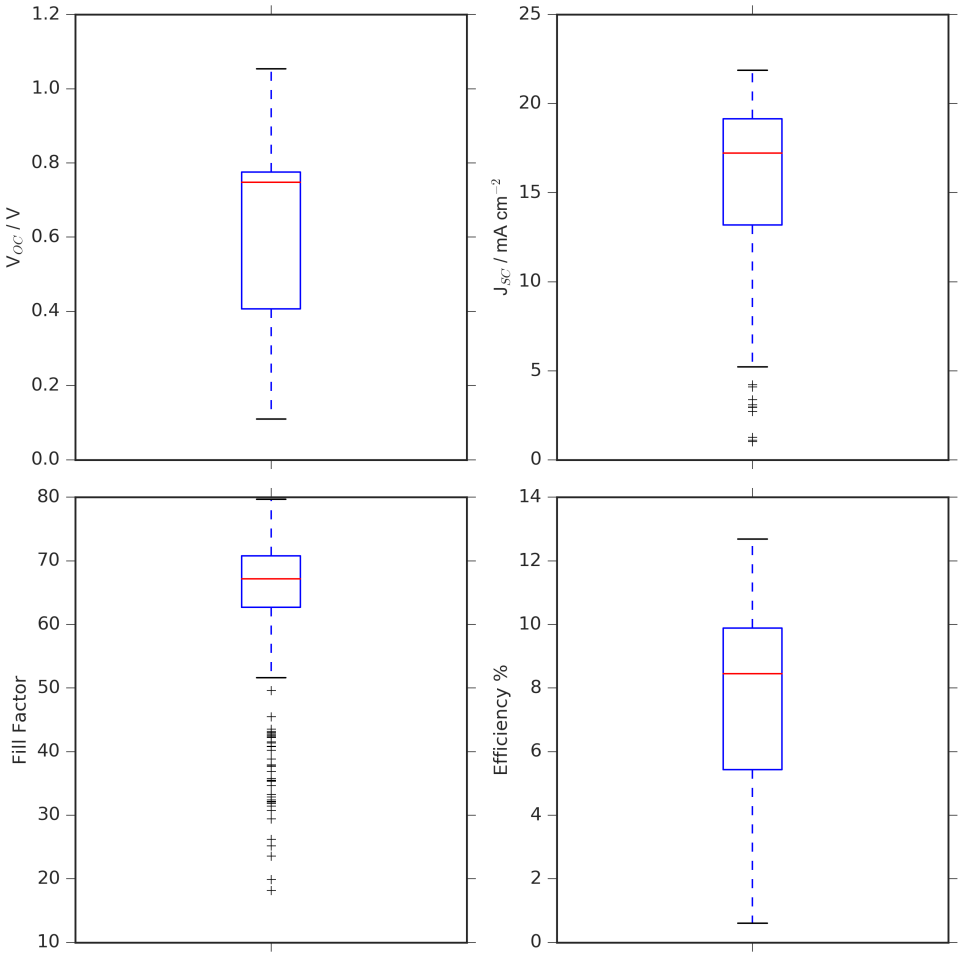

Figure 3-6: Statistics of $MAPbI_3$ solar cell performance. Open circuit voltage, short circuit current, fill factor and device efficiency.

The microscopic origin of hysteresis in perovskite cells has been much discussed in the literature. Mobile ions redistributing in response to applied potential and imbalanced charge extraction between holes and electrons are both implicated in the observed hysteretic IV curves.

Figure 3-6 displays the performance statistics of the $MAPbI_3$ cells made by sequential deposition of the perovskite layer. As can be seen, there is a wide spread in the variability between the best and worst performing cell pixels in open circuit voltage, short circuit current and fill factor. This indicates large variation in the uniformity of material deposition across the cell surface, leading to multiple problems, not least parasitic series and shunt resistances. Given the hysteresis observed in the IV curve (Figure 3-5), efficiencies of the cells were determined by maximum power point tracking, with an average efficiency of 8.4%.

3.4 Methylammonium Lead Halides

This section details further results obtained on $MAPbX_3$, where X = I, Br and Cl. Single crystals of each of the halides were used for a wide series of Raman spectroscopy and ellipsometry experiments by a collaborative team to establish the optical constants, vibrational spectra and phonon lifetimes of these materials. These crystals underpinned experimental results for the following publications:

Reversible Hydration of $CH_3NH_3PbI_3$ in Films, Single Crystals, and Solar Cells. A. M. A. Leguy, Y. Hu, M. Campoy-Quiles, I. M Alonso, O. J. Weber, P. Azarhoosh, M. van Schilfgaarde, M. T. Weller, T. Bein, J. Nelson, P. Docampo, P. R. F. Barnes, *Chem. Mater.*, 2015, **27**, 3397-3407

Lattice dynamics and vibrational spectra of the orthorhombic, tetragonal, and cubic phases of methylammonium lead iodide. F. Brivio, J. M. Frost, J. M. Skelton, A. J. Jackson, O. J. Weber, M. T. Weller, A. R. Goni, A. M. A. Leguy, P. R. F. Barnes, A. Walsh, *Phys. Rev. B*, 2015, **92**, 144308

Experimental and theoretical optical properties of methylammonium lead halide perovskites A. M A. Leguy, P. Azarhoosh, I. M. Alonso, M. Campoy-Quiles, O. J. Weber, J. Yao, D. Bryant, M. T. Weller, J. Nelson, A. Walsh, M. van Schilfgaarde, P. R. F. Barnes, *Nanoscale*, 2016, **8**, 6317-6327

Dynamic disorder, phonon lifetimes, and the assignment of modes to the vibrational spectra of methylammonium lead halide perovskites A. M A. Leguy, A. R. Goni, J. M. Frost, J.

Skelton, F. Brivio, X. Rodrguez-Martnez, O. J. Weber, A. Pallipurath, I. M. Alonso, M. Campoy-Quiles, M. T. Weller, J. Nelson, A. Walsh, P. R. F. Barnes, *Phys. Chem. Chem. Phys.*, 2016, **18**, 27051-27066

3.4.1 Synthesis

The crystals grown for analysis by Raman and ellipsometry are shown in Figure 3-7a. The colour of black / grey iodide, red for bromide and clear / colourless for chloride clearly indicates the effect of halide variation on the band gap of methylammonium lead halide perovskites, with the iodide, bromide and solid solutions between these of interest for photovoltaic applications, due to their strong absorbance of visible light. Figure 3-8 displays the room temperature powder diffraction patterns for each of these crystalline samples, which were crushed to a fine powder using an agate pestle and mortar. The cubic phase of MAPBr/Cl and the tetragonal phase of MAPI are observed.

The Raman and ellipsometry experiments required large single crystals with flat facets of at least 2 mm. Therefore a route involving synthesis in hydrothermal autoclaves was devised in order to carefully control the temperature ramp rate and avoid evaporation of the aqueous acid over the week-long synthesis. While the iodide and bromide syntheses worked straight away, it was necessary to experiment with different reactant ratios and concentrations to obtain phase pure samples of $MAPbCl_3$. A large excess of MACl had a solubilising effect on $PbCl_2$ in HCl and enabled crystals with large enough facets to be grown (Figure 3-7a).

$\mathbf{MAPbI_3}$

Methylammonium lead iodide single crystals were prepared according to the method of Poglitsch and Weber.[209] 2.5 g of lead acetate trihydrate $Pb(CH_3CO_2)_2.3H_2O$, Sigma 99.99%) was dissolved in 10 mL hydroiodic acid ($HI_{(aq)}$, 57 wt%, Sigma) in a 50 mL round bottom flask and heated to 100^oC in an oil bath. Separately, 0.597 g of CH_3NH_2 (aq, 40 %, Sigma) was added dropwise to a further 2 mL of HI(aq) kept at 0^oC in an ice bath under stirring. The methylammonium iodide solution was then added to the lead acetate solution and the mixture was cooled over five days to a temperature of 46^oC, resulting in the formation of black crystals with largest face length around 8 mm. The content of the flasks was subsequently filtered and dried for 12 hours at 100^oC.

$\mathbf{MAPbBr_3}$

Methylammonium lead bromide single crystals were prepared using 10 mL HBr (aq, 48 wt%, Sigma) added to 1.458 g of $Pb(CH_3CO_2)_2.3H_2O$ in a 23 mL Teflon-lined stainless

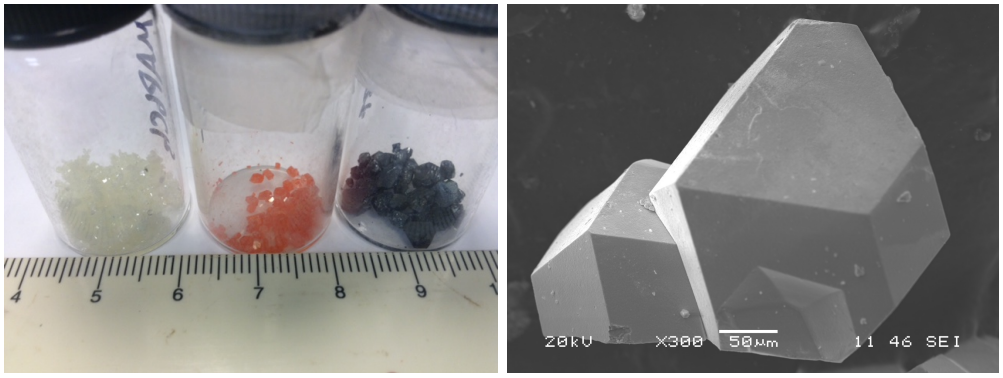

(a) $MAPbX_3$. From Left: X = Cl, Br, I (b) SEM image of $MAPbI_3$ single crystals

Figure 3-7: $MAPbX_3$ single crystals

steel autoclave. Separately, 1 mL HBr was added dropwise to 0.333 mL of methylamine (aq, 40%, Sigma) at 0^{o}C under stirring. The methylamine hydrobromide solution was then added to the autoclave, which was sealed and heated in a fan oven at 140^{o}C for 24 hours. The temperature was decreased from 140^{o}C to room temperature over five days. The red $<$ 2 mm crystals were filtered and dried for 12 hours at 100^{o}C.

$MAPbCl_3$

Methylammonium lead chloride single crystals were synthesised by adding 1.458 g of $Pb(CH_3CO_2)_2.3H_2O$ and 3.892 g methylamine hydrochloride (Sigma)were to a 23 mL Teflon-lined stainless steel autoclave along with 10 mL H2O, affording a 1:15 molar ratio $Pb(CH_3CO_2)_{2.3}H_2O$: MA.HCl. The reactants were heated in a fan oven at 140^{o}C for 24 hours. The temperature was decreased from 140^{o}C to room temperature over five days. The clear $<$ 3 mm crystals were filtered and dried for 12 hours at 100^{o}C.

The as-synthesised crystals are shown in Figure 3-7a Figure 3-7b depicts single crystals of $MAPbI_3$. The phase purity of the samples was checked by powder XRD using a Bruker D5000 diffractometer using Cu $K_{\alpha 1}$ as the X-Ray source. Only the peaks related to the perovskite phases, cubic for X = Br, Cl, tetragonal for X = I, are observed by PXRD (Figure 3-8).

3.4.2 Raman Spectroscopy and Ellipsometry

The following section outlines the characterisation of the Raman spectra and optical constants of methylammonium lead halides. I contributed the synthesis and structural characterisation to provide single crystal materials, while the Raman spectroscopy, spectroscopic

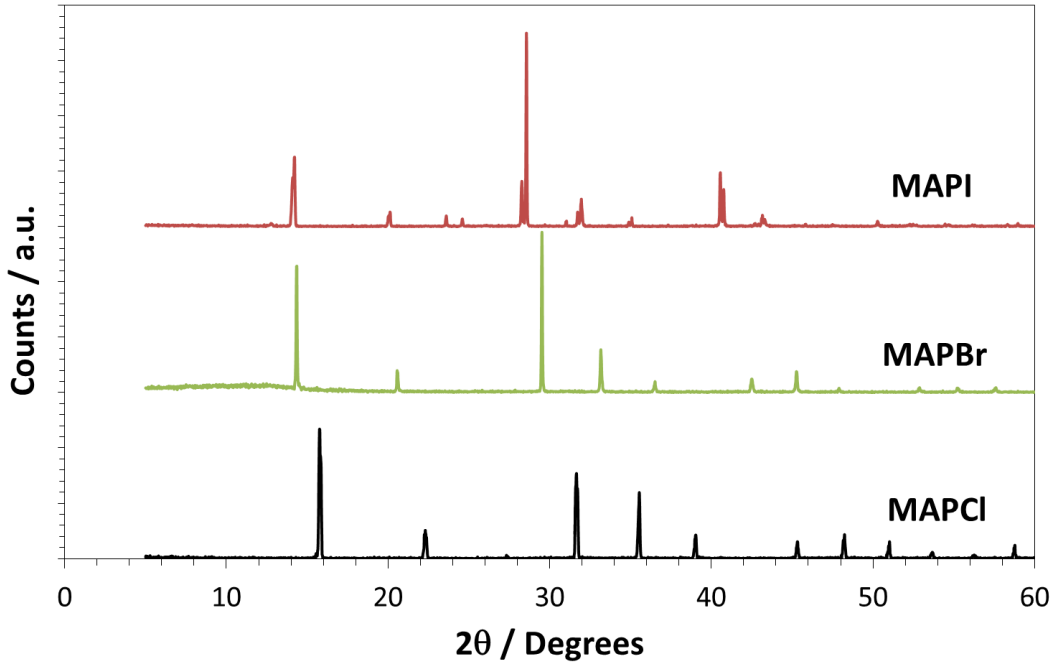

Figure 3-8: MAPI, Br, Cl powder X-ray diffraction patterns

ellipsometry and *ab initio* calculations were carried out by collaborators, as listed in the declaration at the start of this thesis, and the results published in the articles listed on page 88. The calculated Raman active modes across a wide temperature range were compared to experimental measurement for $MAPbX_3$, X = I/Br/Cl. Ellipsometry measurements determined absorption coefficients and optical constants for these materials.

The variation of absorption coefficient with incident photon energy is depicted in Figure 3-9, which also compares the measured values between different techniques. Single crystal ellipsometry, diffuse reflectance spectroscopy of crushed crystalline powders and electroluminescence of thin film MAPI devices. Close agreement is observed in the band gap of $E_g = 1.55(9)$ eV for $MAPbI_3$, 2.42(2) eV for $MAPbBr_3$ and 2.97(3) eV for $MAPbCl_3$. Electroluminescence provides a rather different experimental probe to the other two methods. In ellipsometry change in polarisation of the incident radiation is measured, and reflectance spectroscopy, the material is non-contacted, optically excited by a wavelength dependant light source , while for electroluminescence charge is injected into the material via electrical contacts and the emission from the radiative recombination of charges measured.

The Raman spectra and predicted Raman active modes are plotted in Figure 3-10. The instantaneous orientation of the MA molecular ion breaks the average crystal symmetry and

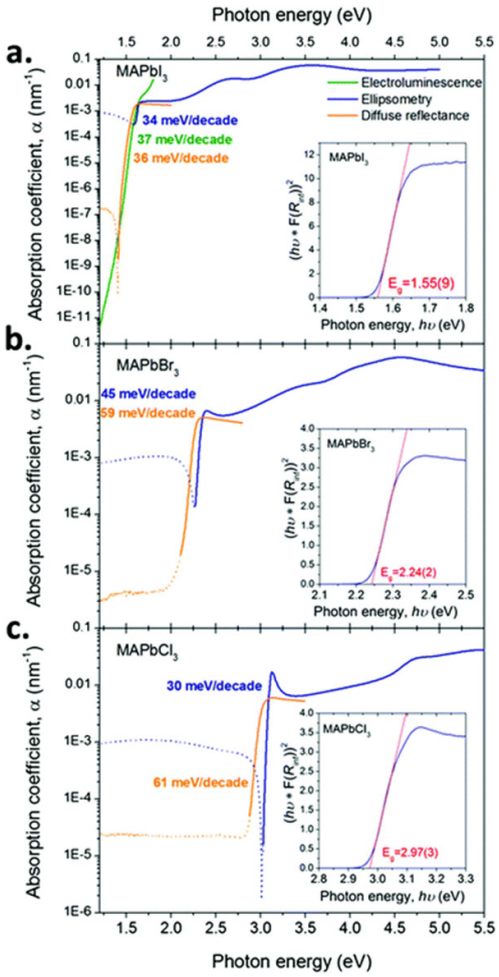

Figure 3-9: Figure 2 from Leguy et al.,[218] reproduced with permission from the RSC. Absorption coefficients for MAPI (top), MAPBr (middle) and MAPCl (lower) determined by spectroscopic ellipsometry (blue lines), diffuse reflectance (orange lines) and electroluminescence (for $MAPbI_3$). Tauc plots from diffuse reflectance data (inset).

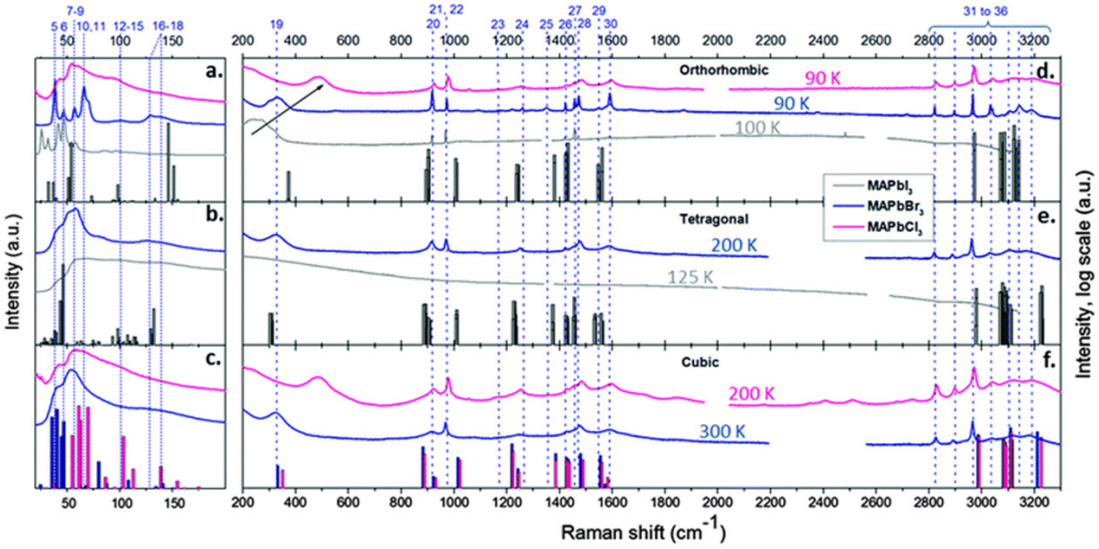

Figure 3-10: Raman spectra of $MAPbX_3$, compared to predicted Raman active modes from *ab initio* calculation. Reproduced from Leguy et al.[219] by permission from the RSC.

results in more structure and splitting of peaks than would otherwise be expected, as well as simultaneous Raman and IR activity, even in the cubic phase.[168] The Raman spectrum for MAPI is split into two distinct regions, below 200 cm^{-1} Pb/I cage modes are observed, coupled to motion of the MA cation. Molecular vibrations of MA are observed > 200 cm^{-1} wavenumbers. These features are broadened above the orthorhombic / tetragonal phase transition at 160 K as the torsional rotation about the C–N axis is unlocked. There is however no Raman peak in particular to describe C–N realignment, as its correlation to cage vibrations results in homogeneous broadening of existing Raman peaks, in all three compounds, rather than new mode frequencies. The broadening for $MAPbBr_3$ is less pronounced than $MAPbI_3$, while $MAPbCl_3$ retains the same Raman features between 90 K and 300 K. These features are indicative of dynamic disorder evenly distributed through the lattice, which broadens the distribution of scattering energies.

Comparison to predicted Raman spectra from ab initio calculations enabled assignments of these modes. for MAPI, use of a 785 nm laser with a maximum power density of 310 W cm-2 was shown to be important to avoid degradation of the sample to PbI_2, since this wavelength at the band edge results in only weak absorption.[220] Use of an IR laser, along with dynamic peak broadening, meant that molecular peaks at high wavenumbers were not well-resolved.

Chapter 4

Structure of α-Formamidinium Lead Iodide at Room Temperature

The results in this chapter are primarily drawn from the following publication, which is reproduced in full by permission of the American Chemical Society, alongside accumulated laboratory data:

The Cubic Perovskite Structure of Black Formamidinium Lead Iodide, α-[$HC(NH_2)_2$]PbI_3, at 298 K, M. T. Weller, O. J. Weber, J. M. Frost, A. Walsh, *J. Phys. Chem. Lett.*, 2015, **6**, 3209-3212

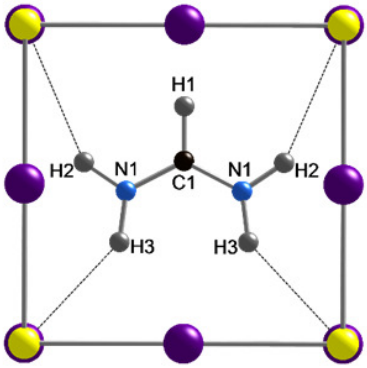

4.1 Commentary

This chapter focuses on the synthesis and structural characterisation of formamidinium lead iodide ($FAPbI_3$ / FAPI). The major contribution is the first correct assignment of crystal class to the metastable high temperature polymorph α-$FAPbI_3$, from high resolution neutron powder diffraction data. This phase is shown to be cubic, analogous to the high temperature phase of $MAPbI_3$ discussed in Chapter 3. These results are further utilised in computational molecular dynamics simulations to analyse the time-dependent behaviour of the disordered molecular cation.

While initial research in hybrid halide perovskite photovoltaics focused on methylammonium lead iodide as the absorber material,[55,221] it was quickly recognised that 'A' site substitution of methylammonium for other organic cations was one of the key parameters for structural manipulation to obtain different perovskites. The number of available, chemically stable organic cations small enough to fit the cubeoctahedral cavity of the $[PbX_6]^{4-}$ lattice is actually extremely limited. The formamidinium cation $HC(NH_2)_2^+$ (FA) has been shown to successfully template the perovskite structure and α-formamidinium lead iodide has been employed as an absorber material in some of the highest efficiency perovskite solar cells reported to date (20.1%).[66,93,222–226]

Formamidinium containing hybrid perovskites were first synthesised by Mitzi and co-workers in the 1990s, who described the cubic perovskite $FASnI_3$ (a=6.316(1) Å) and mixed cation $(MA/FA)SnI_3$ solid solutions, which are not oxidatively stable as Sn(II) is rapidly converted to Sn(IV) in air.[227] The synthesis and phase behaviour of $FAPbI_3$ was first reported by Stoumpos et al. in their seminal hybrid perovskite materials paper,[152] with the high temperature (above room temperature) perovskite phase described as adopting a trigonal unit cell, unlike $MAPbI_3$, by single crystal X-Ray diffraction, space group $P\bar{3}m1$, with a = 8.9817(31) Å and c = 11.006(2) Å.

On exchanging MA for the larger FA cation, the optical band gap of the material decreases from 1.54 eV to 1.47 eV, extending absorption towards the infra-red.[226] 'A' site substitution has a much smaller effect on the band gap than for 'B' or 'X', since the 'A' site cation does not contribute directly to the frontier band density of states for the conduction or valence band, but rather influences the band gap via a steric contribution, with an observed dependence of the optical band gap on the bond angles in the inorganic lattice for differently sized cations.[228,229]

$FAPbI_3$ differs from $MAPbI_3$ and $FASnI_3$ in one particularly important respect: the cubic perovskite phase is not the thermodynamically stable phase at room temperature. Rather,

a 2H-perovskite hexagonal polytype is observed.[152] This yellow δ-phase consists of face-sharing 1D chains of lead iodide octahedra that is not useful for solar cell applications. The structure of δ-$FAPbI_3$ has recently been refined from neutron powder diffraction data in the space group *P6$_3$/mmc*, with a = 8.6226(5), c = 7.9458(5) at 220 K.[230] The black α-phase crystallises preferentially above 60 ^{o}C and the two phases will quickly and reversibly interconvert in the solution in which the crystals were grown, or in a sealed ampoule under vacuum. Conversely, if a batch of the yellow crystals are separated from the growth solution and heated in air or under nitrogen, the resulting black crystals will interconvert only slowly back to the yellow 2H-polytype, as shown in Figure S3 in the research paper following this commentary.

The metastability of α-$FAPbI_3$ results, in the absence of a strategy for stabilisation of the alpha phase, in polymorphism-limited lifetimes of α-$FAPbI_3$ functional devices.[231] Therefore $FAPbI_3$ is typically combined with other cation and anions, resulting in solid solutions such as $(FA/Cs)PbI_3$ and $(FA/MA)Pb(I/Br)_3$, for functional device materials. Both MA (effective ionic radius r_{eff} = 217 pm) and Cs (r_{eff} = 188 pm) are significantly smaller than FA (r_{eff} = 253 pm) and have been demonstrated to stabilise the desired α-phase.[65,151,232,233]

We undertook neutron powder diffraction experiments at the high resolution powder diffractometer (HPRD), ISIS, to study the high temperature phase of α-$FAPbI_3$ and investigate the reported differences between the structures of $FAPbI_3$ and $MAPbI_3$. Immediately apparent from the HRPD data was that the black perovskite phase of $FAPbI_3$ could be described with a higher symmetry unit cell than that proposed in previous XRD studies.[152] In fact, a model analogous to the high temperature cubic phase of $MAPbI_3$, space group *Pm$\bar{3}$m*, with a dynamically disordered FA ion at the centre of the cell provided an excellent description of the observed neutron diffraction pattern. A unit cell parameter of a = 6.3620(8) Å was obtained by Rietveld refinement.[234] The large atomic displacements of the formamidinium cation were further shown to be consistent with rapid molecular reorientation, in agreement with *ab initio* molecular dynamics simulations.

As with MAPI, neutron powder diffraction provides a powerful probe for structure determination of formamidinium-containing heavy metal frameworks, given the ability to distinguish carbon from nitrogen, identify hydrogen positions and to avoid problems inherent in single crystal diffraction, such as the formation of multiple twin domains in crystals, especially across temperature induced phase transitions. The high resolution neutron data, being far more sensitive than X-ray to light atom (C, N and H) positions, provides unambiguous evidence of this (time and space-averaged) symmetry, since any deviation from cubic to hexagonal symmetry would place intensity in additional reflection peaks, which are not observed. The dominance of heavy atom scattering in the X-Ray data means that, despite

the abundance of additional reflection positions in the trigonal unit cell, the overall quality of fit, as measured by least squares regression, is very similar between cubic and trigonal cells.

A primitive cubic unit cell with Pb at the origin (site *1a*) and iodine at (x=0.5,y=0,z=0) and equivalent positions (site *3d*) sufficiently describes the inorganic lattice. The orientation of the planar FA cation was taken from the energy minimisation results of density functional theory calculations (DFT, PBEsol functional) within a regular 6.36 Å cubic lattice. The trial structure calculations were provided by Dr. Federico Brivio. These found the orientation of the N-CH-N molecular fragment to lie on the (2,0,0) *hkl* plane, with C-H pointing towards the cube face and -NH_2 groups oriented towards the unit cell edges. This produces a simple model of the organic molecule in which all atoms sit on a single mirror plane. The carbon and the hydrogen bonded to it are located at (0.5,y,0.5), site *6f*, with site occupancy 0.1667 to generate six orientations of the FA molecule with one formula unit per unit cell. The single nitrogen position and its bonded hydrogens, site *24l*, occupancy 0.0833, are sufficient to describe the complete molecule, disordered across 12 equivalent orientations.

The lattice parameter 6.3620(8) Å, and cell volume 257.51(5) $Å^3$ of α-$FAPbI_3$ at 300 K are significantly larger than those for $MAPbI_3$ at an equivalent temperature (Chapter 3). The Pb–I bond length is also larger for α-$FAPbI_3$ at 3.181(4) Å. The larger formamidinium cation is on the borderline for the size of cation for which a cubic perovskite structure with 3D lead iodide lattice will be tolerated (Chapter 1). The polymorphism displayed by α-$FAPbI_3$ is therefore reflective of a) the expansive stress of the lead iodide framework, with a larger than optimal 'A' site cation and b) the directional nature of NH–I hydrogen bonding interactions between the planar organic ion and the inorganic lattice.

Nanoscale stacking faults and twinning of cubic crystalline phases can present themselves as hexagonal to single-crystal diffraction methods. For example, the 'lonsdaleite' hexagonal phase of diamond was found recently to consist solely of cubic diamond with extensive $\{011\}$ and $\{113\}$ twins and $\{111\}$ stacking faults, with this structural complexity contributing weak, diffuse Bragg scattering features interpreted as the hexagonal phase.[235] In these experiments, α-$FAPbI_3$ is obtained from the phase transition of hexagonal crystallites of δ-$FAPbI_3$; extensive formation of micro-domains of twinned or faulted cubic material seems a credible outcome of this synthesis route.

The disorder and large thermal displacements of the formamidinium molecule within the $FAPbI_3$ structure reinforces a picture of dynamic reorientation of the molecular ion, the averaged results of which are captured on the timescale of diffraction experiments. Molecular dynamics simulations of FA ion reorientation within the inorganic cage at 300 K were

carried out by Dr. Jarvist Frost. The 200 ps MD run with a time-step of 0.5 fs reproduced the molecular rotation, with a time constant of around 2 ps for the rollover of the molecule. This is in close agreement with the reported values from solid state NMR,[117] which indicate, perhaps counterintuitively, that the rotation of the FA is faster than MA at equivalent temperatures. A clear preferential alignment of the C-H bond of the FA cation along $< 100 >$ is observed in the molecular dynamics simulations, in agreement with structure refinement of the HRPD data.

The highly rotationally mobile FA cation and anisotropic displacements for iodide indicate that, similarly to $MAPbI_3$, the cubic unit cell is a time-and-space averaged description of the crystal symmetry. This is analogous to other situations in perovskite materials where the refined high temperature cubic structure is not at a potential energy minimum, but rather represents the saddle point of a double potential well to two locally distorted structures, which average to cubic symmetry when a large volume of unit cells are sampled (as for Bragg diffraction).[118,119,236] The high temperature phases of FAPI and MAPI are structurally very similar, with the isotropically disordered organic molecular ion approximating a spherical ion. The differences in phase behaviour, most notably the polymorphism of $FAPbI_3$, arise from the size of the organic cation and the structure directing effects of directional hydrogen bonding, which are difficult to capture by *ab initio* methods.

4.2 The Cubic Perovskite Structure of Black Formamidinium Lead Iodide, α-$[HC(NH_2)_2]PbI_3$, at 298 K

The following paper is reproduced in full from the original publication and spans thesis pages 99-112.

Statement of Authorship

This declaration concerns the article entitled:									
The Cubic Perovskite Structure of Black Formamidinium Lead Iodide, α-[HC(NH 2) 2]PbI 3 , at 298 K									
Publication status (tick one)									
draft manuscript		**Submitted**		**In review**		**Accepted**		**Published**	✓
Publication details (reference)	M. T. Weller, O. J. Weber, J. M. Frost and A. Walsh, *J. Phys. Chem. Lett.*, 2015, **6**, 3209–3212.								
Candidate's contribution to the paper (detailed, and also given as a percentage).	The candidate contributed to/ considerably contributed to/predominantly executed the… Formulation of ideas: 50% OJW suggested initiating the project, 50% MTW suggested use of neutrons as a structural probe. Design of methodology: MTW planned the HRPD experiments and applied for beamtime. Experimental work: OJW synthesised the samples. OJW, MTW, Kayleigh Marshall, Adam Dennington and Ben Hogan undertook data collection on HRPD. JF and AW carried out ab initio molecular dynamics simulations using the atomic structure developed from HRPD data. Presentation of data in journal format: MTW and OJW wrote the paper in journal format.								
Statement from Candidate	This paper reports on original research I conducted during the period of my Higher Degree by Research candidature.								
Signed						**Date**			

THE JOURNAL OF PHYSICAL CHEMISTRY Letters

Letter

pubs.acs.org/JPCL

Cubic Perovskite Structure of Black Formamidinium Lead Iodide, α-$[HC(NH_2)_2]PbI_3$, at 298 K

Mark T. Weller,* Oliver J. Weber, Jarvist M. Frost, and Aron Walsh

Centre for Sustainable Chemical Technologies and Department of Chemistry, University of Bath, Bath, BA2 7AY, United Kingdom

Supporting Information

ABSTRACT: The structure of black formamidinium lead halide, α-$[HC(NH_2)_2]PbI_3$, at 298 K has been refined from high resolution neutron powder diffraction data and found to adopt a cubic perovskite unit cell, a = 6.3620(8) Å. The trigonal planar $[HC(NH_2)_2]^+$ cations lie in the central mirror plane of the unit cell with the formamidinium cations disordered over 12 possible sites arranged so that the C−H bond is directed into a cube face, whereas the $-NH_2$ groups hydrogen bond (NH···I = 2.75−3.00 Å) with the iodide atoms of the $[PbI_3]^-$ framework. High atomic displacement parameters for the formamidinium cation are consistent with rapid molecular rotations at room temperature as evidenced in *ab initio* molecular dynamic simulations.

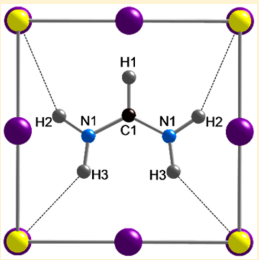

Hybrid halide perovskite solar cells have captured significant research attention due to the demonstration of their use in highly efficient photovoltaic devices produced via low-cost deposition methods.[1−7] The complete structure and dynamics of the systems, covering the inorganic framework, the molecular cation and their mutual interactions, all impact upon the photovoltaic performance of these materials; understanding these fundamental structural and motional behaviors are central to developing this class of materials toward devices.[8,9] The bulk of research has focused on methylammonium lead iodide (MAPI); however, the formamidinium cation $HC(NH_2)_2^+$ (FA) also templates a lead iodide perovskite-type structure for $HC(NH_2)_2PbI_3$ (FAPI) with fully vertex connected PbI_6 octahedra. Solar cells based on FAPI with a maximum power conversion efficiency of 20.1% have been recently demonstrated.[10] The increase of effective cation radius on switching from the methylammonium to the formamidinium cation decreases the optical band gap from 1.54 to 1.47 eV, extending absorption into the near-infrared.[11]

The synthesis, structure, and phase behavior of $FAPbI_3$ has been reported by Stoumpos et al.[12] FAPI crystallizes at room temperature as a nonperovskite, hexagonal yellow phase (δ-phase), in the space group $P6_3mc$, and formed from face-sharing PbI_6 octahedra linked into chains. The structure of the black perovskite phase of FAPI (α-phase), which is formed at higher temperatures, was refined in this work from single crystal X-ray diffraction data using trigonal space groups and 3-fold disordered FA cation. $FASnI_3$ has been reported as adopting a cubic perovskite structure.[13]

The low stability of hybrid perovskite materials toward heat and moisture has been discussed widely and results from the facile phase transitions at or near room temperature and formation of hydrated phases. These stability issues have hindered attempts to scale technology using these materials and serious question marks remain over stability even for sealed devices.[14] The formamidinium cation is believed to exhibit even lower stability than methylammonium.[12] $MAPbI_3$ and $MA_xFA_{1-x}PbI_3$ have recently been shown to be efficient halide ion conductors[15] and undergo structural changes under polarization[16] or illumination.[17] Solid solutions, for example, $FAPI/MAPbBr_3$ have been employed in high efficiency perovskite cells, reportedly displaying greater stability than the parent compounds.[15,18,19] Binek et al.[20] have studied the stabilization of thin films of α-FAPI by inclusion of up to 15% MA^+.

We have previously demonstrated the power of neutron powder diffraction in determining the atomic structure in hybrid perovskite compounds as it circumvents many of the factors limiting the usefulness of single crystal X-ray diffraction for analysis of these hybrid systems. As well the identification of light atom positions, including hydrogen, and distinguishing carbon from nitrogen, it also avoids difficulties in structure refinement stemming from multiple twinning or domain structure of crystals.[9]

Neutron powder diffraction data were obtained on the HRPD instrument at ISIS as summarized in the Supporting Information. Initial inspection of the data showed far fewer reflections than predicted by the hexagonal unit cell model for FAPI proposed by Stoumpos (see Supporting Information Figures S1 and S2) indicating that the true unit cell was probably simpler than used in that work. Peak positions were extracted for 20 reflections and indexed manually from their d-spacings to give a cubic unit cell of dimension ~6.36 Å. This cell indexed all the reflections observed except for a few minor features associated with diffraction from the vanadium slab can

Received: July 7, 2015
Accepted: August 4, 2015
Published: August 4, 2015

DOI: 10.1021/acs.jpclett.5b01432
J. Phys. Chem. Lett. 2015, 6, 3209−3212

(at, for example, 2.14 Å) and off-center aluminum cryoloop tail (these were readily identified from their *d*-spacings and varying intensities and positions in the different HRPD data banks). This cubic unit cell is similar to that found for the cubic phase adopted by MAPI above 327 K though it is slightly larger, which is indicative of the larger size of the formamidinium cation compared to methylammonium. In order to check the validity of this new choice of unit cell, powder X-ray diffraction (PXD) data were also collected from a FAPI phase, Supporting Information Figure S3, and could also be fully indexed of a simple cubic unit cell of dimensions 6.36 Å. Note that the sensitivity of neutron diffraction data to light elements, such as C, N, and H, shows that these atom positions can also be defined using the simple cubic description—and any deviations from cubic to hexagonal symmetry would direct diffraction intensity into additional reflections. Le Bail fits to the PXD data were undertaken using both the new cubic unit cell and the original hexagonal unit cell and showed an excellent fit (χ^2 = 2.18) using the simple cubic cell, Supporting Information, Figure S4.

A structure model for cubic FAPI was developed using that of cubic MAPI with the lead iodide framework described using nontilted PbI_6 octahedra in the space group *Pm*-3*m*. The position of a planar formamidinium cation within this cubic framework was energy minimized within density functional theory (DFT, PBEsol functional) within the regular 6.36 Å cube and found to adopt an orientation with the N−CH−N molecular ion fragment lying in the unit cell midplane, the (200) plane, with the C−H bond pointing directly toward the cube face (thereby minimizing CH···I interactions), and the C−N bonds directed toward adjacent cube faces. This allows the $-NH_2$ groups to be orientated toward the unit cell edges with the potential formation of NH···I hydrogen bonds. Overall, this produces 12 possible orientations for the triangular-planar formamidinium cation in the cubic cage: six orientations of the C−H bond, identified in this work as the *y* direction, and two orientations for the N−C−N plane, in *xy* and *yz*. Reorientation of the organic cation around these 12 orientations would be expected and has been studied by molecular dynamics, vide infra. The crystallographic description of this model in the space group *Pm*-3*m* is very simple with all the atoms on a single mirror plane; the carbon, C, and the directly bonded hydrogen, H1, both located on the 6-fold (1/2, *y*, 1/2), 6f site, with *y* ∼ 0.55 and 0.64 for C and H1, respectively, both with site occupancy 0.1667 representing the six possible formamidinium orientations. A single nitrogen position, (*x*, *y*, 1/2), 24l, with occupancy 0.0833, and two amine hydrogen positions also in the molecular plane on 24l, H2 near (0.81, 0.54, 0.5) and H3 near (0.70, 0.29, 1/2), site occupancies 0.0833. Thus, only 5 atom positions and 8 refinable coordinates are required to define the 12 different orientations of the complete planar $[H_2N{-}CH{-}NH_2]^+$ cation. Pb was placed on 1a (0,0,0) and I on 3d (1/2, 0,0) and the refinable coordinates for the C, N, and H atoms were initially set at values derived from the energy minimization. Isotropic atomic displacement parameters (ADPs) for all atoms were set initially at 0.05 Å^2. This model immediately produced a good overall fit to the data and refinement of profile parameters, unit cell parameter, background functions etcetera, led to a χ^2 value of only ∼4. Refinement of lead and iodine ADPs, anisotropic for iodine, reduced χ^2 to 3.5 and showed thermal motion for the iodine atom to be strongly perpendicular to the Pb−I−Pb direction as found previously in MAPI due to octahedral tilting. ADPs were constrained to a single value for all formamidinium atom sites and this value was refined to yield a value of approximately 0.14 Å^2 with χ^2 = 3.05 indicating significant thermal motion and reorientation of this structural element. Final stages of the refinement included an investigation of the formamidinium cation position which was permitted to translate as a rigid body in the *y* direction; a translation of the whole molecule, with the C−H bond moving toward the cube face by approximately 0.25 Å, yielded the final structural model given in Table 1 and χ^2 = 2.62. Final profile fits to the neutron powder diffraction data are given in Figure 1.

Table 1. Final Refined Atomic Positions

atom	x^d	y	z	$U_{iso}/U_{eq} \times 100$/Å^2
C1	0.5	0.5726(3)[c]	0.5	12.29(23)
N1	0.6820	0.4781(3)[c]	0.5	= C1 U_{iso}
H1	0.5000	0.7447(3)[c]	0.5	= C1 U_{iso}
H2	0.8142	0.5680(3)[c]	0.5	= C1 U_{iso}
H3	0.7025	0.3179(3)[c]	0.5	= C1 U_{iso}
Pb1	0.0	0.0	0.0	2.95(7)
I1	0.5	0.0	0.0	8.20[b]

[a]Space group *Pm*3*m*, *a* = 6.3620(8) Å, *V*= 257.51(5) Å^3. R_{wp}(all) = 1.53%, R_{wp}(all) = 1.20%, R_{wp}(−background) = 4.79%, R_p(−background) = 3.04%, 114 reflections [b]U_{eq} U_{11} = 2.09(20) Å^2 U_{22} = U_{33} = 11.25(17) Å^2 [c]Constrained to have equal shift from DFT modeling values [d]Values from DFT modeling, not refined

The structure of black FAPI, $[H_2N{-}CH{-}NH_2][PbI_3]$ at room temperature consists of a cubic lead iodide, $[PbI_3]^-$ perovskitic framework surrounding orientationally disordered, planar $[H_2N{-}CH{-}NH_2]^+$ cations, Figure 2. The FAPI lattice parameter, 6.3620(8) Å, and cell volume, 257.51(5) Å^3, are significantly larger than those of MAPI (at 298 K), the reduced lattice parameter is 6.304 Å and cell volume 250.5 Å^3, reflecting the larger organic cation size. The Pb−I bond lengths are increased to 3.181(4) Å, implying the lead iodide framework is under some expansive stress with weak Pb−I bonds. This stress may be the origin of the facile phase transition to the yellow phase of FAPI where the Pb−I bonds are significantly shorter. Also of interest are the extracted ADPs for the iodine atom site which show the expected strong anisotropic motion perpendicular to the Pb−I−Pb direction, similar values to those found for iodine in MAPI and representing a soft lead iodide framework.

The refined position of the FA^+ cation within the cubic cage is close to that predicted from the equilibrium athermal structure obtained from DFT-PBEsol calculations. Such calculations tend to underestimate the importance of weak hydrogen bonds such as the NH···I interactions found in FAPI and the cation adopts a site, which allows both terminal amine hydrogen atoms to form weak NH−I hydrogen bonds with the inorganic framework N(H2)···I at 2.992 Å and N(H3)···I at 2.770 Å. This position also maintains the C−H1 to iodide distances at, nonbonded, 3.572 Å. Information on the temporal behavior of the cation positions was obtained from molecular dynamics simulations at 300 K (on the DFT-PBEsol energy landscape; 200 ps production runs using a time-step of 0.5 fs). The molecule is rotationally active around room temperature with a preference for alignment of the C−H bond along ⟨100⟩, in agreement with the structure refinement from powder neutron diffraction, with a time constant of ∼2 ps associated with the rollover process. A video of the rotational dynamics

DOI: 10.1021/acs.jpclett.5b01432
J. Phys. Chem. Lett. 2015, 6, 3209−3212

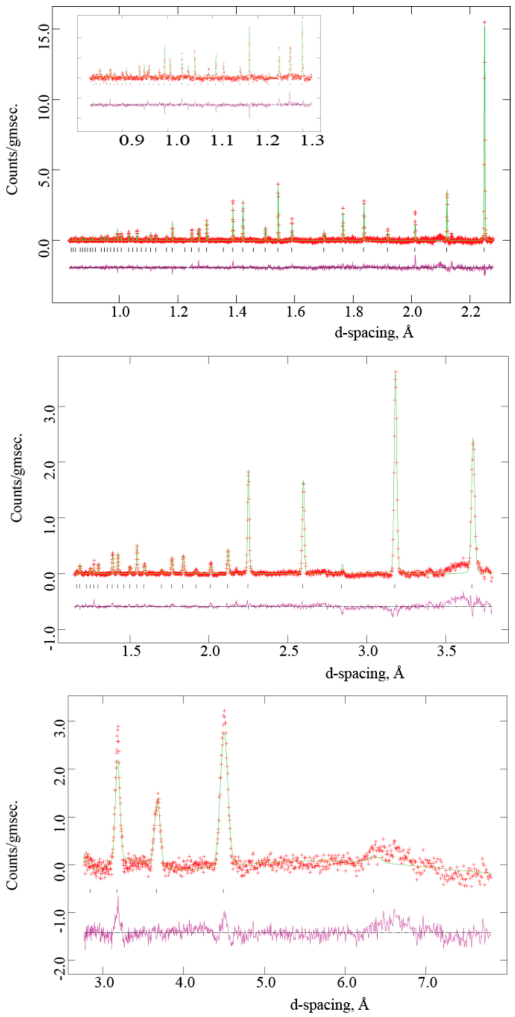

Figure 1. Final profile fits achieved to the neutron powder diffraction data obtained on HRPD from α-FAPI at 298 K. Upper panel, backscattering bank with inset the low d-spacing data magnified; center panel, 90° bank and lower figure the low angle scattering bank. In each profile, crosses represent observed data, upper continuous line the calculated profile, and lower continuous line the difference. Tick marks show calculated reflection positions.

and a statistical analysis of the trajectory are provided in the Supporting Information (Video, Computational section and Figures S6 and S7).

Regarding the low temperature phase behavior, preliminary results indicate that cubic FAPI does undergo a transformation on cooling below room temperature—and by 200 K. Neutron powder data collected at 100 K show a more complex diffraction pattern, which is currently under analysis to determine the unit cell size and any ordering of the FA cation that takes place at low temperatures.

Previous work in the literature describes α-FAPI as being hexagonal,[12] but no evidence of the need to invoke this larger,

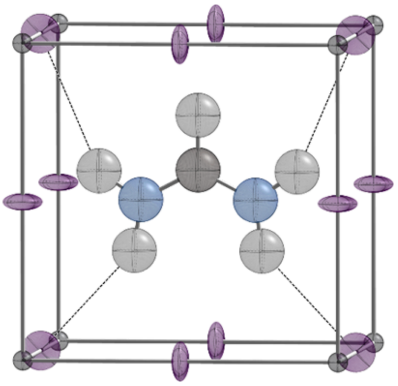

Figure 2. Unit cell structure of α-$[H_2N{-}CH{-}NH_2][PbI_3]$ at 298 K, ADP ellipsoids are shown at 30% probability. Lead (dark gray) at cell corners, iodine (purple) along cell edges, carbon (black), nitrogen (blue), and hydrogen (pale gray). NH···I hydrogen bonds are shown as dotted lines.

more complex unit cell was found in this study, which is much more sensitive to the light atom structural elements. The $[PbI_3]^-$ framework is almost identical in the two studies, with Pb–I bonds near 3.18 Å; PXD patterns generated from the two models are also identical within experimental error. Of note is that faulted and twinned phases at the nanoscale can present themselves as hexagonal to single crystal diffraction methods, such as X-ray and electron diffraction. Recent work on the so-called lonsdaleite phase of diamond found it to consist of solely of cubic phase material that has extensive ⟨113⟩ twins and ⟨111⟩ stacking faults.[21] Given that α-FAPI is normally obtained by a thermally driven phase transition of hexagonal crystals of δ-FAPI it is likely that black FAPI forms as microdomains of twinned or faulted cubic phase material. Indeed our SXD studies of FAPI presented similar unit cells to those reported by Stoumpos but also complex diffraction patterns which could be resolved into multiple cubic twins. It has also been proposed that the conversion of δ-FAPI to α-FAPI might be associated with partial decomposition of the FA cations.[12] Our TGA results from δ-FAPI isolated in this study, Supporting Information Figure S5, show almost no weight loss associated with this process. Indeed, samples of cubic α-FAPI synthesized by the route described in this work (see experimental section) seem relatively stable in comparison with materials described in previous reports. We observe partial, minor conversion back to yellow δ-FAPI after 20 days (see Supporting Information Figure S3).

In conclusion, formamidinium lead iodide adopts a cubic unit cell at room temperature with the FA cations formally disordered over 24 orientations with the perovskitic $[PbI_3]^-$ framework. The molecules are highly rotationally mobile with a turnover frequency of 0.5 THz around room temperature. The structural similarity of the methylammonium and formamidinium lead perovskites has important implications on the understanding, characterization, and stability of their cubic-phase solid-solution, as employed in the current champion efficiency hybrid perovskite solar cells.[10,20]

DOI: 10.1021/acs.jpclett.5b01432
J. Phys. Chem. Lett. 2015, 6, 3209–3212

■ ASSOCIATED CONTENT

Supporting Information

The Supporting Information is available free of charge on the ACS Publications website at DOI: 10.1021/acs.jpclett.5b01432.

Experimental methods (synthesis and data collection), PXD patterns including Le Bail fits, NPD data fitted with hexagonal and cubic unit cells; computational methods (electronic structure and molecular dynamics), and a statistical analysis of the 300 K trajectory. (PDF)

Movie rendering. (MP4)

■ AUTHOR INFORMATION

Corresponding Author

*E-mail: M.T.Weller@bath.ac.uk.

Notes

The authors declare no competing financial interest.

■ ACKNOWLEDGMENTS

O.J.W. would like to thank EPSRC (EP/G03768X/1) for Ph.D. studentship funding via the EPSRC Doctoral Training Centre in Sustainable Chemical Technologies. The experiment at the ISIS Pulsed Neutron and Muon Source was supported by a beamtime allocation from the Science and Technology Facilities Council under Experiment RB1410127. J.M.F. was supported by EPSRC (EP/K016288/1), A.W. was supported by the ERC (Grant No. 277757), and computer time was provided by the U.K.'s HEC Materials Chemistry Consortium, which is funded by EPSRC (EP/L000202).

■ REFERENCES

(1) Snaith, H. J. Perovskites: The Emergence of a New Era for Low-Cost, High-Efficiency Solar Cells. *J. Phys. Chem. Lett.* **2013**, *4*, 3623−3630.

(2) Im, J. H.; Lee, C. R.; Lee, J. W.; Park, S. W.; Park, N. G. 6.5% Efficient Perovskite Quantum-Dot-Sensitized Solar Cell. *Nanoscale* **2011**, *3*, 4088−4093.

(3) Lee, M. M.; Teuscher, J.; Miyasaka, T.; Murakami, T. N.; Snaith, H. J. Efficient Hybrid Solar Cells Based on Meso-Superstructured Organometal Halide Perovskites. *Science* **2012**, *338*, 643−647.

(4) Kim, H. S.; Lee, J. W.; Yantara, N.; Boix, P. P.; Kulkarni, S. A.; Mhaisalkar, S.; Grätzel, M.; Park, N. G. High Efficiency Solid-State Sensitized Solar Cell-Based on Submicrometer Rutile TiO_2 Nanorod and $CH_3NH_3PbI_3$ Perovskite Sensitizer. *Nano Lett.* **2013**, *13*, 2412−2417.

(5) Hu, M.; Liu, L.; Mei, A.; Yang, Y.; Liu, T.; Han, H. Efficient Hole-Conductor-Free, Fully Printable Mesoscopic Perovskite Solar Cells with a Broad Light Harvester $NH_2CH{=}NH_2PbI_3$. *J. Mater. Chem. A* **2014**, *2*, 17115−17121.

(6) Koh, T. M.; Fu, K.; Fang, Y.; Chen, S.; Sum, T. C.; Mathews, N.; Mhaisalkar, S. G.; Boix, P. P.; Baikie, T. Formamidinium-Containing Metal-Halide: An Alternative Material for Near-IR Absorption Perovskite Solar Cells. *J. Phys. Chem. C* **2014**, *118*, 16458−16462.

(7) Lee, J. W.; Seol, D. J.; Cho, A. N.; Park, N. G. High-Efficiency Perovskite Solar Cells Based on the Black Polymorph of $HC(NH_2)_2PbI_3$. *Adv. Mater.* **2014**, *26*, 4991−4998.

(8) Frost, J. M.; Butler, K. T.; Brivio, F.; Hendon, C. H.; van Schilfgaarde, M.; Walsh, A. Atomistic Origins of High-Performance in Hybrid Halide Perovskite Solar Cells. *Nano Lett.* **2014**, *14*, 2584−2590.

(9) Weller, M. T.; Weber, O. J.; Henry, P. F.; Di Pumpo, A. M.; Hansen, T. C. Complete Structure and Cation Orientation in the Perovskite Photovoltaic Methylammonium Lead Iodide between 100 and 352 K. *Chem. Commun.* **2015**, *51*, 4180−4183.

(10) Yang, W. S.; Noh, J. H.; Jeon, N. J.; Kim, Y. C.; Ryu, S.; Seo, J.; Seok, S. I. High-Performance Photovoltaic Perovskite Layers Fabricated through Intramolecular Exchange. *Science* **2015**, *348*, 1234−1237.

(11) Amat, A.; Mosconi, E.; Ronca, E.; Quarti, C.; Umari, P.; Nazeeruddin, M. K.; Grätzel, M.; De Angelis, F. Cation-Induced Band-Gap Tuning in Organohalide Perovskites: Interplay of Spin-Orbit Coupling and Octahedra Tilting. *Nano Lett.* **2014**, *14*, 3608−3616.

(12) Stoumpos, C. C.; Malliakas, C. D.; Kanatzidis, M. G. Semiconducting Tin and Lead Iodide Perovskites with Organic Cations: Phase Transitions, High Mobilities, and near-Infrared Photoluminescent Properties. *Inorg. Chem.* **2013**, *52*, 9019−9038.

(13) Mitzi, D. B.; Liang, K. Synthesis, Resistivity, and Thermal Properties of the Cubic Perovskite $NH_2CH{=}NH_2SnI_3$ and Related Systems. *J. Solid State Chem.* **1997**, *134*, 376−381.

(14) Conings, B.; Drijkoningen, J.; Gauquelin, N.; Babayigit, A.; D'Haen, J.; D'Olieslaeger, L.; Ethirajan, A.; Verbeeck, J.; Manca, J.; Mosconi, E.; et al. Intrinsic Thermal Instability of Methylammonium Lead Trihalide Perovskite. *Adv. Energy Mater.* **2015**, n/a.

(15) Yang, T.; Gregori, G.; Pellet, N.; Grätzel, M.; Maier, J. The Significance of Ion Conduction in a Hybrid Organic−Inorganic Lead-Iodide-Based Perovskite Photosensitizer. *Angew. Chem., Int. Ed.* **2015**, *54*, 7905−7910.

(16) Gottesman, R.; Haltzi, E.; Gouda, L.; Tirosh, S.; Bouhadana, Y.; Zaban, A.; Mosconi, E.; De Angelis, F. Extremely Slow Photoconductivity Response of $CH_3NH_3PbI_3$ Perovskites Suggesting Structural Changes under Working Conditions. *J. Phys. Chem. Lett.* **2014**, *5*, 2662−2669.

(17) Gottesman, R.; Gouda, L.; Kalanoor, B. S.; Haltzi, E.; Tirosh, S.; Rosh-Hodesh, E.; Tischler, Y.; Zaban, A.; Quarti, C.; Mosconi, E.; De Angelis, F. Photoinduced Reversible Structural Transformations in Free-Standing $CH_3NH_3PbI_3$ Perovskite Films. *J. Phys. Chem. Lett.* **2015**, *6*, 2332−2338.

(18) Jeon, N. J.; Noh, J. H.; Yang, W. S.; Kim, Y. C.; Ryu, S.; Seo, J.; Seok, S. Il. Compositional Engineering of Perovskite Materials for High-Performance Solar Cells. *Nature* **2015**, *517*, 476−480.

(19) Eperon, G. E.; Stranks, S. D.; Menelaou, C.; Johnston, M. B.; Herz, L. M.; Snaith, H. J. Formamidinium Lead Trihalide: A Broadly Tunable Perovskite for Efficient Planar Heterojunction Solar Cells. *Energy Environ. Sci.* **2014**, *7*, 982.

(20) Binek, A.; Hanusch, F. C.; Docampo, P.; Bein, T. Stabilization of the Trigonal High Temperature Phase of Formamidinium Lead Iodide. *J. Phys. Chem. Lett.* **2015**, *6*, 1249−1253.

(21) Németh, P.; Garvie, L. A. J.; Aoki, T.; Dubrovinskaia, N.; Dubrovinsky, L.; Buseck, P. R. Lonsdaleite Is Faulted and Twinned Cubic Diamond and Does Not Exist as a Discrete Material. *Nat. Commun.* **2014**, *5*, 5447.

DOI: 10.1021/acs.jpclett.5b01432
J. Phys. Chem. Lett. 2015, 6, 3209−3212

Supporting Information

The Cubic Perovskite Structure of Black Formamidinium Lead Iodide, α-$[HC(NH_2)_2]PbI_3$, at 298 K

Mark T. Weller, Oliver J Weber, Jarvist M. Frost, Aron Walsh

Centre for Sustainable Chemical Technologies and Department of Chemistry, University of Bath, Bath, BA2 7AY, UK

Corresponding Author M.T.Weller@bath.ac.uk

Experimental

Synthesis 6.000 g (0.016 mol) of lead acetate trihydrate (Sigma) was added to a 3 neck round bottom flask equipped with reflux condenser containing 12.4 mL of HI (57 wt %, aq.) and 3.1 mL H_3PO_2 (50 wt%, aq.). 1.647 g of formamidinium acetate (0.016 mol, Sigma) and the solution heated to 100 °C, then immediately left to cool for crystals of black α-$FAPbI_3$ to grow, which converted in solution to yellow crystals δ-$FAPbI_3$ at room temperature. The crystals were filtered, washed with dry diethyl ether and heated to 130 °C in an oven for 2 hours. Final yield: 8.303 g, 83 %.

Powder X-ray diffraction patterns were collected on a Siemens / Bruker D5000 diffractometer using Cu K_α radiation (λ = 0.15418 nm). Figure S1.

Thermogravimetric analysis was carried out using a Polymer Laboratories PL-STA TGA with ISI Thermal Analysis software. Weight loss and heat flow of a 10 mg sample heated in air at 20 °C / min was recorded up to 160 °C.

Neutron powder diffraction data collection and analysis. Approximately 10g of hydrogenous FAPI was loaded into a 5 mm vanadium slab can and neutron powder diffraction data were collected on the HRPD diffractometer at ISS at 298 K over a period of 10 hours. While a large incoherent background is obtained from hydrogen-containing samples in neutron diffraction over longer experimental times this is averaged and may, for crystallographically simple compounds, such as FAPI that give few well resolved diffraction peaks, be subtracted from the raw experimental data.

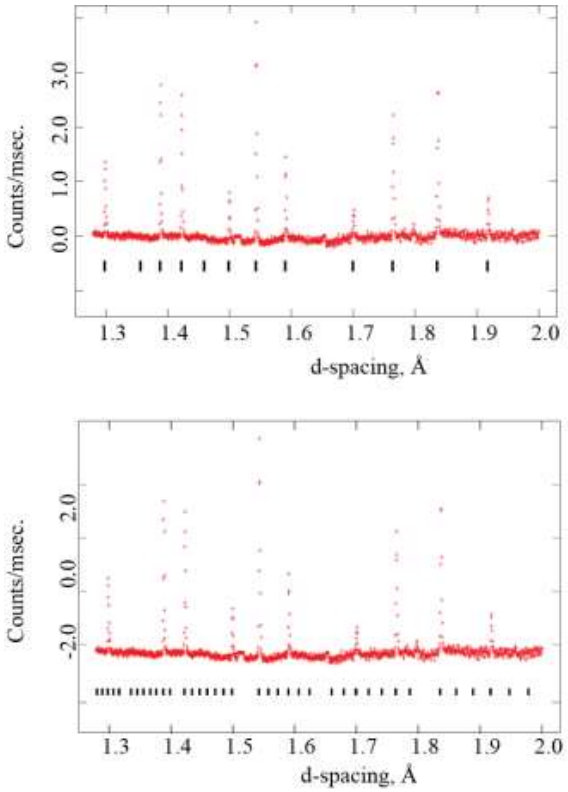

Figure S1 Comparison of reflection positions generated by the cubic unit cell of α-FAPI used in this work (upper) and the hexagonal cell of Stoumpos et al.[1] (lower) in the *d*-spacing region 1.30- 2.0 Å.

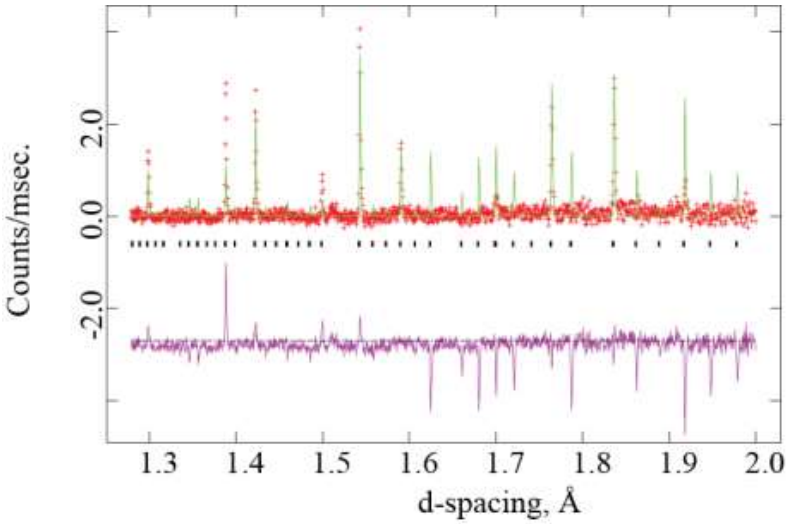

Figure S2. Comparison of observed and calculated NPD profiles of α-FAPI in the d-spacing range 2.3-2.0 Å using the model of Stoumpos.[1] Note the published model had no hydrogen atom position which would strongly affect reflection intensities

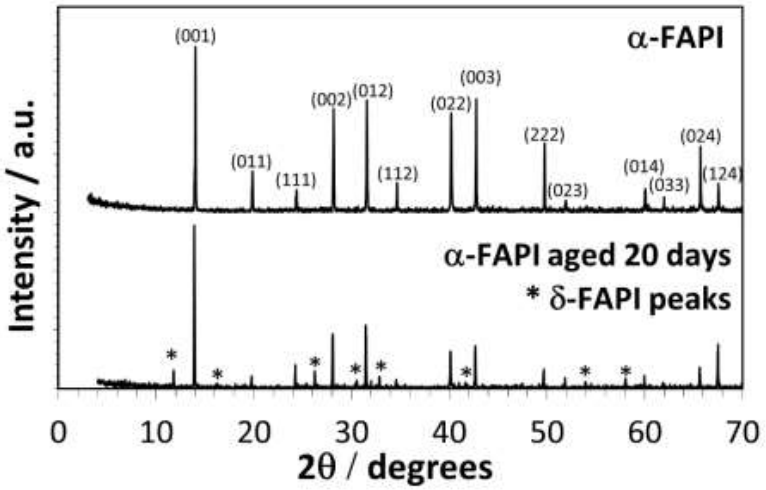

Figure S3. Powder X-ray diffraction data collected on a Siemens / Bruker D5000 diffractometer using Cu K_α radiation (λ = 0.15418 nm, no sample rotation to average peak intensities in a highly crystalline sample). Upper trace – as prepared black α-$FAPbI_3$. Lower trace - the same sample aged for 20 days in a dry ambient atmosphere showing a small level (~20%) conversion to the yellow δ-phase. Of note is that the pattern obtained after 20 days displays changes (in comparison to the freshly prepared material) in the relative intensities of diffraction peaks derived from the α-FAPI still present; this may be interpreted as the result of rate of the phase transition to δ-FAPI occurring at dissimilar rates for different crystallographic growth directions.

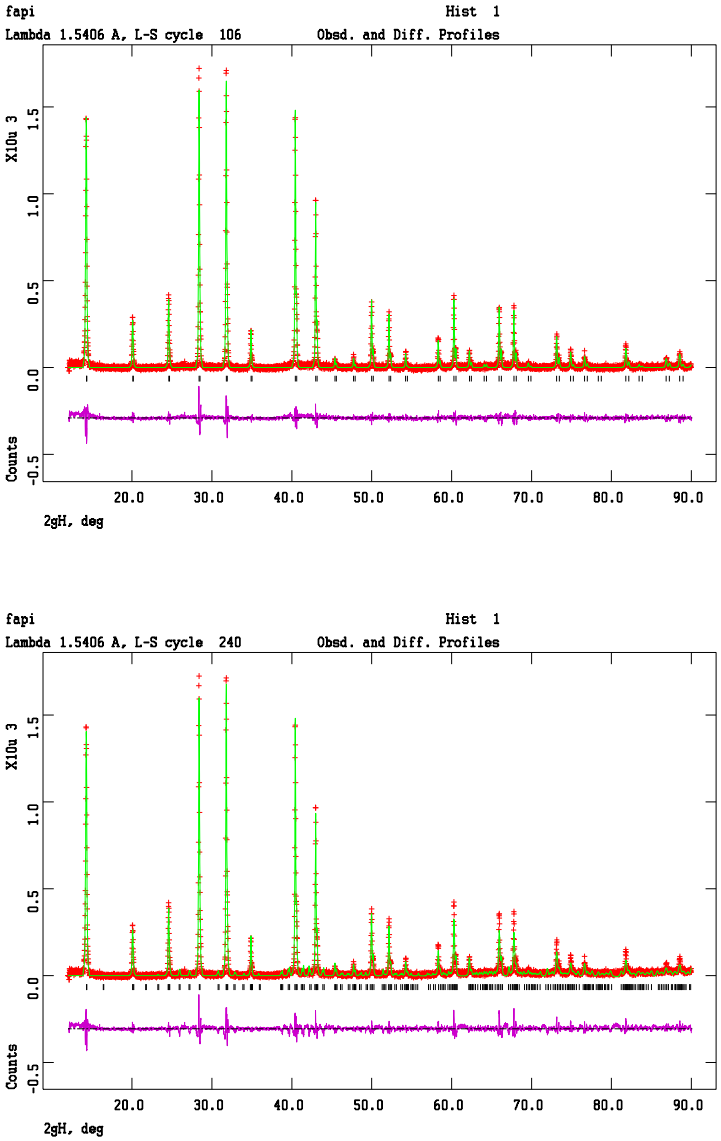

Figure S4. Le Bail fits to PXRD data (Collected on Bruker D8 diffractometer with $CuK_{\alpha1}/K_{\alpha2}$ radiation, phi rotation of sample at 60 rpm) of α-FAPI. Upper pattern - cubic (Pm-3m) model, $\chi^2 = 2.18$. Lower pattern - trigonal (P-3m1) model, $\chi^2 = 3.04$.[1] Note that fits to powder X-ray diffraction data would be expected to be of similar quality as diffraction is dominated by the heavy atom positions. No diffracted intensity was observed at additional reflection positions generated using the hexagonal model.

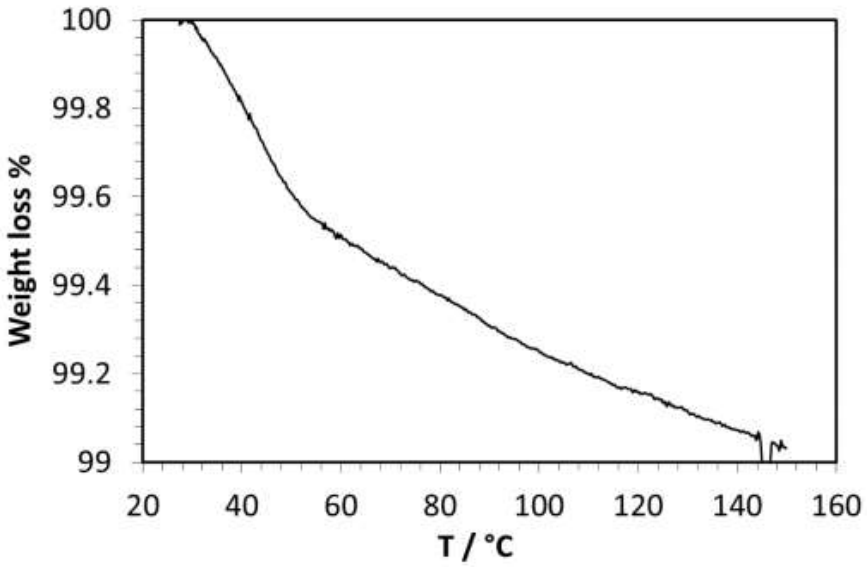

Figure S5. TGA of δ-$FAPbI_3$ in the temperature range 25-160 °C scanned at 5 °C / min. Less than 1% observed weight loss from the sample of α-$FAPbI_3$ over the temperature range scanned probably associated with the loss of surface adsorbed moisture, solvent. The initially yellow material had transformed fully to black α-$FAPbI_3$ by visual inspection at the end of the experiment.

Computational

Setup Calculations were performed on α-FAPI within density functional theory with electron exchange and correlation described using the PBEsol functional form. Periodic boundary conditions with a plane wave basis set (500 eV cut- off with 2×2×2 *k*-points) were employed in the VASP codes. The projector augmented wave method was used to describe the frozen core electrons including scalar relativistic effects. Structure optimisation was performed until all internal atomic forces were within 0.001 eV/Å. We undertook Born-Oppenheimer molecular dynamics at 300 K using a 2×2×2 supercell expansion of the fully optimised pseudo-cubic FAPI structure (see https://github.com/WMD-Bath/Hybrid-perovskites). An integration timestep of 0.5 fs (sufficient to describe C-H and N-H vibrations) was combined with a reduced plane wave cut-off of 300 eV (at the gamma point for the supercell) to enable a sufficiently long production run of 200 ps. Trajectory frames were saved every 50 steps (0.025 ps). The first 10 ps (400 frames) of data were discarded, to provide time for equilibration. The typical 2 ps feature observed for the dynamics of interest suggest that this is sufficient time for decorrelation to occur (within the limit of our small system size), and is sufficient time for the ionic temperature to become well defined and stabilised at the thermostat setting of 300 K.

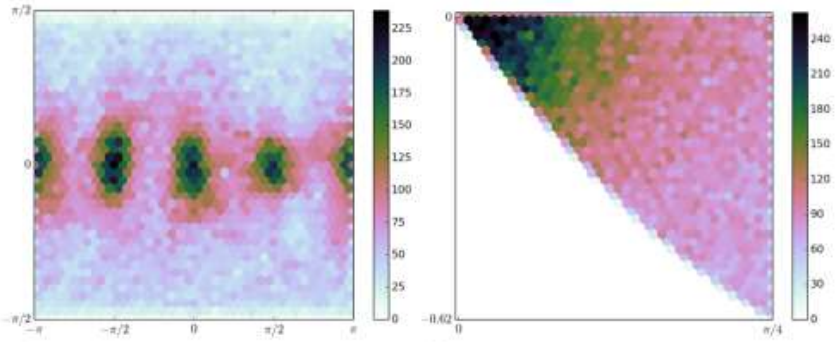

(a) Orientation of the Short-axis of FA, with no symmetry. (b) Applying full O_h symmetry to the orientation of FA.

Figure S6. Density maps (two-dimensional hexagonal histograms in spherical coordinates) of FA alignment within the perovskite cage as determined by molecular dynamics at 300 K. (a) The data are centered on ϕ, θ = 0 being facial <100> orientation. (b) The symmetry folded data bounds the segment between <111> (bottom right), <110> (top right) and <100> (top left) orientations, showing the strong preference for <100> alignment at 300 K.

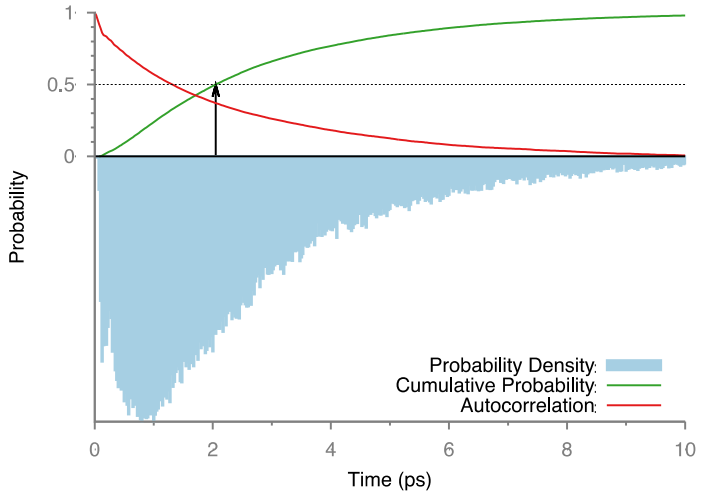

Figure S7. Time correlation analysis of the alignment of the C-H bond in the FAPI system. The probability density (blue) is the autocorrelation time for the dot product of the bond vectors to have decayed to zero (i.e. the distribution of times by which the molecule has rotated by greater than 90 degrees). The cumulative probability (green) is the sum of this distribution. The point at which this cumulative probability is 0.5 defines where 50% of the molecules have had sufficient time to reorient by 90 degrees or more, and is the mean value that we take as the 'rolling over' time constant of 2.0 ps. The standard autocorrelation is also presented (red).

Trajectory Analysis We have generalised our previously reported molecular dynamics analysis tools for MAPI (Frost, APL Materials 2014) to the FAPI system. The toolkit is freely available at https://github.com/jarvist/MAPI-MD-analysis. Taking the C-H bond as the reference vector, we build a histogram of the orientation distribution (in polar coordinates) of the eight FA ions in Figure S6(a). Basins are observed around the equivalent <100> directions. Asymmetry in these distributions is present due to the finite simulation length and the additional correlation imposed by the small simulation size; however, by exploiting the octahedral symmetry of the cube in which the molecule resides, the signal to noise ratio is greatly enhanced as shown in Figure S6(b). While a large fraction of orientational space is sampled at room temperature, there is an unambiguous preference for the molecular to align towards the face of a cube (<100>). Further analysis of the autocorrelation in molecular orientation revealed a time constant for the "rolling over" of the FA cation by 90 degrees to be 2.0 ps.

Reference

1) Stoumpos, C. C.; Malliakas, C. D.; Kanatzidis, M. G. Semiconducting Tin and Lead Iodide Perovskites with Organic Cations: Phase Transitions, High Mobilities, and near-Infrared Photoluminescent Properties. *Inorg. Chem.* **2013**, *52*, 9019–9038.

4.3 Further Results

4.3.1 UV-vis Reflectance Spectroscopy

Diffuse reflectance spectra were measured relative to a Speclatron standard using a Perkin Elmer Lambda 750S spectrophotometer equipped with an integrating sphere. The reflectance spectra for δ-FAPI and α-FAPI are plotted in Figure 4-1a, underlining that the alpha phase is the only polymorph of interest for photovoltaic applications. A Tauc plot of the Kubelka-Munk transform of the α-FAPI reflectance spectrum, assuming a direct band gap, is plotted in Figure 4-1b and was used to extract a value of the band gap from the intercept of linear fits to the initial rise in absorption and the background below 1.4 eV. The observed optical band gap of $E_g = 1.45 \pm 0.1$ eV is in close agreement with previously reported values.

4.3.2 δ-$FAPbI_3$

Crystals of the yellow, 2H-hexagonal polymorph were grown in solution from aqueous hydroiodic acid. Dissolving the reactants in the acidic solution at high temperature, then cooling through the saturation point resulted in crystallisation of the black α-polymorph. However, when the crystals were left standing in solution at room temperature, they rapidly converted to the yellow δ-polymorph, as also occurred when the crystals were removed from solution by vacuum filtration under atmospheric conditions. Only by heating the yellow crystals in the solid state to re-form the α polymorph was this phase stabilised with respect to atmospheric conditions for an appreciable amount of time (days to weeks, depending on storage conditions).

The synthesis of δ-$FAPbI_3$ was investigated. A 3-necked round bottomed flask was charged with 4.158 g PbI_2 and 0.924 g formamidinium acetate (Sigma). To this flask 10.2 ml HI (7.57 M, 57 wt%, stabilised with 1.5% H_3PO_2) was added and the mixture heated to 130°C under reflux in an N_2 atmosphere. Upon cooling a black precipitate formed, turning yellow as the crystals cooled to room temperature. These crystals were filtered and washed with anhydrous DCM before being dried at 60°C. Final yield 63%. The identity of the δ-phase was confirmed by powder X-ray diffraction, carried out on a Bruker D5000 diffractometer using Cu $K_{\alpha 1}$ radiation ($\lambda = 0.15418$ nm). Figure 4-2a displays a Pawley profile fit and expected peak positions of the δ-phase of $FAPbI_3$ from literature,[230] confirming its phase-pure formation.

An experiment was undertaken to synthesis larger crystals of δ-$FAPbI_3$ under hydrothermal

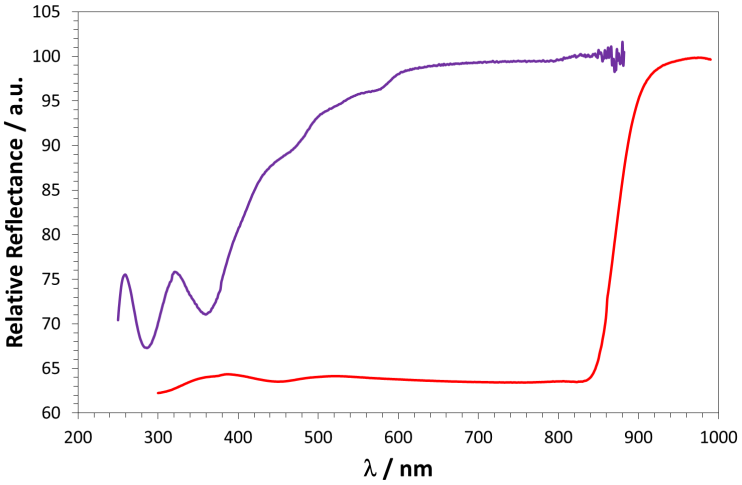

(a)

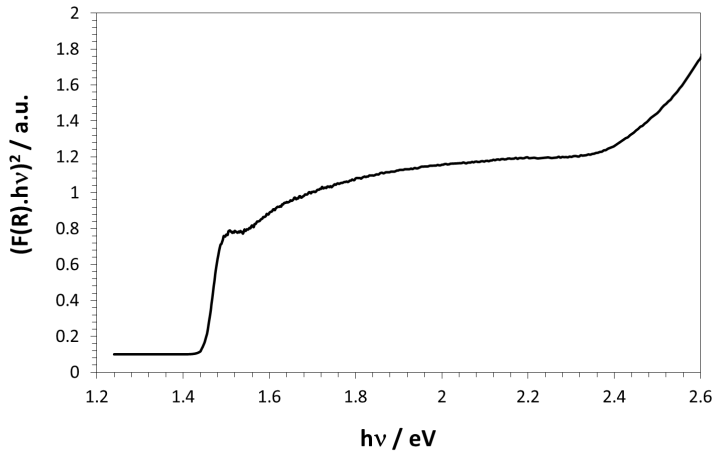

(b)

Figure 4-1: a) UV-vis diffuse reflectance spectra of α-FAPI (red) and δ-FAPI (blue) polymorphs. b) Tauc plot of Kubelka-Munk transformed diffuse reflectance spectrum of α-FAPI to plot pseudo-absorbance for determination of the optical band gap.

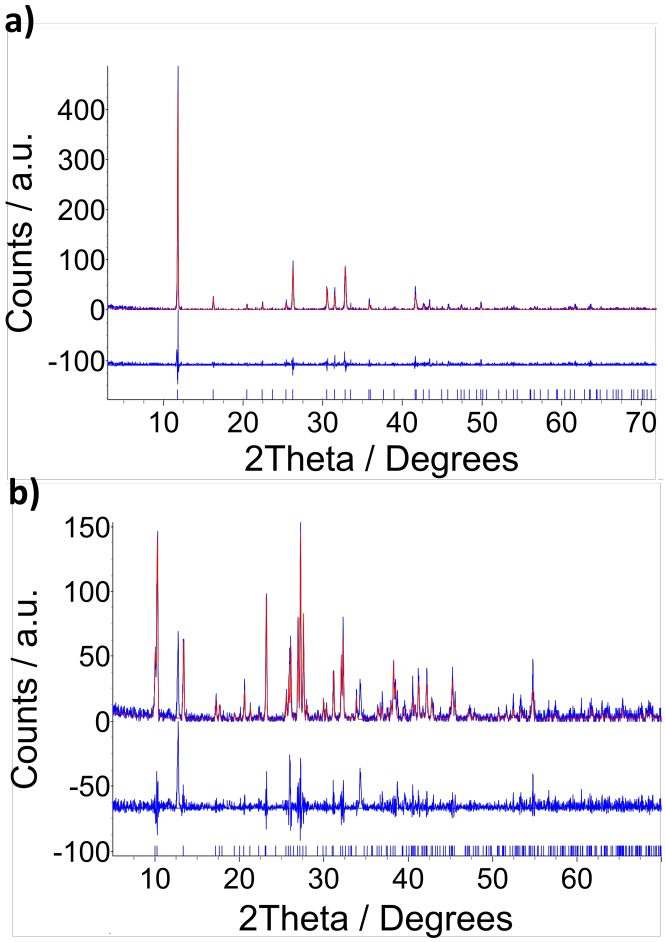

Figure 4-2: Pawley profile fit to a) δ-$FAPbI_3$, *P6$_3$/mmc*, a = 8.5891(5) Å, c = 7.8531(7) Å, χ^2 = 0.947 and b) NH_4PbI_3,[237] *Pnma*, a = 10.3029(14) Å, b = 4.7411(5) Å, c = 17.288(2) Å. χ^2 = 1.344.

conditions. The same reactants as the previous experiment were added to a 30 mL Teflon-lined hydrothermal bomb, which was heated to 140°C and cooled towards room temperature over five days. While this strategy was successful in forming large single crystals of $MAPbX_3$, X=I,Br,Cl, as described in Chapter 3, the formamidinium cation proved to be unstable at elevated temperatures under acidic conditions. Figure 4-2b displays the powder diffraction pattern of the hydrothermal sample, from which yellow / orange crystals were recovered. The powder pattern profile fit reveals the major phase formed to be NH_4PbI_3 due to the degradation of FAI, matching the structure reported in literature.[237] A second phase, with a significant peak observed at 12.7° 2θ, could be ascribed to δ-$FAPbI_3$ or PbI_2.

Chapter 5

Phase Behaviour of Formamidinium Lead Iodide

This Chapter reproduces in full the paper Phase Behaviour and Polymorphism of Formamidinium Lead Iodide, accepted for publication in Chemistry of Materials. Online version: DOI: 10.1021/acs.chemmater.8b00862

5.1 Commentary

Chapter 4 identified new findings on the room temperature phase of the black α-polymorph of formamidinium lead iodide, $FAPbI_3$, showing that this phase is cubic and analogous to the cubic phase of methylammonium lead iodide (Chapter 3), with the FA cation isotropically disordered. Chapter 5 details the variable temperature phase behaviour and polymorphism of $FAPbI_3$, studied by neutron powder diffraction and supported by *ab initio* molecular dynamics simulations. The current literature on $FAPbI_3$ phase behaviour is reviewed extensively in the following paper. Several reports employing neutron, synchrotron X-ray and total scattering techniques have been published, with significant disagreement present regarding the atomic structure of the low temperature phases of $FAPbI_3$.

From our variable temperature neutron powder diffraction data, collected at constant wavelength on D20, ILL and by time-of-flight at GEM, ISIS, we observe the polymorphic transition from the yellow, 2H-perovskite phase δ-$FAPbI_3$ to black, cubic α-$FAPbI_3$. On descending in temperature from this metastable α-phase, a tetragonal phase, β-$FAPbI_3$ is observed below 285 K. Rather than the I-centred cell of tetragonal $MAPbI_3$, β-$FAPbI_3$

adopts a primitive tetragonal cell, *P4/mbm*, with this difference related to the different geometry and hydrogen bonding proclivity of the planar formamidinium cation, which is still dynamically disordered, though now primarily along the elongated lattice directions of the lead iodide cages, along [100] or [010].

Below 140 K further weak peaks of diffracted intensity are observed, however it was not possible to index any of the neutron powder diffraction data at 100 K to a plausible unit cell. Different explanations present in the literature for the identity of the low temperature phase are examined. The following paper also demonstrates that our diffraction patterns are unlikely to stem from either a large commensurate cell expansion, relative to the mid temperature phase, or a mixture of phases due to a partial polymorphic transition.[135,230,238] Neutron total scattering results have suggested that below 140 K the material exhibits extensive disorder, with eventual glassy freezing of the cations below 15 K.[239] Potentially there is no ordered state of the planar FA cations compatible with the octahedral tilting pattern of the surrounding octahedral lead iodide framework. This is contrary to the case of orthorhombic $MAPbI_3$, Chapter 3, in which the linear methylammonium cations are able to arrange in an ordered state, such that the octahedral tilts of the inorganic framework also maximises the bonding interactions between the iodines and amine hydrogen atoms.

5.2 Phase Behaviour and Polymorphism of Formamidinium Lead Iodide

The following paper is reproduced in full from the original publication and spans thesis pages 118-144.

Statement of Authorship

This declaration concerns the article entitled:									
Phase Behaviour and Polymorphism of Formamidinium Lead Iodide									
Publication status (tick one)									
draft manuscript		**Submitted**		**In review**	✓	**Accepted**		**Published**	
Publication details (reference)	O. J. Weber, D. Ghosh, S. Gaines, P. F. Henry, A. B. Walker, M. S. Islam and M. T. Weller, *Chem. Mater*., 2018, Accepted for Publication								
Candidate's contribution to the paper (detailed, and also given as a percentage).	The candidate contributed to/ considerably contributed to/predominantly executed the… Formulation of ideas: 50% OJW suggested initiating the project, 50% MTW suggested use of neutrons as a structural probe. Design of methodology: MTW planned the D20 and GEM experiments and applied for beamtime. OJW developed the synthetic techniques and deuteration, assisted by SG. Experimental work: OJW synthesised the samples. OJW, MTW undertook data collection on GEM, D20. OJW developed the structural models and carried out all data analysis. DG, MSI and ABW carried out ab initio molecular dynamics simulations using the atomic structure developed from GEM & D20 data. Presentation of data in journal format: OJW wrote the paper in journal format.								
Statement from Candidate	This paper reports on original research I conducted during the period of my Higher Degree by Research candidature.								
Signed						**Date**			

Phase Behaviour and Polymorphism of Formamidinium Lead Iodide

Oliver J. Weber,[a] Dibyajyoti Ghosh,[a,b] Sam Gaines,[a] Paul F. Henry,[c] Alison B. Walker,[b] M. Saiful Islam*[a] and Mark T. Weller*[a]

a) Centre for Sustainable Chemical Technologies and Department of Chemistry, University of Bath, Bath, BA2 7AY, UK.
b) Department of Physics, University of Bath, Bath, BA2 7AY, UK.
c) ISIS Neutron and Muon Source, Rutherford Appleton Laboratory, Didcot, Oxfordshire, UK.

ABSTRACT: A greater understanding of the structure-property relationships of hybrid perovskites for solar cells is crucial for enhancing their performance. The low temperature phases of formamidinium lead iodide ($FAPbI_3$) have been investigated using rapid neutron powder diffraction. On cooling, the metastable α-polymorph descends in symmetry from the cubic unit cell phase present at room temperature through two successive phase transitions. Between 285-140 K a tetragonal phase, adopting the space group *P4/mbm*, is confirmed and the orientation of the disordered FA cation over this temperature range determined. The cation dynamics have also been investigated, over the same temperature range, at the atomic scale by using *ab initio* molecular dynamics simulations, which indicate contrasting FA motion in the cubic and tetragonal structures. Below 140 K the neutron powder diffraction data display weak Bragg scattering intensities not immediately indexable to a related unit cell. Data collected at 100 K from N-deuterated $FAPbI_3$ did not reveal any indication of the fundamental Bragg reflections at high d-spacing expected for an expanded supercell model as previously reported. Other hypotheses of a mixture of phases or a simple tetragonal cell below 140 K are also rejected on the basis of the observed data and our observations are consistent with a locally disordered low temperature γ-phase.

INTRODUCTION

Organic-inorganic hybrid halide perovskites are compounds adopting the ABX_3 perovskite structure, with the 'A' site occupied by an organic molecular cation within an inorganic lattice of vertex linked $[BX_6]$ octahedra. Most examples employ one or more components from the systems A^+ = MA^+(methylammonium) /FA^+(formamidinium)/ Cs^+, B^{2+} = Pb^{2+}/Sn^{2+}/Ge^{2+} and X^-= I^-/ Br^-/Cl^-.[1–4] These organic-inorganic hybrid halide perovskites combine the optoelectronic properties commonly associated with high performance semiconductors with materials synthesis and processing routes involving simple laboratory techniques, including solution-based chemistry. Rapid progress in perovskite photovoltaic devices has seen certified efficiencies rise to 22.1% in the past five years, with FA^+ cation ($CH(NH_2)_2$) containing structures contributing to some of the highest observed device efficiencies and stabilities.[5–12] Further progress, especially in device lifetimes under operational conditions, are required for these materials to make a major impact in solar energy technology.[13–15]

In this study fully hydrogenous ($FAPbI_3$-H) and part N-deuterated ($FAPbI_3$-D) samples have been studied by neutron powder diffraction at constant wavelength (D20, ILL) and spallation (GEM, ISIS) sources over the temperature range 430 – 3 K with high resolution in sample temperature and wide angular range. Phase transitions across the δ to α polymorphs and the behaviour of α-$FAPbI_3$ on cooling are reported and key structural parameters extracted as a function of temperature. In addition, the local structural dynamics are investigated over the same temperature range using *ab initio* molecular dynamics techniques.

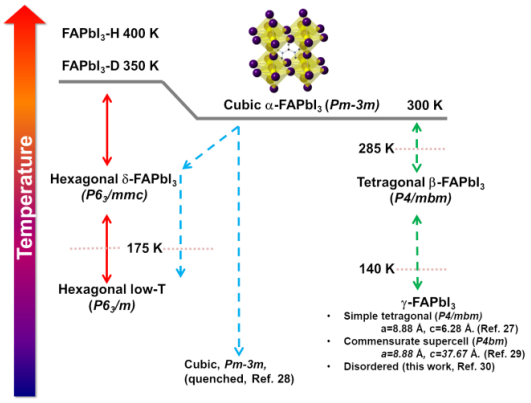

Figure 1. Previously reported phase and polymorphism behaviours of $FAPbI_3$ including hysteresis on heating and cooling for deuterated ($FAPbI_3$-D) and hydrogenous ($FAPbI_3$-H) samples, designated by the grey line. The predicted low temperature phases of $FAPbI_3$ are based on Refs. 16,25-29 identifying tetragonal or mixed phases. The cubic and hexagonal polymorphs potentially interconvert rapidly, depending on the surrounding chemical environment.

Of the three key parent phases $APbI_3$, A = MA, Cs or FA, the phase behaviour of $MAPbI_3$ and $CsPbI_3$ as a function of temperature are reasonably well understood.[16–24] In contrast, the phase behaviour of formamidinium lead iodide

($FAPbI_3$) has been less well resolved, with some significant disagreement among different studies reported in the literature. Neutron and X-Ray studies provide complimentary information, with higher resolution and intensity possible for X-rays, while neutrons provide greater sensitivity to distinguish light atom positions, nearly isoelectronic elements and different isotopes. $FAPbI_3$ may be synthesised as two polymorphs: a yellow hexagonal 2H-perovskite (δ) phase that is more stable and formed from solutions at room temperature and a black phase (α) that is thermodynamically favoured in the growth from solution media above 60 °C.[16] We have previously shown, using high-resolution neutron powder diffraction, that the structure of metastable α-phase is cubic at room temperature.[25] These black and yellow phases can interconvert rapidly and reversibly in the mother liquor used to grow crystals as the temperature is cycled. In the solid state, the black α-phase, required for photovoltaic applications, may be kinetically trapped at room temperature and interconverts much more slowly, over a period of hours to weeks depending on the form and storage conditions of the material.[16]

The recently reported low temperature phase behaviours of $FAPbI_3$ are summarised in Figure 1.[16,26–29] The original single crystal XRD study of $FAPbI_3$, undertaken at 298 K, refined the structure of the α-phase in the trigonal space group *P3m1*; and a low temperature phase, designated β-$FAPbI_3$, the structure of which was refined in space group *P3* for data collected at 150 K.[16] The structure of the hexagonal δ-$FAPbI_3$ (yellow polymorph) at 293 K was also refined, in the space group $P6_3mc$ using single crystal XRD data; the structure of δ-$FAPbI_3$ consists of face-sharing octahedral chains along the [001] direction with the unit cell $a = b = 8.6603(14)$ Å, $c = 7.9022(6)$ Å.[16]

Two subsequent studies on $FAPbI_3$ phase behaviour were published almost simultaneously.[27,28] In the first, δ-$FAPbI_3$ was heated *in-situ* to form α-$FAPbI_3$, the structure of which was found to be cubic, *Pm-3m,* at 300 K using synchrotron X-ray powder diffraction,[27] in agreement with our previous neutron powder data.[25] The material was then observed to undergo a phase transition when cooled below 285 K to a tetragonal β-phase, *P4/mbm*, (a = 8.92276(1) Å, c = 6.32626(1) Å at 200 K). Single crystal X-ray diffraction has also identified this β-phase to be tetragonal at 200 K.[26] At 140 K, a further phase transition was observed,[27] to a phase labelled γ; this re-entrant γ-phase was reported to also adopt the tetragonal space group *P4/mbm*, the same as the as for the β-phase, with a= 8.87516(3) Å and c = 6.27917(4) Å) at 100 K. The atomic positions of the organic cation were not definitively extracted in this X-Ray diffraction study, with the FA^+ cation modelled as a single pseudo-atom.

In the other study, the structure of N-deuterated $FAPbI_3$ ($FAPbI_3$-D) was investigated using neutron powder diffraction and elastic neutron scattering and this analysis reported contrasting phase behaviour.[28] The structure of deuterated yellow δ-$FAPbI_3$ (δ-$FAPbI_3$-D) at room temperature was also reported in the hexagonal space group $P6_3/mmc$, with a = 8.6226(5) Å and c = 7.9458(5) Å. A low temperature hexagonal phase observed below 175(5) K on cooling of δ-$FAPbI_3$-D was also described, refined in space group $P6_3/m$. δ-$FAPbI_3$-D was heated *in-situ* to form cubic deuterated $FAPbI_3$ (α-$FAPbI_3$-D) above 350 K. The sample was then cooled, with α-$FAPbI_3$-D reported as transitioning to a mixed phase region below 290 K, containing both cubic α-$FAPbI_3$-D (40 % of the sample) and a hexagonal δ-$FAPbI_3$-D (60 %). Further cooling of the sample below 165K induced another phase transition of the hexagonal portion of the sample to the low temperature hexagonal phase, while the cubic α-$FAPbI_3$-D phase was reported to remain unchanged. A further experiment quenched the α-$FAPbI_3$-D sample *in situ* from 400 K to 8 K (cooling rate 2.5 K min^{-1}) but observed no formation of any secondary phase or phase transition.

A subsequent combined neutron and X-ray powder diffraction study[29] on both N-deuterated and hydrogenous $FAPbI_3$ indicated that, on heating of a quenched sample of α-$FAPbI_3$ from 77 K, a low temperature tetragonal γ-phase (*P4bm*) was observed below 140(10) K, transitioning to an intermediate tetragonal phase (*P4/mbm*) observed between 140 K and 285 K, above which the room temperature cubic phase of α-$FAPbI_3$ is formed. Synchrotron X-ray powder diffraction patterns were collected for a sample heated *ex situ* to form the α-$FAPbI_3$ polymorph, cooled to 100 K at 4 K min^{-1} and then measured on heating from 100 K to 300 K. The low temperature γ-phase at 100 K displayed a set of weak peaks which the authors modelled using a 1 x 1 x 6 supercell (q = (0,0,1/6)) expansion compared to the mid-temperature tetragonal β-phase. Refinement tensioned jointly against X-ray and neutron data was carried out for this structure at 100 K and the model obtained shows varying orientations of the FA^+ cations along the extended 'c' axis. Final refined lattice parameters were a = 8.8774(1) Å, c = 37.6724(14) Å.

Alongside crystallographic studies of atomic structure, neutron total scattering and solid state NMR have been used to probe local dynamic structure,[30] indicating molecular motion becomes anisotropic in the β phase. Significant signal broadening was observed below 100 K, associated with the slowing of relaxation dynamics. Below 15 K, freezing and static disorder of molecular FA cation coupled to local distortion of the inorganic sub-lattice was observed. Dielectric spectroscopy similarly indicates from the low temperature permittivity that a further phase transition occurs at around 13 K.[31] Unlike $MAPbI_3$, in which an ordered antiferroelectric head-to-tail arrangement of organic cations is obtained for the low temperature orthorhombic phase,[21] γ-$FAPbI_3$ potentially exhibits no long range ordered structure of FA^+ ions compatible with octahedral tilting patterns of the inorganic lattice. The result is a disordered phase in which frustrated molecular-cage interactions defy simple descriptions of long-range order.[30,32]

EXPERIMENTAL

Synthesis

FAI-H

6.0540 g of formamidinium acetate (Sigma) was dissolved in 50 mL isopropanol in a round bottom flask and 7.682 mL hydriodic acid added under stirring. The solution was stirred for 30 mins before the isopropanol was removed by rotary evaporation to a white powder of formamidinium iodide. The crude product was recrystallised in hot ethanol and analysed by ^{1}H solution NMR.

δ-$FAPbI_3$-H

A 3-neck round bottom flask fitted with gas inlet and condenser was purged with N_2 gas and 7.2832 g of PbI_2 (Sigma, 99%) were dissolved in 17.554 mL stabilised hydriodic acid (Sigma, 57 wt%, 7.57 mol dm^{-3}, stabilised with 1.5% H_3PO_2). 2.7168 g of FAI were added, resulting in formation of yellow powder that turned black upon heating to 100 °C. The mixture was left to cool to room temperature, whereupon the black crystals of α-$FAPbI_3$ transitioned back to yellow δ-$FAPbI_3$. The powder was collected by vacuum filtration and washed copiously with anhydrous EtOH.

α-$FAPbI_3$-H

For the hydrogenous sample α-$FAPbI_3$-H, the above procedure was carried out to form δ-$FAPbI_3$-H. This was then heated in a fan oven at 413 K for 120 minutes under an ambient atmosphere to form the alpha phase. The phase transformation was shown to be complete by powder X-Ray diffraction and the sample was stored under a nitrogen atmosphere until employed for neutron diffraction 48 hours later.

Deuteration. FAI-D and α-$FAPbI_3$-D

FAI was dissolved in 10 mL D_2O (Sigma) under an argon atmosphere and stirred for 60 mins. The D_2O was evaporated and the sample dried under mild heating conditions of 90 °C on a hotplate. The extent of deuteration was established by 1H NMR, which was used to track the disappearance of the NH peak. It was found that extended heating under vacuum tended to degrade the formamidinium ion.

Deuterated FAI and PbI_2 (99%, Sigma) were dissolved in DMSO and drop cast onto a glass dish at 140 °C on a hotplate under a nitrogen atmosphere. A black crystalline solid formed as the solvent evaporated and the powder sample was dried on the hotplate for 120 minutes at this temperature. The sample of α-$FAPbI_3$-D was stored under nitrogen and not exposed to ambient atmosphere at any point during the experiment.

D20 & GEM experimental.

Constant wavelength diffraction on D20

The hexagonal to cubic phase transition in fully hydrogenous $FAPbI_3$ ($FAPbI_3$-H) was investigated in situ using neutron powder diffraction on the D20 instrument at the Institut Laue-Langevin, Grenoble.[33] A 10 g sample of crystalline yellow δ-phase powder (Sample 1) was loaded into in an 8mm vanadium sample can under ambient atmosphere and was measured while being heated in situ from 330 K to 430 K at a rate of 1 K min^{-1}. Indexing and Rietveld refinement of the powder patterns were carried out using TOPAS Academic, GSAS and SEQGSAS were used to analyse variation of structural parameters as a function of temperature.

TOF Diffraction

Hydrogenous and deuterated $FAPbI_3$ samples were measured on the GEM instrument at ISIS, Rutherford Appleton Laboratories over a wide Q range of 1 – 30 Å^{-1}.[34] Both powder samples were heated *ex-situ* to form α-$FAPbI_3$ (H/D) and loaded into 6 mm vanadium sample cans. The α-$FAPbI_3$-D sample can was loaded under an argon atmosphere and sealed using an indium O-ring. The samples were cooled in the instrument cryofurnace environment prior to measurement.

TG/MS

A 10 mg sample of a-$FAPbI_3$-H was loaded in a ceramic boat into a Setaram Setsys Evolution 16 TGA-DTA-DSC equipped with Pfeiffer GSD 320 mass spectrometer. The sample was heated at 5 K min^{-1} to 600 K and the weight change recorded simultaneously with analysis of the evolved gases.

^{1}H NMR was measured using a 300 MHz Bruker Avance NMR spectrometer.

Ab initio simulations

Static simulations were performed within the framework of density functional theory (DFT) as implemented in the Vienna *ab initio* simulation package (VASP) using Perdew-Burke-Ernzerhof (PBE) functional within the Generalised Gradient Approximation (GGA).[35] The projected augmented wave method,[36] a plane-wave cutoff energy of 520 eV and non-local functionals, optB86b-vdW were employed.[37,38] Geometry relaxation was performed using the conjugate gradient approach where the interatomic forces were relaxed until 0.005 eV/Å. *Ab initio* molecular dynamics (AIMD) calculations were performed using CP2K.[39] The $FAPbI_3$ lattices were modelled by a large supercell containing 64 A-site cations (768 atoms in total) which allowed us to capture details of dynamical processes for FA and Pb-I lattices. The calculations employed an auxiliary plane wave basis set with an energy cut-off of 300 Ry,[40] an analytical dual-space pseudopotential as implemented by Goedecker, Teter, and Hutter ,[41] GGA-PBE for solids (PBEsol) for exchange-correlation[42] and Grimme's correction for dispersion interaction (DFT-D3).[43] Equilibrium dynamics were maintained in the NPT ensemble using a Nose-Hoover thermostat. The systems were simulated for 25ps, the first 5ps of which were considered as the equilibration-time.

RESULTS AND DISCUSSION

1. Investigation of polymorphic phase transition in hydrogenous $FAPbI_3$.

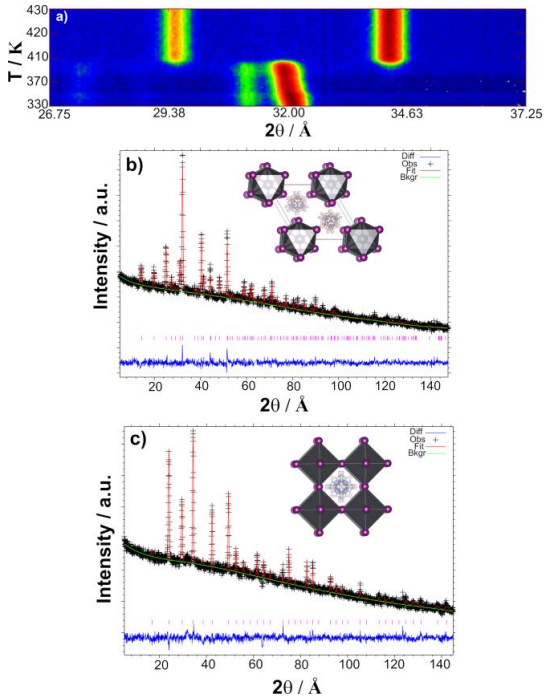

Figure 2 Phase transformation of δ-$FAPbI_3$ to α-$FAPbI_3$ heating *in-situ* in D20 (λ = 1.8691 Å). a) Contour plot in the 2θ range 26° to 37° of stacked X-ray diffractograms varying with temperature. b) Profile fit for the Rietveld refinement of hexagonal δ-$FAPbI_3$ at 300 K; atomic structure of δ-$FAPbI_3$ (inset). c) Profile fit for the Rietveld refinement of cubic α-$FAPbI_3$ at 412 K; atomic structure of α-$FAPbI_3$ (inset).

The polymorphic phase transformation to α-$FAPbI_3$-H was tracked by neutron powder diffraction as a hydrogenous sample of the yellow 2H polymorph (δ-$FAPbI_3$-H, Sample 1) was heated *in situ* in the D20 diffractometer (λ = 1.8691 Å). Figure 2a displays a narrow section of the 2θ range, plotted against temperature. Each y-axis slice of the plot is a diffraction pattern, with the colour contour denoting the intensity of Bragg scattering. The phase transition between hexagonal and cubic polymorphs is observed at approximately 400 K. Data collected at the start (300 K) and end-point (430 K) of the experiment were analysed using Rietveld profile fitting to confirm the identity of each phase (Figures 2b and 2c). The data were binned every 4 K as the sample temperature was ramped at 1 K min^{-1}.

The refined structural parameters for δ-$FAPbI_3$-H at 298 K, space group *P6₃/mmc*, a = 8.5891(5) Å, c = 7.8531(7) Å, final χ^2 = 1.35, are fully reported in the Supporting Information (Figure ESI S2). A Pb—I bond length of 3.193(5) Å

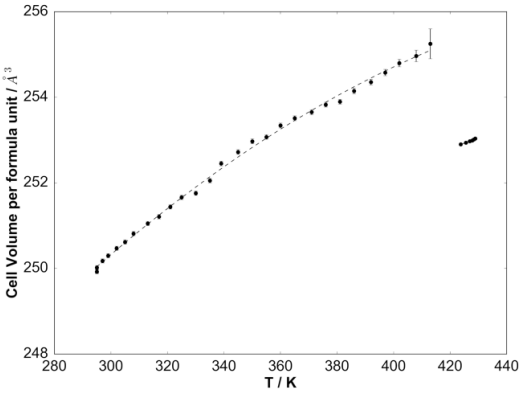

Figure 3 Volumetric expansion per formula unit across hexagonal δ-$FAPbI_3$ and cubic α-$FAPbI_3$.

was obtained for the 1D face-sharing PbI_6 octahedra. Refinement using the model provided in Ref. 16 from X-ray data without hydrogen positions (Figure S3) generated significantly worse fits to the neutron powder pattern, underlining the sensitivity of neutron data to the light atom positions and orientation of the organic cation. The model for cubic α-$FAPbI_3$ given in Ref. 25 was employed for the data analysis above 400 K. A sequential refinement using SEQGSAS tracked unit cell expansion and lattice parameter variation as a function of temperature across both phases (Figure 3). The phase transition from hexagonal to cubic polymorph occurred at approximately 400 K, in agreement with literature.[28] Contraction along the *c* axis, partially compensating for expansion in the *ab* plane, was observed in hexagonal $FAPbI_3$ prior to the phase transition.

To complement our structural data and analysis, we performed density functional theory (DFT)-based computations which extend our recent work on $MAPbI_3$ and $FAPbI_3$-based compounds.[44–46] Relaxing the crystal structure of δ-$FAPbI_3$-H without any constraints, we find good agreement between the simulations and the structure refined against D20 data in terms of bond-lengths and angles (ESI Table S4). The calculated ground state energy between δ- and α-$FAPbI_3$ phases indicate that the δ-phase is more stable by 0.20 eV/formula unit in accord with observed phase stability behaviour. The calculated potential energies from AIMD simulations at 300 K also show increased structural stability of the δ-$FAPbI_3$ compared to the α-phase (see Figure S12 for details). The face-sharing arrangement of PbI_6 octahedra in the δ-phase results in higher structural stability than the α-$FAPbI_3$ which contains corner-shared octahedra.

2. Structure of tetragonal β-$FAPbI_3$ at 200 K

A second sample of fully hydrogenous $FAPbI_3$ (Sample 2) was heated *ex situ* in a fan oven at 140 °C for 120 minutes to form α-$FAPbI_3$. This sample was investigated using the time of flight GEM diffractometer at ISIS at 200 K. The complete thermal history of Sample 2 is provided in Section 4. Indexing of the data collected at 200 K suggested a

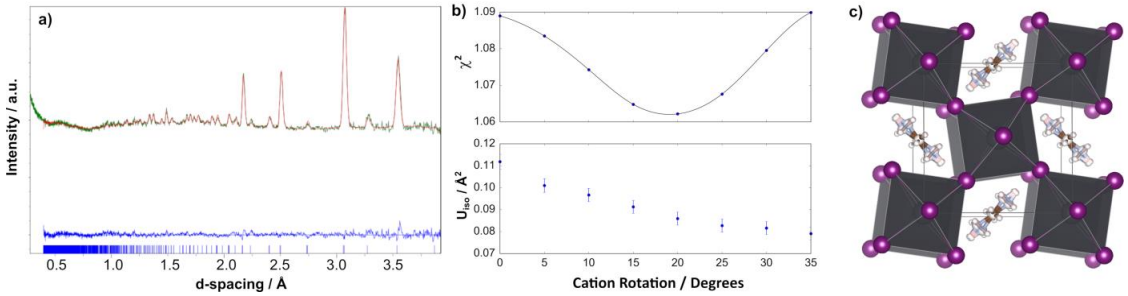

Figure 4 a) Rietveld fit to data collected on GEM diffractometer Bank 4 (62°) at 200 K, difference curves and hkl reflection positions (tick marks). Final refined structure of b-$FAPbI_3$ at 200 K, space group *P4/mbm*, a = 8.9231(4) Å, c= 6.322(5) Å, c^2 = 1.05. b) Rietveld refinement goodness-of-fit (Upper trace) and C,N,H isotropic thermal parameter (U_{iso}, Lower trace) as a function of tilting of the FA molecule out of perpendicular to the *ab* plane. The line in the upper trace is provided as a guide for the eye. c) Atomic structure of β-$FAPbI_3$ at 200 K viewed slightly offset from the '*c*' axis.

tetragonal unit cell, and reflections consistent with the space group *P4bm* or *P4/mbm*, as found previously.[27]

A Rietveld refinement using a model developed in this tetragonal cell and tensioned against the 200 K data rapidly converged to give a final χ^2 = 1.05 (Figure 4a). Options for modelling the position of the FA cation were explored further. Unlike the cubic phase, in which from symmetry considerations FA^+ is formally disordered in all equivalent directions, in the tetragonal phase the cation is likely to be dynamically disordered between preferred orientations and different scenarios can be envisaged for exchange be tween these. The FA cation was modelled using a rigid body model in the Z-matrix formalism, with the carbon atom, carbon-bonded hydrogen and one nitrogen position (and its bonded hydrogens) defined, with the other $-NH_2$ generated by the symmetry of the cell. C, N and H bond lengths were defined as separate refineable parameters and refined within constraints. A model with the planar FA cation aligned perpendicular with the *ab* plane obtained reasonable refinement results.

The offset of the FA molecule in the 'c' axis direction from the centre of the unit cell axis was further defined as a parameter and refined. The offset along this axis preserved the twofold inversion axis generating half the molecule. The effect of tilting the FA^+ cation away from perpendicular to the *ab* plane was explored in 5° steps (Figure 4b). The goodness of fit for Rietveld refinement was minimised for a tilt angle of 20° (4b, upper trace), while the isotropic thermal displacement for the organic ion decreased across the entire angle range (4b, lower trace). This trend is expected on the basis that dynamically disordered orientations of the cation accounts for atomic intensity otherwise modelled by thermal displacement. Figure 4c displays the structural model in which FA is tilted out of the plane perpendicular to the *ab* plane by 20°. This model was used for further full analysis of the NPD data collected between 285 K and 135 K (Section 3). Recent solid state NMR experiments indicate that orientational disorder remains active down to low temperature, with rotation of the C-H and amine hydrogens around an axis defined by the two nitrogen atoms of the molecule.[30] A model was also trialled in which the central carbon atom and hydrogens were free to rotate around an axis defined by N---N and centred on (0.5, 0, 0.5), resulted in 4% higher χ^2 than for the molecule offset along the z axis.

As molecular dynamics simulations provide the atomistic details of cation reorientation in these hybrid perovskites,[47] we further performed *ab initio* molecular dynamics calculations for the different phases of $FAPbI_3$. From Fig 5a we see complete disorder of the FA cations in the cubic phase at 300 K. The PbI_6 octahedra also undergo periodic tilting oscillations which on average produce the pseudo-cubic structure (Fig. 5a). These structural dynamics indicate a weak lattice-cation coupling between the organic cations and inorganic framework.

In contrast, FA cations in the tetragonal β-phase at 200K show restricted motion inside the cage (Fig. 5b). At this temperature, the periodic tilting motion of the PbI_6 octahedra is also partially suppressed, causing permanent 'in-plane' Glazer tilting $a^0a^0c^+$ in the tetragonal lattice (Fig. S11). Consequently, the A-site cage volume distorts in a manner by which it elongates or contracts along the [100] or [010] lattice directions (Fig. S11). At equilibrium, the FA cations preferentially reside along the elongated lattice direction of their host cages and show largely preserved molecular ordering over the simulation. Furthermore, the cations of the nearest-neighbour cages remain perpendicular to each other in the *ab*-plane (Fig. 5b and Fig. S13). This is in good agreement with the model derived from our experimental diffraction data. These preferred orientations of the FA cations are clearly influenced by the octahedral distortion of PbI_6. This also indicates the coupling between the dynamical modes of FA cations and Pb-I in this phase.

Investigating the change in the cation-reorientation dynamics more quantitatively, we have evaluated the vector autocorrelation function for the FA cations in cubic and tetragonal phases of $FAPbI_3$. This function exhibits the

number-averaged correlation among the orientations of a particular FA cation over the simulation-time (see Supporting Information for more details). Physically, it denotes the rate at which the organic cations rotationally relax inside the inorganic cage. The faster the function decays, the quicker the molecules reorient and relax. Figure 5c shows that the rotational relaxation of the cation in the cubic phase is much faster compared to the tetragonal phase. This function further provides the reorientational relaxation time. We obtained a reorientational relaxation time of 8.8 ps for cubic phase (see Supporting Information for details). This is in good agreement with recent experimental work by Fabini *et al*..[30] In contrast, due to the slow decorrelation of the molecular vectors over time, we were not able to calculate cation relaxation time in the tetragonal phase within the time-scale of our simulation. The slow rotational decorrelation in this low-temperature phase further supports the partial cation-ordering found from the cation trajectories in Fig. 5b. The strong dependence of reorientational relaxation on temperature had also been demonstrated previously for MA cations in $MAPbI_3$ (further details in Supporting Information).[48,49]

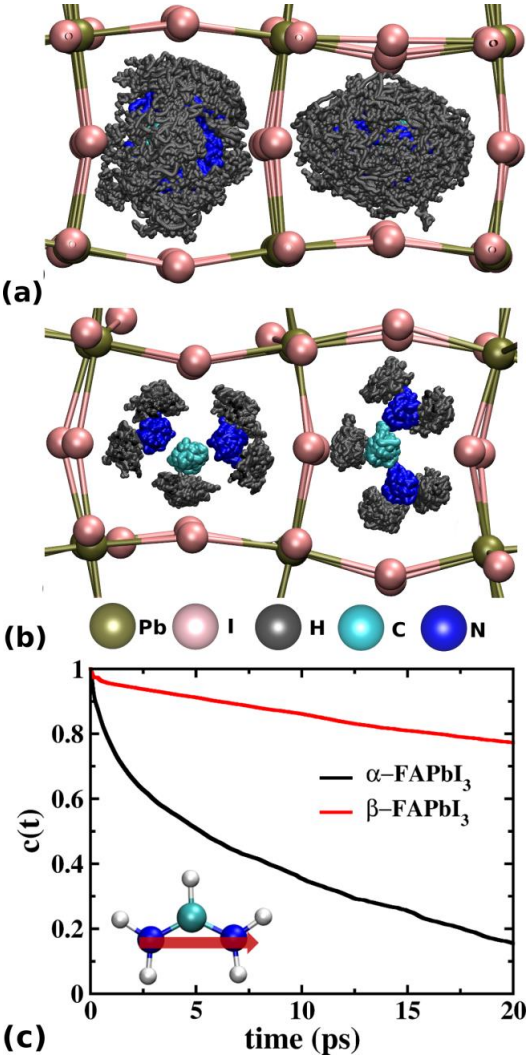

Figure 5 Trajectory of FA cations inside the A-site cages of $FAPbI_3$ (a) pseudo-cubic phase and (b) tetragonal-phase. The green and pink spheres represent the time-average positions of Pb and I, respectively. The trajectory for atoms of the FA cations remain localized over the simulation time for the tetragonal phase only. The increased structural distortion of the inorganic framework with the cubic to tetragonal phase transition is demonstrated by the more pronounced deviation of the Pb-I-Pb angles from the ideal cubic value. (c) Vector autocorrelation function of FA cation showing the correlated orientation of cations over time. The inset shows molecular vector of FA ion by the red arrow.

By analysing the molecular ordering in the tetragonal structure, we find that the FA cations of nearest-neighbour cages alternate direction of the H-C bond with respect to each other in the ab-plane, which is in good agreement with the model derived from our diffraction data. These preferred orientations of FA cations are clearly influenced by the octahedral distortion of PbI_6. At equilibrium, the molecular cations orient themselves along the direction in which the A-site cage gets elongated. This also indicates the coupling between the dynamical modes of FA and Pb-I in this phase. A more detailed analysis reveals that in the tetragonal phase the tumbling of FA-cations becomes mostly suppressed, leaving only the on-axis rotation and libration as the active modes of molecular motion; this is in good agreement with recent solid state NMR experiments.[30] This result further supports our experimental observation that in the tetragonal phase the FA cations are better modelled by tilting them away from perpendicular to the ab plane.

3. Phase behaviour of α-$FAPbI_3$-H on cooling.

A further sample of δ-$FAPbI_3$ (Sample 3) was heated *ex-situ* to the D20 neutron beam to form α-$FAPbI_3$ in a fan oven under ambient atmosphere at 140 °C for two hours before being removed and cooled to room temperature. The phase behaviour of this sample was monitored on cooling in situ on D20, λ = 1.8691 Å, from 300 K to 3 K at a rate of 0.5 K min^{-1}, with data binned every 2.5 K (Figure 6). This sample was observed to undergo two distinct phase transitions upon cooling, the first just below room temperature at around 280 K and another at 140 K, with the observation of additional weak peaks below 140 K, for example at 60.45° in 2θ, corresponding to a d-spacing of 1.86 Å. The observed temperatures for these transitions are consistent with previous neutron scattering and photoluminescence data for a sample of "quenched" α-$FAPbI_3$ measured on heating from 2 K.[29,50] No further phase transitions below 15 K were observed, within the resolution of our diffraction data.

A sequential temperature refinement was undertaken using SEQGSAS over this temperature range in 2.5 K incre-

ments. The tetragonal *P4/mbm* model developed from the 200 K data was used for refinement of the data across the temperature range 295 – 140 K, with the lattice parameters, iodine position and isotropic thermal parameters all refined. The atomic displacement parameters for C, N and H were constrained to one overall value for the molecular ion. The extracted lattice parameters are plotted in Figure 5, while other the parameters are plotted in the Supporting Information (ESI Figure S6). Divergence of the reduced lattice parameters (c and $a/\sqrt{2}$) is observed on cooling in towards 140 K, similar in magnitude to previously reported lattice parameters from X-Ray synchrotron measurements.[27] Convergence of these parameters above 250 K suggest that the degree of tetragonal distortion ($\sqrt{2}.c/a$) is negligible in the 285 – 250 K range, or that it is harder to

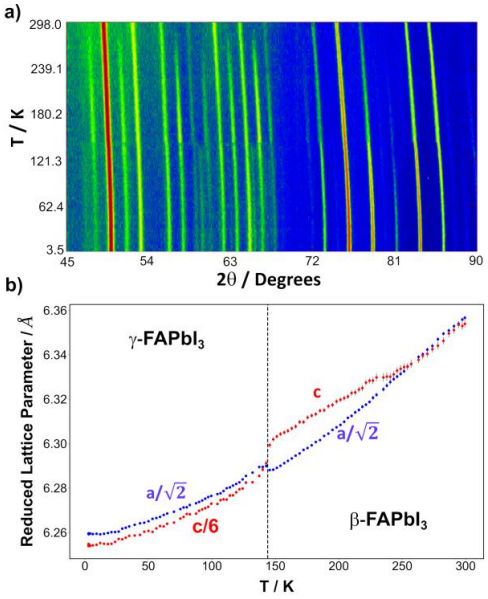

Figure 6 a) Neutron powder diffractograms collected on D20, ILL, stacked by temperature of Sample 3 of α-$FAPbI_3$ cooled from 300 to 3K. b) Reduced unit cell parameters of mid-temperature tetragonal β-$FAPbI_3$ and low temperature γ-$FAPbI_3$.

distinguish a tetragonal from cubic model in this temperature range, compared to X-ray synchrotron data. In addition, the *ab initio* calculations find that the ground state of tetragonal $FAPbI_3$ is more stable than the α phase by 0.16 eV/formula unit. The potential energies calculated from finite temperature *ab initio* molecular dynamics simulations also show same order of phase-stability (See Supporting Information Figure S12). This result supports the experimental finding of a phase transition from the metastable α-phase to the tetragonal phase upon cooling below 280K.

Below 140 K, the data (Figure 6, top) clearly display additional weak peaks that grow in on cooling. Indexing of the observed peaks at 100 K did not immediately suggest a candidate unit cell from which to build a structural model. Several possibilities for the identity of the low temperature phase (<140 K) have been outlined in the literature:

i) Application of a simple tetragonal cell in a Pawley unit cell refinement (P4bm, a=8.87 Å, c=6.28 Å), as employed in Ref. 27, left observed peak intensities in the neutron data unindexed, for example at 60.45° and 66.22° (ESI Table S3).

ii) Another possibility has been suggested of a mix of cubic and hexagonal phases in deuterated $FAPbI_3$.[28] Employing a multiphase cubic / low temperature hexagonal model, or tetragonal / hexagonal, did account for the some of the additional peak intensities observed in the (limited resolution) D20 dataset, however the amount of hexagonal phase was very small, and all the refined parameters were highly correlated to the cubic phase parameters. As shown in ESI Figure S9, the peaks observed to grow in at 100 K in the data collected on GEM could not be indexed to this multiphase model. Furthermore, there is no obvious mechanism for a transition from a tetragonal model (140-285 K data) to a complex multiphase mixture applicable to the lowest temperature range. We note that steady state photoluminescence measurements are consistent with the presence of a low temperature tetragonal phase, with emission for the low temperature phases observed around 1.5 eV as for α-$FAPbI_3$, while the δ-phase has a larger band gap and emits at 1.9 eV.[29,50] This trend in band-gap variation with the structural phase transitions matches very well with our calculated band-gaps from DFT simulations (see Table S1).

iii) A third possibility suggested in recent literature is a 1x1x6 supercell expansion relative to the intermediate temperature tetragonal cell, in which the FA molecular ion is rotated in increments along the long 'c' axis (~37 Å).[29] This model generates many additional reflection positions in the mid-angle range, at which the additional small peak intensities are observed in our D20 data (Figure 6a). This model was therefore employed to extract unit cell parameters from the data obtained between 140 and 5 K, as plotted in Figure 6b. The additional weak reflections will in any case have little effect on the extracted lattice parameters. It was not possible to refine (in a stable manner) the FA cation atom positions across this very lowest temperature range due to the relatively low resolution of D20 data coupled with the complexity of this structural model.

4. Comparison of deuterated and hydrogenous $FAPbI_3$ phase behaviour

Comparative phase behaviour between hydrogenous and part N-deuterated (>80% by ^{1}H NMR, Figure S10) α-$FAPbI_3$ was investigated in this work using the GEM diffractometer at ISIS, RAL. Samples of α-$FAPbI_3$-H (Sample 2) and α-$FAPbI_3$-D (Sample 4) were heated to form the α-phase *ex-situ*, before being sealed into vanadium sample cans under a nitrogen atmosphere. Each sample was cooled to a base temperature before measurement commenced, with data collected at temperature plateaus as the samples were heated. Data collected on GEM detector bank 4 at 100, 200 and 300 K are displayed in Figure 7.

The 100 K GEM data for γ-$FAPbI_3$-D display small additional intensity peaks, for example in Figure 7b at 3.2 Å, that again cannot be satisfactorily indexed either to a simple tetragonal cell or to a multiphase mixture of the tetragonal β-$FAPbI_3$ cell and partial transformation to the hexagonal low temperature *P6₃/m* polymorph (ESI Figure S9).[27,29] Indexing of the low temperature data did not result in a candidate space group. Pawley fits to the 100 K data ruled out partial transition to the hexagonal polymorph (Figure S9). These peaks appear only in the mid-angle range, none at long time-of-flight / d-spacing, and do not appear to be satellite peaks with a characteristic commensurate modulation vector to the main peaks.

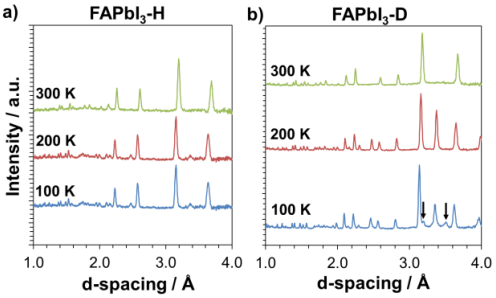

Figure 7 Neutron powder diffraction patterns collected on GEM, ISIS, detector Bank 4 (62°) of a) hydrogenous $FAPbI_3$ ($FAPbI_3$-H) and b) deuterated $FAPbI_3$ ($FAPbI_3$-D) at 100, 200 and 300 K. Weak additional peaks are clearly observed in the deuterated data at 100 K, marked with black arrows.

The deuterated sample provides better resolution for equivalent counting time, as a far better signal to noise ratio is achieved due to a decrease in incoherent scattering from hydrogen, so the peaks that appear in the 100 K data are more apparent than for the hydrogenous γ-$FAPbI_3$-H data (Figure 7a). These deuterated and hydrogenous samples of the α-polymorph appear to undergo the same succession of phase transitions upon heating.

It has been reported previously that α-$FAPbI_3$-D can be quenched from 400 K to 8 K while retaining the cubic phase.[28] Sample 4 was placed into the cryofurnace chamber, already at a base temperature of 10 K, and cooled from 298 K within 60 mins (>5 K min^{-1}). We observed no evidence that quenched α-$FAPbI_3$-D retained the cubic phase to low temperature. We note that analysis of the expected *d*-spacings of *h,k,l* reflections generated from a primitive *P4/mbm* tetragonal cell (a = 8.922 Å, c = 6.326 Å) indicates that for the momentum transfer (*Q*) range plotted in Fig. 3A of Ref. 28, the (0,2,1) peak of this tetragonal cell would overlap directly with the (1,1,1) reflection of an analogous primitive cubic cell (a = 6.326 Å). As there are no distinct reflections from the tetragonal and cubic phases in this *Q* range, it is difficult to distinguish between the cases of a quenched cubic phase and appearance of the mid-temperature tetragonal phase (Figure 6a).

As noted in Section 3, the diffraction data collected on D20 below 140 K exhibited additional reflections and further analysis of the GEM data collected from γ-$FAPbI_3$-D at 100 K was undertaken to determine the effectiveness of the proposed structural models in fitting these diffraction patterns. Figure 8 displays data obtained in GEM detector bank 2, between approximately 1-14 Å (Q <1 $Å^{-1}$), for γ-$FAPbI_3$-D (sample 4) at 100 K, together with the calculated profile using the 1×1×6 supercell expansion model proposed by Chen et al.[29] This attempted profile fit shows that no intensity is observed experimentally for (0,0,n), n = 3, 4 reflections of the 1×1×6 supercell while the published model calculates significant diffraction intensity at these Q-values. This result suggests that no long-range ordering, of

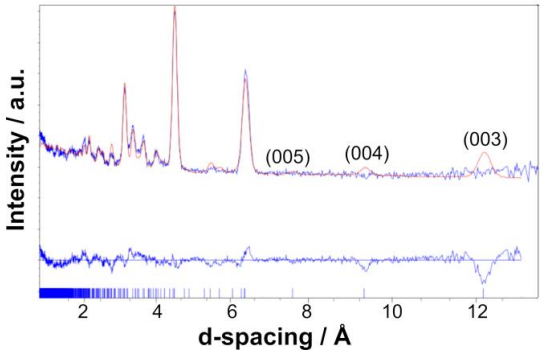

Figure 8 Rietveld refinement of supercell model to GEM data Bank 2 (17°, 17 m primary flight path) for γ-$FAPbI_3$-D at 100 K. No reflection intensity was observed in the expected positions at high TOF / d-spacing, using the 1×1×6 supercell model of Ref. 29 for the 0,0,4 (14,000 ms / 9.418 Å) or 0,0,3 (19,000 ms / 12.56 Å) fundamental reflections for deuterated $FAPbI_3$.

the kind described in this previous work, occurred for this particular sample. It should also be noted that one effect of this very large lattice parameter is to generate a very great number of calculated reflection positions in the mid-Q range, effectively permitting indexing of all the weak peaks observed within that range in our moderate-resolution diffraction data.

Local structure studies of $FAPbI_3$ provide a potential explanation for these observations. These have indicated that disorder, stemming from geometrical frustration between molecular cation orientations and the inorganic cage, dominates in the γ-phase < 140 K. The eventual glass-like freezing of the FA cation orientations,[30,31] is coupled to the local inorganic lattice structure.[37] Orientational glass formation has also been observed in $MA_{1-x}Cs_xPbBr_3$ solid solutions,[32] with the disorder derived from the range of MA^+ orientations frozen-in at low temperature. Unlike in the orthorhombic phase of $MAPbI_3$,[21] static, long-range tilting patterns of the inorganic framework in the solid solution are not compatible with an ordered arrangement of A-site sublattice orientations which is directly coupled through hydrogen bonding.[32] Some elements of ordering of the cations and disruption of the tilting patterns of the PbI_6 octahedra are likely to persist below 140 K, which would produce the weak Bragg diffraction peaks we observe in the γ-

phase of $FAPbI_3$. We consider a description of a disordered γ-phase, in which eventual freezing of molecule-cage interactions generate few, weak diffraction features in the mid-angle range, to be more likely than a long range modulated structure, evidenced by the lack of diffracted intensity at low angle / long time-of-flight where such ordering would be expected.

Our neutron powder diffraction data lack the resolution of X-ray diffraction methods previously employed to describe a very large commensurate supercell for $FAPbI_3$,[29] or incommensurate cell in the single crystal X-ray diffraction of $MAPbBr_3$,[51] but we observe no evidence of an elongated cell axis on the length scales we have measured (d-spacing = 0.5 – 14 Å, Figure S8). A large supercell expansion, and also models incorporating multiple phases, run the risk of overfitting the limited additional information present in the few weak peaks present in our data, as compared to high resolution synchrotron X-ray experiments, which however lack the same sensitivity to light element (C,N,H) atomic positions. We note, further, that the equivalent X-ray single crystal experiment for $FAPbI_3$ presents its own challenges in unambiguous structure determination, with even nominally untwinned crystals of α-$FAPbI_3$ forming multiple crystallographic twins when cooled across phase transitions.[26]

There are, however, differences in the handling of the samples measured in this work (yielding the data presented in Figs. 6 and 7) and those employed for neutron diffraction work (in Ref. 28) and high resolution synchrotron X-Ray diffraction (in Ref. 27). Our samples 2-4 were heated *ex situ* prior to measurement while the sample used in Ref. 28 was heated *in situ*, which may result in retention of volatile components, if the sample was contained for example in a sealed capillary tube. An enclosed, *in situ* heating process is more analogous to the conditions employed in solution synthesis, wherein δ-$FAPbI_3$ and α-$FAPbI_3$ readily interconvert (probably due a high abundance of the starting components in immediate proximity to any crystals forming). Volatile components including residual solvent, excess acid, organic ions and iodide could all be involved in this process. The synthesis method, particle size and heterogeneity, and any residual coating on the isolated crystalline phase may also affect the observed phase transition temperatures; for example it has been shown that a small quantity of HI included in a precursor solution drastically alters the phase transition temperature observed for a thin film sample of $CsPbI_3$.[52] Clearly with the appropriate experimental conditions, the rapid interconversion of δ-$FAPbI_3$ to α-$FAPbI_3$ will be observed, may not occur uniformly within a sample, and measurements of the phase behaviour of $FAPbI_3$ must contend with this polymorphism. The temperature cycling history of the sample is, therefore, extremely relevant and the exact temperature ramp rates may also affect the observed phase behaviour.

CONCLUSIONS

The phase behaviour of formamidinium lead iodide ($FAPbI_3$) has been described by conflicting accounts in the literature. We have shown that results from neutron powder diffraction experiments are consistent with the formation of two low temperature phases related to the room temperature cubic phase of α-$FAPbI_3$. The first transition to a primitive tetragonal cell (β-$FAPbI_3$) occurs just below room temperature at 285 K. At 140 K, a further phase transition occurs, characterised by weak Bragg scattering peaks (γ-$FAPbI_3$). Deuterated and hydrogenous $FAPbI_3$ both show equivalent phase behaviour in this regard.

A 1×1×6 expansion of the unit cell relative to the mid-temperature tetragonal phase generated many more reflection possibilities encompassing the additional weak peaks observed. However, data for deuterated $FAPbI_3$ at 100 K indicates that, at low Q / $Å^{-1}$, the expected (0,0,n) reflections (n = 3-5) of this cell expansion are not observed.

Due to the polymorphism displayed between δ-$FAPbI_3$ and α-$FAPbI_3$, the synthesis conditions, sample environment and cycling temperature all play a role in determining the observed phases of the material. *Ab initio* simulations find greater stability for the hexagonal and tetragonal phases than the cubic α-phase, in accord with experimental trends. The molecular dynamics simulations show significant FA^+ cation tumbling motion and on-axis rotation in the cubic phase. In contrast, for the mid-temperature tetragonal β-phase there is restricted motion of the FA^+ cation with preferred orientations within the A-site cage. Below 140 K, the FA cation positions demonstrate a high level of disorder in a glassy state but some elements of long range ordering of the cations or tilting of the PbI_6 octahedra persist, generating the observed additional diffraction intensity.

ASSOCIATED CONTENT

Supporting Information: Thermogravimetric analysis, additional structural refinement fit data and extracted crystallographic parameters, optimized geometries from computational calculations. This material is available free of charge via the Internet at http://pubs.acs.org. Oliver Weber et al; (2016): 1610285, STFC ISIS Facility, doi:10.5286/ISIS.E.79114391

AUTHOR INFORMATION

Corresponding Authors * E-mail: M.T.Weller@bath.ac.uk; m.s.islam@bath.ac.uk

Author Contributions

The manuscript was written through contributions of all authors. All authors have given approval to the final version of the manuscript. OJW and SG undertook the sample synthesis, OJW, PFH and MTW the diffraction experiments and diffraction data analysis, DG, ABW and MSI performed the computational analysis.

Funding Sources

OJW would like to thank EPSRC for PhD studentship funding via the EPSCRC doctoral training centre in Sustainable Chemical Technologies (EP/G03768X/1). D.G., M.S.I. and A.B.W. acknowledge the support from Energy oriented Centre of Ex-

cellence (EoCoE), grant agreement number 676629, funded within the Horizon2020 framework of the European Union.

ACKNOWLEDGMENT

We would like to thank T. C. Hansen, ILL, and I. da Silva, ISIS, for assistance in neutron diffraction experiments and the application of TOPAS software for TOF neutron data analysis. We would also like to thank the ILL and ISIS for the award of beamtime under Proposals 5-24-567 (ILL)[53] and RB1610285 (ISIS).[54]

ABBREVIATIONS

MA, methylammonium; FA, formamidinium.

REFERENCES

(1) Green, M. A.; Ho-Baillie, A. Perovskite Solar Cells: The Birth of a New Era in Photovoltaics. *ACS Energy Lett.* **2017**, *2* (4), 822–830.

(2) Petrus, M. L.; Schlipf, J.; Li, C.; Gujar, T. P.; Giesbrecht, N.; Müller-Buschbaum, P.; Thelakkat, M.; Bein, T.; Hüttner, S.; Docampo, P. Capturing the Sun: A Review of the Challenges and Perspectives of Perovskite Solar Cells. *Adv. Energy Mater.* **2017**, *7* (16), 1700264.

(3) Yang, S.; Fu, W.; Zhang, Z.; Chen, H.; Li, C.-Z. Recent Advances in Perovskite Solar Cells: Efficiency, Stability and Lead-Free Perovskite. *J. Mater. Chem. A* **2017**, *5* (23), 11462–11482.

(4) Correa-Baena, J.-P.; Saliba, M.; Buonassisi, T.; Grätzel, M.; Abate, A.; Tress, W.; Hagfeldt, A. Promises and Challenges of Perovskite Solar Cells. *Science* **2017**, *358* (6364), 739–744.

(5) deQuilettes, D. W.; Koch, S.; Burke, S.; Paranji, R. K.; Shropshire, A. J.; Ziffer, M. E.; Ginger, D. S. Photoluminescence Lifetimes Exceeding 8 Ms and Quantum Yields Exceeding 30% in Hybrid Perovskite Thin Films by Ligand Passivation. *ACS Energy Lett.* **2016**, *1* (2), 438–444.

(6) Eperon, G. E.; Stranks, S. D.; Menelaou, C.; Johnston, M. B.; Herz, L. M.; Snaith, H. J. Formamidinium Lead Trihalide: A Broadly Tunable Perovskite for Efficient Planar Heterojunction Solar Cells. *Energy Environ. Sci.* **2014**, *7* (3), 982–988.

(7) Rehman, W.; McMeekin, D. P.; Patel, J. B.; Milot, R. L.; Johnston, M. B.; Snaith, H. J.; Herz, L. M. Photovoltaic Mixed-Cation Lead Mixed-Halide Perovskites: Links between Crystallinity, Photo-Stability and Electronic Properties. *Energy Environ. Sci.* **2017**, *10* (1), 361–369.

(8) Snaith, H. J. Perovskites: The Emergence of a New Era for Low-Cost, High-Efficiency Solar Cells. *J. Phys. Chem. Lett.* **2013**, *4* (21), 3623–3630.

(9) Yang, W. S.; Park, B.-W.; Jung, E. H.; Jeon, N. J.; Kim, Y. C.; Lee, D. U.; Shin, S. S.; Seo, J.; Kim, E. K.; Noh, J. H.; Seok, S. Il. Iodide Management in Formamidinium-Lead-Halide–based Perovskite Layers for Efficient Solar Cells. *Science (80-.).* **2017**, *356* (6345), 1376–1379.

(10) Zhao, J.; Zheng, X.; Deng, Y.; Li, T.; Shao, Y.; Gruverman, A.; Shield, J.; Huang, J. Is Cu a Stable Electrode Material in Hybrid Perovskite Solar Cells for a 30-Year Lifetime? *Energy Environ. Sci.* **2016**, *9* (12), 3650–3656.

(11) Jain, S. M.; Qiu, Z.; Häggman, L.; Mirmohades, M.; Johansson, M. B.; Edvinsson, T.; Boschloo, G. Frustrated Lewis Pair-Mediated Recrystallization of CH 3 NH 3 PbI 3 for Improved Optoelectronic Quality and High Voltage Planar Perovskite Solar Cells. *Energy Environ. Sci.* **2016**, *9* (12), 3770–3782.

(12) Kojima, A.; Teshima, K.; Shirai, Y.; Miyasaka, T. Organometal Halide Perovskites as Visible-Light Sensitizers for Photovoltaic Cells. *J. Am. Chem. Soc.* **2009**, *131* (17), 6050–6051.

(13) Brunetti, B.; Cavallo, C.; Ciccioli, A.; Gigli, G.; Latini, A. On the Thermal and Thermodynamic (In)Stability of Methylammonium Lead Halide Perovskites. *Sci. Rep.* **2016**, *6*, 6050–6051.

(14) Zhao, L.; Kerner, R. A.; Xiao, Z.; Lin, Y. L.; Lee, K. M.; Schwartz, J.; Rand, B. P. Redox Chemistry Dominates the Degradation and Decomposition of Metal Halide Perovskite Optoelectronic Devices. *ACS Energy Lett.* **2016**, *1* (3), 595–602.

(15) Nagabhushana, G. P.; Shivaramaiah, R.; Navrotsky, A. Direct Calorimetric Verification of Thermodynamic Instability of Lead Halide Hybrid Perovskites. *Proc. Natl. Acad. Sci.* **2016**, *113* (28), 7717–7721.

(16) Stoumpos, C. C.; Malliakas, C. D.; Kanatzidis, M. G. Semiconducting Tin and Lead Iodide Perovskites with Organic Cations: Phase Transitions, High Mobilities, and near-Infrared Photoluminescent Properties. *Inorg. Chem.* **2013**, *52* (15), 9019–9038.

(17) Baikie, T.; Fang, Y.; Kadro, J. M.; Schreyer, M.; Wei, F.; Mhaisalkar, S. G.; Graetzel, M.; White, T. J. Synthesis and Crystal Chemistry of the Hybrid Perovskite (CH3NH3)PbI3 for Solid-State Sensitised Solar Cell Applications. *J. Mater. Chem. A* **2013**, *1* (18), 5628.

(18) Gesi, K. Effect of Hydrostatic Pressure on the Structural Phase Transitions in CH 3 NH 3 PbX 3 (X = Cl, Br, I). *Ferroelectrics* **1997**, *203* (1), 249–268.

(19) Onoda-Yamamuro, N.; Yamamuro, O.; Matsuo, T.; Suga, H. P-T Phase Relations of CH3NH3PbX3 (X = Cl, Br, I) Crystals. *J. Phys. Chem. Solids* **1992**, *53* (2), 277–281.

(20) Weber, D. CH3NH3PbX3, a Pb(II)-System with Cubic Perovskite Structure. *Zeitschrift für Naturforsch. B* **1978**, *33b* (August 1978), 1443–1445.

(21) Weller, M. T.; Weber, O. J.; Henry, P. F.; Di Pumpo, A. M.; Hansen, T. C. Complete Structure and Cation Orientation in the Perovskite Photovoltaic Methylammonium Lead Iodide between 100 and 352 K. *Chem. Commun.* **2015**, *51* (20), 4180–4183.

(22) Swainson, I. P.; Hammond, R. P.; Soullière, C.; Knop, O.; Massa, W. Phase Transitions in the Perovskite Methylammonium Lead Bromide, CH3ND3PbBr3. *J. Solid State Chem.* **2003**, *176* (1), 97–104.

(23) Whitfield, P. S.; Herron, N.; Guise, W. E.; Page, K.; Cheng, Y. Q.; Milas, I.; Crawford, M. K. Structures, Phase Transitions and Tricritical Behavior of the Hybrid Perovskite Methyl Ammonium Lead Iodide. *Sci. Rep.* **2016**, *6*, 35685.

(24) Moller, C. K. Crystal Structure and Photoconductivity of Cæsium Plumbohalides. *Nature* **1958**, *182* (4647), 1436–1436.

(25) Weller, M. T.; Weber, O. J.; Frost, J. M.; Walsh, A. Cubic Perovskite Structure of Black Formamidinium Lead Iodide, α-[HC(NH2)2]PbI3, at 298 K. *J. Phys. Chem. Lett.* **2015**, *6*, 3209–3212.

(26) Sun, S.; Deng, Z.; Wu, Y.; Wei, F.; Halis Isikgor, F.; Brivio, F.; Gaultois, M. W.; Ouyang, J.; Bristowe, P. D.; Cheetham, A. K.; Kieslich, G.; Bein, T. B.; Snaith, H. J.; Friend, R. H.; Mao, H.-K. Variable Temperature and High-Pressure Crystal Chemistry of Perovskite Formamidinium Lead Iodide: A Single Crystal X-Ray Diffraction and Computational Study. *Chem. Commun.* **2017**, *53* (54), 7537–7540.

(27) Fabini, D. H.; Stoumpos, C. C.; Laurita, G.; Kaltzoglou, A.; Kontos, A. G.; Falaras, P.; Kanatzidis, M. G.; Seshadri, R. Reentrant Structural and Optical Properties and Large Positive Thermal Expansion in Perovskite Formamidinium Lead Iodide. *Angew. Chemie Int. Ed.* **2016**, *55* (49), 15392–15396.

(28) Chen, T.; Foley, B. J.; Park, C.; Brown, C. M.; Harriger, L. W.; Lee, J.; Ruff, J.; Yoon, M.; Choi, J. J.; Lee, S.-H. Entropy-Driven Structural Transition and Kinetic Trapping in Formamidinium Lead Iodide Perovskite. *Sci. Adv.* **2016**, *2* (10), e1601650.

(29) Chen, T.; Chen, W.-L.; Foley, B. J.; Lee, J.; Ruff, J. P. C.; Ko, J. Y. P.; Brown, C. M.; Harriger, L. W.; Zhang, D.; Park, C.; Yoon, M.; Chang, Y.-M.; Choi, J. J.; Lee, S.-H. Origin of Long Lifetime of

Band-Edge Charge Carriers in Organic–inorganic Lead Iodide Perovskites. *Proc. Natl. Acad. Sci.* **2017**, *114*, 7519–7524.

(30) Fabini, D. H.; Siaw, T. A.; Stoumpos, C. C.; Laurita, G.; Olds, D.; Page, K.; Hu, J. G.; Kanatzidis, M. G.; Han, S.; Seshadri, R. Universal Dynamics of Molecular Reorientation in Hybrid Lead Iodide Perovskites. *J. Am. Chem. Soc.* **2017**, *139* (46), 16875–16884.

(31) Fabini, D. H.; Hogan, T.; Evans, H. A.; Stoumpos, C. C.; Kanatzidis, M. G.; Seshadri, R. Dielectric and Thermodynamic Signatures of Low-Temperature Glassy Dynamics in the Hybrid Perovskites $CH_3NH_3PbI_3$ and $HC(NH_2)_2PbI_3$. *J. Phys. Chem. Lett.* **2016**, *7* (3), 376–381.

(32) Mozur, E. M.; Maughan, A. E.; Cheng, Y.; Huq, A.; Jalarvo, N.; Daemen, L. L.; Neilson, J. R. Orientational Glass Formation in Substituted Hybrid Perovskites. *Chem. Mater.* **2017**, *29* (23), 10168–10177.

(33) Hansen, T. C.; Henry, P. F.; Fischer, H. E.; Torregrossa, J.; Convert, P. The D20 Instrument at the ILL: A Versatile High-Intensity Two-Axis Neutron Diffractometer. *Meas. Sci. Technol.* **2008**, *19* (3), 34001.

(34) Day, P.; Enderby, J.; Williams, W.; Chapon, L.; Hannon, A.; Radaelli, P.; Soper, A. Scientific Reviews: GEM: The General Materials Diffractometer at ISIS-Multibank Capabilities for Studying Crystalline and Disordered Materials. *Neutron News* **2004**, *15* (1), 19–23.

(35) Perdew, J. P.; Burke, K.; Ernzerhof, M. Generalized Gradient Approximation Made Simple. *Phys. Rev. Lett.* **1996**, *77* (18), 3865–3868.

(36) Kresse, G.; Joubert, D. From Ultrasoft Pseudopotentials to the Projector Augmented-Wave Method. *Phys. Rev. B* **1999**, *59* (3), 1758–1775.

(37) Thonhauser, T.; Cooper, V. R.; Li, S.; Puzder, A.; Hyldgaard, P.; Langreth, D. C. Van Der Waals Density Functional: Self-Consistent Potential and the Nature of the van Der Waals Bond. *Phys. Rev. B* **2007**, *76* (12), 125112.

(38) Klimeš, J.; Bowler, D. R.; Michaelides, A. Chemical Accuracy for the van Der Waals Density Functional. *J. Phys. Condens. Matter* **2010**, *22* (2), 22201.

(39) Chai, J.-D.; Head-Gordon, M. Systematic Optimization of Long-Range Corrected Hybrid Density Functionals. *J. Chem. Phys.* **2008**, *128* (8), 84106.

(40) VandeVondele, J.; Krack, M.; Mohamed, F.; Parrinello, M.; Chassaing, T.; Hutter, J. Quickstep: Fast and Accurate Density Functional Calculations Using a Mixed Gaussian and Plane Waves Approach. *Comput. Phys. Commun.* **2005**, *167* (2), 103–128.

(41) Goedecker, S.; Teter, M.; Hutter, J. Separable Dual-Space Gaussian Pseudopotentials. *Phys. Rev. B* **1996**, *54* (3), 1703–1710.

(42) Perdew, J. P.; Ruzsinszky, A.; Csonka, G. I.; Vydrov, O. A.; Scuseria, G. E.; Constantin, L. A.; Zhou, X.; Burke, K. Restoring the Density-Gradient Expansion for Exchange in Solids and Surfaces. *Phys. Rev. Lett.* **2008**, *100* (13), 136406.

(43) Grimme, S.; Antony, J.; Ehrlich, S.; Krieg, H. A Consistent and Accurate *Ab Initio* Parametrization of Density Functional Dispersion Correction (DFT-D) for the 94 Elements H-Pu. *J. Chem. Phys.* **2010**, *132* (15), 154104.

(44) Aristidou, N.; Eames, C.; Sanchez-Molina, I.; Bu, X.; Kosco, J.; Islam, M. S.; Haque, S. A. Fast Oxygen Diffusion and Iodide Defects Mediate Oxygen-Induced Degradation of Perovskite Solar Cells. *Nat. Commun.* **2017**, *8*, 15218.

(45) Charles, B.; Dillon, J.; Weber, O. J.; Islam, M. S.; Weller, M. T. Understanding the Stability of Mixed A-Cation Lead Iodide Perovskites. *J. Mater. Chem. A* **2017**, *5* (43), 22495–22499.

(46) Ghosh, D.; Walsh Atkins, P.; Islam, M. S.; Walker, A. B.; Eames, C. Good Vibrations: Locking of Octahedral Tilting in Mixed-Cation Iodide Perovskites for Solar Cells. *ACS Energy Lett.* **2017**, *2* (10), 2424–2429.

(47) Mattoni, A.; Filippetti, A.; Caddeo, C. Modeling Hybrid Perovskites by Molecular Dynamics. *J. Phys. Condens. Matter* **2017**, *29* (4), 43001.

(48) Lahnsteiner, J.; Kresse, G.; Kumar, A.; Sarma, D. D.; Franchini, C.; Bokdam, M. Room-Temperature Dynamic Correlation between Methylammonium Molecules in Lead-Iodine Based Perovskites: An *Ab Initio* Molecular Dynamics Perspective. *Phys. Rev. B* **2016**, *94* (21), 214114.

(49) Mattoni, A.; Filippetti, A.; Saba, M. I.; Delugas, P. Methylammonium Rotational Dynamics in Lead Halide Perovskite by Classical Molecular Dynamics: The Role of Temperature. *J. Phys. Chem. C* **2015**, *119* (30), 17421–17428.

(50) Wright, A. D.; Verdi, C.; Milot, R. L.; Eperon, G. E.; Perez-Osorio, M.; Snaith, H. J.; Giustino, F.; Johnston, M. B.; Herz, L. M. Electron–phonon Coupling in Hybrid Lead Halide Perovskites. *Nat. Commun.* **2016**, *7*, 11755.

(51) Guo, Y.; Yaffe, O.; Paley, D. W.; Beecher, A. N.; Hull, T. D.; Szpak, G.; Owen, J. S.; Brus, L. E.; Pimenta, M. A. Interplay between Organic Cations and Inorganic Framework and Incommensurability in Hybrid Lead-Halide Perovskite $CH_3NH_3PbBr_3$. *Phys. Rev. Mater.* **2017**, *1* (4), 42401.

(52) Eperon, G. E.; Paternò, G. M.; Sutton, R. J.; Zampetti, A.; Haghighirad, A. A.; Cacialli, F.; Snaith, H. J. Inorganic Caesium Lead Iodide Perovskite Solar Cells. *J. Mater. Chem. A* **2015**, *3* (39), 19688–19695.

(53) Weller, M. T.; Hansen, T. C.; Henry, P. F.; Marshall, K. L.; Weber, O. J. Hydration and Dehydration of Photovoltaic Methylammonium Lead Iodide. Institut Laue-Langevin 2016, p DOI:10.5291/ill-data.5-24–567.

(54) Weber, O. J.; Henry, P. F.; Weller, M. T.; Da Silva Gonzalez, I.; Charles, B. The Structure of Formamidinium Lead Iodide between 10 and 450 K. STFC ISIS Facility 2016, p DOI:10.5286/ISIS.E.79114391.

Supporting Information

Phase Behaviour and Polymorphism of Formamidinium Lead Iodide

Oliver J. Weber,[a] Dibyajyoti Ghosh,[a,b] Sam Gaines,[a] Paul F. Henry,[c] Alison B. Walker,[b] M. Saiful Islam*[a] and Mark T. Weller*[a]

a) Centre for Sustainable Chemical Technologies and Department of Chemistry, University of Bath, Bath, BA2 7AY, UK. b) Department of Physics, University of Bath, Bath, BA2 7AY, UK.
c) ISIS Neutron and Muon Source, Rutherford Appleton Laboratory, Didcot, Oxfordshire, UK.

* E-mail: M.T.Weller@bath.ac.uk; m.s.islam@bath.ac.uk

List of Figures

List of Tables

Thermochemistry

To investigate the possibility of volatile components leaving the sample during the temperature cycling, thermogravimetric analysis was undertaken on the same sample used for the D20 experiment (Sample 1), with the degradation product outflow coupled to a mass spectrometer (TG-MS). No significant mass loss by TGA or degradation products observed by mass spectrometry until T = 500 K, at which point a single degradation curve leads to 25.8% mass loss. This temperature is 100 K higher than the maximum temperature reached in neutron powder diffraction experiments. Major loss components correspond to molecular weights indicating the potential presence of FA, H_2O, NH_3 and s-triazine.

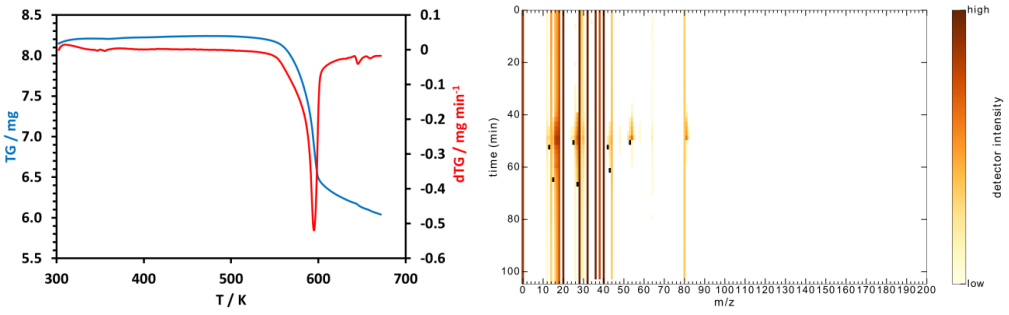

Figure S1. Thermogravimetric analysis and coupled mass spectrometry of Sample 2 of α-$FAPbI_3$-H.

Hexagonal δ-$FAPbI_3$ at 300 K

The room temperature structure of δ-$FAPbI_3$-H was refined against neutron powder diffraction data gathered on D20 diffractometer, ILL. A hexagonal unit cell, space group *P63/mmc* was employed as in Chen et al..[1] The final atomic positions and displacement parameters are given in Table 1. The formamidinium cation was modelled as a rigid body, in which the translation and rotation of the whole molecule were refineable parameters, along with the iodine coordinates and isotropic thermal displacement parameters. C—H, N—H and C—N bond lengths within the organic molecule were each defined as separate parameters and refined with constraints. A Chebyshev polynomial with 6 coefficients was sufficient to fit the background, while TCHZ pseudo-Voigt functions were defined to fit the sample peaks. This model rapidly converged to give a final χ^2 = 1.35 (Figure 2). For comparison, Figure 3 displays Rietveld refinement of the same D20 data using the structural model obtained from single crystal X-Ray diffraction in the reference given, underlining the sensitivity of the neutron refinement to hydrogen positions.[2] Sequential refinement over the temperature range 300-430 K was carried out using SEQGSAS. Variation in lattice parameters and cell volume are plotted in Figure S4.

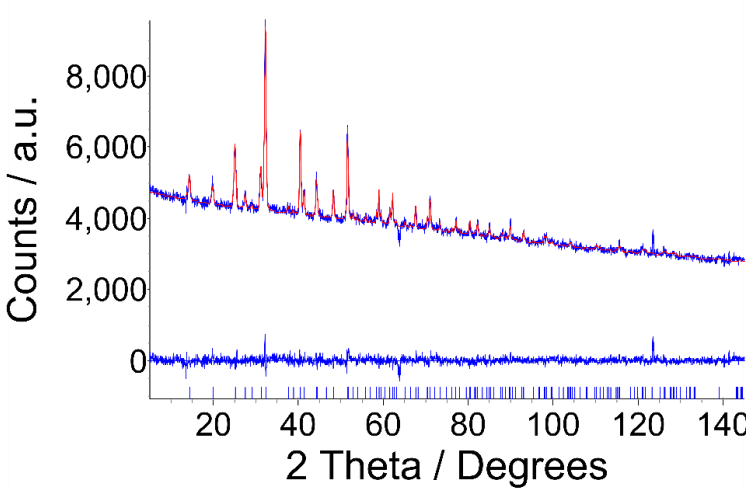

Figure S2. Constant wavelength (λ = 1.8691 Å) neutron powder diffraction collected on D20. Rietveld refinement fit to rigid body model of δ-$FAPbI_3$ at 300 K. a = b = 8.5891 (49) Å, c = 7.853 (71) Å. α = β = 90°, γ = 120°. Space group: *P63/mmc.* Final χ^2 = 1.35. 10 min data collection.

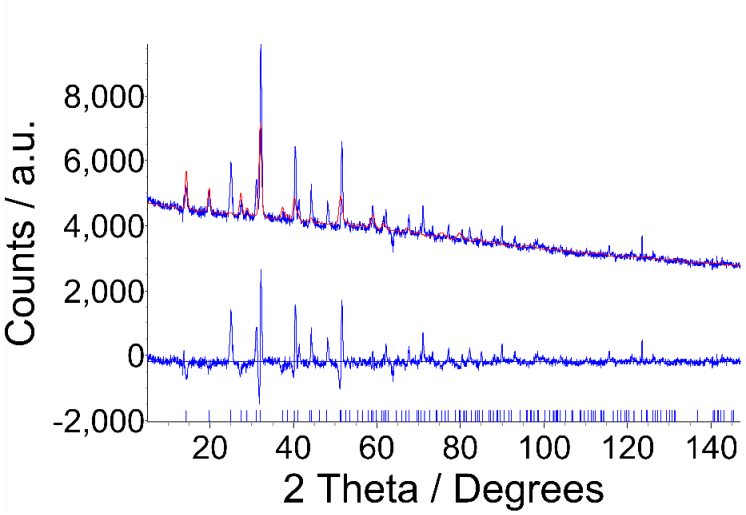

Figure S3. Model of δ-$FAPbI_3$ from (Ref. 2) with no hydrogen positions. Final $\chi^2 = 3.34$. λ = 1.8691 Å.

Table S1. Refined atomic positions and displacement parameters for δ-$FAPbI_3$ at 300 K.

Atom	Site	x	y	z	Occupancy	U_{iso} / Å^2
PB1	*2a*	0	0	0	1	0.0320(26)
I2	*6h*	0.82957(56)	0.17043(56)	0.25	1	0.0507(31)
N3	*24l*	0.2612(43)	0.6414(67)	0.1224(41)	1/12	0.0693(55)
N4	*24l*	0.3518(49)	0.7322(76)	0.3914(43)	1/12	*= N3 Uiso*
C5	*24l*	0.3889(35)	0.7128(39)	0.2351(34)	1/12	*= N3 Uiso*
H6	*24l*	0.5221(39)	0.7548(89)	0.1999(43)	1/12	*= N3 Uiso*
H7	*24l*	0.2261(71)	0.69264(141)	0.4247(57)	1/12	*= N3 Uiso*
H8	*24l*	0.4491(66)	0.7867(73)	0.4774(49)	1/12	*= N3 Uiso*
H9	*24l*	0.2895(59)	0.6266(69)	0.0033(53)	1/12	*= N3 Uiso*
H10	*24l*	0.1355(55)	0.6017(130)	0.1557(56)	1/12	*= N3 Uiso*

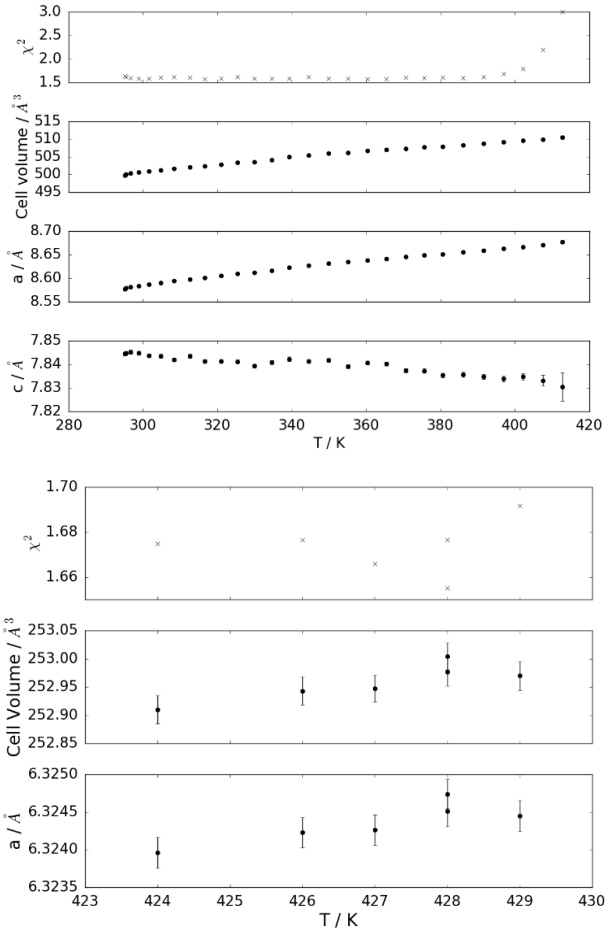

Figure S4. Evolution of lattice parameters and cell volume, in the relevant temperature range, for the hexagonal phase (upper) and cubic phase (lower) for a sample heated from 290 K to 430 K.

Tetragonal β-FAPI at 200 K

Table S2 displays the atomic positions and displacement parameters for final Rietveld refinement of β-$FAPbI_3$, space group *P4/mbm*, a = 8.92312(35), c= 6.3222(47), χ^2 = 1.05. against data collected on GEM diffractometer.

Table S2. Refined atomic positions and displacement parameters for β-FAPI at 200 K against GEM data at 200 K.

Atom	Site	x	y	z	Occupancy	U_{iso} / Å^2
Pb	*2a*	0	0	0	1	0.0227(28)
I1	*2b*	0	0	0.5	1	0.0182(38)
I2	*4g*	0.78586(64)	0.28586(64)	0	1	0.0610(41)
C1	*4f*	0.5	0	0.57638(127)	0.5	0.0883(40)
N1	*16l*	0.57077(78)	0.10716(103)	0.48056(154)	0.25	=C1U_{iso}
H1	*8k*	0.52940(121)	0.97060(121)	0.73117(485)	0.25	=C1U_{iso}
H2	*16l*	0.54568(149)	0.13225(163)	0.34842(369)	0.25	=C1U_{iso}
H3	*16l*	0.64466(191)	0.15595(150)	0.54663(221)	0.25	=C1U_{iso}

Rietveld refinement of the tetragonal phase was also carried out against D20 data. Final fit obtained in TOPAS shown in Figure. This model was refined at every temperature step from 290 to 140 K using SEQGSAS, allowing key structural parameters to vary with each step. One isotropic temperature factor for the organic ion was defined, and the temperature evolution of the iodide coordinates, U_{iso} (organic) and the reduced lattice parameter ratio is plotted in Figure S6. The formamidinium ion was defined as a rigid body comprising C, C---H1, a single N atom and two amine H atoms (H2 and H3). Parameters were defined for C—N, C—H, and N—H bonds, which were refined with constraints, while the rigid body was allowed to translate along the z direction. The lattice parameter ratio converges to unity above 250 K, while the organic temperature factor increases with temperature (Figure S6).

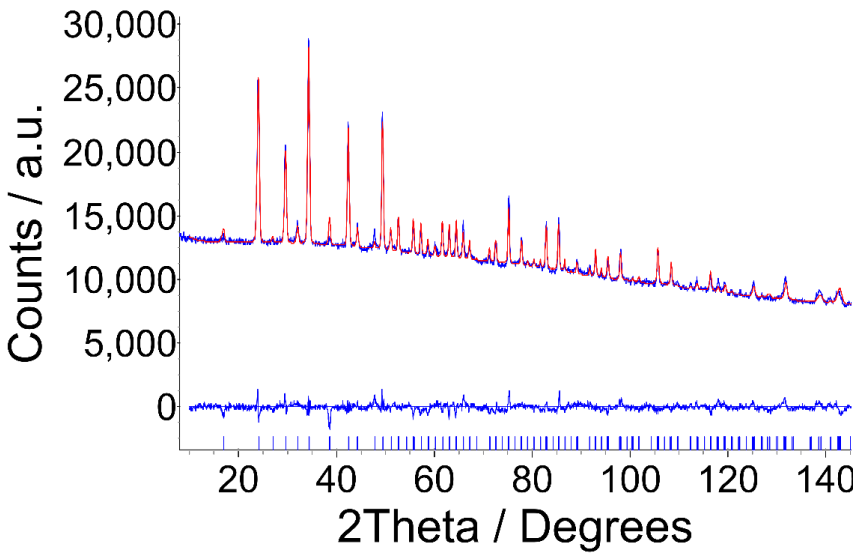

Figure S5. Tetragonal, space group *P4/mbm*, fit to D20 data of β- $FAPbI_3$ at 200 K. Final χ^2 = 2.18.

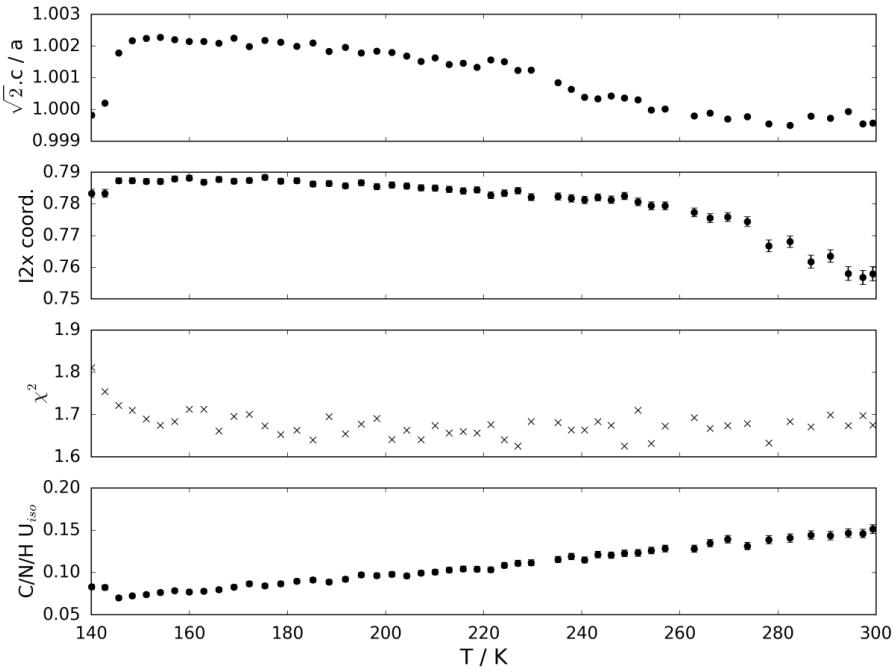

Figure S6. SEQGSAS refinements of D20 data for tetragonal $FAPbI_3$ cooled across the mid-temperature range. Lattice parameters, co-ordinates and isotropic thermal parameter for the FA cation.

γ-FAPI at 100 K

Figure S7 displays a Pawley fit to the 100 K $FAPbI_3$-H data collected on D20 on sample 2. This primitive tetragonal cell leaves observed unindexed reflection intensities, listed in Table S3.

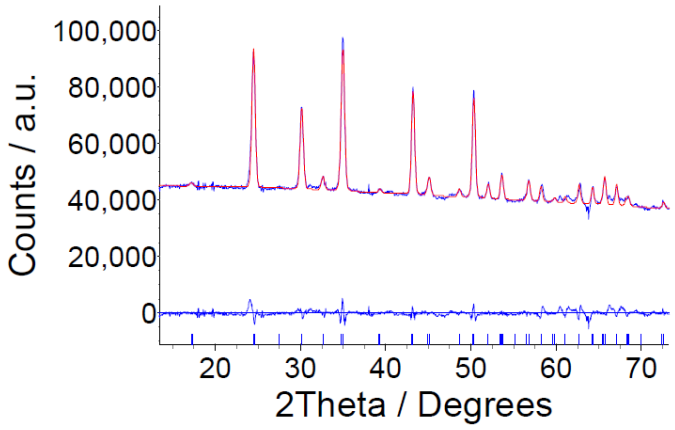

Figure S7. D20 Pawley fit at 100 K to tetragonal P4bm a = 8.788462 Å, c = 6.249353 Å.

Table S3. Unindexed peak reflections for primitive tetragonal cell, space group P4bm, a = 8.788462 Å, c = 6.249353 Å.

2theta	d / Å
66.223	1.711
60.454	1.856
94.580	1.272

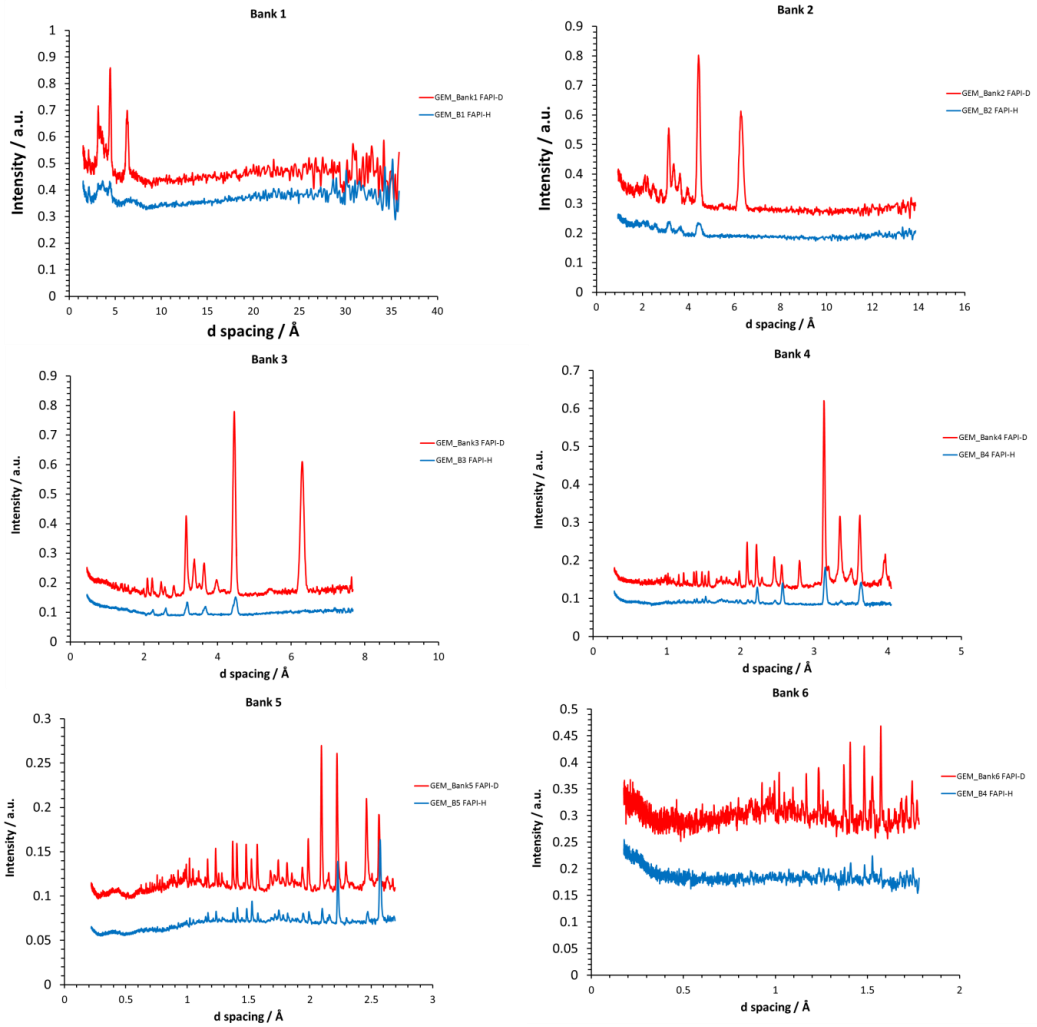

Figure S8. GEM data at 100 K for γ- $FAPbI_3$-H (blue) and γ- $FAPbI_3$-D (red) for detector banks 1-6

Figure S8 compares all the data collected on GEM detector banks 1-6 for deuterated ($FAPbI_3$-D) and hydrogenous ($FAPbI_3$-H) samples at 100 K. A Pawley fit to a multiphase model combining the β-$FAPbI_3$ phase with the low temperature hexagonal polymorph, space group *P63/m*, demonstrates that the additional intensity peaks observed in the low temperature data, for example the peak at 3.2 Å, cannot be satisfactorily indexed to a multiphase model containing both polymorphs.

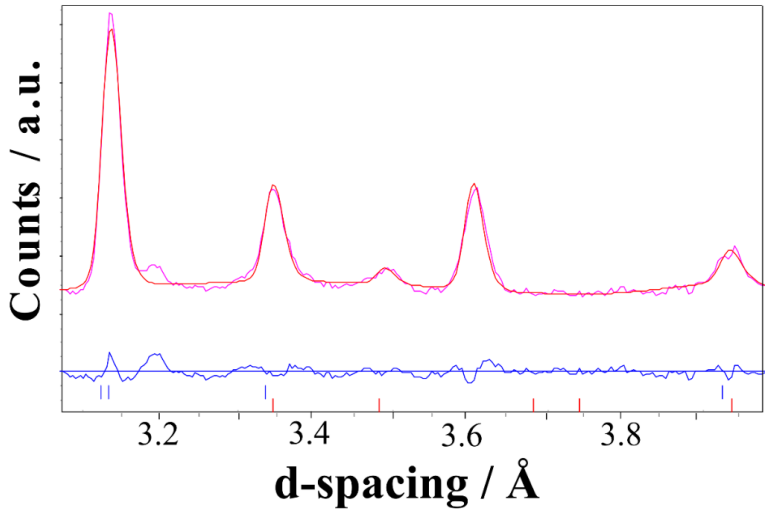

Figure S9. Pawley fit of γ-$FAPbI_3$-D at 100 K, GEM detector bank 4 to a multiphase model of both low temperature polymorphs of $FAPbI_3$. Tetragonal cell, space group *P4/mbm*, a = 8.894 Å, c = 6.3116 Å, (blue ticks). Hexagonal low temperature phase, space group *P6₃/m*, a = 8.548 Å, c = 7.954 Å (red ticks).[1]

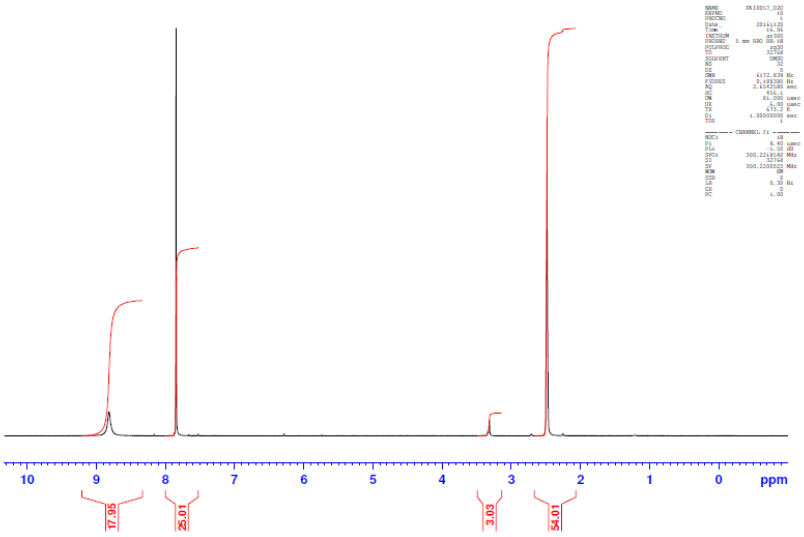

Figure S10. ^{1}H NMR spectrum of deuterated FAI, δ = 8.92 ppm N; δ = 7.83 ppm CH; δ = 7.83 2.48 ppm DMSO.

The ratio of peak integrals (NH/CH ratio) (4-0.718) / 4 = 0.821

These NMR data (SI) indicate the sample was at least 82% N-deuterated, given the possibility of exchange with residual H_2O in the NMR solvent (DMSO-d6). This value agrees well with Rietveld refinement of the mid-temperature tetragonal phase using the H/D stoichiometric ratio as a refineable parameter.

Computational Calculations

I. Computational Details

A. Calculation of optimized structures and energies of different phases of $FAPbI_3$:

In cubic $FAPbI_3$, the cations are rotationally disordered. To model this disorder cations in static DFT-based computations, we performed geometry optimizations starting from 8 randomly generated orientations. We found that the orientation of cations produces small differences in the ground-state energies. We have considered the lowest energy conformation among these structures for further calculations.

For tetragonal and hexagonal $FAPbI_3$, we have considered the cation ordering as suggested by our neutron-scattering experiments for our DFT-based simulations.

While calculating the relative energy differences among the different phases of $FAPbI_3$, we did not consider the vibrational and configurational entropy contributions as these are found not to affect the relative stability trends in the hybrid perovskite materials.[3,4]

B. **Calculation of the reorientational relaxation time:**

To determine the rotational mobility of cations in the cubic and tetragonal $FAPbI_3$, we calculated the average reorientational relaxation time (τ) of these cations. The vector connecting two nitrogen atoms of the FA cations (shown in the inset of Fig. 5c) was considered as the molecular vector, the reorientation of which was investigated. We calculated the reorientational relaxation time by extracting the vector autocorrelation function,

$$c(\tau) = N.\langle \sum_{t=0}^{T-\tau} \boldsymbol{a}_i(t).\boldsymbol{a}_i(t+\tau)\rangle_i$$

where $\boldsymbol{a_i(t)}$ is the molecular vector of i^{th} molecule at time t, T is the total simulation time and N is the normalization factor.

As the vector autocorrelation functions decay non-exponentially, we fit these functions with stretched exponential functions,

$$f(t') = \exp(-t'/\tau)^{\beta}$$

The best fit for the autocorrelation function in the cubic phase found with the parameters, $\beta = 0.64$ and $\tau = 8.84$ ps.

II. Results

A. Optimized geometry of δ-$FAPbI_3$-H:

To verify the experimentally refined structure of δ- $FAPbI_3$-H, first, the internal geometry of it has been optimized by performing DFT simulations. The Pb-I, Pb-Pb, N-H…I bond-lengths and Pb-I-Pb angles match very well with the experimental data and further supports the validity of our claim of finding δ-FAPI-H with a space group *$P6_3/mmc$*.

Table S4. The comparison between the experimentally reported and computationally optimized structural data of **δ- $FAPbI_3$-H.**

	Pb-I (Å)	Pb-Pb (Å)	Pb-I-Pb (deg.)	H_N…I (Å)
Experimental	3.193	3.930	75.87, 75.86	2.75-3.02
Computational	3.192	3.926	75.87, 75.85	2.88, 3.05, 3.13, 3.31

Relaxing the lattice parameters during geometry optimization also results in very similar ground state geometries. The optimized lattice parameters without any constraints are a_0 =8.61Å, b_0 =8.53 Å, c_0= 8.05 Å which is in good agreement with experimentally reported one.

B. Optimized geometry of different phases of $FAPbI_3$-H:

To compare the structure and relative stability of different phases of $FAPbI_3$, we consider the experimental geometries as the initial structure. As the neutron diffraction study gives reliable structural information, here we keep the geometry of inorganic framework fixed and relaxed the FA-cation geometry only. It allows us to simulate the $FAPbI_3$ structures of different phases most resemble corresponding experimental one. The non-covalent hydrogen bond-lengths i.e. H_N … I agree well with the experimental data.

Table S5. The optimized distances (<3.5 Å) between amine hydrogen and iodide anions and the band-gap of $FAPbI_3$ in different phases.

Phase	H_N…I(Å)	Band-gap (eV)
Hexagonal	2.88, 3.21	2.89
Tetragonal	3.07, 3.16, 3.36	1.54
Cubic	2.90, 2.82	1.56

C. Optimized geometry of tetragonal-$FAPbI_3$-H:

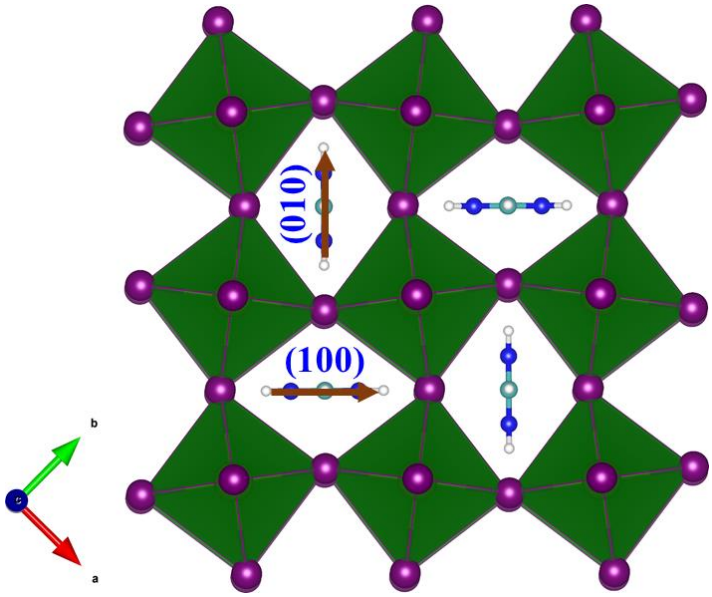

Figure S11. The optimised geometry of tetragonal phase of $FAPbI_3$. The cuboctahedral cages elongate in [100] or [010] lattice directions. The FA cations also orient themselves in that elongated direction, shown by the brown arrow. Note that, as shown in Fig. X in the main text, time-averaged equilibrated structure from *ab initio* molecular dynamics simulations also exhibit similar octahedral tilting pattern and orientation of FA cations inside the cage.

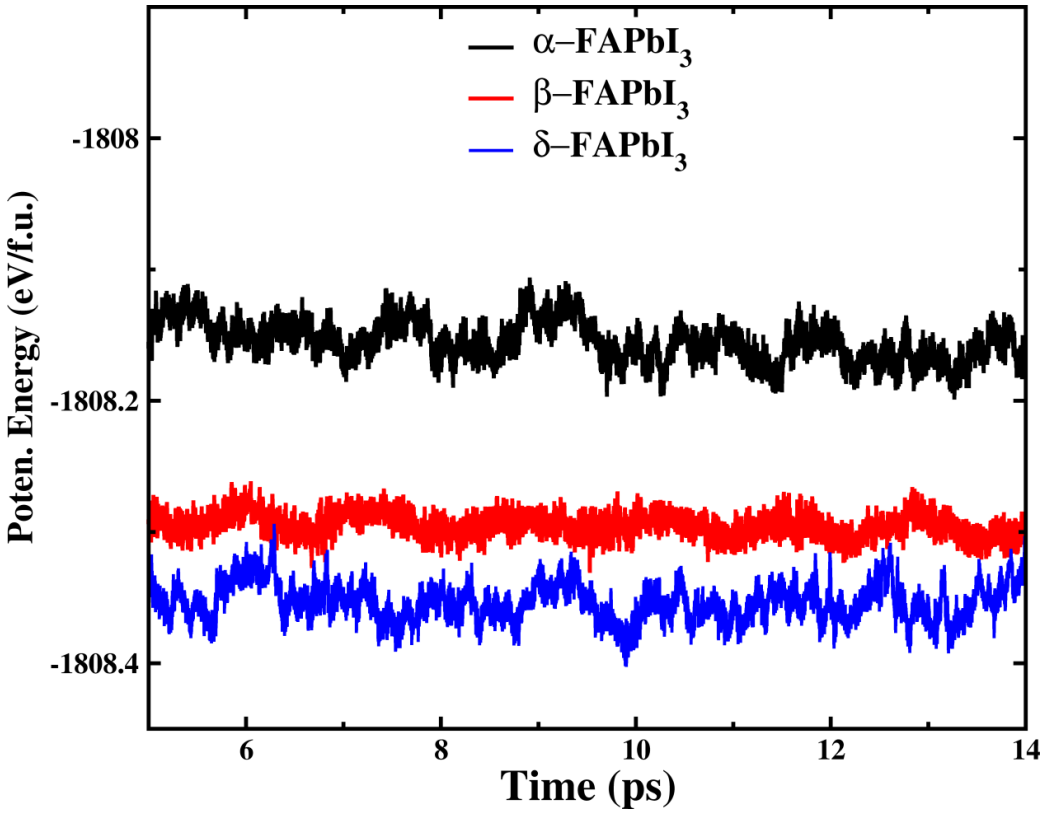

Figure S12: Evolution of potential energy for different phases of $FAPbI_3$ during *ab initio* molecular dynamics simulations. Relative structural stability order i.e. δ-$FAPbI_3$ > β-$FAPbI_3$ > α-$FAPbI_3$ is in line with the experimental results.

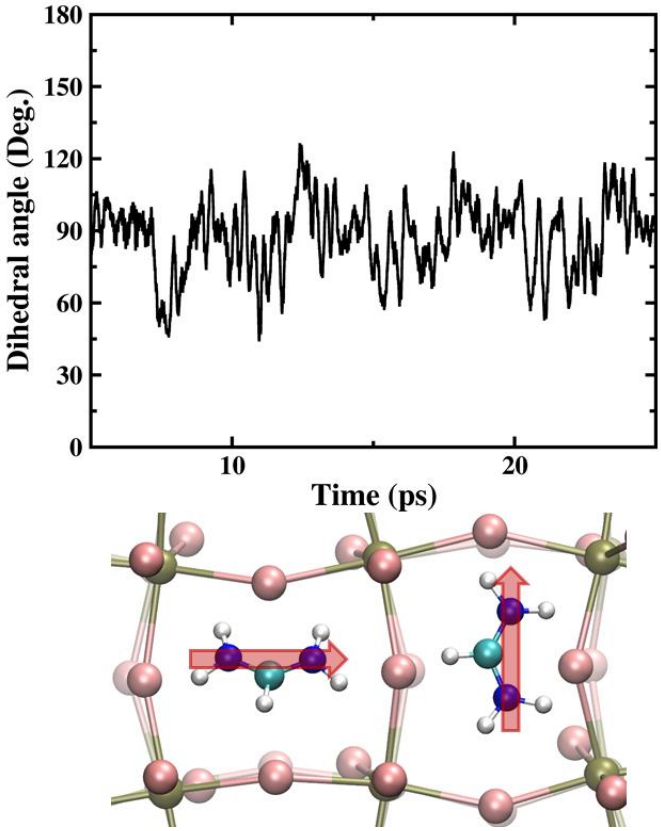

Fig S13. Time evolution of the dihedral angle between two nearest neighbour FA molecules at *ab*-plane in β-$FAPbI_3$ is shown in the upper panel. The molecules were selected randomly. The dihedral angle over time indicate the mutual perpendicular orientation of the cations. The representative orientation of cations at a particular time has been shown in the lower panel. The red arrows indicate the orientation of molecular axis and PbI framework is time-averaged over the simulation time.

1 T. Chen, B. J. Foley, C. Park, C. M. Brown, L. W. Harriger, J. Lee, J. Ruff, M. Yoon, J. J. Choi and S.-H. Lee, Entropy-driven structural transition and kinetic trapping in formamidinium lead iodide perovskite, *Sci. Adv.*, 2016, **2**, e1601650.

2 C. C. Stoumpos, C. D. Malliakas and M. G. Kanatzidis, Semiconducting tin and lead iodide perovskites with organic cations: phase transitions, high mobilities, and near-infrared photoluminescent properties., *Inorg. Chem.*, 2013, **52**, 9019–38.

3 A. S. Thind, X. Huang, J. Sun and R. Mishra, First-Principles Prediction of a Stable Hexagonal Phase of $CH_3NH_3PbI_3$, *Chem. Mater.*, 2017, **29**, 6003–6011.

4 Y.-Y. Zhang, S. Chen, P. Xu, H. Xiang, X.-G. Gong, A. Walsh and S.-H. Wei, Intrinsic Instability of the Hybrid Halide Perovskite Semiconductor CH 3 NH 3 PbI 3, *Chinese Phys. Lett.*, 2018, **35**, 36104.

Chapter 6

Methylammonium / Formamidinium Solid Solutions

This chapter is comprised of the following published work, which is reproduced in its entirety by permission of The Royal Society of Chemistry.

Phase Behaviour and Composition in the Formamidinium-Methylammonium Hybrid Lead Iodide Perovskite Solid Solution. O. J. Weber, B. Charles and M. T. Weller, *J. Mater. Chem. A*, 2016, **4**, 15375-15382. Link to online version:
http://pubs.rsc.org/en/Content/ArticleLanding/2016/TA/C6TA06607K

6.1 Commentary

Following investigation into the phase behaviour of $MAPbI_3$ and $FAPbI_3$ detailed in Chapters 3-5, we decided to investigate the composition phase space between these compounds by forming 'A' site solid solutions. At the time this study, the composition space in between $FAPbI_3$ and $MAPbI_3$ remained poorly characterised for structure and phase behaviour. While previous reports indicated that solid solutions were formable, most of the published work focused solely on thin films, with limited structural information available.[152,240]

Single crystals were synthesised over the whole composition range $FA_{1-x}MA_xPbI_3$ in steps of $x = 0.1$. Two synthetic methods were compared: solution growth in aqueous hydroiodic acid and inverse solubility solution growth in γ-butyrolactone. The inverse or retrograde solubility method (IS) takes advantage of the fact that in certain solvents and for certain

compositions, hybrid perovskites exhibit a substantial decrease in solubility as the temperature is increased.[147,154,217,241] This unusual property has been theorised to depend on the formation of solvent-molecule complexes in solution. As the temperature is increased, dissociation of solvent complexes increases the concentration of unbound molecules, leading to supersaturation and precipitation of crystalline material. Whereas the aqueous acid method is more versatile for crystallisation of various hybrid perovskite, the inverse solubility method is highly composition specific. However very corrosive environment (HI, 7.57 M) and extended exposure to acidic conditions will degrade FAI to NH_4I, as detailed in Chapter 5, Figure 4-2a.

While A-site substitution has only a small effect on the optical band gap, solid solutions display superior stability both in their phase stability, with respect to polymorphism, and also towards external environmental factors. Geometrical tolerance factors certainly play a role in the observed phase behaviour and stability, along with an entropic contribution from the configurational entropy of cation mixing.[242] The effective radius r_{eff} for pseudo-spherical disordered MA^+ has been calculated to be 2.16 Åand FA^+ $r_{eff} = 2.53$ Å.[243] Using the revised ionic radii of Travis et al.,[112] for a lead iodide framework of VI coordinate Pb^{2+} the ionic radius for Pb is $r_{ion} = 1.03$ Å and iodide $I^- = 2.20$ Å. From consideration of the Goldschmidt tolerance factor, the ideal radius for an ion occupying the 'A' site in a lead iodide perovskite structure is 2.37 Å. This being in between the values of MA and FA, solid solutions would be expected to tune the tolerance factor closer to unity, resulting in a cubic perovskite phase, as is observed. Local strain in one unit cell from occupancy of an A-site cation that is larger than ideal can be relieved by smaller A-site cations in adjacent cells. Improved crystallinity in perovskite solid solutions has been shown to be intimately linked to observed stability and lack of hysteretic behaviour in devices.[91]

Determination of actual compositions of the A-site solutions had not been previously reported before this study. For B-site or X-site substitutions of heavy atoms, techniques such as EDX or XRF are highly appropriate for quantitative determination of atomic composition, however this is not the case for A-site substitution between two similar organic cations. We therefore turned to solution ^{1}H NMR, dissolving up 10 mg powder samples in deuterated polar solvents such as dimethyl sulfoxide-d6 (d6-DMSO). Measurement of NMR peak integrals for MA and FA cations proved to be a sensitive quantitative probe to determine atomic composition in these solid solutions. This appears to be the first study to employ this technique for the quantitative chemical composition analysis of hybrid perovskite A-site solid solutions. The correlation between linear increase in lattice parameters, determined by powder and single crystal XRD, and the cation ratio determined by solution ^{1}H NMR provided evidence that the composition of the solid solution precisely matched

the concentration of the reactants.

The optical band gap variation, measured using reflectance spectroscopy, is also shown to match the expected phase behaviour. A linear shift in band gap is observed across the composition range that present as cubic to XRD techniques at room temperature, while deviation from this linear trend was observed for $MAPbI_3$ and $MA_{0.1}FA_{0.9}PbI_3$, which present as tetragonal (as shown in Figure 3a of the following paper). This observation is in agreement with previous theory, which indicates that rather than contribute directly to the electronic density of states either side of the optical band gap, A-site cations influence the band gap by affecting the bond angles in the inorganic lattice, on account of the steric size of the cation and its specific directional interactions with the lattice via hydrogen bonds.[244] The tetragonal to cubic (or quasi-cubic) has been shown to induce marked differences in the electronic and optical properties of perovskite materials, which underlie the high performance solar cells observed for FA-rich compositions.[66,229]

One question arising from formation of quite complex compositions of hybrid perovskites is whether these intermix on the atomic scale, or phase segregate into regions enriched in particular ions. XRD, as carried out in this study, does not provide categorical evidence in the situation, as for MA/FA, both dynamically disordered cations within a heavy atom lattice are composed of the same light elements C, N and H and indistinguishable by X-ray diffraction. Solid state MAS NMR using a range of isotopes (^{133}Cs, ^{87}Rb, ^{13}C, ^{14}1, ^{2}H, ^{207}Pb) has proven a very useful technique in studying the microscopic phase composition and cation reorientation dynamics within these materials.[78,117] Results from MAS NMR studies indicate that MA/FA solid solutions are indeed intermixed at the atomic scale, though reorientation of the FA molecular dipole has been shown to be faster than MA.[78] Compositions for thin film solar cells employ as many as four A-site cations: MA, FA, Cs and Rb, though there is increasing evidence that Rb^+ cations are not distributed within the bulk structure.[117,245]

6.2 Phase Behaviour and Composition in the FA-MA Hybrid Lead Iodide Perovskite Solid Solution

The following paper is reproduced in full from the original publication and spans thesis pages 148-161.

Statement of Authorship

This declaration concerns the article entitled:									
Phase Behaviour and Composition in the Formamidinium-Methylammonium Hybrid Lead Iodide Perovskite Solid Solution									
Publication status (tick one)									
draft manuscript		**Submitted**		**In review**		**Accepted**		**Published**	✓
Publication details (reference)	O. J. Weber, B. Charles and M. T. Weller, *J. Mater. Chem. A*, 2016, **4**, 15375–15382.								
Candidate's contribution to the paper (detailed, and also given as a percentage).	The candidate contributed to/ considerably contributed to/predominantly executed the… Formulation of ideas: MTW, OJW and BC all contributed to defining the project. Design of methodology: OJW developed the synthetic techniques and analysis, assisted by BC. Experimental work: OJW and BC synthesised samples and collected PXRD. OJW analysed the PXRD, single crystal and NMR data. Presentation of data in journal format: OJW wrote the paper in journal format. BC produced supporting info Figure 2.								
Statement from Candidate	This paper reports on original research I conducted during the period of my Higher Degree by Research candidature.								
Signed						**Date**			

Journal of Materials Chemistry A

PAPER

View Article Online
View Journal | View Issue

Cite this: J. Mater. Chem. A, 2016, 4, 15375

Phase behaviour and composition in the formamidinium–methylammonium hybrid lead iodide perovskite solid solution†

O. J. Weber, B. Charles and M. T. Weller*

Received 2nd August 2016
Accepted 8th September 2016

DOI: 10.1039/c6ta06607k

www.rsc.org/MaterialsA

The phase behaviour of mixed A-site cation methylammonium (MA)/formamidinium (FA) lead iodide hybrid perovskites $FA_xMA_{1-x}PbI_3$ has been investigated using powder and variable temperature single crystal X-ray diffraction, with A site composition determined by ^1H solution NMR. At room temperature, the crystal class is cubic across the composition range $0.2 \leq x \leq 1$ but a tetragonal phase is observed for $x = 0$ ($MAPbI_3$) and $x = 0.1$. Cooling cubic $FA_xMA_{1-x}PbI_3$, $0.2 \leq x \leq 1$, phases below room temperature results in a phase change to a larger unit cell with tilted [PbI_6] octahedra and the temperature at which this occurs, $T_{C\rightarrow T}$, decreases sharply until $x = 0.2$ ($T_{C\rightarrow T} = 257$ K) before steadily increasing to $T_{C\rightarrow T} = 283$ K for $FA_{0.9}MA_{0.1}PbI_3$. The lattice parameters and optical band gap of cubic $FA_xMA_{1-x}PbI_3$, $0.2 \leq x \leq 1$ at 298 K have been shown to vary in accordance with Vegard's law, though a larger band gap is observed for the tetragonal phases, $0.0 \leq x \leq 0.1$.

Introduction

Lead halide hybrid perovskites have swiftly become an important class of materials for optoelectronic devices, most notably in high efficiency (>20%) thin film solar cells.[1] While the bulk of this intensive research has focused on methylammonium (MA) lead iodide (MAPI), increasing attention is being paid to formamidinium (FA) lead iodide (FAPI) and solid solutions between these two compounds. The ease of synthesis of A, B and X site solid solutions from the ABX_3 hybrid or inorganic perovskite family provides an effective and simple route to control their physical properties. Impressive solar cell efficiencies and greater stability, upon which successful deployment of hybrid perovskite technologies may well depend, have been reported for site-substituted solid solutions compared to the parent compounds.[2–5] Some of the highest cell efficiencies have been reported for MA/FA and I/Br mixtures (20.8%),[6] while triple A-site cation MA/FA/Cs, X-site I/Br, cells have displayed stabilised 18% power output for 250 hours.[7]

Despite the recent champion performance of mixed cation MA/FA solar cells, A-site mixtures are the least well studied system for any site-substitution within hybrid perovskites and remain poorly characterised with respect to their structure and true composition. This reflects the challenges of obtaining structural information on the organic components of hybrid perovskites using conventional laboratory X-ray sources in the presence of the heavy atoms Pb and I.

Recently the composition space of FA/MA and I/Br perovskites has been explored by Jacobsson *et al.*,[8] and Yang *et al.*,[9] who demonstrate the linear dependence of lattice parameter and band gap for FA/MA mixtures. However, in both cases the crystal systems of the thin film samples were not definitively determined and the compositions of as-deposited mixed cation/anion compounds were assumed, as throughout device literature, to reflect initial concentrations of the reactants in solution. In fact uptake of MA^+ and FA^+ and crystallisation of a solid solution $FA_xMA_{1-x}PbI_3$, $0 < x < 1$ may not reflect the solution concentrations. Furthermore incorporation of MA^+ and FA^+ cations may be strongly method dependent, resulting in notionally identical compounds with, in reality, very different optoelectronic performance. In addition, structure determination by powder X-ray diffraction is correspondingly more difficult for the thin, potentially highly oriented and textured films, used in solar cells, than for bulk materials.

FAPI and $FAPbI_yBr_{3-y}$ were originally characterised as adopting tetragonal unit cells,[10] and Noh *et al.* have reported a transition from tetragonal to cubic $MAPbI_yBr_{1-y}$ above $y = 0.13$.[11] The perovskite α-phase of FAPI has also been refined as trigonal from single crystal X-ray diffraction (SXD).[12] However, we have previously shown the structure of α-FAPI to be cubic at room temperature, space group $Pm\bar{3}m$, using high resolution neutron powder diffraction data, with the FA ion fully rotationally

Department of Chemistry and Centre for Sustainable Chemical Technologies, University of Bath, Claverton Down, Bath, BA2 7AY, UK. E-mail: m.t.weller@bath.ac.uk

† Electronic supplementary information (ESI) available: Reactant quantities used for crystal synthesis, Tables S1 & S2. SXD lattice parameters for every composition at 300 K, Table S3. NMR spectra, assignments and integrals, Fig. S1. PXD patterns for every composition, Fig. S2. CELREF unit cell refinements for $FA_{0.1}MA_{0.9}PbI_3$, Fig. S3. Pawley fits to cubic $Pm\bar{3}m$ PXD patterns, Fig. S4. Pawley fits for tetragonal and cubic unit cells for $FA_{0.1}MA_{0.9}PbI_3$, Fig. S5. See DOI: 10.1039/c6ta06607k

disordered,[13] a more recent SXD refinement study also adopts this cubic cell.[14] Neutron diffraction is far more sensitive to light atom positions than X-ray methods, for which the similarity of $[PbI_3]^-$ lattice between cubic and trigonal models generate near identical powder X-ray diffraction (XRD) patterns. MAPI, in contrast, is tetragonal at 298 K, adopting the space group *I*4/*mcm*, with a reduced lattice parameter splitting ($c/\sqrt{2} \times a$) of approximately 1% and the organic cation disordered in the ab plane.[15] The a and c lattice vectors of tetragonal MAPI converge on heating to 327 K to form the cubic $Pm\bar{3}m$ phase, with a fully disordered central organic cation.

The structural behaviour in the system $FA_xMA_{1-x}PbI_3$, $0 < x < 1$, between the two end member phases MAPI and FAPI, has not previously been analysed in detail. However, this is of direct and crucial interest for the technological application of these materials due to the apparent increase in material stability and device performance of mixed cation systems. Density functional theory calculations[16] and calorimetric measurements[17] have revealed MAPI to have a positive enthalpy of formation with respect to disproportionation into its binary components PbI_2 and MAI, meaning that even with perfect protection from atmospheric conditions, devices with a single phase $MAPbI_3$ active layer may be fundamentally unstable in the long term. It is, however, notable that $MAPbI_3$ is readily formed from solid PbI_2 and MAI as soon as these components are brought into contact, suggesting experimentally this process to be energetically favourable. For a thermodynamically open system, MAPI decomposition to lead(II) iodide, methylamine and HI can occur *via* loss of volatile components, as evidenced by non-ambient X-ray diffraction and Knudsen effusion-mass spectrometry measurements at 60 °C.[18]

The high susceptibility of MAPI to hydrolytic degradation is well established.[19] A solar cell with effective encapsulation, or appropriate device layers, could both block water ingress and volatile perovskite component egress (as a closed system); however, other degradation pathways may still remain from chemical interaction of MAPI with the other device layers. Redox chemistry between metal (Ag, Al, Cr) contacts and MAPI has been shown to contribute to degradation in MAPI LEDs,[20] while the exact contribution of ion migration within MAPI to cell degradation remains to be better evaluated.

At the other end of the composition range, FAPI, a further problem is encountered. During the synthesis and deposition of cubic FAPI (α-phase), a competing yellow, non-perovskite δ-phase forms preferentially at room temperature, with the level generated dependent on the synthetic route and local chemical/strain environment. Theory has indicated that MA/FA solid solutions should be thermodynamically more stable,[16] and form the perovskite α-phase at room temperature with no competing non-perovskite δ-phase, which is indeed observed experimentally.[21] Such materials would be strongly preferred for technological applications, as is becoming increasingly apparent in the device literature, including high efficiency solar cells[2,5,6] and nanowire lasers.[3] Solid solutions of $FA_xCs_{1-x}PbI_3$ have similarly displayed stabilisation of the cubic perovskite phase, with respect to the room temperature non-perovskite phases of the parent compounds.[22] A further aspect of solar cell devices is that for many applications they will need to operate over a large temperature range and so an understanding of changes in structure, and therefore optoelectronic properties, of the absorber material as a function of temperature is needed.

Herein we report the detailed analysis of mixed cation structures in the $FA_xMA_{1-x}PbI_3$ $x = 0$–1.0 system using variable temperature single crystal (VT-SXD) and powder (PXD) X-ray diffraction, solution NMR analysis of composition and UV-Vis spectroscopy. Two different methods for preparing the hybrid perovskites in this solid solution, namely precipitation from aqueous hydroiodic acid and inverse solubility crystallisation in γ-butyrolactone, have been employed and the compositions and lattice parameters are compared to ensure equivalence between the two methods. Materials with the nominal compositions, based on the reactant concentrations, $FA_xMA_{1-x}PbI_3$ $0 \leq x \leq 1$, with x in 0.1 increments, were synthesised using the two routes described in the Experimental section. The product phases are denoted $FA_xMA_{1-x}PbI_3$ (HI), obtained from cooling in HI, and $FA_xMA_{1-x}PbI_3$ (IS), obtained from inverse solubility in γ-butyrolactone, respectively. Actual product compositions were determined after dissolution by solution ^{1}H NMR.

Experimental

Materials synthesis

All reagents were purchased from Sigma Aldrich, solvents from Alfa Aesar, unless otherwise noted.

Precursor synthesis of methylammonium iodide (MAI) was carried out. 16.620 mL hydroiodic acid (57 wt%, + 1.5 wt% H_3PO_2 stabiliser) was added dropwise to 10.891 mL of methylamine (40 wt% in H_2O) in an ice bath under stirring. After 2 hours H_2O was removed by rotary evaporation and the product was recrystallised from hot ethanol to remove impurities, potentially introduced from H_3PO_2, washed with diethyl ether and oven dried. Formamidinium iodide (FAI) was synthesised in analogous manner using 12.108 g of formamidinium acetate dissolved in 100 mL ethanol, to which 15.36 mL HI was added.

Crystal growth by precipitation from HI mixed cation perovskites, $MA_xFA_{1-x}PbI_3$, were prepared based on the method of Polglitsch and Weber.[23] Methylammonium iodide, formamidinium iodide and lead acetate trihydrate were added to HI(+1.5 wt% H_3PO_2) at 1 M concentration. The solution was heated under nitrogen to 100 °C. The temperature was then gradually lowered to 46 °C. The precipitate of black perovskite crystals was filtered and oven dried at 100 °C overnight. Average yield 55%. Full details of the reaction compositions are provided in the ESI, Table S1.†

Crystal growth by inverse solubility in γ-butyrolactone: following the method of Saidaminov *et al.*[24] Methylammonium iodide, formamidinium iodide and lead iodide were dissolved at 60 °C in γ-butyrolactone at 1 M concentration, filtered using 0.22 μm filters and placed in clean vials. The solutions were initially heated to 110 °C, the temperature was then increased to 120 °C for 1 hour before the solution was filtered and crystals dried in an oven at 100 °C overnight. Full details of the reaction compositions are provided in the ESI, Table S2.†

Characterisation methods

Single crystal X-ray diffraction data were collected on an Agilent SuperNova dual tube Eos S2 CCD diffractometer operating graphite monochromated Mo-Kα (λ = 0.7093 Å) radiation. Variable temperature data were collected in 5 or 15 K steps from 300 K to 150 K. A dwell time of two minutes before each data collection was introduced to ensure a stable temperature. Structure solution and refinement was carried out in WinGX using XPREP and SHELXS-2013 to solve structures by direct methods and SHELXL-2013 for structure refinement.

Powder diffraction patterns were collected on Bruker Advance D8 diffractometer using $Cu_{K\alpha1}$ radiation $\lambda = 1.54060$ Å. CELREF (LMPG)[25] was used to fit peak positions and to refine a cubic unit cell parameter, in space group $Pm\bar{3}m$. A zero point error on each dataset was refined simultaneously with the lattice parameter. Indexing, peak fitting and Pawley refinement were carried out in TOPAS Academic. NMR spectra were collected on an Agilent 300 MHz NMR spectrometer and the spectra were analysed in MNova (Mestrelab). 5 mg of the perovskite was dissolved in d_6-DMSO and the MA/FA ratio within each by comparison of the integrals of the NH_3 group peak of MA (7.47, s) to the NH_2 peaks of FA (8.65, d; 8.99, s).

Results and discussion

Comparison of synthesis methods

Solution ^1H NMR spectra obtained from dissolved $FA_xMA_{1-x}PbI_3$ crystals are displayed in Fig. 1 and the full spectra, integrals and multiplet assignments for MAPI, FAPI and $FA_{0.5}MA_{0.5}PbI_3$ are plotted in the ESI Fig. S1.† The ratio of peak integrals of the characteristic MA and FA cation resonances were compared for each spectrum to determine the stoichiometry of the compound (Table 1). For example for the target $x = 0.1$ ($FA_{0.1}MA_{0.9}PbI_3$), the theoretical ratio of the NMR integrals of the proton resonances for MA : FA is 0.9/0.1 = 9, while the experimentally observed ratios determined from $[NH_3/3]/[(NH_2 + NH_2)/4]$, were found to be 7.98 (HI) and 9.16 (IS), giving x (FA) = 0.11 (HI) and 0.10 (IS). The predicted stoichiometry based on reactant concentration is very close to the ratio of the two organic cations by NMR, within ±0.04 of ideal stoichiometry for every composition.

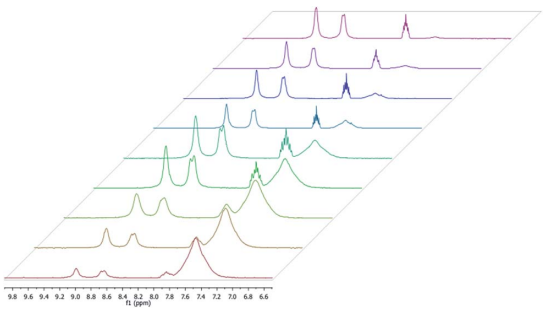

Fig. 1 Sections from ^{1}H solution NMR for $FA_xMA_{1-x}PbI_3$ (HI), for $x = 0.1$ (bottom) to $x = 0.9$ (top) in 0.1 increments. Assignments for MA^+:^{1}H NMR (300 MHz, d_6-DMSO) δ 7.46 (3H, NH_3). FA^+:^{1}H NMR (300 MHz, d_6-DMSO) δ 7.83 (1H, tt, CH), 8.63 (2H, d, NH_2), 8.98 (2H, s, NH_2).

Single crystal X-ray diffraction

The inverse, or retrograde, solubility (IS) crystallisation enabled the growth of large (a few millimetres in each dimension) crystals across the full composition range. Single crystals could also be grown by precipitation from HI, though a prolonged cooling ramp from 100 °C to 46 °C (to avoid hydrate formation in the case of MAPI) is required to grow crystals suitable for single crystal diffraction. For the HI method the crystallite size tended to decrease with increasing formamidinium content. Single crystal X-ray diffraction data were obtained at 300 K for $FA_xMA_{1-x}PbI_3$, $0 < x < 1$, IS method, with the lattice parameter tending to increase along with the amount of the larger organic FA cation (ESI, Table S3†). For the solid solution compositions $FA_xMA_{1-x}PbI_3$, $0.2 < x < 1$, a cubic unit cell with dimensions of approximately 6.3 Å was obtained from the single crystal diffraction data at 300 K. For $FA_{0.1}MA_{0.9}PbI_3$, the 300 K data showed additional reflections and these were preliminarily indexed using a larger, doubled, 12.6 Å cubic unit cell.

Variable temperature single crystal diffraction (VT-SXD) was used to investigate the phase behaviour of solid solutions. Initial experiments were carried out on $FA_{0.5}MA_{0.5}PbI_3$. SXD was carried out in 5 K steps on cooling from 300 K to 150 K. The reduced lattice parameters of $FA_{0.5}MA_{0.5}PbI_3$, as a function of temperature, are plotted in Fig. 2a. A doubling of unit cell parameters for this composition was observed on cooling from 265 to 260 K.

Thermal expansion coefficients are readily extracted from the linear temperature dependence of the cell parameters and volume. For $FA_{0.5}MA_{0.5}PbI_3$ these were found to be $a_L = 7.9 \times 10^{-4}$ K^{-1} for the linear thermal expansion along the lattice vector a (all three directions equivalent for a cubic cell) and $a_V = 2.2 \times 10^{-4}$ K^{-1} for the volumetric expansion coefficient. The expression for the volumetric coefficient is given in eqn (1). The values obtained are higher than the values reported for pure $MAPbI_3$ from powder XRD,[26] which as noted in this reference are up to an order of magnitude higher than typical solar cell substrate materials.

Further variable temperature experiments SXD were carried out in 5 K steps for all other IS synthesis route samples, $FA_xMA_{1-x}PbI_3$, $0 < x < 1$, to identify and locate any phase transition temperature for each composition. On cooling, weak additional diffraction spots in the 0*kl*, *h*0*l* and *hk*0 planes appear at intervals halfway between those of the cubic cell of the 300 K pattern for each composition, indicating formation of a larger unit cell expanded from the high temperature 6.3 Å cubic perovskite phase (Fig. 2b) and suggesting an additional degree of ordering within the low temperature structures. It was found from the VT-SXD patterns that the transition temperature decreases sharply for samples with $x \leq 0.2$ across the rest of the composition range the transition temperature,but then recovers to gradually rise back towards room temperature, Fig. 2c.

$$a_V = \frac{1}{V}\frac{\partial V}{\partial t} \quad (1)$$

Table 1 ^{1}H NMR in d_6-DMSO for each composition of $FA_xMA_{1-x}PbI_3$ comparing the ration of integrals of 1/3 of the NH_3 peak in $CH_3NH_3^+$ (MA^+) to $\frac{1}{4}$ of the two NH_2 peaks of $CH(NH_2)_2^+$ (FA^+), MA : FA = [NH_3/3]/[(NH_2 + NH_2)]/4]. Errors on determined stoichiometries are estimated to be ±0.02

	MA : FA integral ratio			Stoichiometry		
x = FA	theo.	HI(obs)	IS(obs)	theo.	HI(obs)	IS(obs)
0.1	9.000	7.98	9.16	$FA_{0.1}MA_{0.9}PbI_3$	$FA_{0.11}MA_{0.89}PbI_3$	$FA_{0.10}MA_{0.90}PbI_3$
0.2	4.000	3.79	4.70	$FA_{0.2}MA_{0.8}PbI_3$	$FA_{0.21}MA_{0.79}PbI_3$	$FA_{0.18}MA_{0.82}PbI_3$
0.3	2.333	2.53	2.74	$FA_{0.3}MA_{0.7}PbI_3$	$FA_{0.28}MA_{0.72}PbI_3$	$FA_{0.27}MA_{0.73}PbI_3$
0.4	1.500	1.50	1.66	$FA_{0.4}MA_{0.6}PbI_3$	$FA_{0.40}MA_{0.60}PbI_3$	$FA_{0.38}MA_{0.62}PbI_3$
0.5	1.000	0.86	1.07	$FA_{0.5}MA_{0.5}PbI_3$	$FA_{0.54}MA_{0.46}PbI_3$	$FA_{0.48}MA_{0.52}PbI_3$
0.6	0.667	0.68	0.63	$FA_{0.6}MA_{0.4}PbI_3$	$FA_{0.59}MA_{0.41}PbI_3$	$FA_{0.61}MA_{0.39}PbI_3$
0.7	0.429	0.41	0.45	$FA_{0.7}MA_{0.3}PbI_3$	$FA_{0.71}MA_{0.29}PbI_3$	$FA_{0.69}MA_{0.31}PbI_3$
0.8	0.250	0.24	0.22	$FA_{0.8}MA_{0.2}PbI_3$	$FA_{0.81}MA_{0.19}PbI_3$	$FA_{0.82}MA_{0.18}PbI_3$
0.9	0.111	0.12	0.09	$FA_{0.9}MA_{0.1}.PbI_3$	$FA_{0.89}MA_{0.11}PbI_3$	$FA_{0.92}MA_{0.08}PbI_3$

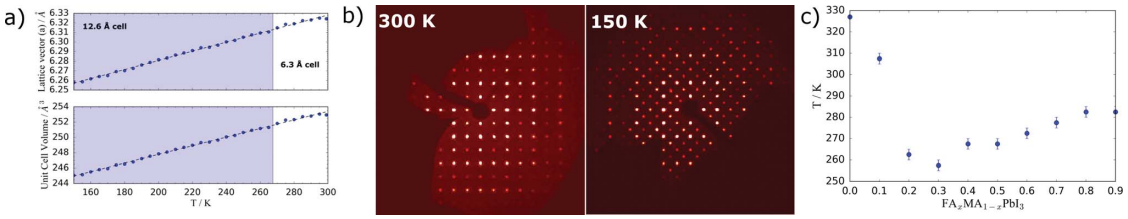

Fig. 2 (a) VT-SXD $FA_{0.5}MA_{0.5}PbI_3$ reduced lattice parameters and cell volume, cooled from 300 K to 150 K in 5 K steps. (b) SXD patterns displaying the *hk*0 plane reflections for $FA_{0.2}MA_{0.8}PbI_3$ at 300 K (6.3 Å unit cell) and 150 K (12.6 Å unit cell). (c) Variation in phase transition temperature from 6.3 Å to 12.6 Å unit cell with composition.

Powder X-ray diffraction

Powder X-ray diffraction (PXD) generally provides less structural information than SXD (where suitable crystals exist). However, ambiguities can arise in the analysis of SXD data for the correct identification of the crystal system after a crystal has undergone twinning caused by a phase transition. In such cases analysis of PXD data can provide a more rapid and clear-cut identification of the crystal system.

PXD patterns ($Cu_{K\alpha}$ radiation, $28° \leq 2\theta \leq 33°$) for the phases with $0 \leq x \leq 0.3$ (HI) are shown in Fig. 3a; full patterns for all compositions are plotted in the ESI (Fig. S2†). In the powder pattern of MAPI, well known to be tetragonal at room temperature, the clear splitting of diffraction peaks at 28.5°, the (004)/(220) reflection pair, and 32° is observed, along with the {213} reflection at 31.1°. For the $x = 0.1$ structure, a weak reflection is seen at $\theta = 31.2°$ and obviously "broader" peaks at 28.5 and 32°, this suggests that a tetragonal cell still exists at room temperature for $x = 0.1$ in $FA_{0.1}MA_{0.9}PbI_3$.

Indexing the $x = 0.1$ PXD data in TOPAS Academic suggested tetragonal *I*4*cm*, cubic *F*23 and trigonal *R*3 cells with high figures of merit. The room temperature tetragonal phase of MAPI crystallises in *I*4/*mcm* (it should be noted that tetragonal space groups *I*4*cm*, *I*4/*mcm* and $I\bar{4}c2$ all have identical reflection conditions and hence generate identical *hkl* possibilities in PXD patterns). The predicted diffraction pattern peak positions in CELREF are shown in the ESI Fig. S3.† The reduced lattice parameter ratio, $\gamma = (c/\sqrt{2} \times a)$,

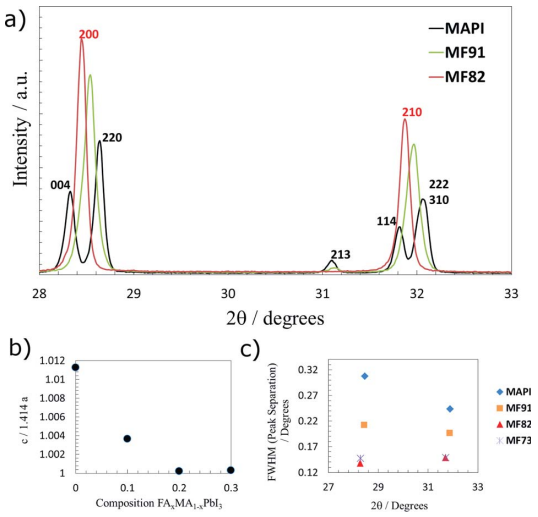

Fig. 3 (a) Room temperature powder X-ray diffraction patterns 28–34° 2θ for MAPI (black), $FA_{0.9}MA_{0.1}PbI_3$ (MF91, yellow) and $FA_{0.2}MA_{0.8}PbI_3$ (MF82, red). The solid solutions $1 > x > 0.1$ display no tetragonal peak splitting and no {213} peak at 31.1° 2θ (inconsistent with cubic symmetry). (b) Reduced lattice parameter ratio from a Pawley fit to the diffraction patterns $0 \leq x \leq 0.3$. (c) FWHM of pseudo-Voight peak fits to individual peaks for $0.1 \leq x \leq 0.3$ and peak–peak separation of {004} to {220} reflections for $x = 0$ MAPI.

of Pawley fits to the data using tetragonal *I4cm* is displayed in Fig. 3b. Full pattern Pawley fits for $0.1 \leq x \leq 0.3$ are plotted in the ESI Fig. S4 and 5.† The reduced lattice parameter ratio shows that while for MAPI $\gamma = 1.01$, $FA_{0.1}MA_{0.9}PbI_3$ $\gamma = 1.003$ and $FA_{0.2}MA_{0.8}PbI_3$ $\gamma = 1.0002$ as the value tends to 1, within the resolution ($\Delta d/d$) of the diffractometer, *i.e.* a cubic cell exists for $x \geq 0.2$. Further confirmation of a tetragonal unit cell for $FA_{0.1}MA_{0.9}PbI_3$ was obtained from the measured peak half-widths. Fig. 3c plots the full width, half height maximum for pseudo-Voigt functions fit to individual peaks in the powder patterns $0.1 \leq x \leq 0.3$ and the peak–peak separation for the {004} to {220} reflections in $x = 0$ MAPI. A clear trend is observed in which the peak width tends to a constant value (the instrumental peak width of $\sim 0.12^\circ$) by $x = 0.2$, with "broader" peak widths obtained for the $x = 0.1$ pattern as the program attempts to fit the two close reflections in tetragonal $FA_{0.1}MA_{0.9}PbI_3$.

Crystal systems and unit cell parameters in the $FA_xMA_{1-x}PbI_3$ solid solution

Assignment of the correct crystal system and space group to the low temperature phase of phases $FA_xMA_{1-x}PbI_3$ using just X-ray diffraction data needs to be undertaken with caution. While the SXD data obtained from $FA_{0.1}MA_{0.9}PbI_3$ at 300 K are best indexed using a 12.6 Å cubic cell (and that from all other compositions below $T_{C\rightarrow T}$), the room temperature PXD pattern for $FA_{0.1}MA_{0.9}PbI_3$ provides evidence that a tetragonal cell is the correct choice for this system. The lower temperature structure is derived from the higher temperature 6.3 Å cubic cell; with a 2a × 2a × 2a for the cubic crystal system ($a = \sim 12.6$ Å) or √2a × √2a × 2c unit cell for the closely related tetragonal description.

For hybrid perovskites, X-ray scattering is dominated by the heavy atom framework lead and iodine, with little contribution from the organic cations, which are further dynamically disordered over several orientations. We have routinely observed twinning in the SXD patterns of hybrid perovskite crystals as they are cooled through phase transition temperatures. Data obtained from multiply twinned crystals leads to further problems in extracting the correct lattice parameters and crystal system, as has been seen with the original trigonal crystal system assignment of FAPI.[12]

Unit cell refinements of the room temperature powder diffraction data (Fig. 4) for the MA/FAPI (HI) samples were carried out in CELREF.[25] These display a very near linear increase in reduced lattice parameter and volume as composition is varied across the series and the amount of the larger FA cation increases. The agreement in reduced lattice parameter between these X-ray data ($0.1 < x < 0.9$) and neutron data for $MAPbI_3$ (D20, ILL)[15] and $FAPbI_3$ (HRPD, ISIS)[13] is excellent. The room temperature unit cells and cell volumes for IS crystals, determined by SXD (Table ESI S3†), are included for comparison of the two synthesis methods, with lattice parameters displaying very close agreement.

UV-vis spectroscopy

Solid state reflectance UV-vis spectroscopy data revealed a linear decrease in optical band gap with increasing FA content from

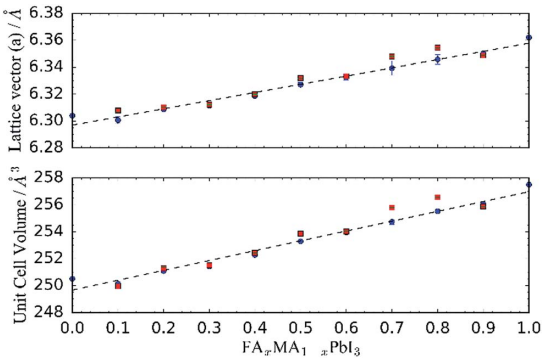

Fig. 4 Reduced lattice parameter for $MAPbI_3$ and $FA_{0.1}MA_{0.9}PbI_3$ (tetragonal values are approximately √2a, √2a and 2a) and cubic lattice parameters for $FA_xMA_{1-x}PbI_3$, $x \geq 0.2$, in $x = 0.1$ increments. Bottom – unit cell volume expansion across the same composition range. The data for the terminal compositions, *i.e.* $FAPbI_3$ and $MAPbI_3$, are taken from neutron powder diffraction data (NPD) on HRPD at ISIS for $FAPbI_3$ (ref. 13) and from D20 at ILL for $MAPbI_3$.[14] PXD for HI powders – blue circles. SXD for IS single crystals – red squares. Error bars are the esd from the least squares fit in CELREF for PXD data, esd errors for the SXD measurements lie within the data points.

$0.2 \leq x \leq 1$ (Fig. 5), *i.e.* the range of compositions adopting a cubic unit cell at room temperature. The overall shift in the band gap of 100 meV across the whole composition range is much smaller than for B or X site substitution, which is unsurprising given the lack of contribution of the A site cation to the density of states close to valence or conduction band edges.[27–29]

A band gap for MAPI of 1.55 eV was obtained from the Tauc plot, by extrapolation of the linear component of the absorption onset, entirely consistent with previous published values for bulk materials[30] and slightly smaller than the values for thin films.[8] Absorption onset is also markedly sharper for cubic solid solution compositions $0.2 \leq x \leq 1$. MAPI ($x = 0$) shows the greatest deviation from the linear trend in the optical band gap absorption onset, with the R^2 value for a linear least squares fit

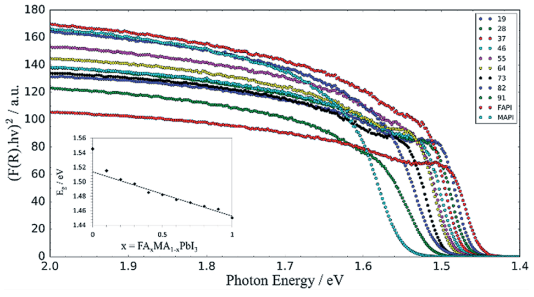

Fig. 5 Tauc plot of UV-vis reflectance spectra for each composition (HI). Inset: variation of band gap with composition from extrapolation of the linear part of increasing absorbance. Inset – absorption onset variation with composition. A linear trend line for $0.2 \leq x \leq 1$ is extrapolated to demonstrate the deviation for tetragonal $x = 0.1$ and 0.

to the data increasing from 0.91 to 0.98 upon exclusion of tetragonal MAPI and $x = 0.1$ from the dataset (Fig. 5, inset).

The deviation from this trend for MAPI and $FA_{0.1}MA_{0.9}PbI_3$ reflects the dependence of hybrid perovskite band gaps on Pb–I–Pb bonding angle,[28,29,31] with tetragonal MAPI tilted $a^0a^0c^-$ in Glazer notation. In this work we now observe this behaviour for $FA_{0.1}MA_{0.9}PbI_3$ as can be seen in Fig. 5 (inset) where the absorption onset lies at a slightly higher energy than would be expected from linear extrapolation of the data from the cubic $FA_xMA_{1-x}PbI_3$, $0.2 \leq x \leq 1$ compounds. The observed shift in absorption edge to longer wavelengths (smaller band gap) with increasing FA content is monotonic across the cubic range $0.2 \leq x \leq 1$; across this same compositional range the lattice parameter increase follows Vegard's law. In contrast, MAPI has been found to possess a positive band gap temperature coefficient, *i.e.* an increase in band gap is observed with increasing temperature as the lattice parameter expands.[32,33] How this behaviour relates to the variable temperature optical behaviour in solid solutions remains to be established, but it is probably related to increased thermal vibration and local tilting of the PbI_6 octahedra.

Formally, in the room temperature $Pm\bar{3}m$ phases $FA_xMA_{1-x}PbI_3$ $0.2 \leq x \leq 1$, all the Pb–I–Pb angles are fixed at 180° so no dependence of the band gap on this measured bond angle would be expected. Diffraction data provide a time and space averaged representation of these materials, while the local and dynamic structure are likely to contribute to the observed optical behaviour. The impact of such local structure effects on the electronic structure, and therefore optical properties, in these materials is a topic for further theoretical and experimental development. In the $FA_xMA_{1-x}PbI_3$, $0.2 \leq x \leq 1$ compounds it is possible that that the PbI_3 framework becomes more rigid with increasing levels of the larger $[FA]^+$ cation and this reduces the band gap, despite the overall increase in lattice parameter.

Discussion

These results, demonstrating phase-pure solid solutions from $FA_xMA_{1-x}PbI_3$, $0.0 \leq x \leq 1$, disagree with some of the observations reported in the literature. Binek *et al.*[21] studied inclusion of MA^+ in $FA_xMA_{1-x}PbI_3$ *via* solvent cation exchange with 5–15% MAI in FAI solution, reporting no significant shift in the lattice parameter upon increasing MAI concentration. However, analysis of final perovskite composition was not reported to establish correspondence to the starting solution ratios and herein we have shown that the lattice parameter varies linearly across the whole composition range, in agreement with the findings of Yang *et al.*,[9] who however observed partial formation of δ-FAPI for $x \geq 0.6$ for thin films on ITO, indicating non-uniformity of the cation distribution in the films, while we observe no secondary phase formation, except for pure FAPI.

The stoichiometry and defect structure in each compound may depend on the idiosyncrasies of the synthesis method, particularly the chemical potential of the reactants and the crystallisation dynamics, which are drastically different between the iodide rich HI crystal growth and thin film deposition from stoichiometric solutions, a 3 : 1 excess of the organic iodide *versus* PbI_2, or a two-step deposition with a large excess of organic iodide in the second step. The two methods employed in this study both depend on crystallisation from stoichiometric solutions due to a reduction in solubility as the temperature changes. Inverse solubility is an unusual effect in which hybrid perovskites display significant loss of solubility upon heating in certain solvents.[24,34,35] This effect is highly solvent and compound specific and results in rapid crystal growth as the temperature is raised. Heterovalent dopant inclusion, *e.g.* Bi^{3+} for Pb^{2+}, has also been demonstrated by the same method.[36] The temperature required to induce crystallisation can be reduced by solvent engineering by adding up to 30 wt% chlorobenzene to the γ-butyrolactone.[37]

The phase behaviour of the $FA_xMA_{1-x}PbI_3$ system as a function of temperature has not previously been explored. We have shown using VT-SXD that a phase transition from cubic occurs on cooling a little below room temperature across the complete compositional range, $0.2 \leq x \leq 0.9$. In the case of $FA_{0.1}MA_{0.9}PbI_3$ the phase transition temperature ($T_{C\rightarrow T}$) takes place slightly above room temperature so that the PXD pattern collected at 298 K shows reflections that require indexing using a tetragonal unit cell. For all compositions the SXD data obtained below $T_{C\rightarrow T}$ are best indexed using a doubled (~12.6 Å) cubic unit cell, though an I-centred tetragonal cell can also be used but yields a higher R_{int}. In both cases it is likely that the increased unit cell size results from tilting of the Pb–I octahedra. However, the dominance of X-ray scattering from the heavy atom inorganic framework, with minimal information on the orientations of the organic cations, means that it is not possible to definitively distinguish between the different crystal systems from the SXD data. We believe that the lattice parameter ratios, peak broadening and additional reflections observed in the room temperature PXD data (Fig. 3) provides the strongest evidence for a tetragonal structure for the low temperature phase of $FA_{0.1}MA_{0.9}PbI_3$.

It is apparent from the data presented herein that only a small amount of FA inclusion into MAPI, between $0.1 \leq x \leq 0.2$, is required to induce a change from tetragonal to cubic perovskite structure, at room temperature. Using the approach of Kieslich *et al.*[38] to estimate the effective radius of organic cations, MA $r_{eff} = 217$ pm and FA $r_{eff} = 253$ pm, to calculate a tolerance factor, as routinely undertaken for perovskite oxides, we find that $\alpha = 0.91$ for $MAPbI_3$ *versus* 0.98 for $FAPbI_3$. Inorganic ionic radii used were $r_{Pb(II)} = 119$ pm and $r_{I(I)} = 220$ pm, from Shannon's tables for halides.[39] Since it is commonly assumed that for $0.81 < \alpha < 1.01$ the perovskite structure is observed, this approach is clearly insufficient for explaining the formation of δ-$FAPbI_3$ and the structural dissimilarities between $MAPbI_3$ and $FAPbI_3$. The shape and hydrogen bonding capabilities of each organic species, not captured by the spherical ion assumption in the Goldschmidt tolerance equation, are theorised to play crucial roles in the structural evolution of these and related hybrid compounds.[40]

Recent DFT calculations suggest that in the absence of H–bonding the structure of MAPI would be cubic.[41] For all compositions, $0 \leq x \leq 0.9$, the materials tend towards cubic perovskite symmetry (with a fully disordered A-site cation

orientation) as the temperature increases. This behaviour is associated with an expansion in the lattice parameters and changes in the hydrogen bonding between the organic cation hydrogen atoms and the iodide ion of the inorganic lattice – an interaction which becomes an increasingly unimportant compared to thermal energy and motion. The disruption of hydrogen bonding due to the introduction of two different organic cations, MA and FA, with dissimilar hydrogen bonding strengths, directionality and acidities (FA being less acidic), may be a factor in determining the temperature profile of the phase transition as the cation ratio is changed across the series.

The estimation of effective ionic radii presents another complication for hybrid halide perovskites over and above their inorganic counterparts. Recently Travis *et al.*[42] have derived ionic radii for heavy metal halides, noting the differences from Shannon radii for large, less electronegative ions and define a revised tolerance space for hybrid halide perovskites. Suppression of the δ-phase of $CsPbI_3$/$FAPbI_3$ has been studied in terms of the mixing entropy contribution to the free energy of each phase, with entropic stabilisation of the α-phase perovskite for mixed Cs/FA calculated to be on the order of 0.05 eV.[22]

Conclusions

Uptake of MA^+ and FA^+ cations from solution into bulk phase crystals of $FA_xMA_{1-x}PbI_3$ has been shown to be statistical for two different synthesis methods – crystallisation from hydroiodic acid and inverse solubility in γ-butyrolactone. Phases formed with $x \geq 0.2$ in the $FA_xMA_{1-x}PbI_3$ solid solution are cubic at room temperature, but for $x = 0.1$ and $x = 0$ a tetragonal phase is observed. In the mixed cation systems no transition to a non-perovskite δ-phase is observed immediately following the synthesis, except for $x = 0$, FAPI, which begins to partially decompose to δ-FAPI, as previously reported.[13] The lattice parameters and optical band gap of $FA_xMA_{1-x}PbI_3$, $0.2 \leq x \leq 1$ at 298 K vary in accordance with Vegard's law, but with a larger band gap observed for the tetragonal phase, $0.0 \leq x \leq 0.1$.

The results presented here summarise a robust and simple means to determine the A-site cation composition, and therefore band gap, of $FA_xMA_{1-x}PbI_3$ solid solutions from refined lattice parameters derived from PXD data.

For every composition in the $FA_xMA_{1-x}PbI_3$ system a phase transition is observed upon cooling the sample (from above room temperature for $x = 0$ and 0.1). X-ray diffraction data obtained below the transition temperature may, in all cases, be indexed using a tetragonal or doubled cubic unit cell. However, distinguishing different possible structures for the low temperature phase for $x \geq 0.1$ from X-ray diffraction data alone is not possible due to the dominance of the scattering by the heavy atoms Pb and I. Future planned low temperature neutron diffraction studies of phases in the $FA_xMA_{1-x}PbI_3$, $0.1 \leq x \leq 1.0$ should help resolve the low temperature structures of these materials.

Acknowledgements

OJW and BC would like to thank the EPSRC for PhD and M. Res. studentship funding *via* the EPSCRC doctoral training centre in Sustainable Chemical Technologies (EP/G03768X/1, EP/L016354/1) and also Dr Mary Mahon, University of Bath, for help and advice on crystallography.

Notes and references

1 W. S. Yang, J. H. Noh, N. J. Jeon, Y. C. Kim, S. Ryu, J. Seo and S. I. Seok, *Science*, 2015, **348**, 1234–1237.
2 M. Hu, L. Liu, A. Mei, Y. Yang, T. Liu and H. Han, *J. Mater. Chem. A*, 2014, **2**, 17115–17121.
3 Y. Fu, H. Zhu, A. Schrader, D. Liang, Q. Ding, P. Joshi, L. Hwang, X.-Y. Zhu and S. Jin, *Nano Lett.*, 2016, **16**, 1000–1008.
4 N. Pellet, P. Gao, G. Gregori, T.-Y. Yang, M. K. Nazeeruddin, J. Maier and M. Grätzel, *Angew. Chem., Int. Ed.*, 2014, **53**, 3151–3157.
5 N. J. Jeon, J. H. Noh, W. S. Yang, Y. C. Kim, S. Ryu, J. Seo and S. II Seok, *Nature*, 2015, **517**, 476–480.
6 D. Bi, W. Tress, M. I. Dar, P. Gao, J. Luo, C. Renevier, K. Schenk, A. Abate, F. Giordano, J.-P. Correa Baena, J.-D. Decoppet, S. M. Zakeeruddin, M. K. Nazeeruddin, M. Gratzel and A. Hagfeldt, *Sci. Adv.*, 2016, **2**, e1501170.
7 M. Saliba, T. Matsui, J.-Y. Seo, K. Domanski, J.-P. Correa-Baena, N. Mohammad K., S. M. Zakeeruddin, W. Tress, A. Abate, A. Hagfeldt and M. Grätzel, *Energy Environ. Sci.*, 2016, **9**, 1989–1997.
8 J. T. Jacobsson, J. P. Correa Baena, M. Pazoki, M. Saliba, K. Schenk, M. Grätzel and A. Hagfeldt, *Energy Environ. Sci.*, 2016, **9**, 1706–1724.
9 Z. Yang, C.-C. Chueh, P.-W. Liang, M. Crump, F. Lin, Z. Zhu and A. K.-Y. Jen, *Nano Energy*, 2016, **22**, 328–337.
10 G. E. Eperon, S. D. Stranks, C. Menelaou, M. B. Johnston, L. M. Herz and H. J. Snaith, *Energy Environ. Sci.*, 2014, **7**, 982–988.
11 J. H. Noh, S. H. Im, J. H. Heo, T. N. Mandal and S. I. Seok, *Nano Lett.*, 2013, **4**, 1764–1769.
12 C. C. Stoumpos, C. D. Malliakas and M. G. Kanatzidis, *Inorg. Chem.*, 2013, **52**, 9019–9038.
13 M. T. Weller, O. J. Weber, J. M. Frost and A. Walsh, *J. Phys. Chem. Lett.*, 2015, **6**, 3209–3212.
14 A. A. Zhumekenov, M. I. Saidaminov, M. A. Haque, E. Alarousu, S. P. Sarmah, B. Murali, I. Dursun, X.-H. Miao, A. L. Abdelhady, T. Wu, O. F. Mohammed and O. M. Bakr, *ACS Energy Lett.*, 2016, **1**, 32–37.
15 M. T. Weller, O. J. Weber, P. F. Henry, A. M. Di Pumpo and T. C. Hansen, *Chem. Commun.*, 2015, **51**, 4180–4183.
16 Y.-Y. Zhang, S. Chen, P. Xu, H. Xiang, X.-G. Gong, A. Walsh and S.-H. Wei, 2015, arXiv:1506.01301 [cond-mat.mtrl-sci].
17 G. P. Nagabhushana, R. Shivaramaiah and A. Navrotsky, *Proc. Natl. Acad. Sci. U. S. A.*, 2016, **113**, 7717–7721.
18 B. Brunetti, C. Cavallo, A. Ciccioli, G. Gigli and A. Latini, *Sci. Rep.*, 2016, **6**, 6050–6051.
19 A. M. A. Leguy, Y. Hu, M. Campoy-Quiles, M. I. Alonso, O. J. Weber, P. Azarhoosh, M. van Schilfgaarde, M. T. Weller, T. Bein, J. Nelson, P. Docampo, P. R. F. F. Barnes, M. van Schilfgaarde, M. T. Weller, T. Bein, J. Nelson, P. Docampo and P. R. F. F. Barnes, *Chem. Mater.*, 2015, **27**, 3397–3407.

20 L. Zhao, R. A. Kerner, Z. Xiao, Y. L. Lin, K. M. Lee, J. Schwartz and B. P. Rand, *ACS Energy Lett.*, 2016, **1**, 595–602.
21 A. Binek, F. C. Hanusch, P. Docampo and T. Bein, *J. Phys. Chem. Lett.*, 2015, **6**, 1249–1253.
22 C. Yi, J. Luo, S. Meloni, A. Boziki, N. Ashari-Astani, C. Grätzel, S. M. Zakeeruddin, U. Rothlisberger and M. Grätzel, *Energy Environ. Sci.*, 2015, **9**, 656–662.
23 A. Poglitsch and D. Weber, *J. Chem. Phys.*, 1987, **87**, 6373.
24 M. I. Saidaminov, A. L. Abdelhady, B. Murali, E. Alarousu, V. M. Burlakov, W. Peng, I. Dursun, L. Wang, Y. He, G. Maculan, A. Goriely, T. Wu, O. F. Mohammed and O. M. Bakr, *Nat. Commun.*, 2015, **6**, 7586.
25 J. laugier and B. Bochu, *LMGP-Suite Suite of Programs for the interpretation of X-ray Experiments*, ENSP/Laboratoire des Matériaux et du Génie Physique, BP 46, 38042 Saint Martin d'Hères, France.
26 J. T. Jacobsson, J. L. Schwan, M. Ottosson, A. Hagfeldt and T. Edvinsson, *Inorg. Chem.*, 2015, **54**, 10678–10685.
27 F. Brivio, K. T. Butler, A. Walsh and M. Van Schilfgaarde, *Phys. Rev. B: Condens. Matter Mater. Phys.*, 2014, **89**, 155204.
28 I. Borriello, G. Cantele and D. Ninno, *Phys. Rev. B: Condens. Matter Mater. Phys.*, 2008, **77**, 235214.
29 T. Umebayashi, K. Asai, T. Kondo and A. Nakao, *Phys. Rev. B: Condens. Matter Mater. Phys.*, 2003, **67**, 155405.
30 A. Leguy, P. Azarhoosh, M. I. Alonso, M. Campoy-Quiles, O. J. Weber, J. Yao, D. Bryant, M. T. Weller, J. Nelson, A. Walsh, M. van Schilfgaarde and P. R. F. Barnes, *Nanoscale*, 2016, **8**, 6317–6327.
31 M. R. Filip, G. E. Eperon, H. J. Snaith and F. Giustino, *Nat. Commun.*, 2014, **5**, 5757.
32 B. J. Foley, D. L. Marlowe, K. Sun, W. A. Saidi, L. Scudiero, M. C. Gupta and J. J. Choi, *Appl. Phys. Lett.*, 2015, **106**, 243904.
33 V. D'Innocenzo, G. Grancini, M. J. P. Alcocer, A. R. S. Kandada, S. D. Stranks, M. M. Lee, *et al.*, *Nat. Commun.*, 2014, **5**, 3586.
34 M. I. Saidaminov, A. L. Abdelhady, G. Maculan and O. M. Bakr, *Chem. Commun.*, 2015, **51**, 17658–17661.
35 J. M. Kadro, K. Nonomura, D. Gachet, M. Grätzel and A. Hagfeldt, *Sci. Rep.*, 2015, **5**, 11654.
36 L. Abdelhady, M. I. Saidaminov, B. Murali, V. Adinolfi, O. Voznyy, K. Katsiev, E. Alarousu, R. Comin, I. Dursun, L. Sinatra, E. H. Sargent, O. F. Mohammed and O. M. Bakr, *J. Phys. Chem. Lett.*, 2016, **7**, 295–301.
37 M. Luan, J. Song, X. Wei, F. Chen and J. Liu, *CrystEngComm*, 2016, **18**, 5257–5261.
38 G. Kieslich, S. Sun and T. Cheetham, *Chem. Sci.*, 2014, **5**, 4712–4715.
39 R. D. Shannon, *Acta Crystallogr., Sect. A: Cryst. Phys., Diffr., Theor. Gen. Crystallogr.*, 1976, **32**, 751–767.
40 A. Amat, E. Mosconi, E. Ronca, C. Quarti, P. Umari, M. K. Nazeeruddin, M. Grätzel and F. De Angelis, *Nano Lett.*, 2014, **14**, 3608–3616.
41 J. H. Lee, N. C. Bristowe, J. H. Lee, S.-H. Lee, P. D. Bristowe, A. K. Cheetham and H. M. Jang, *Chem. Mater.*, 2016, **28**, 4259–4266.
42 W. Travis, E. N. K. Glover, H. Bronstein, D. O. Scanlon and R. Palgrave, *Chem. Sci.*, 2016, **7**, 4548–4556.

Electronic Supplementary Information

Phase Behaviour and Composition in the Formamidinium-Methylammonium Hybrid Lead Iodide Perovskite Solid Solution

O. J. Weber, B. Charles and M. T. Weller

Department of Chemistry and Centre for Sustainable Chemical Technologies, University of Bath, Claverton Down, Bath. BA2 7AY. UK. E-mail: m.t.weller@bath.ac.uk.

Contents

Table S1 Reactant quantities used for crystal synthesis via precipitation from hydroiodic acid (method HI)

	Ratios		Weights (g)			Volume HI (ml)
Sample	**MA**	**FA**	**MAI**	**FAI**	**$Pb(CH_3CO_2)_2 \cdot 3H_2O$**	**1 molar**
1	1	0	0.2564	0	0.6119	1.6130
2	0.9	0.1	0.2303	0.0277	0.6106	1.6096
3	0.8	0.2	0.2043	0.0552	0.6093	1.6062
4	0.7	0.3	0.1784	0.0827	0.6080	1.6029
5	0.6	0.4	0.1526	0.1100	0.6068	1.5996
6	0.5	0.5	0.1269	0.1373	0.6055	1.5962
7	0.4	0.6	0.1013	0.1644	0.6043	1.5929
8	0.3	0.7	0.0758	0.1914	0.6030	1.5896
9	0.2	0.8	0.0504	0.2182	0.6018	1.5864
10	0.1	0.9	0.0252	0.2450	0.6005	1.5831
11	0	1	0	0.2717	0.5993	1.5798

Table S2 Reactant quantities used for crystal synthesis via Inverse solubility (method IS)

0.001	**mol**	**1 M solutions in 1 mL γ-butyrolactone**							
Ratio MA/FA	**9:1**	**8:2**	**7:3**	**6:4**	**5:5**	**4:6**	**3:7**	**2:8**	**1:9**
	wgt / g								
MAI	0.1431	0.1272	0.1113	0.0954	0.0795	0.0636	0.0477	0.0318	0.0159
FAI	0.0172	0.0344	0.0516	0.0688	0.0860	0.1032	0.1204	0.1376	0.1548
PbI2	0.4610	0.4610	0.4610	0.4610	0.4610	0.4610	0.4610	0.4610	0.4610

Table S3 Lattice Parameters and Cell Volumes at 300K of $FA_xMA_{1-x}PbI_3$ crystals grown via inverse solubility (IS) method.

x in $FA_xMA_{1-x}PbI_3$	**Reduced lattice parameter / Å**	**Cell Volume / Å^3**
0.1	6.3047(15)	249.946(14)
0.2	6.3102(15)	251.267(1)
0.3	6.3122(2)	251.501(17)
0.4	6.3199(3)	252.42(2)
0.5	6.3319(15)	253.859(1)
0.6	6.3333(3)	254.03(2)
0.7	6.3479(2)	255.795(18)
0.8	6.3543(2)	256.573(2)
0.9	6.3486(2)	255.878(15)

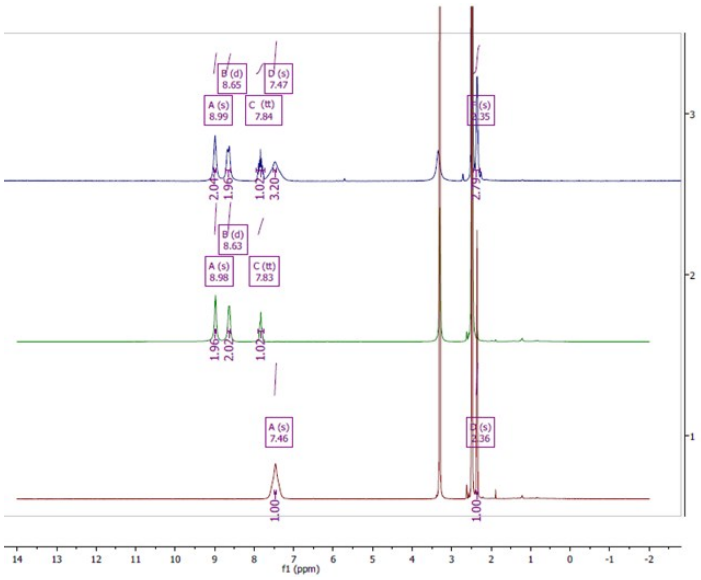

Figure 1 ^{1}H NMR in d_6-DMSO of 1) $MAPbI_3$ (HI), 2) $FAPbI_3$ (HI) and 3) $FA_{0.5}MA_{0.5}PbI_3$ (IS).

Assignments:

$MAPbI_3$ ^{1}H NMR (300 MHz, d6-DMSO) δ 2.36 (3H, s, CH_3), 7.46 (3H, NH_3).
$FAPbI_3$ ^{1}H NMR (300 MHz, d6-DMSO) δ 7.83 (1H, tt, CH), 8.63 (2H, d, NH_2), 8.98 (2H, s, NH_2).
$FA_{0.5}MA_{0.5}PbI_3$ ^{1}H NMR (300 MHz, d6-DMSO) δ 2.35 (3H, s, CH_3), 7.46 (3H, NH_3), 7.83 (1H, tt, CH), 8.63 (2H, d, NH_2), 8.97 (2H, s, NH_2).

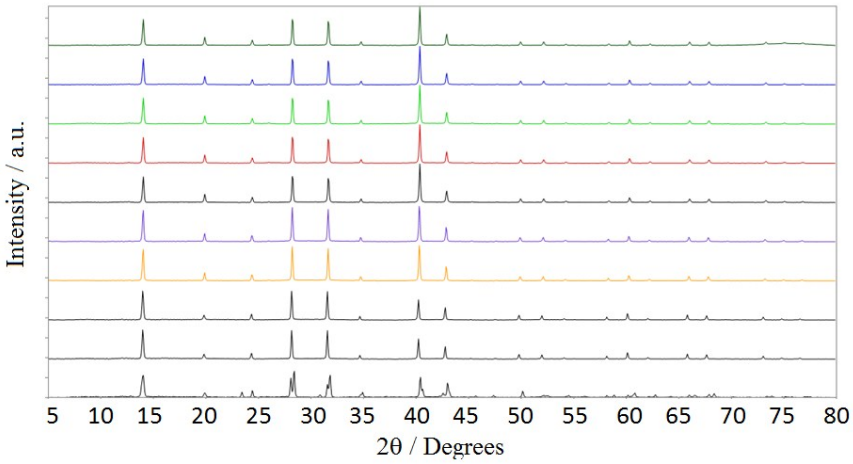

Figure 2 Powder X-ray diffraction patterns of HI method $MAPbI_3$ (bottom) $FA_xMA_{1-x}PbI_3$ $0 \leq x \leq 1$ in x = 0.1 increments to the top.

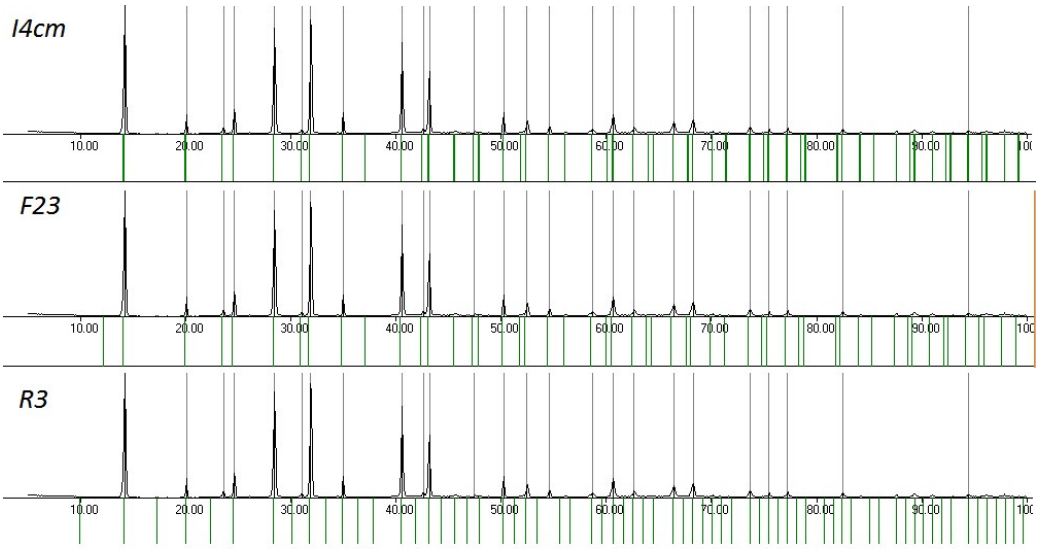

Figure 3 $FA_{0.1}MA_{0.9}PbI_3$ (HI) PXD pattern (black lines), peaks used for unit cell refinement (grey lines) and calculated peak positions (green lines) from CELREF for *I4cm* a= 8.89 c= 12.61, *F23* a = 12.6 and *R3* a = 8.91.

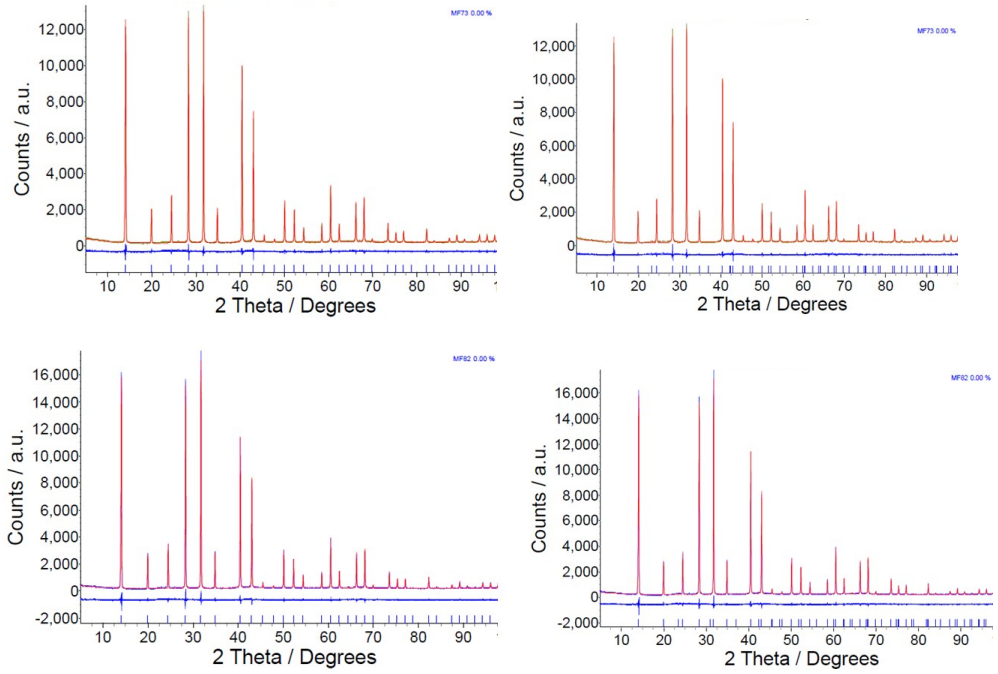

Figure 4 Pawley fits to PXD patterns of $FA_{0.3}MA_{0.7}PbI_3$, cubic *Pm-3m*, a ≈ 6.31 Å (top left) and tetragonal *I4cm* a≈ 8.90 Å, c ≈ 12.59 Å (top right). $FA_{0.2}MA_{0.8}PbI_3$ *Pm-3m* (bottom left) and *I4cm* (bottom right). Both samples were synthesised by the HI method. Difference profiles are plotted in blue and calculated peak positions are designated by pink ticks.

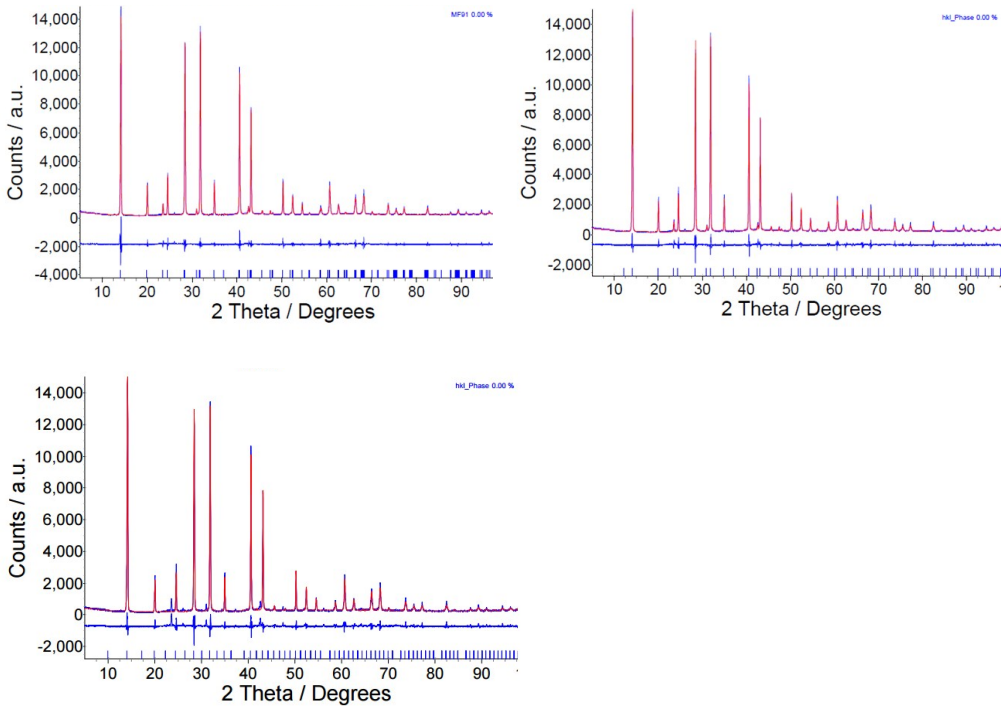

Figure 5 Pawley fits to the room temperature PXD pattern of $FA_{0.1}MA_{0.9}PbI_3$ for *I4cm*, a ≈ 8.91 Å c ≈ 12.59 Å (top left), *F23* a ≈ 12.6 Å (top right) and *Im-3* a ≈ 12.6 Å (bottom left).

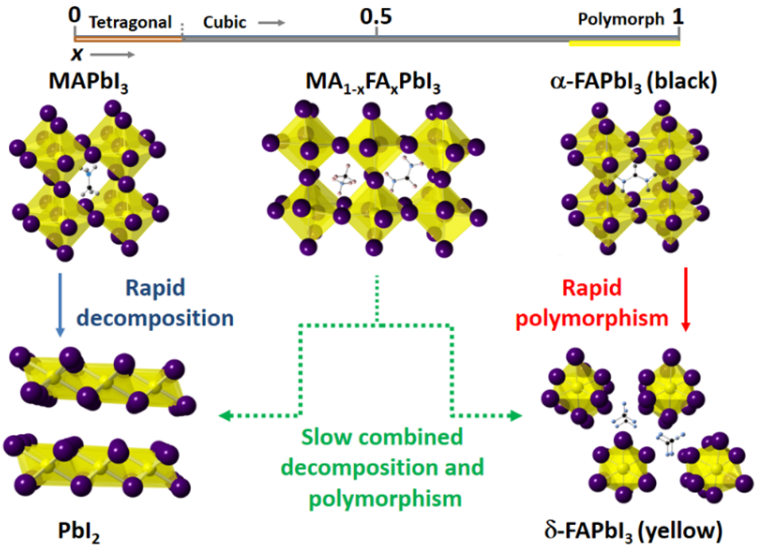

Figure 6-1: Decomposition pathways of methylammonium / formamidinium lead iodide solid solutions.

6.3 Solid Solution Decomposition Kinetics

A follow up study was carried out into the degradation of $MA_{1-x}FA_xPbI_3$ solid solutions. The results of this study are published in

Understanding the stability of mixed A-cation lead iodide perovskites B. Charles, J. Dillon, O. J. Weber, M. S. Islam, M. T. Weller, *J. Mat. Chem. A*, 2017, **5**, 22495-22499

The PXRD data collection and analysis was carried out by Bethan Charles. The decomposition of thin films of the perovskite phase to PbI_2 under atmospheric conditions was monitored by powder X-ray diffraction and modelled using Avrami kinetics Johnson-Mehl-Avrami-Kolmogorov (JMAK) equation.

$$\alpha = 1 - exp(-(kt)^m) \tag{6.1}$$

where α is the product phase fraction, k the rate constant and m the Avrami exponent dependent on the crystallisation mechanism. The rate at which PbI_2 formed at the expense of the perovskite phase was approximated by the peak areas of the most intense reflection (001 for PbI_2).

Extracting the rate constant from the linear relationship plotted in Figure 6-2a, it was found

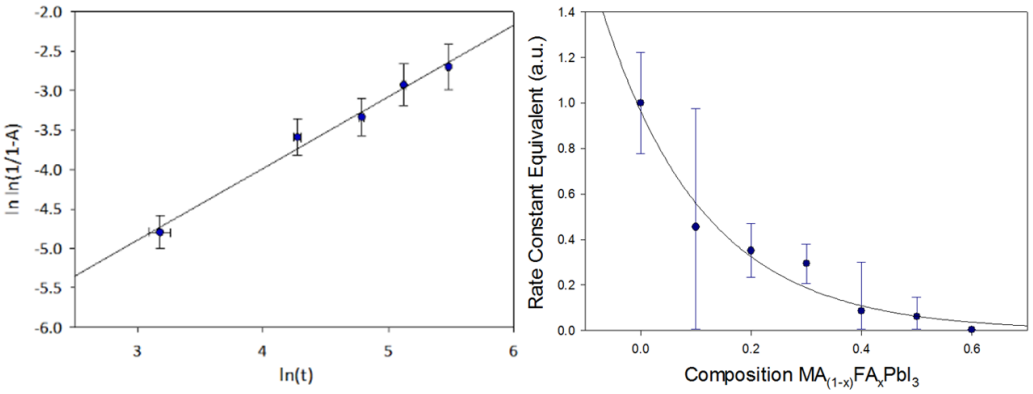

Figure 6-2: Decomposition rate of methylammonium / formamidinium lead iodide solid solutions.

that the rate constant varied exponentially for $0.0 < x < 0.6$, i.e. the mixed cation compositions display greater stability than $MAPbI_3$ up to $MA_{0.4}FA_{0.6}PbI_3$. For phase fractions of 0.7 and above, the degradation mechanism changed to rapid phase transformation to hexagonal δ-$FAPbI_3$.

The perovskite thin films were spin coated onto microscopy glass substrates. The substrates were cleaned sequentially using hellmanex solution, acetone and ethanol in an ultrasonic bath for 10 minutes each. MAI and FAI and PbI_2 1 to 0 were dissolved in DMF (0.6 molar). 100 L of the DMF solutions were spin coated at 4000 rpm for 30 s under a low humidity atmosphere and heated to 110°C for 30 minutes. Powder X-ray diffraction was carried out using a Bruker Advance D8 X-ray diffractometer with a Cu-K radiation. The diffraction angle was scanned from 10° to 50° using a step size of 0.016°.

Chapter 7

Lead Iodide Hybrid Compounds

The results in this Chapter on structure determination of novel hybrid materials are reproduced in full from the original publication by permission of the International Union of Crystallography. CIFs of the crystal structures reported are available at the online version of this publication:

Structural diversity in hybrid organic-inorganic lead iodide materials O. J. Weber, K. L. Marshall, L. M. Dyson, and M. T. Weller, *Acta Crystallogr. B. Struct. Sci. Cryst. Eng. Mater.*, 2015, **71**, 66–78. DOI:10.1107/S2052520615019885

7.1 Commentary

This chapter details the synthesis and structure determination of novel hybrid lead iodide compounds beyond the perovskite structure. While hybrid perovskites have garnered most of the research attention due to their photovoltaic applications, there is a vast range of halometallate frameworks templated by organic cations in non-perovskite structures that may also prove to be of interest for optoelectronic applications. These results contribute to the search for compounds beyond halide perovskites that also function as high performance hybrid semiconductors.

Dimensionality, both atomic and electronic, is an important factor in identifying hybrid materials for optoelectronics.[246] While highly porous compounds such as metal-organic frameworks (MOFs) consist of isolated metal clusters connected by organic linkers, many other hybrid compounds formed of dense continuous networks have also been synthesised. In their perspective 'There's Room in the Middle', Cheetham and Rao highlight the synthetic

possibilities for hybrid materials, defined as containing inorganic and organic moieties with infinite bonding connectivity in at least one direction.[247,248]

These synthetic efforts have not reached the stage of predictive crystal engineering, however there are some trends in the structures templated by inorganic building blocks and organic cations. The molecular shape, rigidity and directional bonding of the organic component all impact the observed structure. For low dimensional structures, intermolecular interactions between adjacent organic molecules including hydrogen bonding, π-π interactions and steric effects will also play a role in determining crystal structure.[141] Metal halide connectivity also changes with cations and synthesis conditions,[249] with vertex-sharing, edge-sharing and face-sharing frameworks all observed, providing many degrees of structural freedom.

Sn(II), Pb(II), Sb(III) and Bi(III) ions tend to be octahedrally coordinated. The higher charge density of Bi and Sb tends to result in lower dimensional structures and more examples of metal halide clusters than infinite networks, with many examples incorporating solvent molecules.[250,251] 2D layered hybrid perovskites containing Sn(II) or Pb(II) tend to be observed when the organic cation meets the requirements that the cation is sufficiently flexible, with a width not exceeding the footprint of one square face of the metal iodide layer, such that adjacent cation sterically fit within the layered perovskite structure.[48]

Hybrid metal halide frameworks with reduced dimensionality tend to lack absorption in the visible spectrum as exhibited by 3D hybrid perovskites. Exceptions to this include compounds templated using light absorbing organic molecules, e.g. viologens.[252,253] However, these compounds lack the solution processability of hybrid perovskites and the localised nature of the excitation within the organic moiety or from ligand-to-metal charge transfer may limit their applicability as photovoltaic materials.

7.2 Structural Diversity in Hybrid Organic-Inorganic Lead Iodide Materials

The following paper spans thesis pages 166-178.

Statement of Authorship

<table>
<tr><th colspan="10">This declaration concerns the article entitled:</th></tr>
<tr><td colspan="10">Structural diversity in hybrid organic-inorganic lead iodide materials</td></tr>
<tr><td colspan="10">Publication status (tick one)</td></tr>
<tr><td>draft manuscript</td><td></td><td>Submitted</td><td></td><td>In review</td><td></td><td>Accepted</td><td></td><td>Published</td><td>✓</td></tr>
<tr><td>Publication details (reference)</td><td colspan="9">O. J. Weber, K. L. Marshall, L. M. Dyson and M. T. Weller, Acta Crystallogr. B. Struct. Sci. Cryst. Eng. Mater., 2015, 71, 668–78.</td></tr>
<tr><td>Candidate's contribution to the paper (detailed, and also given as a percentage).</td><td colspan="9">The candidate contributed to/ considerably contributed to/predominantly executed the…

Formulation of ideas:
MTW and OJW defined the project.

Design of methodology:
OJW developed the synthetic techniques and analysis

Experimental work:
OJW synthesised samples, collected and analysed single crystal XRD, assisted by KLM and MTW. LMD synthesised compound 1.

Presentation of data in journal format:
OJW wrote the paper in journal format.</td></tr>
<tr><td>Statement from Candidate</td><td colspan="9">This paper reports on original research I conducted during the period of my Higher Degree by Research candidature.</td></tr>
<tr><td>Signed</td><td colspan="5"></td><td>Date</td><td colspan="3"></td></tr>
</table>

electronic reprint

STRUCTURAL SCIENCE
CRYSTAL ENGINEERING
MATERIALS

ISSN: 2052-5206
journals.iucr.org/b

Structural diversity in hybrid organic–inorganic lead iodide materials

Oliver J. Weber, Kayleigh L. Marshall, Lewis M. Dyson and Mark T. Weller

Acta Cryst. (2015). B**71**, 668–678

STRUCTURAL SCIENCE CRYSTAL ENGINEERING MATERIALS

ISSN 2052-5206

Structural diversity in hybrid organic–inorganic lead iodide materials

Oliver J. Weber, Kayleigh L. Marshall, Lewis M. Dyson and Mark T. Weller*

Centre for Sustainable Chemical Technologies and Department of Chemistry, University of Bath, Claverton Down, Bath BA2 7AX, England. *Correspondence e-mail: m.t.weller@bath.ac.uk

Received 25 June 2015
Accepted 21 October 2015

Edited by S. Parsons, University of Edinburgh, Scotland

Keywords: organic–inorganic hybrid; lead iodide; photovoltaic.

CCDC references: 1432453; 1432454; 1432455; 1432456; 1432457; 1432458; 1432459

Supporting information: this article has supporting information at journals.iucr.org/b

The structural chemistry of hybrid organic–inorganic lead iodide materials has become of increasing significance for energy applications since the discovery and development of perovskite solar cells based on methylammonium lead iodide. Seven new hybrid lead iodide compounds have been synthesized and structurally characterized using single-crystal X-ray diffraction. The lead iodide units in materials templated with bipyridyl, 1,2-bis(4-pyridyl)ethane, 1,2-di(4-pyridyl)ethylene and imidazole adopt one-dimensional chain structures, while crystallization from solutions containing piperazinium cations generates a salt containing isolated $[PbI_6]^{4-}$ octahedral anions. Templating with 4-chlorobenzylammonium lead iodide adopts the well known two-dimensional layered perovskite structure with vertex shared sheets of composition $[PbI_4]^{2-}$ separated by double layers of organic cations. The relationships between the various structures determined, their compositions, stability and hydrogen bonding between the protonated amine and the iodide ions of the PbI_6 octahedra are described.

1. Introduction

Hybrid lead iodide compounds comprised of isolated and linked PbI_6 octahedral units and organic cations form the basis for a wide range of structures of varying dimensionality, from isolated $[PbI_6]^{4-}$ octahedra in simple salt-like materials through to three-dimensional halide perovskites formed from fully connected PbI_6 octahedral units. The structural diversity of iodoplumbate and iodobismuthate hybrid compounds has been recently reviewed (Teo *et al.*, 2009; Fan *et al.*, 2006). These compounds have become of increasing technological importance since the discovery of high efficiency photovoltaic cells based on the three-dimensional hybrid perovskite methylammonium lead iodide (Lee *et al.*, 2012). These compounds self-assemble from solution (Mitzi, 2001) making them extremely attractive functional materials from a processing perspective. A wide range of important physical properties including photoluminescence (Dammak *et al.*, 2009), ferroelectricity (Liao *et al.*, 2015), non-linear optical activity (Innocenzi & Lebeau, 2005) and conductivity from wide band-gap semiconductivity to metallic (Mitzi *et al.*, 1994) can be induced as a result of the structure-directing and functional effects of different organic moieties.

The two-dimensional layered perovskite structure, of the general composition A_2BX_4, $[A^+]_2[PbI_4^{2-}]$, is adopted in combination with a wide range of mono- and dialkylammonium cations, such as hexylamine. These compounds have been particularly well explored as solution processable semiconductors that display a wide range of properties including thermochromic phase transitions (Billing & Lemmerer, 2007) and excitonic effects stemming from their multiple quantum

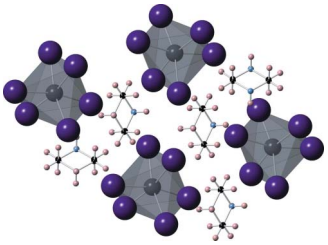

Table 1
Experimental details.

	(1)	(2)	(3)	(4)
Crystal data				
Chemical formula	$C_{5.60}H_{7.20}Cl_{0.80}I_{1.60}N_{0.80}Pb_{0.40}$	$C_{10}H_{10}I_4N_2Pb$	$C_{7.47}H_{11.73}I_{3.20}N_{1.07}O_{1.07}Pb_{1.07}S_{1.07}$	$C_{36}H_{52}I_{12}N_8O_4Pb_4$
M_r	400.00	872.99	794.79	3012.41
Crystal system, space group	Monoclinic, $P2_1$	Monoclinic, $I2/a$	Orthorhombic, $Pbca$	Monoclinic, $P2_1/c$
Temperature (K)	150	150	150	150
a, b, c (Å)	8.5992 (3), 8.9125 (3), 15.8039 (6)	7.7839 (3), 14.1821 (5), 15.3644 (7)	8.0519 (1), 23.4398 (3), 32.8901 (5)	11.8465 (4), 17.6887 (6), 8.1762 (3)
β (°)	95.502 (3)	90.434 (4)	90	98.798 (3)
V (Å^3)	1205.64 (7)	1696.06 (12)	6207.51 (15)	1693.16 (10)
Z	5	4	15	1
Radiation type	Mo $K\alpha$	Mo $K\alpha$	Mo $K\alpha$	Mo $K\alpha$
μ (mm^{-1})	12.34	17.21	16.95	15.42
Crystal size (mm)	0.4 × 0.2 × 0.1	0.3 × 0.2 × 0.1	0.5 × 0.2 × 0.1	0.3 × 0.1 × 0.05
Data collection				
Diffractometer	SuperNova, Dual, Cu at zero, EosS2	SuperNova, Dual, Cu at zero, EosS2	SuperNova, Dual, Cu at zero, EosS2	SuperNova, Dual, Cu at zero, EosS2
Absorption correction	Multi-scan	Multi-scan	Multi-scan	Multi-scan
T_{min}, T_{max}	0.625, 1.000	0.792, 1.000	0.448, 1.000	0.626, 1.000
No. of measured, independent and observed [$I > 2\sigma(I)$] reflections	5488, 4219, 3773	2612, 1652, 1440	15 898, 7106, 5859	7910, 3869, 3069
R_{int}	0.029	0.023	0.033	0.050
(sin $\theta/\lambda)_{max}$ (Å^{-1})	0.686	0.682	0.692	0.689
Refinement				
$R[F^2 > 2\sigma(F^2)]$, $wR(F^2)$, S	0.031, 0.054, 0.87	0.028, 0.054, 0.97	0.033, 0.066, 1.05	0.044, 0.093, 1.02
No. of reflections	4219	1652	7106	3869
No. of parameters	211	78	257	142
No. of restraints	1	0	0	0
H-atom treatment	H-atom parameters constrained	H-atom parameters constrained	H atoms treated by a mixture of independent and constrained refinement	H-atom parameters constrained
$\Delta\rho_{max}$, $\Delta\rho_{min}$ (e Å^{-3})	1.50, −1.86	0.80, −1.08	1.09, −1.33	2.47, −2.47
Absolute structure	Refined as an inversion twin	–	–	–
Absolute structure parameter	0.114 (10)	–	–	–

	(5)	(6)	(7)
Crystal data			
Chemical formula	$C_{10}H_{18}I_3NO_2PbS_2$	$C_3H_5I_3N_2Pb$	$C_{3.20}H_{9.60}I_{2.40}N_{1.60}Pb_{0.40}$
M_r	836.26	656.98	457.96
Crystal system, space group	Monoclinic, $P2_1/c$	Hexagonal, $P6_3/m$	Monoclinic, $P2/n$
Temperature (K)	150	150	150
a, b, c (Å)	15.0068 (15), 16.9568 (15), 8.1667 (5)	15.5643 (6), 15.5643 (6), 8.0123 (5)	9.8058 (3), 9.2603 (3), 12.4081 (4)
β (°)	95.491 (9)	90	93.553 (3)
V (Å^3)	2068.6 (3)	1680.92 (17)	1124.55 (6)
Z	4	6	5
Radiation type	Mo $K\alpha$	Mo $K\alpha$	Mo $K\alpha$
μ (mm^{-1})	12.83	23.26	15.73
Crystal size (mm)	0.4 × 0.1 × 0.05	0.3 × 0.1 × 0.05	0.4 × 0.3 × 0.1
Data collection			
Diffractometer	SuperNova, Dual, Cu at zero, EosS2	SuperNova, Dual, Cu at zero, EosS2	SuperNova, Dual, Cu at zero, EosS2
Absorption correction	Multi-scan	Multi-scan	Multi-scan
T_{min}, T_{max}	0.623, 1.000	0.246, 1.000	0.923, 1.000
No. of measured, independent and observed [$I > 2\sigma(I)$] reflections	7724, 4632, 2814	3203, 1277, 977	5870, 2624, 2339
R_{int}	0.082	0.034	0.030
(sin $\theta/\lambda)_{max}$ (Å^{-1})	0.687	0.676	0.690
Refinement			
$R[F^2 > 2\sigma(F^2)]$, $wR(F^2)$, S	0.089, 0.197, 1.07	0.096, 0.225, 1.12	0.027, 0.049, 1.04
No. of reflections	4632	1277	2624
No. of parameters	97	35	87
No. of restraints	15	0	0
H-atom treatment	H-atom parameters constrained	H-atom parameters constrained	H-atom parameters constrained

Table 1 (continued)

	(5)	(6)	(7)
$\Delta\rho_{max}$, $\Delta\rho_{min}$ (e Å^{-3})	2.87, −2.29	5.09, −10.08	1.30, −1.14
Absolute structure	–	–	–
Absolute structure parameter	–	–	–

Computer programs: *SHELXL*2014 (Sheldrick, 2015).

Table 2
Bond length range (Å) for Pb—I bonds in the PbI_6 octahedral unit for each compound, these and the bond angle range (°) for apical iodine – lead – equatorial iodine provides a measure of the distortions from ideal octahedral geometry.

Compound	Organic component (solvate) and compound composition	Pb—I octahedra bond length range	I_{ap}—Pb—I_{eq} octahedra bond angle range
(1)	4-Chlorobenzylamine, $[ClC_6H_4CH_2NH_3]_2[PbI_4]$	3.1444 (1)–3.2428 (1)	86.97 (1)–94.06 (1)
(2)	4,4′-Bipyridyl, $[H_2$-4,4′-bipyridyl$][PbI_4]$	3.1233 (5)–3.2765 (5)	85.261 (11)–96.398 (12)
(3)	4,4′-Bipyridyl (DMSO); $[H_2$-4,4′-bipyridyl$][PbI_3]_2\cdot$2DMSO	3.0201 (8)–3.5200 (8)	81.60 (2)–97.67 (2)
(4)	1,2-Bis(4-pyridyl)ethane (DMF); $[(HC_5H_4NCH_2)_2][PbI_3]_2\cdot$2DMF	3.1897 (1)–3.3286 (1)	79.91 (1)–106.82 (1)
(5)	1,2-Di(4-pyridyl)ethylene (DMSO); $[(HC_5H_4NCH_2)_2][PbI_3]_2\cdot$4dmso	3.1769 (3)–3.3093 (3)	80.46 (1)–107.64 (1)
(6)	Imidazole; $[C_3N_2H_5]PbI_3$	3.2247 (2)–3.2397 (2)	84.57 (5)–95.28 (7)
(7)	Piperazine; $[H_2C_4N_2H_{10}]_2PbI_6$	3.1995 (4)–3.2819 (4)	85.313 (9)–102.502 (14)

Bond length and angle data calculated using *PLATON* (Spek, 2009).

well band structure (Kitazawa, 1997). Most of the known hybrid layered perovskites are of the ⟨100⟩ type, where the set of directions refer to cuts of the three-dimensional perovskite ABX_3 structure. The primary factor governing the adoption of a layered perovskite is the cross-sectional area of the organic molecule normal to ⟨100⟩ compared with the area defined by four adjacent apical halides (about 40 Å^2 for Pb—I octahedra), as exposited by Mercier *et al.* (2009). Steric effects are, therefore, of primary importance and a wide range of relatively non-bulky or small end-group organic cations have been demonstrated to be suitable for generating layered perovskites. Rigidity of the organic component can also play a major role in structure determination, since flexible molecules can adopt conformations to maximize hydrogen bonding to the lattice and energetically favourable inter-chain interactions. Flexibility through tilts and distortions to the highly polarisable lead iodide lattice also increases the range of molecules that can successfully fit the layered perovskite structure.

Beyond the two-dimensional layered perovskites, a wide range of interatomic interactions and size effects are important for determining the type of structure formed and also the nature of the lead iodide network in hybrid amine-lead iodides. These factors which include the basicity of the amine, potential for hydrogen bonding, solvate formation, π–π interactions in aromatic amines and dispersion forces mean that, for a given organic amine cation, it is not possible to predict the likely resulting dimensionality of the Pb—I network. Indeed even for simple amines the existence of multiple structural phases and solvates for a single organic species indicate that very subtle interactions between the inorganic and organic structural elements exist. In this study, a range of organic cations has been employed to template hybrid lead iodide compounds. One of the most important goals of the field is to generate compounds with light absorption properties spanning the visible spectrum, yet with radically increased stability towards hydrolysis compared with the poorly performing methylammonium lead iodide. In general, lower-dimensional lead iodide structures display wider optical band gaps; however, use of conjugated or aromatic nitrogen containing heterocycles forming charge-transfer bands with the inorganic framework may be one approach to increase absorption of low-dimensional compounds across the visible spectrum (Li *et al.*, 2012).

2. Experimental

2.1. Synthesis and crystallization

Synthesis of precursor iodide salts for each compound was carried out by neutralization with concentrated aqueous HI (57 wt%, Sigma). For 1,2-bis(4-pyridyl)ethane·2HI, 1,2-bis(4-pyridyl)ethane (0.001 mol, 0.184 g; Sigma) was dissolved in 20 ml ethanol in a round bottom flask and kept at 273 K in an ice bath. HI (2 equiv., 0.264 ml, 0.002 mol) was pipetted dropwise to the flask under stirring. A white precipitate resulted, which was filtered, washed with ethanol and dried at 323 K in ambient conditions. Yield: 0.2603 g, 59.2%. Other iodide salts were prepared in an analogous manner.

2.1.1. 4-Chlorobenzylamine, $[ClC_6H_4CH_2NH_3]_2[PbI_4]$. 4-Chlorobenzylammonium iodide was synthesized by neutralization of 4-chlorobenzylamine with hydroiodic acid (57 wt% aq.) in ice-cold ethanol. The solvent was removed by rotary evaporation. A three-neck round bottom flask equipped with nitrogen inlet and reflux condenser was charged with 6.8 ml HI and 1.7 ml H_3PO_2. The acid was degassed for 10 min and stirred until the colour had changed from brown to yellow.

Table 3
Hydrogen-bonding parameters (Å, °) for 4-chlorobenzylammonium lead iodide (1).

D—H···A	$d(D$—H)	d(H···A)	$d(D$···$A)$	$\angle(DHA)$
N2—H2A···I5^{i}	0.91	2.83	3.649 (13)	150.5
N2—H2B···I3	0.91	2.88	3.735 (13)	156.8
N2—H2C···I2^{ii}	0.91	2.70	3.578 (16)	161.7
C10—H10A···I2^{iii}	0.99	3.17	4.110 (13)	158.3
N1—H1A···I2^{iv}	0.91	2.74	3.622 (12)	164.9
N1—H1B···I1^{v}	0.91	3.01	3.682 (13)	131.9
N1—H1B···I5^{iv}	0.91	3.06	3.611 (15)	120.6
N1—H1C···I3^{v}	0.91	2.68	3.573 (17)	168.6

Symmetry codes: (i) $x+1, y, z$; (ii) $-x+1, y+\frac{1}{2}, -z+2$; (iii) $x-1, y, z-1$; (iv) $x, y, z-1$; (v) $-x, y-\frac{1}{2}, -z+1$.

PbI_2 (0.462 g, 1 mmol) and 4-chlorobenzylammonium iodide (0.539 g, 2 mmol) were added to the flask and the mixture heated to 373 K under reflux to dissolve the reactants. Upon cooling, a golden crystalline precipitate of 4-chlorobenzylammonium lead iodide (1) formed.

2.1.2. 4,4′-Bipyridyl, [H_2-4,4′-bipyridyl][PbI_4]. 4,4′-Bipyridyl diiodide (0.236 g) and PbI_2 (0.264 g) were combined with 5 mL of hydroiodic acid (57 wt% aq.) and sealed in a 23 ml Teflon^{TM}-lined stainless steel autoclave. The mixture was heated to 413 K for 24 h before cooling to room temperature at a rate of 5 K h^{-1}. The black crystals of the product (2) obtained were filtered, washed with ethanol and dried at 323 K.

2.1.3. 4,4′-Bipyridyl DMSO solvate, [H_2-4,4′-bipyridyl][PbI_3]$_2$·2DMSO. The DMSO solvate crystals of 4,4′-bipyridyl lead iodide (3) were obtained by slow evaporation of ethyl acetate into 1 ml DMSO solution containing 4,4′-bipyridyl iodide (0.103 g, 0.25 mmol) and PbI_2 (0.115 g, 0.25 mmol).

2.1.4. 1,2-Bis(4-pyridyl)ethane DMF solvate, [(H-$C_5H_4NCH_2$)$_2$][PbI_3]$_2$·2DMF. The DMF solvate structure (4) was recovered by the slow vapour diffusion of ethanol into a solution of 1,2-bis(4-pyridyl)ethane·2HI (0.25 mmol, 0.11 g) and PbI_2 (0.25 mmol, 0.115 g) in 1 ml DMF over 12 h to yield yellow needles up to 1 mm in length.

2.1.5. 1,2-Di(4-pyridyl)ethylene DMSO solvate, [(H-$C_5H_4NCH_2$)$_2$][PbI_3]$_2$·4DMSO. The DMSO solvate for 1,2-di(4-pyridyl)ethylene lead iodide (5) was obtained in an identical manner to 1,2-bis(4-pyridyl)ethane using 1,2-di(4-pyridyl)ethylene (Sigma) in DMSO with slow vapour diffusion of ethyl acetate.

2.1.6. Imidazole, [$C_3N_2H_5$]PbI_3. Imidazole·2HI (0.224 g) and PbI_2 (0.264 g) were combined with 5 mL hydroiodic acid (57 wt% aq.) and sealed in a 23 ml Teflon^{TM}-lined stainless steel autoclave. The mixture was heated to 413 K for 24 h before cooling to room temperature at a rate of 5 K h^{-1}. The yellow crystals of the product (6) obtained were filtered, washed with ethanol and dried at 323 K.

2.1.7. Piperizine, [H_2—$C_4N_2H_{10}$]$_2$$PbI_6$. Piperazine lead iodide (7) was prepared in an analogous manner to imidazole: piperazine·2HI (0.196 g) and PbI_2 (0.264 g) were combined with 5 mL hydroiodic acid (57 wt% aq.) and sealed in a 23 ml Teflon^{TM}-lined stainless steel autoclave. The mixture was heated to 413 K for 24 h before cooling to room temperature at a rate of 5 K h^{-1}. The yellow crystals obtained were filtered, washed with ethanol and dried at 323 K.

2.2. X-ray structure determination

Single crystal data for compounds (1)–(7) were collected at 150 K with an Aglient SuperNova dual tube Eos S2 CCD diffractometer operating graphite-monochromated Mo $K\alpha$ (λ = 0.7093 Å) radiation. Structure solution and refinement was carried out in *WinGX* using *XPREP* (Sheldrick, 2008) and *SHELXS*2013 (Sheldrick, 2015) to solve structures by direct methods, and *SHELXL*2013 (Sheldrick, 2015) for structure

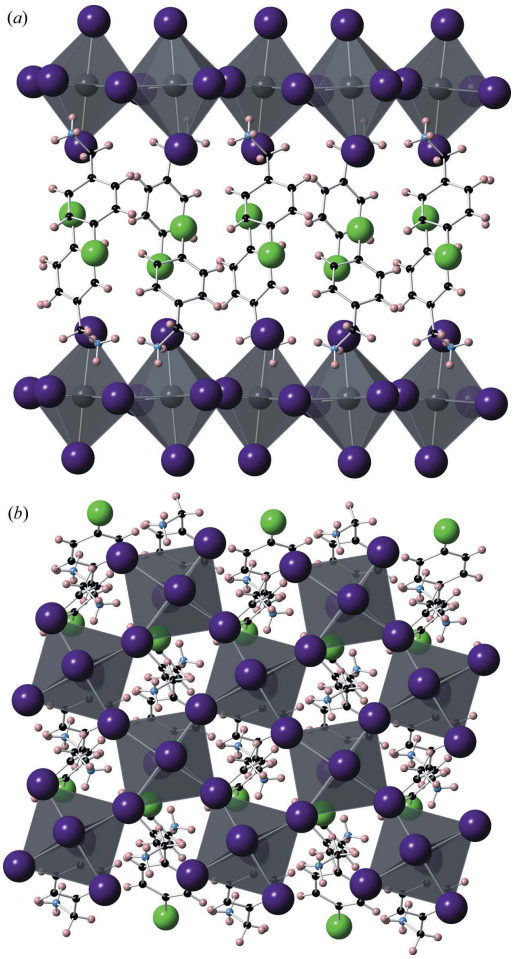

Figure 1
4-Chlorobenzylammonium lead iodide (1) layered perovskite structure viewed in (*a*) down the *a* axis with the *c* axis vertical, displaying the interlayer spacing of lead iodide octahedra and (*b*) down the *c* axis with the *a* axis vertical. Lead iodide octahedra are shaded in grey with iodide ions as dark purple spheres. Carbon (black), nitrogen (light blue), hydrogen (pale pink), chloride (bright green) comprising the organic component are interleaved between the inorganic sheets.

refinement. All H-atoms were refined by the riding model. Experimental details are given in Table 1 and selected bond lengths and angles in Table 2.

3. Crystal structure results

4-Chlorobenzylammonium lead iodide, $[ClC_6H_4NH_3]_2[PbI_4]$ (1), crystallizes in $P2_1$ at 150 K with an interlayer spacing of 15.77 Å and is representative of the layered hybrid perovskites taken from ⟨100⟩ cuts of the three-dimensional perovskite lattice. The $([PbI_4]^{2-})_n$ sheets are formed from $[PbI_6]$ octahedra sharing four vertices in a plane and are charge balanced by *N*-protonated 4-chlorobenzylammonium cations forming slightly interleaved double sheets between the lead iodide layers, Figs. 1 and 2. Many hybrid perovskites show distortions of the octahedra due to the stereoactivity of the Pb^{II} $6s^2$ lone pair of electrons, although these effects are generally more pronounced for Sn^{II} and Ge^{II} than for Pb, and for Cl and Br than I (Mitzi, 1996). As a means to quantify the distortions to the pristine layered perovskite structure, the in-plane rotation *a* is given by the *M*—I—*M* bond angle, generally around 160° for hybrid lead iodides (Mercier *et al.*, 2009), while $a = 154°$ for chlorobenzylammonium iodide. The out-of-plane rotation, *b*, or relative tilt of octahedra with respect to the plane of Pb ions is 91°. Comparison to the materials studied by Liu *et al.* (2004) shows that 4-chloroaniline lead iodide displays severely distorted Pb—I octahedra and tilted layers ($b = 144°$, $a = 85°$) to accommodate the *p*-chloroaniline, which displays a similar cross-sectional area to 4-chlorobenzylamine, but reduced flexibility with the lack of rotational freedom that the methylene unit provides. The Pb—I octahedra show minor distortions with Pb—I bond lengths in the range 3.1444 (1)–

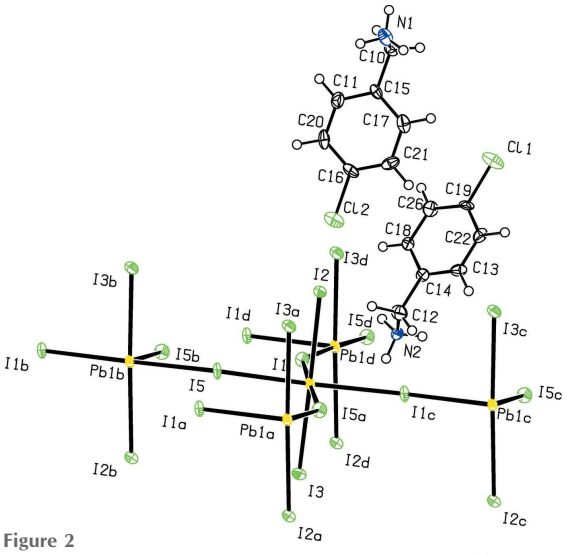

Figure 2
ORTEP drawing of 4-chlorobenzylammonium lead iodide (1) showing the asymmetric unit plus iodide ions to complete the lead iodide polyhedral. Symmetry-related atoms are identified and share the numbering scheme of hydrogen bonding in Table 3.

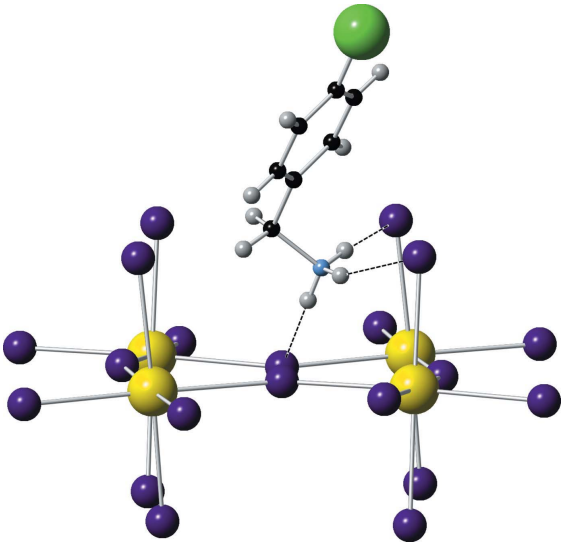

Figure 3
Hydrogen-bonding interactions between the NH_3 group on 4-chlorobenzylammonium and the lead iodide inorganic framework, for the key see the caption to Fig. 1. Tilting of the inorganic octahedra is such that NH···I distances are decreased, while the apical iodides on adjacent octahedra tilt away from the $-CH_2-$ group

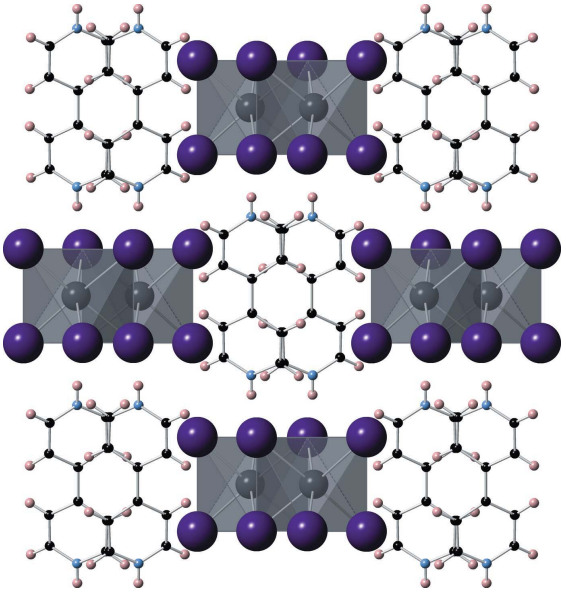

Figure 4
The structure of 4,4′-bipyridyl lead iodide, viewed along the *a* axis with the *c* axis vertical. The one-dimensional chains of edge-sharing lead iodide octahedra are interspersed horizontally and vertically by one-dimensional chains of H_2-4,4′-bipyridyl molecular cations. For the key see the caption to Fig. 1.

Table 4
Hydrogen-bonding parameters (Å, °) for 4,4′-bipyridyl lead iodide (2).

D—H···A	$d(D$—H)	d(H···A)	$d(D$···$A)$	$\angle(DHA)$
N1—H1···I2^{i}	0.86	3.04	3.664 (5)	131.4
N1—H1···I3	0.86	3.05	3.688 (5)	132.8
C6—H6···I3^{i}	0.93	3.23	3.803 (6)	121.6
C3—H3···I2	0.93	3.11	3.760 (6)	128.3
C3—H3···I3	0.93	3.11	3.725 (7)	125.3
C1—H1*A*···I2^{i}	0.93	3.13	3.720 (7)	123.0
C1—H1*A*···I3^{i}	0.93	3.25	3.809 (7)	120.6
C4—H4···I2	0.93	3.21	3.816 (6)	124.6
C4—H4···I3^{ii}	0.93	3.27	3.877 (6)	125.3

Symmetry codes: (i) $-x+1, y+\frac{1}{2}, -z+\frac{1}{2}$; (ii) $x, -y+\frac{1}{2}, z+\frac{1}{2}$.

Table 5
Hydrogen-bonding parameters (Å, °) for 4,4′-bipyridyl lead iodide DMSO solvate (3).

D—H···A	$d(D$—H)	d(H···A)	$d(D$···$A)$	$\angle(DHA)$
N2—H2···S2	0.86	2.86	3.679 (7)	160.3
N2—H2···O4	0.86	1.75	2.604 (8)	171.0
C9—H9···I4	0.93	3.28	3.901 (6)	126.4
C9—H9···I4^{i}	0.93	3.32	3.842 (6)	117.7
C8—H8···I3^{ii}	0.93	3.20	3.833 (7)	126.6
C7—H7···I3^{iii}	0.93	3.26	3.731 (6)	113.6
C7—H7···I3^{ii}	0.93	3.16	3.810 (7)	129.0
C6—H6···I5^{ii}	0.93	3.20	3.831 (6)	127.0
C3—H3···I6	0.93	3.24	3.871 (6)	127.2
C5—H5···I5^{ii}	0.93	3.12	3.790 (7)	130.6
C4—H4···I6	0.93	3.19	3.849 (6)	129.7
C10—H10···I4	0.93	3.19	3.857 (7)	130.2
C15—H15*A*···I7^{iv}	0.96	3.29	4.094 (7)	142.0
C15—H15*B*···O4^{v}	0.96	2.50	3.406 (8)	156.7
C13—H13*A*···I8^{vi}	0.96	3.13	3.970 (9)	147.6
C13—H13*C*···I6^{i}	0.96	3.25	4.083 (8)	145.9
C11—H11*A*···I5^{vii}	0.96	3.31	4.063 (9)	136.6
N1—H17···S1	0.87 (7)	2.81 (7)	3.657 (7)	167 (5)
N1—H17···O3	0.87 (7)	1.70 (7)	2.534 (8)	160 (6)
C16—H16*C*···I7^{vii}	0.96	3.32	4.217 (8)	155.7

Symmetry codes: (i) $x-\frac{1}{2}, y, -z+\frac{1}{2}$; (ii) $-x+\frac{1}{2}, y-\frac{1}{2}, z$; (iii) $-x+1, y-\frac{1}{2}, -z+\frac{1}{2}$; (iv) $-x, y-\frac{1}{2}, -z+\frac{1}{2}$; (v) $x+\frac{1}{2}, y, -z+\frac{1}{2}$; (vi) $x, -y+\frac{1}{2}, z-\frac{1}{2}$; (vii) $x-\frac{1}{2}, -y+\frac{1}{2}, -z+1$.

3.2428 (1) Å and I_{ap}—Pb—I_{eq} angles 86.89 (1)–94.06 (1)° (Table 3).

The protonated amine group of the chlorobenzylammonium cation 'docks' into the lead iodide layer in a manner very reminiscent of the position of the methylammonium cation in the perovskitic methylammonium lead iodide (Weller *et al.*, 2015), Fig. 3; four corner-sharing PbI_6 octahedra produce a 'square antiprismatic box' of iodide ions. The terminal $[-CH_2-NH_3]^+$ element of the chlorobenzylammonium cation is situated and directed towards the one side of this box forming moderately strong hydrogen bonds to the iodide anions, with NH···I distances in the range 2.68–3.06 Å. This hydrogen-bonding interaction, which is strongest with two apical iodide ions, pulls the terminal $[-CH_2-NH_3]^+$ group towards one side of the box so that the benzyl H atoms do not interact with the opposing iodide ions, with the CH···I distance greater than 3.10 Å. The chlorobenzylammonium cations alternate in positions either side of the $[PbI_4]^{2-}$ layer along the orthogonal ⟨110⟩ and ⟨1$\bar{1}$0⟩ directions and this also allows the $[Cl-C_6H_5-]$ groups to interleave slightly in the interlayer space with the $[PbI_4]^{2-}$ layers directly stacked in the *c*-direction.

The structural chemistry of Pb—I frameworks with *N*-heterocyclic organic cations has been relatively less well explored, although a few examples have been reported. 4,4′-Bipyridyl lead iodide, $[H_2$-4,4′-bipyridyl$][PbI_4]$ (2), has previously been mentioned in one paper (Yin & Cui, 2004); however, detailed structural information from this source is not available. In this work the structure of $[H_2$-4,4′-bipyridyl$][PbI_4]]$ was found to consist of edge-sharing PbI_6 octahedra forming $[PbI_4^{2-}]_n$ chains oriented along [100]. The diprotonated bipy molecular cations occupy channels formed between $[PbI_4^{2-}]_n$ chains along the [100] direction to give a chequerboard-like structure when viewed along the *a* axis, Figs. 4 and 5. There is no appreciable hydrogen bonding between the protonated bipy and iodide ions with the shortest NH···I distance at 3.04 Å (Table 4). The aromatic rings of the bipy molecular cations are slightly tilted relative to each other with a torsion angle of 28.2°.

A solvate of 4,4′-bipyridyl with lead iodide containing DMSO (3) was obtained from solvent interdiffusion. This compound of stoichiometry $[H_2$-4,4′-bipyridyl$][PbI_3]_2\cdot$2DMSO displays staggered chains of edge-sharing Pb—I distorted octahedra separated along [010] by $[H_2$-4,4′-bipyridyl] dications and along [001] by DMSO molecules, Figs. 6 and 7. The lead iodide chains of composition $[Pb_2I_6]_n^{2n-}$ are formed from pairs of $[PbI_6]$ octahedra, of composition $[Pb_2I_{10}]$, which are in turn edge-shared along the *a* direction to form a ladder with

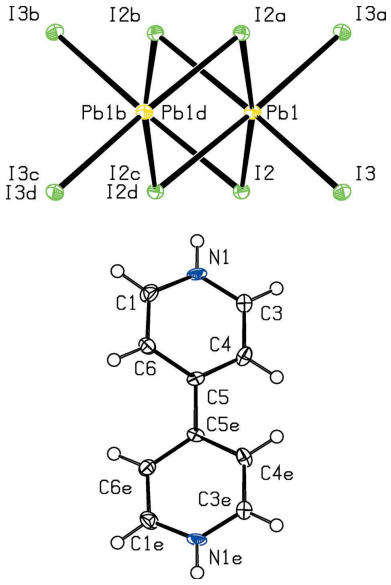

Figure 5
ORTEP drawing of 4,4′-bipyridyl lead iodide showing the asymmetric unit, iodide ions to complete the lead iodide polyhedral, with symmetry-related atoms identified.

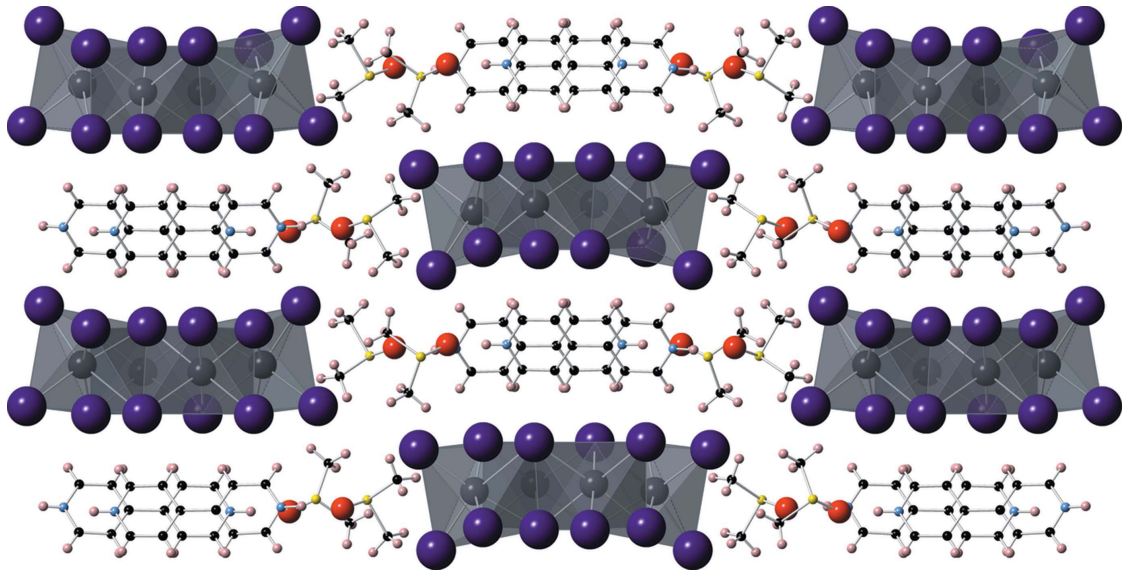

Figure 6
The DMSO solvate structure of 4,4′-bipyridyl lead iodide (3) displays curving of the octahedral columns, running in waves along the *c* axis. Atom colours as Fig. 1, with oxygen (red) and sulfur (yellow).

off-set 'rungs' (each rung is a $[Pb_2I_{10}]$ unit). The individual PbI_6 octahedra are strongly distorted with Pb—I bond lengths between 3.0201 (8) and 3.5200 (8) Å and I—Pb—I bond angles between 81.60 (2) and 97.67 (2)°. These distortions have the effect of slightly curving the individual 'rungs' of the ladder – the direction of the curve in neighbouring chains repeated along the *b* axis but inverted along the *c* axis, such that the structure has a 'wave'-like appearance when viewed perpendicular to the *yz* plane. The dihedral angle between the pyridyl rings of bipy for (2) is 28.2°, while for (3) it is only 2.7°. This solvate's columnar structure is rather unusual, but is reminiscent of the $[Pb_3I_9]_n^{3n-}$ chains observed in *N*,*N*′-diethyl-4,4′-bipyridinium and *N*,*N*′-dipropyl-4,4′-bipyridinium lead iodide described in Chen *et al.* (2011), although in the present case every $[Pb_2I_6]^{2-}$ unit in the $[Pb_2I_6]_n^{2n-}$ chain is staggered relative to the adjacent pair (Table 5).

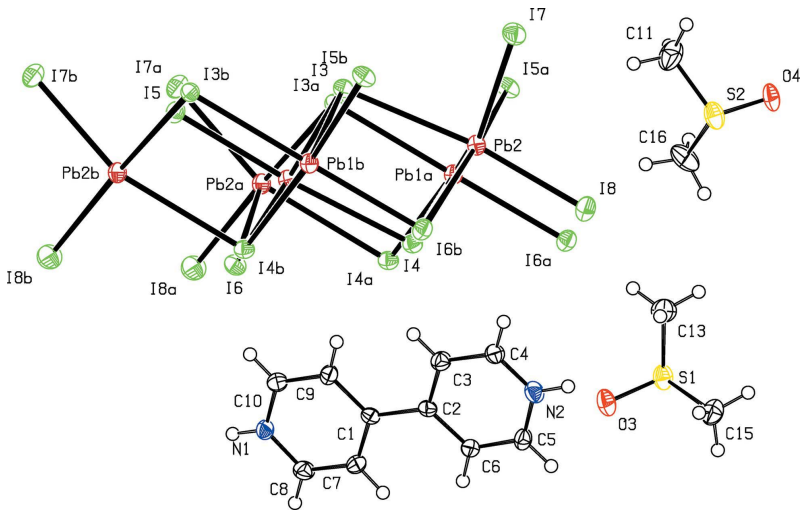

Figure 7
ORTEP view of the DMSO solvate of 4,4′-bipyridyl lead iodide (3).

The DMF solvate of 1,2-bis(4-pyridyl)ethane, $[(H\text{-}C_5H_4NCH_2)_2][PbI_3]_2{\cdot}2DMF$ (4), and DMSO solvate of 1,2-di(4-pyridyl)ethylene lead iodide, $[(H\text{—}C_5H_4NCH_2)_2][PbI_3]_2{\cdot}4DMSO$ (5), both form structures containing one-dimensional face-sharing PbI_6 octahedra in chains of the composition $[PbI_3^-]_n$. Figs. 8, 9 and 10. This face-sharing motif is commonly found for one-dimensional chains based on PbI_6 octahedra (Teo *et al.*, 2009), although these may show significant deviation from ideal octahedral geometry, even so far as trigonal prismatic coordination around the Pb atom, as found in 1,1′-dimethyl-4,4′-bipyridinium lead iodide (Tang & Guloy, 1999). In the case of (4), Pb—I bond lengths vary between 3.1897 (1) and 3.3286 (1) Å, and I—Pb—I

Table 6
Hydrogen-bonding parameters (Å, °) for 1,2-bis(4-pyridyl)ethane lead iodide DMF solvate (4).

D—H···A	$d(D$—H)	d(H···A)	$d(D$···$A)$	$\angle(DHA)$
N1—H1···O1	0.86	1.84	2.631 (9)	151.4
C4—H4···I2^{i}	0.93	3.04	3.957 (11)	169.3
C6—H6···I1^{ii}	0.93	3.25	3.938 (10)	132.9
C11—H11*C*···I3	0.96	3.09	3.997 (12)	157.6
C10—H10*C*···I2^{i}	0.96	3.33	4.122 (11)	141.2

Symmetry codes: (i) $x-1, y, z$; (ii) $-x+2, -y+2, -z+1$.

Table 7
Hydrogen-bonding parameters (Å, °) for 1,2-di(4-pyridyl)ethylene lead iodide DMSO solvate (5).

D—H···A	$d(D$—H)	d(H···A)	$d(D$···$A)$	$\angle(DHA)$
N1—H4···O1^{i}	0.86	1.76	2.61 (2)	166.5
N1—H4···S5^{i}	0.86	2.95	3.777 (19)	163.2
C1—H1···I3^{ii}	0.93	2.97	3.850 (19)	158.4
C5—H5···S6	0.93	2.94	3.52 (2)	122.1
C9—H9*B*···O2^{iii}	0.96	2.54	3.50 (3)	172.0
C8—H8*B*···O2	0.96	2.43	3.29 (3)	149.1
C2—H2···I2^{iv}	0.93	3.14	4.02 (3)	158.0
C11—H11*B*···I4^{v}	0.96	3.24	4.02 (3)	140.3
C11—H11*C*···I4^{vi}	0.96	3.28	4.20 (3)	161.4
C10—H10*B*···I2^{v}	0.96	3.23	3.96 (4)	133.7

Symmetry codes: (i) $x, y, z-1$; (ii) $-x+1, -y+1, -z$; (iii) $x, -y+\frac{1}{2}, z+\frac{1}{2}$; (iv) $-x+1, y-\frac{1}{2}, -z+\frac{1}{2}$; (v) $-x+2, y-\frac{1}{2}, -z+\frac{1}{2}$; (vi) $-x+2, -y+1, -z$.

bond angles between 77.69 (1) and 106.82 (1)°, representing a significant distortion from perfect octahedral geometry around the lead centre. Similar geometry around lead centres and chain geometry were found in compound (5). The distribution of solvent molecules and molecular cations [which differ only with the rigidity of one conjugated bond in the middle of the molecular ion in (5)] around the $[PbI_3^-]_n$ chains is similar in compounds (4) and (5) – with two cations and two (DMF) or four (DMSO) alternating around each lead iodide chain and forming a sheathe between it and four (DMSO) or six (DMSO) neighbouring inorganic chains. No significant NH···I hydrogen bonding exists in either of the main residues of these structures (Tables 6 and 7).

Imidazolium lead iodide (6), $[C_3N_2H_5]PbI_3$, likewise forms one-dimensional face-sharing chains, in this case six imidazole ions are arranged hexagonally around the octahedral chain and the compound crystallizes in hexagonal space group $P6_3/m$. Distortions of the PbI_6 octahedra are far less pronounced than in compounds (4) and (5) (Table 2). Viewed down the chain, along the c axis, Figs. 11 and 12, the iodide ions adopt a fully staggered conformation, unlike in compounds (4) and (5) (Fig. 8), in which the iodide ions are partially eclipsed (Table 8).

The basic structural model consists of chains of face-sharing PbI_6 octahedra separated by weakly hydrogen-bonded imidazolium cations. The orientational disorder in the imidazolium cations is also linked to rotational disorder of the $[PbI_3]^-$ infinite chains along their main axis. This results in significant local positional disorder of the iodide ions which the basic structural model does not fully represent, leading to significant electron density peaks ($\sim +5$ e Å^{-3}) and holes (~ -10 e Å^{-3}) associated with the three iodide ion positions. Disordering iodine over these possible sites produces a better model reducing the electron and hole density and improves the fit parameters marginally. However, this much more complex model still does not fully account for the local positional disorder and, therefore, only the simpler structural

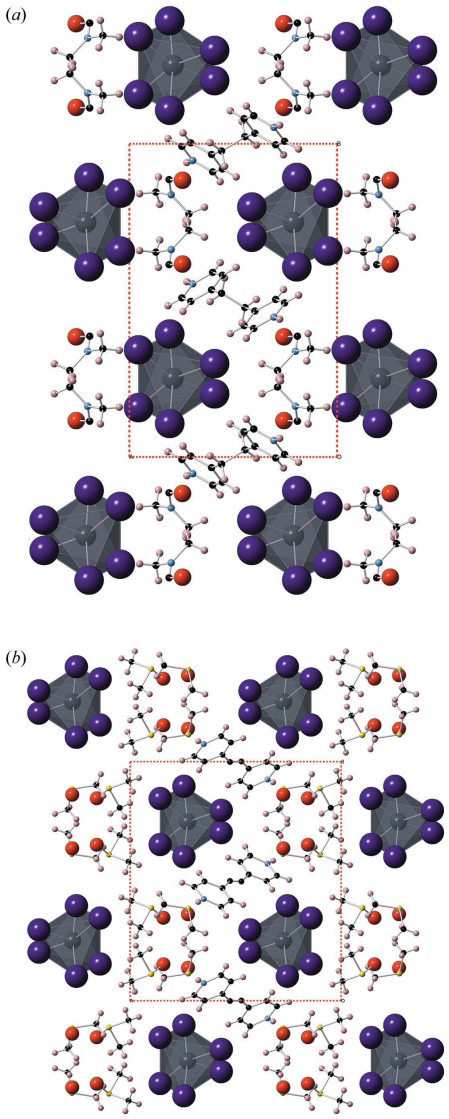

Figure 8
(*a*) The DMF solvate of 1,2-bis(4-pyridyl)ethane, $[(HC_5H_4NCH_2)_2][PbI_3]_2{\cdot}2$DMF (4), and (*b*) DMSO solvate of 1,2-di(4-pyridyl)ethylene lead iodide, $[(HC_5H_4NCH_2)_2][PbI_3]_2{\cdot}4$DMSO (5). Both solvate structures are viewed down the c axis (b axis vertical), which is along the one-dimensional face-sharing lead iodide chains, and can be seen to adopt very similar structure types in the arrangement of both organic and inorganic components.

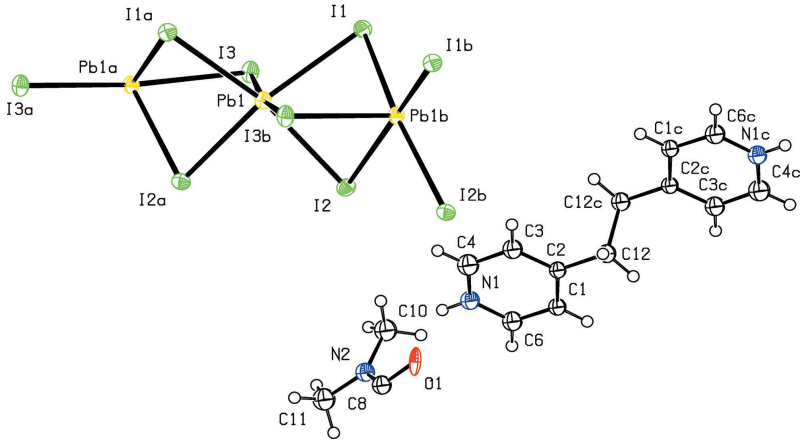

Figure 9
ORTEP drawing of $[(HC_5H_4NCH_2)_2][PbI_3]_2{\cdot}2DMF$ (4).

Table 8
Hydrogen-bonding parameters (Å, °) for imidazolium lead iodide (6).

D—H···A	$d(D$—H)	d(H···A)	$d(D\cdots A)$	$\angle(DHA)$
C3—H3···I4	0.93	3.23	3.73 (5)	115.6
C3—H3···I4^{i}	0.93	2.95	3.81 (5)	155.3
N1—H1···I3^{ii}	0.86	3.23	3.95 (6)	142.8

Symmetry codes: (i) $-x+y+1, -x+1, z$; (ii) $y, -x+y, -z+1$.

Table 9
Hydrogen-bonding parameters (Å, °) for imidazolium lead iodide (6).

D—H···A	$d(D$—H)	d(H···A)	$d(D\cdots A)$	$\angle(DHA)$
N1—H5A···I3^{i}	0.89	2.75	3.596 (4)	158.1
N1—H5B···I2^{ii}	0.89	3.31	3.890 (4)	125.1
N1—H5B···I3^{iii}	0.89	3.07	3.691 (4)	128.6
N1—H5B···I4^{iii}	0.89	3.12	3.672 (4)	122.3
N2—H6A···I2	0.89	2.76	3.582 (4)	154.6
N2—H6B···I2^{iv}	0.89	3.21	3.777 (4)	124.1
N2—H6B···I4	0.89	3.03	3.629 (4)	125.9
C4—H4A···I3^{i}	0.97	3.12	3.923 (5)	140.8
C4—H4B···I2^{iv}	0.97	3.08	3.744 (5)	126.8
C4—H4B···I4^{iv}	0.97	3.22	3.915 (5)	129.9
C2—H2A···I3^{iii}	0.97	3.17	3.771 (5)	121.5
C2—H2A···I4^{i}	0.97	3.13	3.842 (5)	131.5
C2—H2B···I2	0.97	3.12	3.906 (5)	139.4
C3—H3A···I3^{v}	0.97	3.12	3.885 (5)	137.2
C3—H3A···I4	0.97	3.29	3.886 (5)	121.6
C3—H3B···I3^{vi}	0.97	3.18	3.912 (6)	133.9
C3—H3B···I4^{i}	0.97	3.28	3.880 (5)	121.6
C1—H1A···I2^{ii}	0.97	3.20	3.886 (6)	129.6
C1—H1A···I4^{iv}	0.97	3.31	3.935 (5)	124.3
C1—H1B···I2^{vii}	0.97	3.17	3.900 (5)	133.3
C1—H1B···I4^{iii}	0.97	3.27	3.899 (5)	123.8

Symmetry codes: (i) $-x+1, -y+1, -z+1$; (ii) $-x+\frac{1}{2}, y, -z+\frac{3}{2}$; (iii) $x-1, y, z$; (iv) $-x+1, -y+2, -z+1$; (v) $-x+\frac{3}{2}, y, -z+\frac{3}{2}$; (vi) $x-\frac{1}{2}, -y+1, z-\frac{1}{2}$; (vii) $x-\frac{1}{2}, -y+2, z-\frac{1}{2}$.

model for compound (6) is presented in this work. This disorder may be associated with rotational disorder of the imidazolium cation ring over the five possible orientations and in this study this was modelled using a planar cyclopentadienyl ring with 1.07 occupancy for each 'carbon' atom position.

Piperazinium lead iodide (7) forms yellow crystals containing isolated $[PbI_6]^{4-}$ octahedra under hydrothermal conditions in aqueous hydroiodic acid. The diprotonated piperazinium molecular cations are packed in a herringbone fashion along the (110) plane, Figs. 13 and 14. Examples of hybrid inorganic organic structures containing isolated $[PbI_6]^{4-}$ octahedra are not nearly so extensively described in the literature as one-dimensional and two-dimensional frameworks; however, one key example is the dihydrated methylammonium lead iodide $(CH_3NH_3)_4PbI_6{\cdot}2H_2O$ (Vincent *et al.*, 1987), which is a well studied material found in the degradation of perovskite-type solar cells under humid conditions (Leguy *et al.*, 2015). The methylammonium lead iodide dihydrate displays far less distortion from ideal octahedral geometry (Pb—I range: 3.195–3.231 Å, I—Pb—I bond angles 87.6–92.4°), likely due to the conformational requirements of incorporating the six-membered ring of piperazine into the inter-octahedral void (Table 9).

4. Conclusions

With the growing focus of research on the next generation of sustainable energy materials hybrid inorganic organic photo-

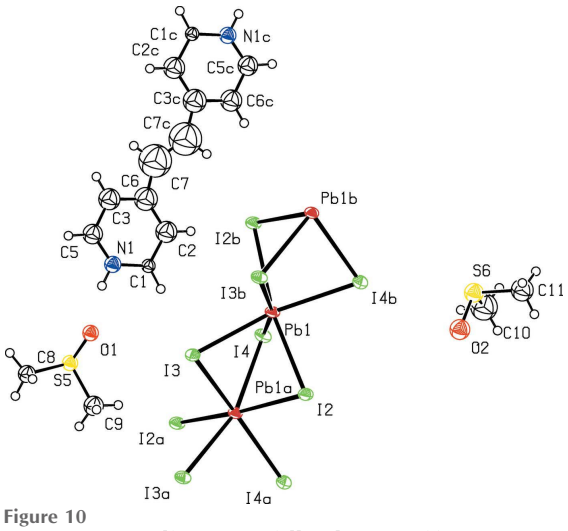

Figure 10
ORTEP drawing of $[(HC_5H_4NCH_2)_2][PbI_3]_2{\cdot}4DMSO$ (5).

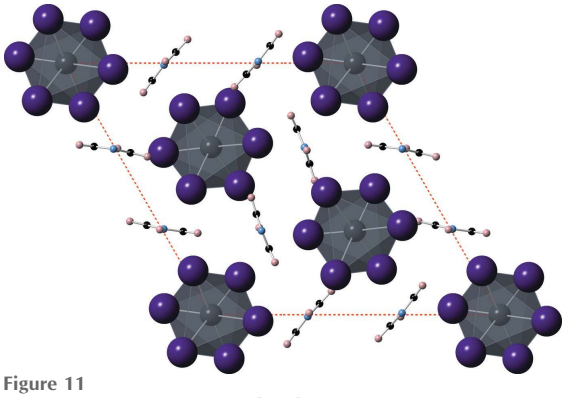

Figure 11
Face-sharing chain structure of $[PbI_3]^-$ in imidazolium lead iodide (6) viewed down the *c* axis (*b* axis horizontal) which is parallel to lead iodide chains.

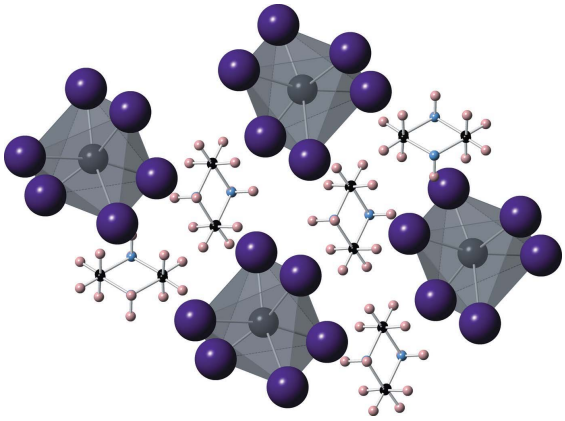

Figure 13
Piperazinium lead iodide (7) displaying isolated $[PbI_6]^{4-}$ octahedra with significant distortions from ideal octahedral geometry.

voltaic materials, containing PbI_6 octahedra have become of increasing technological importance. As well as studying the photoactive materials themselves and developing new functional semiconducting compounds understanding how these materials can be processed directly from solutions and how they degrade through the formation of solvates are topics that will be central to their deployment into usable devices.

A wide range of structural motifs are accessible through alteration to the connectivity between octahedral units, template by specific organic cations. 4-Chlorobenzylammonium lead iodide is typical of the layered two-dimensional perovskite structures adopted by sterically undemanding, linear-terminating organic cations. Of note is the way in which the $-CH_2-NH_3$ end group interacts with the lead iodide layer in a similar way to the methylamine cation in the photovoltaic MAPI (methylammonium lead iodide) forming three NH$\cdots$I hydrogen bonds with the PbI_6 iodide ions. The aliphatic end group, $R-CH_2-NH_3$, is sufficiently narrow and flexible to dock into the perovskite layer and form these hydrogen bonds. However, for organic amine cations with a larger cross-sectional profile corner-sharing PbI_6 octahedra seems to become a less favourable structural feature possibly due to the inability of the protonated amine end groups to form suitable hydrogen-bonded coordination geometries. This leads to the formation of lower dimensional structures, including predominantly one-dimensional polymeric lead iodide chains, with no hydrogen bonding between the protonated amine and iodide ions. For a small organic cation with high charge density such as the diprotonated [H_2-piperazinium]$^{2+}$ cation it is possible to stabilize a rather unusual structure containing isolated $[PbI_6]^{4-}$ octahedra.

The ability of hybrid organic inorganic lead(II) iodides and their solvates to adopt structures in which very different structural motifs for the inorganic lead-iodide networks exist is of some significance. These structural units range all the way from fully vertex-sharing PbI_6 octahedra, through various vertex, edge- and face-sharing chains to discrete $[PbI_6]^{4-}$

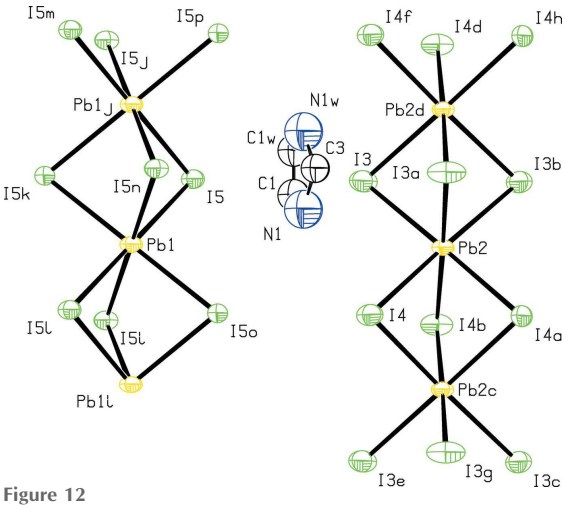

Figure 12
ORTEP drawing of imidazolium lead iodide.

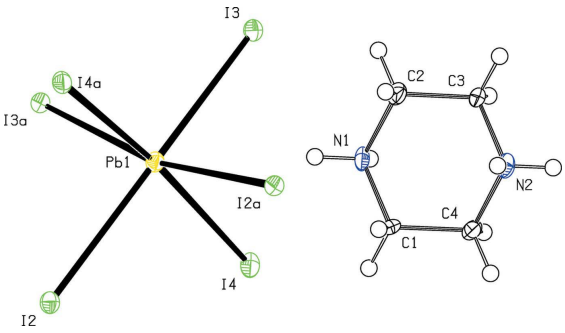

Figure 14
ORTEP drawing of piperazinium lead iodide (7) displaying one isolated $[PbI_6]^{4-}$ octahedron and a cyclohexane-like piperazinium ion.

octahedra. One reason why studying these different structures and understanding the factors that stabilize them, such as hydrogen bonding between the protonated amine and iodide anions, is to comprehend their phase stability and ability to undergo solvation. Thus, compounds such as formamidinium lead iodide (FAPI) rapidly interconverts at room temperature between the yellow and black phases – the former containing $[PbI_3]^-$ chains, seen in structures (4) and (5) here, and the latter fully vertex linked octahedra in a perovskite structure (Weller *et al.*, 2015). This very facile phase transformation has inhibited the investigation and use of FAPI for solar cell applications (Binek *et al.*, 2015). Similarly methylammonium lead iodide undergoes rapid hydration from a perovskitic phase to a monohydrate containing $[PbI_3]^-$ chains and a dihydrate containing discrete $[PbI_6]^{4-}$ octahedra (Leguy *et al.*, 2015): again this is an important factor limiting the development of solar cells using this material. Through the development of the structural chemistry of hybrid organic inorganic lead(II) iodides and their solvates, as presented in this paper, useful insights into these phase transformation and solvation routes will become possible.

Acknowledgements

OJW would like to thank EPSRC (EP/G03768X/1) for PhD studentship funding *via* the EPSRC Doctoral Training Centre in Sustainable Chemical Technologies.

References

Billing, D. G. & Lemmerer, A. (2007). *Acta Cryst.* B**63**, 735–747.
Binek, A., Hanusch, F. C., Docampo, P. & Bein, T. (2015). *J. Phys. Chem. Lett.* **6**, 1249–1253.
Chen, Y., Yang, Z., Guo, C.-X., Ni, C.-Y., Li, H.-X., Ren, Z.-G. & Lang, J.-P. (2011). *CrystEngComm*, **13**, 243–250.
Dammak, T., Koubaa, M., Boukheddaden, K., Bougzhala, H., Mlayah, A. & Abid, Y. (2009). *J. Phys. Chem. C*, **113**, 19305–19309.
Fan, L.-Q., Wu, L.-M. & Chen, L. (2006). *Inorg. Chem.* **45**, 3149–3151.
Innocenzi, P. & Lebeau, B. (2005). *J. Mater. Chem.* **15**, 3821.
Kitazawa, N. (1997). *Mater. Sci. Eng. B*, **49**, 233–238.
Lee, M. M., Teuscher, J., Miyasaka, T., Murakami, T. N. & Snaith, H. J. (2012). *Science*, **338**, 643–647.
Leguy, A. M. A., Hu, Y., Campoy-Quiles, M., Alonso, M. I., Weber, O. J., Azarhoosh, P., van Schilfgaarde, M., Weller, M. T., Bein, T., Nelson, J., Docampo, P. & Barnes, P. (2015). *Chem. Mater.* **27**, 3397–3407.
Li, H.-H., Wang, Y.-J., Lian, Z.-X., Xu, Y.-F., Wang, M., Huang, S.-W. & Chen, Z.-R. (2012). *J. Mol. Struct.* **1016**, 118–125.
Liao, W.-Q., Zhang, Y., Hu, C.-L., Mao, J.-G., Ye, H.-Y., Li, P.-F., Huang, S. D. & Xiong, R.-G. (2015). *Nat. Commun.* **6**, 7338.
Liu, Z., Yu, W.-T., Tao, X.-T., Jiang, M.-H., Yang, J.-X. & Wang, L. Z. (2004). *Kristallogr. New Cryst. Struct.* **219**, 457.
Mercier, N., Louvain, N. & Bi, W. (2009). *CrystEngComm*, **11**, 720.
Mitzi, D. B. (1996). *Chem. Mater.* **8**, 1–12.
Mitzi, D. B. (2001). *J. Chem. Soc. Dalton Trans.* pp. 1–12.
Mitzi, D. B., Feild, C. A., Harrison, W. T. A. & Guloy, A. M. (1994). *Nature*, **369**, 467–469.
Sheldrick, G. M. (2008). *Acta Cryst.* A**64**, 112–122.
Sheldrick, G. M. (2015). *Acta Cryst.* C**71**, 3–8.
Spek, A. L. (2009). *Acta Cryst.* D**65**, 148–155.
Tang, Z. & Guloy, A. M. (1999). *J. Am. Chem. Soc.* **121**, 452–453.
Teo, B. K., Wu, L.-M., Wu, X.-T. & Chen, L. (2009). *Coord. Chem. Rev.* **253**, 2787–2804.
Vincent, B. R., Robertson, K. N., Cameron, T. S. & Knop, O. (1987). *Can. J. Chem.* **65**, 1042–1046.
Weller, M. T., Weber, O. J., Frost, J. M. & Walsh, A. (2015). *J. Phys. Chem. Lett.* **6**, 3209–3212.
Weller, M. T., Weber, O. J., Henry, P. F., Di Pumpo, A. M. & Hansen, T. C. (2015). *Chem. Commun.* **51**, 4180–4183.
Yin, H.-D. & Cui, J.-C. (2004). *Chem. Res. Chin. Univ.* **20**, 548–550.

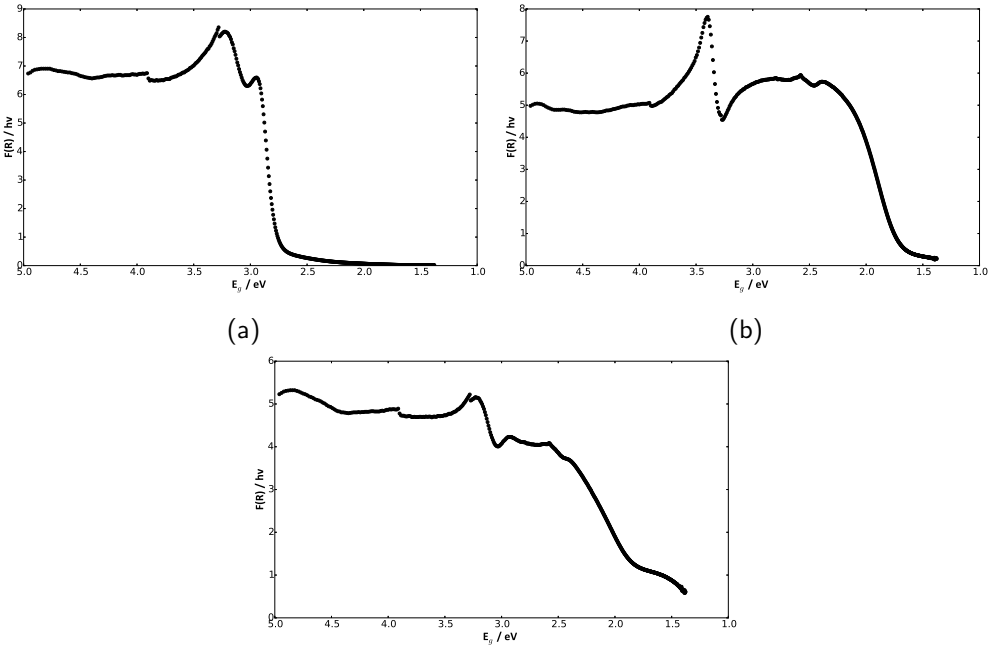

Figure 7-1: UV-vis reflectance spectra for compounds

7.3 Further Results

The UV-vis reflectance spectra for compounds **2**, **4** and **5** described in the preceding paper with highly conjugated organic ions demonstrate that these compounds absorb significantly across the visible spectrum. The reflectance spectra of compound **2** [H_2-4,4'-bipyridyl][PbI_4], and **4**, 1,2-bis(4-pyridyl)ethane DMF solvate, $[(HC_5H_4NCH_2)_2][PbI_3]_2 \cdot 2DMF$, are shown in Figure 7-1a and 7-1b. Comparing these spectra, it is apparent that the sharp onset of absorption in **4** around 3.0 eV may stem from the 1D inorganic framework. While **2** displays broad absorption in visible, with a further sharp transition above 3.0 eV potentially due to lead iodide framework.

In addition to the hybrid organic lead iodide phases described in the preceding research paper, two organic polyiodide structures, rather than hybrid lead iodide framework compounds, were recovered from syntheses in concentrated hydroiodic acid carried out under hydrothermal conditions. When 1,2-di(4-pyridyl)ethylene iodide or 1,2-bis(4-pyridyl)ethane iodide are combined with lead iodide under acidic hydrothermal conditions, the synthesis conditions favour the formation of organic polyiodides, leaving the lead iodide unreacted.

In solution I^- and I_3^- ions dominate iodide chemistry, while in the solid state a wide va-

riety of polyiodides are accessible given suitable templating counterions.[254] Diiodide ions were observed for the acidic hydrothermal synthesis of 1,2-bis(4-pyridyl)ethane iodide, with an I–I bond length of 2.8050(9) Å, longer than molecular iodine, and a greater distance 3.3660(2) Å between adjacent I_2 ions, the latter of which is smaller than the sum of van der Waals radii (3.96 Å) and classified as a secondary bonding interaction.[255]

1,2-di(4-pyridyl)ethylene forms an equivalent polyiodide structure with an II bonding distance of 2.8111(11)Å. Both polyiodide materials were composed of dark, lustrous crystals, indicating that these materials may display interesting electronic and optical properties deserving of further study. The 1,2-di(4-pyridyl)ethylene differs to 1,2-bis(4-pyridyl)ethane only by the conjugation of the central C-C bond, restricting the flexibility of the molecule. An organic iodide was formed under acidic hydrothermal conditions, crystallising in space group *Pnma*, in exactly analogous manner to 1,2-bis(4-pyridyl)ethane (I-I bond length 3.3751(2) Å).

The organic iodide phase was recovered from synthesis under acidic hydrothermal conditions. 0.251 g 1,2-bis(4-pyridyl)ethane.2HI and 0.264 g PbI_2 were combined with 5mL hydroiodic acid (57wt% aq.) and sealed in a 23 mL Teflon-lined stainless steel autoclave. The mixture was heated to 140°C for 24 hours before cooling to room temperature at a rate of 5°C / hour. Black needle crystals up to 5 mm in length and a yellow powder were recovered from the autoclave, washed with ethanol and dried at 50°C. When 1,2-di(4-pyridyl)ethylene.2HI was used in place of 1,2-bis(4-pyridyl)ethane.2HI under identical experimental conditions, an equivalent polyiodide framework was recovered.

Single crystal data was collected at 150 K with an Aglient SuperNova dual tube Eos S2 CCD diffractometer operating graphite-monochromated Mo K_α ($\lambda = 0.7093$ Å) radiation. Structure solution and refinement was carried out in WinGX using XPREP and SHELXS2013 to solve structures by direct methods, and SHELXL2013 for structure refinement.

Table 7.1: Single crystal structure refinement of 1,2-bis(4-pyridyl)ethane iodide (bpaI) and 1,2-di(4-pyridyl)ethylene iodide (dpeI)

Compound	**bpaI**	**dpeI**
Empirical formula	C24 H28 I8 N4	C24 H24 I8 N4
Formula weight	1387.7	106.44
Temperature	150(2) K	293(2) K
Wavelength	0.71073 Å	0.71073 Å
Crystal system	Orthorhombic	Orthorhombic
Space group	P m n a	P m n a
Unit cell dimensions	a = 8.4961(5) Å a= 90°.	a = 4.6745(2 α= 90°.
	b = 4.6373(2) Å b= 90°.	b = 8.4958(4 β= 90°.
	c = 22.2544(12) Å g = 90°.	c = 22.3318(γ = 90°.
Volume	876.80(8) Å3	886.88(6) Å3
Z	1	1
Density (calculated)	2.628 Mg/m3	2.591 Mg/m3
Absorption coefficient	7.095 mm-1	7.014 mm-1
F(000)	624	620
Crystal size	0.4 x 0.2 x 0.1 mm3	0.5 x 0.2 x 0.1 mm3
Theta range for data collection	3.646 to 29.313°.	3.639 to 29.355°.
Index ranges	-11<=h<=11, -6<=k<=6, -29<=l<=29	-6<=h<=6, -11<=k<=11, -30<=l<=29
Reflections collected	6434	12114
Independent reflections	1190 [R(int) = 0.0402]	1238 [R(int) = 0.0361]
Completeness to theta = 25.242°	99.80%	99.80%
Refinement method	Full-matrix least-squares on F2	Full-matrix least-squares on F2
Data / restraints / parameters	1190 / 0 / 49	1238 / 0 / 30
Goodness-of-fit on F2	1.072	1.089
Final R indices [I>2sigma(I)]	R1 = 0.0314, wR2 = 0.0664	R1 = 0.0356, wR2 = 0.0724
R indices (all data)	R1 = 0.0388, wR2 = 0.0699	R1 = 0.0425, wR2 = 0.0751
Extinction coefficient	n/a	n/a
Largest diff. peak and hole	0.696 and -1.439 e.Å-3	1.010 and -1.098 e.Å-3

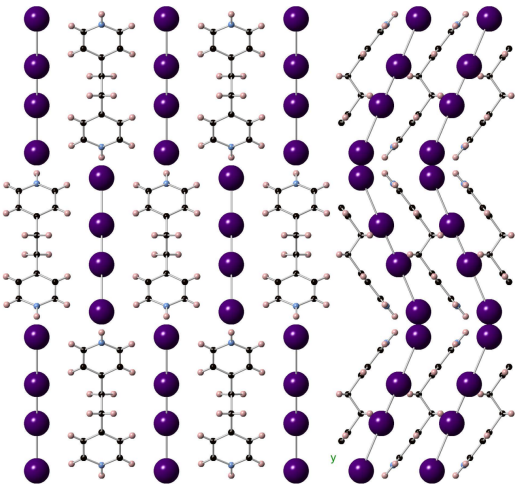

Figure 7-2: 1,2-bis(4-pyridyl)ethane iodide viewed along the b axis (left hand panel) and a axis (right hand panel)

Chapter 8

Conclusions

The structural chemistry of hybrid (organic-inorganic) halide perovskites and hybrid framework compounds has been explored in detail in the results presented in this thesis. Review of the scientific literature in Chapter 1 emphasises the growing role of these materials in high performance optoelectronic devices and the current state of understanding of their physicochemical material properties. Crystallographic diffraction techniques are central to understanding the atomic structure of these crystalline semiconductors. In this thesis, neutron diffraction has been demonstrated to be a particularly powerful technique for understanding the atomic structure and bonding interactions within these hybrid materials.

The complete phase behaviour of methylammonium lead iodide has been described for the first time by refinement of the atomic structure from constant wavelength neutron powder diffraction patterns, collected on D20 at the Institut Laue-Langevin over a wide temperature range of 100-352 K. The structural models include refinement of carbon, nitrogen and hydrogen positions, providing experimental evidence of the effects hydrogen bonding between the molecular ion and the inorganic lattice on the observed phase behaviour. In the orthorhombic phase below 152 K, the methylammonium cations are ordered, with cations in adjacent cells arranged head-to-tail. These orientations optimise hydrogen bonding interactions between the N-H hydrogens and the iodide ions of the inorganic framework. Above 152 K, a first order phase transition to a tetragonal phase is observed, with rotation of organic cations around the C-N axis unlocked, with this rotation predominantly occurring in the *ab* plane. The tetragonal phase diffraction peaks coalesce as a high symmetry cubic phase is formed above 327 K, above which the MA cation is disordered isotropically on the timescale of the diffraction experiment. Large atomic displacements support a picture of a high degree of thermal fluctuation in both the organic and inorganic components

at and above room temperature. Methylammonium lead halide single crystals have been synthesised and the optical and vibrational spectra of these crystals measured by ellipsometry and Raman spectroscopy, with assignment of spectral features supported by *ab initio* computational calculations.

Formamidinium lead iodide displays more complex phase behaviour than methylammonium lead iodide, including polymorphism. The room temperature phase of the metastable α-polymorph is shown for the first time to be cubic, analogous to the cubic phase of methylammonium lead iodide, using high-resolution, time-of-flight neutron powder diffraction at HRPD, ISIS. A lattice parameter of a = 6.3620(8) Å was obtained at 300 K, considerably larger than $MAPbI_3$ and the formamidinium ions within this structure were shown to be rotationally mobile, with a turnover frequency of 0.5 THz, by molecular dynamics simulations. The polymorphism and variable temperature phase behaviour of $FAPbI_3$ has been further investigated by both constant wavelength and time-of-flight neutron powder diffraction. A tetragonal phase is confirmed in the 285-140 K range, while competing hypotheses present in the literature are evaluated for the identity of the phase present below 140 K.

The composition and phase behaviour of methylammonium / formamidinium lead iodide solid solutions has been investigated. Solution ^{1}H NMR has been shown to be a useful technique for quantitative composition determination. The phase transition temperatures and transition at room temperature from tetragonal to cubic crystal systems has been investigated by powder and single crystal X-ray diffraction. Further studies elucidated the kinetics of degradation of these perovskite phases to PbI_2, with solid solutions shown to be more stable with respect to environmental conditions and polymorphic transformation than the parent compounds. Novel hybrid lead iodide frameworks with varying dimensionality, templated by different organic cations, have also been synthesised and their structures determined by single crystal X-ray diffraction.

These new results expand knowledge of the atomic structure and phase behaviour of hybrid organic-inorganic lead iodide materials, with direct relevance for both basic understanding of fundamental material properties and application in semiconductor devices, including thin film photovoltaic cells. For solar cell applications knowledge of the phase behaviour is highly relevant, since the temperature range at which these transitions occur overlaps with the temperature operating range of a practical device. Since many physical material properties are affected by the crystal symmetry and dynamic behaviour, dramatic phase shifts, for example at the tetragonal / orthorhombic transition of $MAPbI_3$, are relevant considerations for device design and in Chapter 6, exchanging methylammonium for formamidinium cations to form A-site solid solutions is shown to affect the temperature of the cubic / tetragonal phase transition.

Identification of promising candidate solar cell absorbers through exploratory materials synthesis may yield new materials that retain the privileged electronic structure of hybrid perovskites while displaying improved stabilities. While the hybrid framework compounds reported in Chapter 7 display lower dimensionality and wider band gaps than hybrid perovskites, the higher stability of these frameworks and the visible light absorption of frameworks incorporating highly conjugated molecular ions, such as 4,4'-bipyridyl ions, suggests that candidate materials for solar energy conversion may be identified as a result of synthetic screening.

Atomic structural information is crucial for providing starting models to calculate electronic structure and defect structure through computation. To move from atomic structure towards an understanding of the atomic and electronic defect structure in these materials is crucial for semiconductor material design, yet largely unmapped for hybrid perovskites. Understanding the long range ordered atomic structure is a first step along this road. Both point defect structure and extended defects will impact the performance and stability of these materials in photovoltaic cells. The role of hydrogen bonding in the observed phase behaviour is also unique to hybrid perovskites among high performance semiconductor materials. The results obtained in this thesis on the atomic coordinates of hydrogen in $MAPbI_3$ are already being put to use in comparison to first principles calculations.[256]

Future directions for perovskites materials chemistry include improved understanding of the phase behaviour and phase stability of solid solutions, which are increasingly important in solar cell applications. Extensive modifications beyond the perovskite structure using larger (e.g. alkyl chain primary amines) and smaller (e.g. rubidium) cations, are possible in active device layers, but the role these play, whether taken up into bulk crystal structures or residing at grain boundaries and interfaces, remains to be better understood. Efficient heterovalent doping of known hybrid perovskites to control the doping densities and majority charge carrier is also yet to be rationalised, which would open more opportunities in optoelectronics, include formation of perovskite PN junctions.

These materials represent the first family of high performance semiconductors that can be crystallised from solution, near room temperature. If environmental stability of the materials can be developed and demonstrated, this carries huge implications for the possibilities of high volume manufacture of efficient, thin photovoltaic cells for the generation of renewable energy.

References

[1] World Bank, *https://openknowledge.worldbank.org/handle/10986/2135*, 2017.

[2] S. L. Lewis and M. A. Maslin, *Nature*, 2015, **519**, 171–180.

[3] T. P. Hughes, M. L. Barnes, D. R. Bellwood, J. E. Cinner, G. S. Cumming, J. B. C. Jackson, J. Kleypas, I. A. van de Leemput, J. M. Lough, T. H. Morrison, S. R. Palumbi, E. H. van Nes and M. Scheffer, *Nature*, 2017, **546**, 82–90.

[4] J. H. Ryther and W. M. Dunstan, *Science (New York, N.Y.)*, 1971, **171**, 1008–13.

[5] A. Seaton, D. Godden, W. MacNee and K. Donaldson, *The Lancet*, 1995, **345**, 176–178.

[6] L. Jarup, *British Medical Bulletin*, 2003, **68**, 167–182.

[7] R. C. Thompson, C. J. Moore, F. S. vom Saal and S. H. Swan, *Philosophical transactions of the Royal Society of London. Series B, Biological sciences*, 2009, **364**, 2153–66.

[8] V. Smil, *The earth's biosphere : evolution, dynamics, and change*, MIT Press, 2002, p. 346.

[9] S. A. Marcott, J. D. Shakun, P. U. Clark and A. C. Mix, *Science (New York, N.Y.)*, 2013, **339**, 1198–201.

[10] J. R. Petit, J. Jouzel, D. Raynaud, N. I. Barkov, J.-M. Barnola, I. Basile, M. Bender, J. Chappellaz, M. Davis, G. Delaygue, M. Delmotte, V. M. Kotlyakov, M. Legrand, V. Y. Lipenkov, C. Lorius, L. PÉpin, C. Ritz, E. Saltzman and M. Stievenard, *Nature*, 1999, **399**, 429–436.

[11] A. D. Barnosky, N. Matzke, S. Tomiya, G. O. U. Wogan, B. Swartz, T. B. Quental, C. Marshall, J. L. McGuire, E. L. Lindsey, K. C. Maguire, B. Mersey and E. A. Ferrer, *Nature*, 2011, **471**, 51–57.

[12] D. B. Wake and V. T. Vredenburg, *Proceedings of the National Academy of Sciences of the United States of America*, 2008, **105 Suppl**, 11466–73.

[13] M. L. McCallum, *Biodiversity and Conservation*, 2015, **24**, 2497–2519.

[14] G. Ceballos, P. R. Ehrlich and R. Dirzo, *Proceedings of the National Academy of Sciences of the United States of America*, 2017, **114**, E6089–E6096.

[15] B. D. Santer, K. E. Taylor, P. J. Gleckler, C. Bonfils, T. P. Barnett, D. W. Pierce, T. M. L. Wigley, C. Mears, F. J. Wentz, W. Brüggemann, N. P. Gillett, S. A. Klein, S. Solomon, P. A. Stott and M. F. Wehner, *Proceedings of the National Academy of Sciences of the United States of America*, 2009, **106**, 14778–83.

[16] C. Parmesan and G. Yohe, *Nature*, 2003, **421**, 37–42.

[17] J. A. Church and N. J. White, *Geophysical Research Letters*, 2006, **33**, n/a–n/a.

[18] N. Gruber, *Philosophical transactions. Series A, Mathematical, physical, and engineering sciences*, 2011, **369**, 1980–96.

[19] A. M. Haywood, H. J. Dowsett, P. J. Valdes, D. J. Lunt, J. E. Francis and B. W. Sellwood, *Philosophical transactions. Series A, Mathematical, physical, and engineering sciences*, 2009, **367**, 3–17.

[20] P. J. Landrigan, R. Fuller, N. J. Acosta, O. Adeyi, R. Arnold, N. Basu, A. B. Baldé, R. Bertollini, S. Bose-O'Reilly, J. I. Boufford, P. N. Breysse, T. Chiles, C. Mahidol, A. M. Coll-Seck, M. L. Cropper, J. Fobil, V. Fuster, M. Greenstone, A. Haines, D. Hanrahan, D. Hunter, M. Khare, A. Krupnick, B. Lanphear, B. Lohani, K. Martin, K. V. Mathiasen, M. A. McTeer, C. J. Murray, J. D. Ndahimananjara, F. Perera, J. Potočnik, A. S. Preker, J. Ramesh, J. Rockström, C. Salinas, L. D. Samson, K. Sandilya, P. D. Sly, K. R. Smith, A. Steiner, R. B. Stewart, W. A. Suk, O. C. van Schayck, G. N. Yadama, K. Yumkella and M. Zhong, *The Lancet Commission on pollution and health*, 2017, `http://www.ncbi.nlm.nih.gov/pubmed/29056410`.

[21] D. G. Nocera, *Energy & Environmental Science*, 2010, **3**, 993.

[22] W. Shockley and H. J. Queisser, *Journal of Applied Physics*, 1961, **32**, 510–519.

[23] C. Fritts, *Van Nostrands Engineering Magazine*, 1885, **32**, 388–395.

[24] W. Siemens, *Van Nostrands Engineering Magazine*, 1885, **32**, 514–516.

[25] D. Chapin, C. Fuller and G. Pearson, *Journal of Applied Physics*, 1954, **25**, 676–677.

[26] M. A. Green, Y. Hishikawa, E. D. Dunlop, D. H. Levi, J. Hohl-Ebinger and A. W. Ho-Baillie, *Progress in Photovoltaics: Research and Applications*, 2018, **26**, 3–12.

[27] K. Yoshikawa, H. Kawasaki, W. Yoshida, T. Irie, K. Konishi, K. Nakano, T. Uto, D. Adachi, M. Kanematsu, H. Uzu and K. Yamamoto, *Nature Energy*, 2017, **2**, 17032.

[28] F. Dimroth and S. Kurtz, *MRS Bulletin*, 2007, **32**, 230–235.

[29] E. Yablonovitch, O. D. Miller and S. R. Kurtz, 2012 38th IEEE Photovoltaic Specialists Conference, 2012, pp. 001556–001559.

[30] P. Jackson, D. Hariskos, R. Wuerz, O. Kiowski, A. Bauer, T. M. Friedlmeier and M. Powalla, *physica status solidi (RRL) - Rapid Research Letters*, 2015, **9**, 28–31.

[31] W. Wang, M. T. Winkler, O. Gunawan, T. Gokmen, T. K. Todorov, Y. Zhu and D. B. Mitzi, *Advanced Energy Materials*, 2014, **4**, 1301465.

[32] S. Kim, J.-S. Park and A. Walsh, *ACS Energy Letters*, 2018, **3**, 496–500.

[33] V. M. Fthenakis, *Renewable and Sustainable Energy Reviews*, 2004, **8**, 303–334.

[34] M. Marwede and A. Reller, *Resources, Conservation and Recycling*, 2012, **69**, 35–49.

[35] R. A. J. Janssen and J. Nelson, *Advanced Materials*, 2013, **25**, 1847–1858.

[36] C. J. Brabec, J. A. Hauch, P. Schilinsky and C. Waldauf, *MRS Bulletin*, 2005, **30**, 50–52.

[37] G. Lakhwani, A. Rao and R. H. Friend, *Annual Review of Physical Chemistry*, 2014, **65**, 557–581.

[38] B. O'Regan and M. Grätzel, *Nature*, 1991, **353**, 737–740.

[39] L. M. Peter, *Philosophical transactions. Series A, Mathematical, physical, and engineering sciences*, 2011, **369**, 1840–56.

[40] A. Zakutayev, *Current Opinion in Green and Sustainable Chemistry*, 2017, **4**, 8–15.

[41] A. Zakutayev, C. M. Caskey, A. N. Fioretti, D. S. Ginley, J. Vidal, V. Stevanovic, E. Tea and S. Lany, *The Journal of Physical Chemistry Letters*, 2014, **5**, 1117–1125.

[42] A. Polman, M. Knight, E. C. Garnett, B. Ehrler and W. C. Sinke, *Science (New York, N.Y.)*, 2016, **352**, aad4424.

[43] U. Bach, *Nature Chemistry*, 2015, **7**, 616–617.

[44] H. J. Snaith, *The Journal of Physical Chemistry Letters*, 2013, **4**, 3623–3630.

[45] Q. A. Akkerman, G. Rainò, M. V. Kovalenko and L. Manna, *Nature Materials*, 2018, 1.

[46] K. A. Bush, A. F. Palmstrom, Z. J. Yu, M. Boccard, R. Cheacharoen, J. P. Mailoa, D. P. McMeekin, R. L. Z. Hoye, C. D. Bailie, T. Leijtens, I. M. Peters, M. C. Minichetti, N. Rolston, R. Prasanna, S. Sofia, D. Harwood, W. Ma, F. Moghadam, H. J. Snaith, T. Buonassisi, Z. C. Holman, S. F. Bent and M. D. McGehee, *Nature Energy*, 2017, **2**, 17009.

[47] A. Kojima, K. Teshima, Y. Shirai and T. Miyasaka, *Journal of the American Chemical Society*, 2009, **131**, 6050–6051.

[48] D. B. Mitzi, *Journal of the Chemical Society, Dalton Transactions*, 2001, 1–12.

[49] S. Wang, D. B. Mitzi, C. a. Feild and A. Guloy, *Journal of the American Chemical Society*, 1995, **117**, 5297–5302.

[50] D. B. Mitzi, *Chemistry of Materials*, 1996, **8**, 791–800.

[51] D. B. Mitzi, C. A. Feild, W. T. A. Harrison and A. M. Guloy, *Nature*, 1994, **369**, 467–469.

[52] K. Chondroudis and D. B. Mitzi, *Chemistry of Materials*, 1999, **11**, 3028–3030.

[53] J.-H. Im, C.-R. Lee, J.-W. Lee, S.-W. Park and N.-G. Park, *Nanoscale*, 2011, **3**, 4088.

[54] H.-S. Kim, C.-R. Lee, J.-H. Im, K.-B. Lee, T. Moehl, A. Marchioro, S.-J. Moon, R. Humphry-Baker, J.-H. Yum, J. E. Moser, M. Grätzel and N.-G. Park, *Scientific reports*, 2012, **2**, 591.

[55] M. M. Lee, J. Teuscher, T. Miyasaka, T. N. Murakami and H. J. Snaith, *Science*, 2012, **338**, 643–647.

[56] M. Liu, M. B. Johnston and H. J. Snaith, *Nature*, 2013, **501**, 395–398.

[57] G. Xing, N. Mathews, S. Sun, S. S. Lim, Y. M. Lam, M. Gratzel, S. Mhaisalkar and T. C. Sum, *Science*, 2013, **342**, 344–347.

[58] I. Chung, B. Lee, J. He, R. P. H. Chang and M. G. Kanatzidis, *Nature*, 2012, **485**, 486–9.

[59] M. T. Klug, A. Osherov, A. A. Haghighirad, S. D. Stranks, P. R. Brown, S. Bai, J. T.-W. Wang, X. Dang, V. Bulović, H. J. Snaith and A. M. Belcher, *Energy Environ. Sci.*, 2017, **131**, 6050–6051.

[60] M. Beck, P. Seidel, G. Kleiss, J. Althaus, G. Volberg, A. Roth and B. Jaeckel, *29th European Photovoltaic Solar Energy Conference and Exhibition*, 2014, 3477–3482.

[61] G. E. Eperon, T. Leijtens, K. A. Bush, R. Prasanna, T. Green, J. T.-W. Wang, D. P. McMeekin, G. Volonakis, R. L. Milot, R. May, A. Palmstrom, D. J. Slotcavage, R. A. Belisle, J. B. Patel, E. S. Parrott, R. J. Sutton, W. Ma, F. Moghadam, B. Conings, A. Babayigit, H.-G. Boyen, S. Bent, F. Giustino, L. M. Herz, M. B. Johnston, M. D. McGehee and H. J. Snaith, *Science*, 2016, **354**, 861–865.

[62] J. Baker, K. Hooper, S. Meroni, A. Pockett, J. McGettrick, Z. Wei, R. Escalante, G. Oskam, M. Carnie and T. Watson, *Journal of Materials Chemistry A*, 2017, **5**, 18643–18650.

[63] S. Yakunin, L. Protesescu, F. Krieg, M. I. Bodnarchuk, G. Nedelcu, M. Humer, G. De Luca, M. Fiebig, W. Heiss and M. V. Kovalenko, *Nature Communications*, 2015, **6**, 8056.

[64] A. Mei, X. Li, L. Liu, Z. Ku, T. Liu, Y. Rong, M. Xu, M. Hu, J. Chen, Y. Yang, M. Gratzel and H. Han, *Science*, 2014, **345**, 295–298.

[65] O. Nazarenko, S. Yakunin, V. Morad, I. Cherniukh and M. V. Kovalenko, *NPG Asia Materials*, 2017, **9**, e373.

[66] W. S. Yang, J. H. Noh, N. J. Jeon, Y. C. Kim, S. Ryu, J. Seo and S. I. Seok, *Science*, 2015, **348**, 1234–1237.

[67] M. Saliba, T. Matsui, J.-Y. Seo, K. Domanski, J.-P. Correa-Baena, M. K. Nazeeruddin, S. M. Zakeeruddin, W. Tress, A. Abate, A. Hagfeldt and M. Grätzel, *Energy & Environmental Science*, 2016, **9**, 1989–1997.

[68] Y. Hou, X. Du, S. Scheiner, D. P. McMeekin, Z. Wang, N. Li, M. S. Killian, H. Chen, M. Richter, I. Levchuk, N. Schrenker, E. Spiecker, T. Stubhan, N. A. Luechinger, A. Hirsch, P. Schmuki, H. P. Steinrück, R. H. Fink, M. Halik, H. J. Snaith and C. J. Brabec, *Science*, 2017, **358**, 1192–1197.

[69] G. Grancini, C. Roldán-Carmona, I. Zimmermann, E. Mosconi, X. Lee, D. Martineau, S. Narbey, F. Oswald, F. De Angelis, M. Graetzel and M. K. Nazeeruddin, *Nature Communications*, 2017, **8**, 15684.

[70] J. Liang, J. Liu and Z. Jin, *Solar RRL*, 2017, **1**, 1700086.

[71] L. Protesescu, S. Yakunin, M. I. Bodnarchuk, F. Krieg, R. Caputo, C. H. Hendon, R. X. Yang, A. Walsh and M. V. Kovalenko, *Nano Letters*, 2015, **15**, 3692–3696.

[72] M. Saliba, T. Matsui, J.-Y. Seo, K. Domanski, J.-P. Correa-Baena, M. K. Nazeeruddin, S. M. Zakeeruddin, W. Tress, A. Abate, A. Hagfeldt and M. Grätzel, *Energy & Environmental Science*, 2016, **9**, 1989–1997.

[73] Y. Hu, S. Si, A. Mei, Y. Rong, H. Liu, X. Li and H. Han, *Solar RRL*, 2017, **1**, 1600019.

[74] A. M. Ganose, C. N. Savory and D. O. Scanlon, *Chemical Communications*, 2017, **53**, 20–44.

[75] D. W. DeQuilettes, S. Koch, S. Burke, R. K. Paranji, A. J. Shropshire, M. E. Ziffer and D. S. Ginger, *ACS Energy Letters*, 2016, **1**, 438–444.

[76] S. M. Jain, Z. Qiu, L. Häggman, M. Mirmohades, M. B. Johansson, T. Edvinsson and G. Boschloo, *Energy & Environmental Science*, 2016, **9**, 3770–3782.

[77] T. Duong, Y. Wu, H. Shen, J. Peng, X. Fu, D. Jacobs, E.-C. Wang, T. C. Kho, K. C. Fong, M. Stocks, E. Franklin, A. Blakers, N. Zin, K. McIntosh, W. Li, Y.-B. Cheng, T. P. White, K. Weber and K. Catchpole, *Advanced Energy Materials*, 2017, **7**, 1700228.

[78] D. J. Kubicki, D. Prochowicz, A. Hofstetter, S. M. Zakeeruddin, M. Grätzel and L. Emsley, *Journal of the American Chemical Society*, 2017, **139**, 14173–14180.

[79] D. Zhao, Y. Yu, C. Wang, W. Liao, N. Shrestha, C. R. Grice, A. J. Cimaroli, L. Guan, R. J. Ellingson, K. Zhu, X. Zhao, R.-G. Xiong and Y. Yan, *Nature Energy*, 2017, **2**, 17018.

[80] Y. Yang, M. Yang, D. T. Moore, Y. Yan, E. M. Miller, K. Zhu and M. C. Beard, *Nature Energy*, 2017, **2**, 16207.

[81] D. H. Cao, C. C. Stoumpos, C. D. Malliakas, M. J. Katz, O. K. Farha, J. T. Hupp and M. G. Kanatzidis, *APL Materials*, 2014, **2**, 091101.

[82] H. Tan, A. Jain, O. Voznyy, X. Lan, F. P. García de Arquer, J. Z. Fan, R. Quintero-Bermudez, M. Yuan, B. Zhang, Y. Zhao, F. Fan, P. Li, L. N. Quan, Y. Zhao, Z.-H. Lu, Z. Yang, S. Hoogland and E. H. Sargent, *Science*, 2017, **355**, 722–726.

[83] M. Kaltenbrunner, G. Adam, E. D. Głowacki, M. Drack, R. Schwödiauer, L. Leonat, D. H. Apaydin, H. Groiss, M. C. Scharber, M. S. White, N. S. Sariciftci and S. Bauer, *Nature Materials*, 2015, **14**, 1032–1039.

[84] M. Stolterfoht, C. M. Wolff, Y. Amir, A. Paulke, L. Perdigón-Toro, P. Caprioglio and D. Neher, *Energy & Environmental Science*, 2017, **10**, 1530–1539.

[85] A. Mei, X. Li, L. Liu, Z. Ku, T. Liu, Y. Rong, M. Xu, M. Hu, J. Chen, Y. Yang, M. Grätzel and H. Han, *Science (New York, N.Y.)*, 2014, **345**, 295–8.

[86] H. Chen and S. Yang, *Carbon-Based Perovskite Solar Cells without Hole Transport Materials: The Front Runner to the Market?*, 2017, `http://doi.wiley.com/10.1002/adma.201603994`.

[87] Y. Lin, B. Chen, F. Zhao, X. Zheng, Y. Deng, Y. Shao, Y. Fang, Y. Bai, C. Wang and J. Huang, *Advanced Materials*, 2017, **29**, 1700607.

[88] H. J. Snaith, A. Abate, J. M. Ball, G. E. Eperon, T. Leijtens, N. K. Noel, S. D. Stranks, J. T.-W. Wang, K. Wojciechowski and W. Zhang, *The Journal of Physical Chemistry Letters*, 2014, **5**, 1511–1515.

[89] B. C. O'Regan, P. R. F. Barnes, X. Li, C. Law, E. Palomares and J. M. Marin-Beloqui, *Journal of the American Chemical Society*, 2015, **137**, 5087–5099.

[90] P. Calado, A. M. Telford, D. Bryant, X. Li, J. Nelson, B. C. O'Regan and P. R. Barnes, *Nature Communications*, 2016, **7**, 13831.

[91] W. Rehman, D. P. McMeekin, J. B. Patel, R. L. Milot, M. B. Johnston, H. J. Snaith and L. M. Herz, *Energy Environ. Sci.*, 2017, **10**, 361–369.

[92] C. Wang, C. Xiao, Y. Yu, D. Zhao, R. A. Awni, C. R. Grice, K. Ghimire, I. Constantinou, W. Liao, A. J. Cimaroli, P. Liu, J. Chen, N. J. Podraza, C.-S. Jiang, M. M. Al-Jassim, X. Zhao and Y. Yan, *Advanced Energy Materials*, 2017, **7**, 1700414.

[93] A. A. Zhumekenov, M. I. Saidaminov, M. A. Haque, E. Alarousu, S. P. Sarmah, B. Murali, I. Dursun, X.-H. Miao, A. L. Abdelhady, T. Wu, O. F. Mohammed and O. M. Bakr, *ACS Energy Letters*, 2016, **1**, 32–37.

[94] D. Shi, V. Adinolfi, R. Comin, M. Yuan, E. Alarousu, A. Buin, Y. Chen, S. Hoogland, A. Rothenberger, K. Katsiev, Y. Losovyj, X. Zhang, P. A. Dowben, O. F. Mohammed, E. H. Sargent and O. M. Bakr, *Science (New York, N.Y.)*, 2015, **347**, 519–22.

[95] C. Wehrenfennig, G. E. Eperon, M. B. Johnston, H. J. Snaith and L. M. Herz, *Advanced Materials*, 2014, **26**, 1584–1589.

[96] E. Edri, S. Kirmayer, S. Mukhopadhyay, K. Gartsman, G. Hodes and D. Cahen, *Nature Communications*, 2014, **5**, 3461.

[97] K. Miyano, N. Tripathi, M. Yanagida and Y. Shirai, *Accounts of Chemical Research*, 2016, **49**, 303–310.

[98] K. Miyano, M. Yanagida, N. Tripathi and Y. Shirai, *Applied Physics Letters*, 2015, **106**, 093903.

[99] R. E. Brandt, J. R. Poindexter, P. Gorai, R. C. Kurchin, R. L. Z. Hoye, L. Nienhaus, M. W. B. Wilson, J. A. Polizzotti, R. Sereika, R. Žaltauskas, L. C. Lee, J. L. MacManus-Driscoll, M. Bawendi, V. Stevanović and T. Buonassisi, *Chemistry of Materials*, 2017, **29**, 4667–4674.

[100] Y. Chen, H. T. Yi, X. Wu, R. Haroldson, Y. N. Gartstein, Y. I. Rodionov, K. S. Tikhonov, A. Zakhidov, X. Y. Zhu and V. Podzorov, *Nature Communications*, 2016, **7**, 12253.

[101] Z. Shao and S. M. Haile, *Nature*, 2004, **431**, 170–173.

[102] J. Wang, J. B. Neaton, H. Zheng, V. Nagarajan, S. B. Ogale, B. Liu, D. Viehland, V. Vaithyanathan, D. G. Schlom, U. V. Waghmare, N. A. Spaldin, K. M. Rabe, M. Wuttig and R. Ramesh, *Science (New York, N.Y.)*, 2003, **299**, 1719–22.

[103] R. H. Mitchell, M. D. Welch, A. R. Chakhmouradian and S. Mills, *Mineralogical Magazine*, 2017, **81**, 411–461.

[104] P. M. Woodward and IUCr, *Acta Crystallographica Section B Structural Science*, 1997, **53**, 32–43.

[105] C. J. Howard, H. T. Stokes and IUCr, *Acta Crystallographica Section B Structural Science*, 1998, **54**, 782–789.

[106] H. T. Stokes, E. H. Kisi, D. M. Hatch and C. J. Howard, *Acta crystallographica. Section B, Structural science*, 2002, **58**, 934–8.

[107] A. M. Glazer, *Acta Crystallographica Section B Structural Crystallography and Crystal Chemistry*, 1972, **28**, 3384–3392.

[108] H. L. Wells, G. F. Campbell, P. T. Walden and A. P. Wheeler, *American Journal of Science*, 1893, **44**, 121.

[109] C. K. Moller, *Nature*, 1958, **182**, 1436–1436.

[110] D. Weber, *Zeitschrift für Naturforschung B*, 1978, **33b**, 1443–1445.

[111] A. Walsh, *The Journal of Physical Chemistry C*, 2015, **119**, 5755–5760.

[112] W. Travis, E. N. K. Glover, H. Bronstein, D. O. Scanlon and R. G. Palgrave, *Chem. Sci.*, 2016, **7**, 4548–4556.

[113] J. M. Frost, K. T. Butler and A. Walsh, *APL Materials*, 2014, **2**, 081506.

[114] N. Onoda-Yamamuro, *Doctoral Thesis*, Osaka University, 1992.

[115] T. Chen, B. J. Foley, B. Ipek, M. Tyagi, J. R. D. Copley, C. M. Brown, J. J. Choi and S.-H. Lee, *Physical Chemistry Chemical Physics*, 2015, **17**, 31278–31286.

[116] A. M. A. Leguy, J. M. Frost, A. P. McMahon, V. G. Sakai, W. Kochelmann, C. Law, X. Li, F. Foglia, A. Walsh, B. C. O'Regan, J. Nelson, J. T. Cabral and P. R. F. Barnes, *Nature Communications*, 2015, **6**, 7124.

[117] D. Kubicki, D. Prochowicz, A. Hofstetter, P. Pechy, S. M. Zakeeruddin, M. Gratzel and L. Emsley, *Journal of the American Chemical Society*, 2017, **139**, 10055–10061.

[118] A. N. Beecher, O. E. Semonin, J. M. Skelton, J. M. Frost, M. W. Terban, H. Zhai, A. Alatas, J. S. Owen, A. Walsh and S. J. L. Billinge, *ACS Energy Letters*, 2016, **1**, 880–887.

[119] A. Bernasconi and L. Malavasi, *ACS Energy Letters*, 2017, **2**, 863–868.

[120] O. Yaffe, Y. Guo, L. Z. Tan, D. A. Egger, T. Hull, C. C. Stoumpos, F. Zheng, T. F. Heinz, L. Kronik, M. G. Kanatzidis, J. S. Owen, A. M. Rappe, M. A. Pimenta and L. E. Brus, *Physical Review Letters*, 2017, **118**, 136001.

[121] K. Drużbicki, R. S. Pinna, S. Rudić, M. Jura, G. Gorini and F. Fernandez-Alonso, *The Journal of Physical Chemistry Letters*, 2016, **7**, 4701–4709.

[122] D. H. Fabini, J. G. Labram, A. J. Lehner, J. S. Bechtel, H. A. Evans, A. Van der Ven, F. Wudl, M. L. Chabinyc and R. Seshadri, *Inorganic Chemistry*, 2017, **56**, 11–25.

[123] R. Comin, M. K. Crawford, A. H. Said, N. Herron, W. E. Guise, X. Wang, P. S. Whitfield, A. Jain, X. Gong, A. J. H. McGaughey and E. H. Sargent, *Physical Review B - Condensed Matter and Materials Physics*, 2016, **94**, 094301.

[124] R. Gottesman, L. Gouda, B. S. Kalanoor, E. Haltzi, S. Tirosh, E. Rosh-Hodesh,

Y. Tischler, A. Zaban, C. Quarti, E. Mosconi and F. De Angelis, *The Journal of Physical Chemistry Letters*, 2015, 2332–2338.

[125] R. Gottesman, E. Haltzi, L. Gouda, S. Tirosh, Y. Bouhadana, A. Zaban, E. Mosconi and F. De Angelis, *The Journal of Physical Chemistry Letters*, 2014, **5**, 2662–2669.

[126] E. T. Hoke, D. J. Slotcavage, E. R. Dohner, A. R. Bowring, H. I. Karunadasa and M. D. McGehee, *Chem. Sci.*, 2014, **6**, 613–617.

[127] Y. Zhou, L. You, S. Wang, Z. Ku, H. Fan, D. Schmidt, A. Rusydi, L. Chang, L. Wang, P. Ren, L. Chen, G. Yuan, L. Chen and J. Wang, *Nature communications*, 2016, **7**, 11193.

[128] D. W. DeQuilettes, W. Zhang, V. M. Burlakov, D. J. Graham, T. Leijtens, A. Osherov, V. Bulović, H. J. Snaith, D. S. Ginger and S. D. Stranks, *Nature Communications*, 2016, **7**, 11683.

[129] X. Wu, L. Z. Tan, X. Shen, T. Hu, K. Miyata, M. T. Trinh, R. Li, R. Coffee, S. Liu, D. A. Egger, I. Makasyuk, Q. Zheng, A. Fry, J. S. Robinson, M. D. Smith, B. Guzelturk, H. I. Karunadasa, X. Wang, X. Zhu, L. Kronik, A. M. Rappe and A. M. Lindenberg, *Science Advances*, 2017, **3**, e1602388.

[130] H. Tsai, R. Asadpour, J.-C. Blancon, C. C. Stoumpos, O. Durand, J. W. Strzalka, B. Chen, R. Verduzco, P. M. Ajayan, S. Tretiak, J. Even, M. A. Alam, M. G. Kanatzidis, W. Nie and A. D. Mohite, *Science (New York, N.Y.)*, 2018, **360**, 67–70.

[131] G. Y. Kim, A. Senocrate, T.-Y. Yang, G. Gregori, M. Grätzel and J. Maier, *Nature Materials*, 2018, **17**, 445–449.

[132] R. M. Lynden-Bell and K. H. Michel, *Reviews of Modern Physics*, 1994, **66**, 721–762.

[133] J. Even, M. Carignano and C. Katan, *Nanoscale*, 2016, **8**, 6222–6236.

[134] N. Onoda-Yamamuro, O. Yamamuro, T. Matsuo and H. Suga, *Journal of Physics and Chemistry of Solids*, 1992, **53**, 277–281.

[135] D. H. Fabini, C. C. Stoumpos, G. Laurita, A. Kaltzoglou, A. G. Kontos, P. Falaras, M. G. Kanatzidis and R. Seshadri, *Angewandte Chemie International Edition*, 2016, **55**, 15392–15396.

[136] E. M. Mozur, A. E. Maughan, Y. Cheng, A. Huq, N. Jalarvo, L. L. Daemen and J. R. Neilson, *Chemistry of Materials*, 2017, **29**, 10168–10177.

[137] M. T. Weller, O. J. Weber, P. F. Henry, A. M. Di Pumpo and T. C. Hansen, *Chem. Commun.*, 2015, **51**, 4180–4183.

[138] D. B. Mitzi, *Inorganic Chemistry*, 2000, **39**, 6107–6113.

[139] B. Saparov and D. B. Mitzi, *Chemical Reviews*, 2016, **116**, 4558–4596.

[140] O. J. Weber, K. L. Marshall, L. M. Dyson and M. T. Weller, *Acta crystallographica Section B, Structural science, crystal engineering and materials*, 2015, **71**, 668–78.

[141] N. Mercier, N. Louvain and W. Bi, *CrystEngComm*, 2009, **11**, 720.

[142] J. M. Ball, M. M. Lee, A. Hey and H. Snaith, *Energy & Environmental Science*, 2013, **6**, 1739–1743.

[143] J. Burschka, N. Pellet, S.-J. Moon, R. Humphry-Baker, P. Gao, M. K. Nazeeruddin and M. Grätzel, *Nature*, 2013, **499**, 316–9.

[144] D. Prochowicz, M. Franckevičius, A. M. Cieślak, S. M. Zakeeruddin, M. Grätzel and J. Lewiński, *Journal of Materials Chemistry A*, 2015, **3**, 20772–20777.

[145] Q. Dong, Y. Fang, Y. Shao, P. Mulligan, J. Qiu, L. Cao and J. Huang, *Science*, 2015, **347**, 967–970.

[146] T. Baikie, Y. Fang, J. M. Kadro, M. Schreyer, F. Wei, S. G. Mhaisalkar, M. Graetzel and T. J. White, *Journal of Materials Chemistry A*, 2013, **1**, 5628.

[147] M. I. Saidaminov, A. L. Abdelhady, B. Murali, E. Alarousu, V. M. Burlakov, W. Peng, I. Dursun, L. Wang, Y. He, G. Maculan, A. Goriely, T. Wu, O. F. Mohammed and O. M. Bakr, *Nature Communications*, 2015, **6**, 7586.

[148] C. C. Stoumpos and M. G. Kanatzidis, *Advanced Materials*, 2016, **28**, 5778–5793.

[149] A. A. Petrov, N. A. Belich, A. Y. Grishko, N. M. Stepanov, S. G. Dorofeev, E. G. Maksimov, A. V. Shevelkov, S. M. Zakeeruddin, M. Graetzel, A. B. Tarasov and E. A. Goodilin, *Materials Horizons*, 2017, **4**, 625–632.

[150] E. L. Unger, A. R. Bowring, C. J. Tassone, V. L. Pool, A. Gold-Parker, R. Cheacharoen, K. H. Stone, E. T. Hoke, M. F. Toney and M. D. McGehee, *Chemistry of Materials*, 2014, **26**, 7158–7165.

[151] Z. Li, M. Yang, J.-S. Park, S.-H. Wei, J. Berry and K. Zhu, *Chemistry of Materials*, 2016, **28**, 284–292.

[152] C. C. Stoumpos, C. D. Malliakas and M. G. Kanatzidis, *Inorganic chemistry*, 2013, **52**, 9019–38.

[153] G. P. Nagabhushana, R. Shivaramaiah and A. Navrotsky, *Proceedings of the National Academy of Sciences*, 2016, **113**, 7717–7721.

[154] A. L. Abdelhady, M. I. Saidaminov, B. Murali, V. Adinolfi, O. Voznyy, K. Katsiev, E. Alarousu, R. Comin, I. Dursun, L. Sinatra, E. H. Sargent, O. F. Mohammed and O. M. Bakr, *The Journal of Physical Chemistry Letters*, 2016, **7**, 295–301.

[155] P. K. Nayak, M. Sendner, B. Wenger, Z. Wang, K. Sharma, A. J. Ramadan, R. Lovrinčić, A. Pucci, P. K. Madhu and H. J. Snaith, *Journal of the American Chemical Society*, 2018, **140**, 574–577.

[156] J. Navas, A. Sánchez-Coronilla, J. J. Gallardo, N. Cruz Hernández, J. C. Piñero, R. Alcántara, C. Fernández-Lorenzo, D. M. De los Santos, T. Aguilar and J. Martín-Calleja, *Nanoscale*, 2015, **7**, 6216–6229.

[157] L. A. Frolova, D. V. Anokhin, K. L. Gerasimov, N. N. Dremova and P. A. Troshin, *The Journal of Physical Chemistry Letters*, 2016, **7**, 4353–4357.

[158] J. S. Manser, M. I. Saidaminov, J. A. Christians, O. M. Bakr and P. V. Kamat, *Accounts of Chemical Research*, 2016, **49**, 330–338.

[159] Y.-Y. Zhang, S. Chen, P. Xu, H. Xiang, X.-G. Gong, A. Walsh and S.-H. Wei, *Chinese Physics Letters*, 2018, **35**, 036104.

[160] U.-G. Jong, C.-J. Yu, G.-C. Ri, A. P. McMahon, N. M. Harrison, P. R. F. Barnes and A. Walsh, *Journal of Materials Chemistry A*, 2018, **6**, 1067–1074.

[161] T. M. Koh, V. Shanmugam, X. Guo, S. S. Lim, O. Filonik, E. M. Herzig, P. Müller-Buschbaum, V. Swamy, S. T. Chien, S. G. Mhaisalkar and N. Mathews, *Journal of Materials Chemistry A*, 2018, **6**, 2122–2128.

[162] A. Babayigit, D. Duy Thanh, A. Ethirajan, J. Manca, M. Muller, H.-G. Boyen and B. Conings, *Scientific Reports*, 2016, **6**, 18721.

[163] B. Hailegnaw, S. Kirmayer, E. Edri, G. Hodes and D. Cahen, *The Journal of Physical Chemistry Letters*, 2015, **6**, 1543–1547.

[164] K. Cheyns, S. Peeters, D. Delcourt and E. Smolders, *Environmental Pollution*, 2012, **164**, 242–247.

[165] J. Buekers, E. Steen Redeker and E. Smolders, *Science of The Total Environment*, 2009, **407**, 3431–3438.

[166] L. D. Whalley, J. M. Frost, Y.-K. Jung and A. Walsh, *The Journal of Chemical Physics*, 2017, **146**, 220901.

[167] Y. Yin, Y. Huang, Y. Wu, G. Chen, W.-J. Yin, S.-H. Wei and X. Gong, *Chemistry of Materials*, 2017, **29**, 9429–9435.

[168] F. Brivio, J. M. Frost, J. M. Skelton, A. J. Jackson, O. J. Weber, M. T. Weller, A. R. Goni, A. M. A. M. A. Leguy, P. R. F. Barnes, A. Walsh, A. R. Goñi, A. M. A. M. A. Leguy, P. R. F. Barnes and A. Walsh, *Physical Review B*, 2015, **92**, 144308.

[169] V. D'Innocenzo, G. Grancini, M. J. P. Alcocer, A. R. S. Kandada, S. D. Stranks, M. M. Lee, G. Lanzani, H. J. Snaith and A. Petrozza, *Nature Communications*, 2014, **5**, 3586.

[170] K. Tanaka, T. Takahashi, T. Ban, T. Kondo, K. Uchida and N. Miura, *Solid State Communications*, 2003, **127**, 619–623.

[171] S. De Wolf, J. Holovsky, S.-J. Moon, P. Löper, B. Niesen, M. Ledinsky, F.-J. Haug, J.-H. Yum and C. Ballif, *The Journal of Physical Chemistry Letters*, 2014, **5**, 1035–1039.

[172] T. M. Brenner, D. A. Egger, A. M. Rappe, L. Kronik, G. Hodes and D. Cahen, *The Journal of Physical Chemistry Letters*, 2015, **6**, 4754–4757.

[173] M. Kepenekian, R. Robles, C. Katan, D. Sapori, L. Pedesseau and J. Even, *ACS Nano*, 2015, **9**, 1557–11567.

[174] D. Niesner, M. Wilhelm, I. Levchuk, A. Osvet, S. Shrestha, M. Batentschuk, C. Brabec and T. Fauster, *Physical Review Letters*, 2016, **117**, 126401.

[175] T. Wang, B. Daiber, J. M. Frost, S. A. Mann, E. C. Garnett, A. Walsh and B. Ehrler, *Energy Environ. Sci.*, 2017, **10**, 509–515.

[176] P. Azarhoosh, S. McKechnie, J. M. Frost, A. Walsh and M. Van Schilfgaarde, *APL Materials*, 2016, **4**, 091501.

[177] E. M. Hutter, M. C. Gélvez-Rueda, A. Osherov, V. Bulović, F. C. Grozema, S. D. Stranks and T. J. Savenije, *Nature Materials*, 2016, **16**, 115–120.

[178] J. M. Frost, K. T. Butler, F. Brivio, C. H. Hendon, M. van Schilfgaarde and A. Walsh, *Nano letters*, 2014, **14**, 2584–90.

[179] A. Walsh, D. O. Scanlon, S. Chen, X. G. Gong and S.-H. Wei, *Angewandte Chemie International Edition*, 2015, **54**, 1791–1794.

[180] L. Yin, G. Cheng, Y. Feng, Z. Li, C. Yang and X. Xiao, *RSC Advances*, 2015, **5**, 40369–40374.

[181] C. Eames, J. M. Frost, P. R. F. Barnes, B. C. O'Regan, A. Walsh and M. S. Islam, *Nature Communications*, 2015, **6**, 7497.

[182] T. Yang, G. Gregori, N. Pellet, M. Grätzel and J. Maier, *Angewandte Chemie International Edition*, 2015, **54**, 7905–7910.

[183] J. Mizusaki, K. Arai and K. Fueki, *Solid State Ionics*, 1983, **11**, 203–211.

[184] J. Oberschemidt and D. Lazarus, *Physical Review B*, 1980, **21**, 5813–5822.

[185] J. M. Azpiroz, E. Mosconi, J. Bisquert and F. De Angelis, *Energy Environ. Sci.*, 2015, **8**, 2118–2127.

[186] G. Richardson, S. O'Kane, R. G. Niemann, T. A. Peltola, J. M. Foster, P. J. Cameron, A. Walker, S. E. J. O'Kane, R. G. Niemann, T. A. Peltola, J. M. Foster, P. J. Cameron and A. B.Walker, *Energy Environ. Sci.*, 2016, **9**, 1476–1485.

[187] G. E. Eperon and D. S. Ginger, *ACS Energy Letters*, 2017, **2**, 1190–1196.

[188] G. Nedelcu, L. Protesescu, S. Yakunin, M. I. Bodnarchuk, M. Grotevent and M. V. Kovalenko, *Nano Letters*, 2015, **15**, 5635–5640.

[189] M. Bag, L. A. Renna, R. Y. Adhikari, S. Karak, F. Liu, P. M. Lahti, T. P. Russell, M. T. Tuominen and D. Venkataraman, *Journal of the American Chemical Society*, 2015, **137**, 13130–13137.

[190] O. S. Game, G. J. Buchsbaum, Y. Zhou, N. P. Padture and A. I. Kingon, *Advanced Functional Materials*, 2017, **27**, 1606584.

[191] I. Anusca, S. Balčinas, P. Gemeiner, Š. Svirskas, M. Sanlialp, G. Lackner, C. Fettkenhauer, J. Belovickis, V. Samulionis, M. Ivanov, B. Dkhil, J. Banys, V. V. Shvartsman and D. C. Lupascu, *Advanced Energy Materials*, 2017, **7**, 1700600.

[192] N. Onoda-Yamamuro, T. Matsuo and H. Suga, *Journal of Physics and Chemistry of Solids*, 1992, **53**, 935–939.

[193] C. N. Savory, A. Walsh and D. O. Scanlon, *ACS Energy Letters*, 2016, **1**, 949–955.

[194] N. N. Shlenskaya, N. A. Belich, M. Grätzel, E. A. Goodilin and A. B. Tarasov, *Journal of Materials Chemistry A*, 2018, **6**, 1780–1786.

[195] M. Chen, M.-G. Ju, A. D. Carl, Y. Zong, R. L. Grimm, J. Gu, X. C. Zeng, Y. Zhou and N. P. Padture, *Joule*, 2018, In Press.

[196] B. Saparov, F. Hong, J.-P. Sun, H.-S. Duan, W. Meng, S. Cameron, I. G. Hill, Y. Yan and D. B. Mitzi, *Chemistry of Materials*, 2015, **27**, 5622–5632.

[197] H. C. Sansom, G. F. S. Whitehead, M. S. Dyer, M. Zanella, T. D. Manning, M. J. Pitcher, T. J. Whittles, V. R. Dhanak, J. Alaria, J. B. Claridge and M. J. Rosseinsky, *Chemistry of Materials*, 2017, **29**, 1538–1549.

[198] I. Turkevych, S. Kazaoui, E. Ito, T. Urano, K. Yamada, H. Tomiyasu, H. Yamagishi, M. Kondo and S. Aramaki, *ChemSusChem*, 2017, **10**, 3754–3759.

[199] B. Vargas, E. Ramos, E. Pérez-Gutiérrez, J. C. Alonso and D. Solis-Ibarra, *Journal of the American Chemical Society*, 2017, **139**, 9116–9119.

[200] N. T. Hahn, A. J. E. Rettie, S. K. Beal, R. R. Fullon and C. B. Mullins, *The Journal of Physical Chemistry C*, 2012, **116**, 24878–24886.

[201] J. Nelson, *The Physics of Solar Cells*, Imperial College Scientific Publishing, 2003.

[202] O. D. Miller, E. Yablonovitch and S. R. Kurtz, *IEEE Journal of Photovoltaics*, 2012, **2**, 303–311.

[203] W. Clegg, A. J. Blake, J. M. Cole, J. S. O. Evans, P. Main, S. Parsons and D. J. Watkin, *Crystal Structure Analysis*, Oxford University Press, 2009.

[204] W. David, D. Akporiaye, R. Ibberson and C. Wilson, *The high resolution powder diffractometer at ISIS - an introductory user's guide*, 1988, `https://inis.iaea.org/search/search.aspx?orig{_}q=RN:20027124`.

[205] R. M. Ibberson, W. I. F. David and K. S. Knight, *The high resolution powder diffractometer (HRPD) at ISIS - a user guide*, 1992, `https://inis.iaea.org/search/search.aspx?orig{_}q=RN:23079613`.

[206] G. Kieslich, S. Sun and A. K. Cheetham, *Chem. Sci.*, 2015, **6**, 3430–3433.

[207] R. Wasylishen, O. Knop and J. Macdonald, *Solid State Communications*, 1985, **56**, 581–582.

[208] I. Swainson, R. Hammond, C. Soullière, O. Knop and W. Massa, *Journal of Solid State Chemistry*, 2003, **176**, 97–104.

[209] A. Poglitsch and D. Weber, *The Journal of Chemical Physics*, 1987, **87**, 6373.

[210] A. A. Bakulin, O. Selig, H. J. Bakker, Y. L. A. Rezus, C. Müller, T. Glaser, R. Lovrincic, Z. Sun, Z. Chen, A. Walsh, J. M. Frost and T. L. C. Jansen, *The Journal of Physical Chemistry Letters*, 2015, **6**, 3663–3669.

[211] O. Selig, A. Sadhanala, C. Müller, R. Lovrincic, Z. Chen, Y. L. A. Rezus, J. M. Frost, T. L. C. Jansen and A. A. Bakulin, *Journal of the American Chemical Society*, 2017, **139**, 4068–4074.

[212] M. I. Aroyo, A. Kirov, C. Capillas, J. M. Perez-Mato, H. Wondratschek and IUCr, *Acta Crystallographica Section A Foundations of Crystallography*, 2006, **62**, 115–128.

[213] Y. Ren, I. W. H. Oswald, X. Wang, G. T. McCandless and J. Y. Chan, *Crystal Growth & Design*, 2016, **16**, 2945–2951.

[214] P. S. Whitfield, N. Herron, W. E. Guise, K. Page, Y. Q. Cheng, I. Milas and M. K. Crawford, *Scientific Reports*, 2016, **6**, 35685.

[215] M. Szafrański and A. Katrusiak, *The Journal of Physical Chemistry Letters*, 2016, **7**, 3458–3466.

[216] M. U. Rothmann, W. Li, Y. Zhu, U. Bach, L. Spiccia, J. Etheridge and Y.-B. Cheng, *Nature Communications*, 2017, **8**, 14547.

[217] J. M. Kadro, K. Nonomura, D. Gachet, M. Grätzel and A. Hagfeldt, *Scientific reports*, 2015, **5**, 11654.

[218] A. Leguy, P. Azarhoosh, M. I. Alonso, M. Campoy-Quiles, O. J. Weber, J. Yao, D. Bryant, M. T. Weller, J. Nelson, A. Walsh, M. van Schilfgaarde and P. R. F. Barnes, *Nanoscale*, 2016, **8**, 6317–6327.

[219] A. M. A. Leguy, A. R. Goñi, J. M. Frost, J. Skelton, F. Brivio, X. Rodríguez-Martínez, O. J. Weber, A. Pallipurath, M. I. Alonso, M. Campoy-Quiles, M. T. Weller, J. Nelson, A. Walsh and P. R. F. Barnes, *Phys. Chem. Chem. Phys.*, 2016, **18**, 27051–27066.

[220] M. Ledinský, P. Löper, B. Niesen, J. Holovský, S.-J. Moon, J.-H. Yum, S. De Wolf, A. Fejfar and C. Ballif, *The journal of physical chemistry letters*, 2015, **6**, 401–6.

[221] J. H. Noh, S. H. Im, J. H. Heo, T. N. Mandal and S. I. Seok, *Nano Letters*, 2013, **13**, 1764–1769.

[222] M. Hu, L. Liu, A. Mei, Y. Yang, T. Liu and H. Han, *Journal of Materials Chemistry A*, 2014, **2**, 17115–17121.

[223] J.-W. Lee, D.-J. Seol, A.-N. Cho and N.-G. Park, *Advanced Materials*, 2014, **26**, 4991–8.

[224] T. M. Koh, K. Fu, Y. Fang, S. Chen, T. C. Sum, N. Mathews, S. G. Mhaisalkar, P. P. Boix and T. Baikie, *The Journal of Physical Chemistry C*, 2014, **118**, 16458–16462.

[225] S. Pang, H. Hu, J. Zhang, S. Lv, Y. Yu, F. Wei, T. Qin, H. Xu, Z. Liu and G. Cui, *Chemistry of Materials*, 2014, **26**, 1485–1491.

[226] G. E. Eperon, S. D. Stranks, C. Menelaou, M. B. Johnston, L. M. Herz and H. J. Snaith, *Energy & Environmental Science*, 2014, **7**, 982–988.

[227] D. Mitzi and K. Liang, *Journal of Solid State Chemistry*, 1997, **134**, 376–381.

[228] M. R. Filip, G. E. Eperon, H. J. Snaith and F. Giustino, *Nature Communications*, 2014, **5**, 5757.

[229] A. Amat, E. Mosconi, E. Ronca, C. Quarti, P. Umari, M. K. Nazeeruddin, M. Grätzel and F. De Angelis, *Nano letters*, 2014, **14**, 3608–3616.

[230] T. Chen, B. J. Foley, C. Park, C. M. Brown, L. W. Harriger, J. Lee, J. Ruff, M. Yoon, J. J. Choi and S.-H. Lee, *Science Advances*, 2016, **2**, e1601650.

[231] Q. Han, S.-H. Bae, P. Sun, Y.-T. Hsieh, Y. M. Yang, Y. S. Rim, H. Zhao, Q. Chen, W. Shi, G. Li and Y. Yang, *Advanced Materials*, 2016, **28**, 2253–2258.

[232] A. Binek, F. C. Hanusch, P. Docampo and T. Bein, *The Journal of Physical Chemistry Letters*, 2015, **6**, 1249–1253.

[233] O. J. Weber, B. Charles and M. T. Weller, *J. Mater. Chem. A*, 2016, **4**, 15375–15382.

[234] M. T. Weller, O. J. Weber, J. M. Frost and A. Walsh, *The Journal of Physical Chemistry Letters*, 2015, **6**, 3209–3212.

[235] P. Németh, L. A. J. Garvie, T. Aoki, N. Dubrovinskaia, L. Dubrovinsky and P. R. Buseck, *Nature communications*, 2014, **5**, 5447.

[236] R. X. Yang, J. M. Skelton, E. L. da Silva, J. M. Frost and A. Walsh, *The Journal of Physical Chemistry Letters*, 2017, **8**, 4720–4726.

[237] L.-Q. Fan, J.-H. Wu and IUCr, *Acta Crystallographica Section E Structure Reports Online*, 2007, **63**, i189–i189.

[238] T. Chen, W.-L. Chen, B. J. Foley, J. Lee, J. P. C. Ruff, J. Y. P. Ko, C. M. Brown, L. W. Harriger, D. Zhang, C. Park, M. Yoon, Y.-M. Chang, J. J. Choi and S.-H. Lee, *Proceedings of the National Academy of Sciences*, 2017, **114**, 7519–7524.

[239] D. H. Fabini, T. A. Siaw, C. C. Stoumpos, G. Laurita, D. Olds, K. Page, J. G. Hu, M. G. Kanatzidis, S. Han and R. Seshadri, *Journal of the American Chemical Society*, 2017, **139**, 16875–16884.

[240] J. T. Jacobsson, J. P. Correa Baena, M. Pazoki, M. Saliba, K. Schenk, M. Grätzel and A. Hagfeldt, *Energy Environ. Sci.*, 2016, **9**, 1706–1724.

[241] M. I. Saidaminov, A. L. Abdelhady, G. Maculan and O. M. Bakr, *Chemical communications (Cambridge, England)*, 2015, **51**, 17658–61.

[242] C. Yi, J. Luo, S. Meloni, A. Boziki, N. Ashari-Astani, C. Grätzel, S. M. Zakeeruddin, U. Röthlisberger and M. Grätzel, *Energy & Environmental Science*, 2016, **9**, 656–662.

[243] G. Kieslich, S. Sun and T. Cheetham, *Chemical Science*, 2014, **5**, 4712–4715.

[244] M. R. Filip, G. E. Eperon, H. J. Snaith and F. Giustino, *Nature Communications*, 2014, **5**, 5757.

[245] T. Bu, X. Liu, Y. Zhou, J. Yi, X. Huang, L. Luo, J. Xiao, Z. Ku, Y. Peng, F. Huang, Y.-B. Cheng and J. Zhong, *Energy & Environmental Science*, 2017, **10**, 2509–2515.

[246] Z. Xiao, W. Meng, J. Wang, D. B. Mitzi and Y. Yan, *Materials Horizons*, 2017, **4**, 206–216.

[247] A. K. Cheetham and C. N. R. Rao, *Science (New York, N.Y.)*, 2007, **318**, 58–9.

[248] A. K. Cheetham, C. N. R. Rao and R. K. Feller, *Chem. Commun.*, 2006, **0**, 4780–4795.

[249] M. E. Kamminga, G. A. de Wijs, R. W. A. Havenith, G. R. Blake and T. T. Palstra, *Inorganic Chemistry*, 2017, **56**, 8408–8414.

[250] A. J. Dennington and M. T. Weller, *Dalton Transactions*, 2016, **45**, 17974–17979.

[251] A. J. Dennington and M. T. Weller, *Dalton Transactions*, 2018, **47**, 3469–3484.

[252] O. Toma, N. Mercier and C. Botta, *European Journal of Inorganic Chemistry*, 2013, **2013**, 1113–1117.

[253] G. Xu, G.-C. Guo, M.-S. Wang, Z.-J. Zhang, W.-T. Chen and J.-S. Huang, *Angewandte Chemie International Edition*, 2007, **46**, 3249–3251.

[254] P. H. Svensson and L. Kloo, *Chemical Reviews*, 2003, **103**, 1649–1684.

[255] N. Alcock, *Advances in Inorganic Chemistry and Radiochemistry*, 1972, **15**, 1–58.

[256] J.-H. Lee, N. Bristowe, P. Bristowe and T. Cheetham, *Chem. Commun.*, 2015, **51**, 6434–6437.